Two-Window Heterodyne Methods to Characterize Light Fields

by

Frank Reil

Department of Physics
Duke University

Date:_____
Approved:

_____
Dr. John E. Thomas, Supervisor

_____
Dr. Daniel J. Gauthier

_____
Dr. Robert Behringer

_____
Dr. Moo-Young Han

_____
Dr. Bob Guenther

Dissertation submitted in partial fulfillment of the
requirements for the degree of Doctor of Philosophy
in the Department of Physics
in the Graduate School of
Duke University

2003

ABSTRACT

(Physics)

Two-Window Heterodyne Methods to Characterize Light Fields

by

Frank Reil

Department of Physics
Duke University

Date:_____
Approved:

_____
Dr. John E. Thomas, Supervisor

_____
Dr. Daniel J. Gauthier

_____
Dr. Robert Behringer

_____
Dr. Moo-Young Han

_____
Dr. Bob Guenther

An abstract of a dissertation submitted in partial fulfillment of
the requirements for the degree of Doctor of Philosophy
in the Department of Physics
in the Graduate School of
Duke University

2003

Abstract

In this dissertation, I develop a novel Two-Window heterodyne technique for measuring the time-resolved Wigner function of light fields, which allows their complete characterization. A Wigner function is a quasi-probability density that describes the transverse position and transverse momentum of a light field and is Fourier-transform related to its mutual coherence function. It obeys rigorous transport equations and therefore provides an ideal way to characterize a light field and its propagation through various media. I first present the experimental setup of our Two-Window technique, which is based on a heterodyne scheme involving two phase-coupled Local Oscillator beams we call the Dual-LO. The Dual-LO consists of a focused beam ('SLO') which sets the spatial resolution, and a collimated beam ('BLO') which sets the momental resolution. The resolution in transverse position and transverse momentum can be adjusted individually by the size of the SLO and BLO, which enables a measurement resolution surpassing the uncertainty principle associated with Fourier-transform pairs which limits the resolution when just a single LO is used. We first use our technique to determine the beam size, transverse coherence length and radius of curvature of a Gaussian-Schell beam, as well as its longitudinal characteristics, which are related to its optical spectrum. We then examine Enhanced Backscattering at various path-lengths in the turbid medium. For the first time ever, we demonstrate the phase-conjugating properties of a turbid medium by observing the change in sign of the radius of curvature for a

non-collimated field incident on the medium. We also perform time-resolved measurements in the transmission regime. In tenuous media we observe two peaks in phase-space confined by a hyperbola which are due to low-order scattering. Their distance depends on the chosen path-delay. Some coherence and even spatial properties of the incident field are preserved in those peaks as measurements with our Two-Window technique show. Various other applications are presented in less detail, such as the Wigner function of the field inside a speckle produced by a piece of glass containing air bubbles.

Acknowledgments

First, I would like to thank John Thomas for being a great advisor. His love of physics has been contagious and his insight inspirational; this helped me change my mind when I had thought about switching to economics. From a human side, John has always been a very decent person who was fun to be around.

Thank you also to all my friends I made at Duke. Among my fellow graduate students I would first like to mention Jon Blakely, with whom I had many political discussions. He's a perfect example that you can disagree with someone on a great many political topics and be good friends with the same time. The same is true for Rob Macri, who I've been with to China Inn numerous times over the past years. I would also like to mention Steve-O Nelson, Shigeyuki Tajima, Konstantin Sabourov and Bob Hartley, with whom I hung out on many occasions, when the busy schedule in graduate school permitted, as well as Meenakshi Dutt, Marina Brozovic and Michael Stenner, which I liked to socialize with in the department.

I'm also thankful to all my fellow co-workers in our group who provided a very pleasant environment to work in: My predecessor Adam and post-doc Samir, who left in 1999 and 2000; then Ken, Mike, Stephen and Lee, and also the students who joined the group after me, Staci and Joe.

I would also like to thank my friends at home who I kept in contact with over the years, most of all my good buddy of 17 years, Martin Nolte. He is one of the funniest and most decent people I know, and manages to organize circle of friends

reunion-parties each time I visit home.

Most of all I'm thankful to my parents back in Germany who have instilled my early interest in science by giving me vividly illustrated books of astronomy and paleontology when I was about 5, while never pushing me to do or read stuff I didn't like to. Oftentimes my father would sat down with me to translate some of those huge numbers appearing next to the pictures of Jupiter, Saturn and the Andromeda galaxy into some hand-drawn figure which was more accessible to my mind at that stage - and still is :-). Next came the electronics kit I got for chrismas when I was 8. I wasn't allowed to use the soldering iron by myself since my father was afraid I could hurt my fingers which would have interfered with me playing piano. One night, when everyone was asleep, I went down to the basement anyway to finish that multivibrator - needless to say, I ended up with a couple of blisters on my fingers. Despite that first, rather unpleasant experience with experimental physics, a decade of distorted radio reception for my poor mother during her favorite radio shows ensued, which she bravely put up with in the name of science - thank you, Mama! Also thanks to my sister Margarete who has been a great sibling and friend over the years we grew up together.

For my beloved parents and sister

Contents

List of Figures

Chapter 1

Introduction

Over the past two decades, optical tomographic methods have become increasingly important tools to investigate architectural and chemical features of small objects in various fields. For example, optical wavelengths are small enough to allow the distinction of a variety of features of interest in biological samples, also by exploiting coherent properties of the field. Pulsed light or broadband light enable time-resolved measurements, i.e., the exclusive detection of light that has travelled a given path length in a medium under investigation, by superposing it with a reference beam and measuring the interference (Optical Coherence Tomography, 'OCT'). For measurements of reflection from layered structures, this allows the imaging of layers at various depth, by varying the path delay of the reference beam. In the measurement of transmitting light in strongly scattering media this method can be used to enhance the image quality by suppressing scattered light which takes a longer path in the medium than non-scattered ('ballistic') light. OCT has especially been of interest for medical applications, as for the investigation of outer skin layers or the interior of the eye. With the advent of new low-cost broadband semiconductor light sources of almost any spectral composition and coherence properties over the past couple of years, time-resolved measurements do not rely on bulky pulsed lasers any more. In our experiment we use a 'superluminescent diode ('SLD'), which has

a transverse coherence close to a laser diode but longitudinal coherence length of just 25 microns. In Chapter 2 I will give an overview over the most common optical tomographic methods.

In this dissertation I present a novel Two-Window Heterodyne method which allows the direct measurement of the Wigner function of a light field [1]. Wigner functions are a convenient way to fully characterize light fields up to their first-order-coherence properties: A Wigner function simultaneously describes the transverse position and momentum of a light field while preserving all phase and amplitude information of the field. Wigner functions obey rigorous transport equations and are a convenient way to describe the propagation of fields, through turbid, multiple scattering media, for example.

Our Two-Window technique allows the phase-sensitive measurement of light fields, unlike intensity measurements, as well as the *immediate* distinction between coherent and incoherent contributions to the field, unlike the Single-Window technique employed previously [2–5].

We use the Two-Window technique to classify the beams generated by our SLD, i.e., its transverse phase front as well as its first-order coherence properties both transversely and longitudinally. The main part of this thesis deals with the measurements of Wigner functions backscattered and transmitted through turbid media. Our method allows the immediate distinction between coherent and incoherent light exiting the medium. It allows us to observe Enhanced Backscattering ("EBS"), which causes the intensity of backscattered light to be twice as big opposite of the direction of incidence than in other directions, thanks to constructive interference of pairs of wavelets oppositely travelling along the same sequence of scatterers. For the first time we are able to observe the change of sign of the radius of curvature for

a curved wavefront experiencing EBS: A divergent beam incident on the medium generates a converging wavefront exiting the sample, and the other way around.

We also observe conservation of coherence for scattered light in transmission, and look inside the speckle. The presented study will hopefully open new avenues to examine and classify light fields in various fields, in particular in biomedical imaging. In the following, I will briefly outline the inner workings of the Two-Window technique.

1.1 Wigner functions and their measurement

Wigner functions describe the position and momentum distribution of a light field in a plane perpendicular to its direction of propagation and contains all phase- and amplitude information about it. It is Fourier-transform related to the correlation function $\Gamma(x, x') = \langle \mathcal{E}^*(x)\mathcal{E}(x')\rangle$ of the field:

$$W(x,p) = \int \frac{d\epsilon}{2\pi} \exp(i\epsilon p)\langle \mathcal{E}^*(x+\frac{\epsilon}{2})\mathcal{E}(x-\frac{\epsilon}{2})\rangle \tag{1.1}$$

For Gaussian beams, the Wigner function bears many similarities to the geometrical description of rays; for all other fields though it contains negative interference terms. A detailed treatment of Wigner functions is given in Chapter 3.

In this thesis, we present a novel Two-Window heterodyne detection scheme which allows the mapping of the *true* Wigner function in a given direction within a transverse plane [1]. Figure 1.1 demonstrates how it works: A signal beam is frequency shifted by means of an acousto-optical modulator by 110 MHz and incident on to a sample. The emerging field is superposed with a combination of two local oscillator beams ('Dual-LO'), each LO shifted by 120 MHz and 120.003 MHz

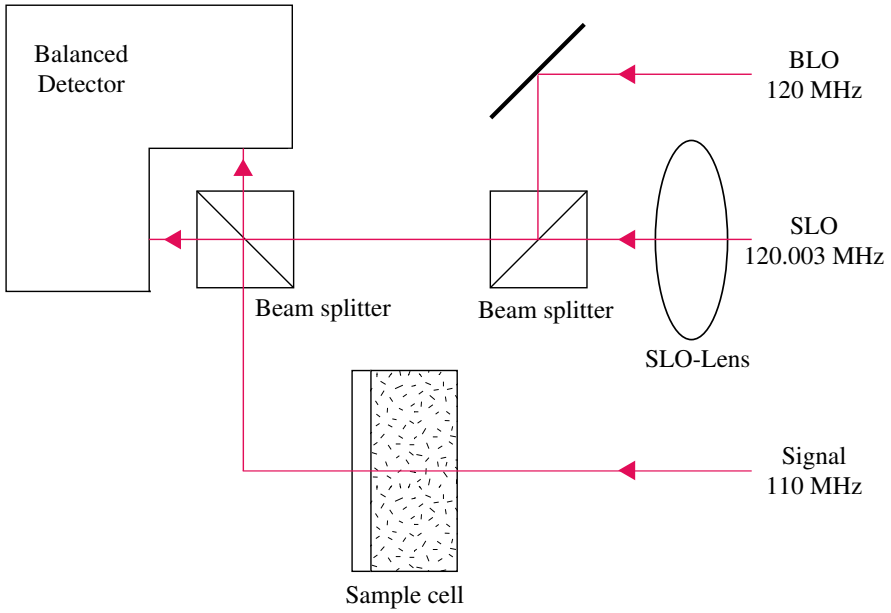

Figure 1.1: Basic scheme for Two-Window technique. The Signal field emerging from the sample is superposed with a Dual-LO, which consists of a collimated LO ('big' LO or 'BLO') and a focused LO ('small' LO or 'SLO'). The combined field is detected by a balanced detector in a heterodyne scheme.

respectively. This Dual-LO consists of a focused beam ("SLO") and collimated ("BLO") beam; the SLO determining the spatial resolution, the BLO the angular distribution. The two beat notes at 10 and 10.003 MHz are detected while moving the Dual-LO relative to the Signal field in a grid-like fashion in position and momentum. The relative phase between the two beat notes is measured by a Lock-In amplifier, whose quadrature signals then contain all the information necessary to calculate the field's Wigner function. Those quadrature signals are recorded during the scanning process and the Wigner function is retrieved afterwards by performing a simple transformation.

Like the One-Window technique, the Two-Window technique has a high dynamic range of 130 dB [5], with the lowest detectable power level of about 10^{-16} W (300 photons/s).

The resolution for position and momentum in this technique can be adjusted individually, unlike in the Single-LO technique, where a single LO causes a trade-off between position x- and momentum p-resolution, due to the inverse relationship between spread of x and p of the LO. Therefore, the Two-Window technique has a much better phase-space resolution than the Single-LO technique; it allows the measurement of *true* as opposed to *smoothed* Wigner functions. Figure 1.2 shows the sizes of a single-LO (a) and a Dual-LO (b) in phase-space, which determine the resolution in each method.

The high resolution and phase sensitivity allows new measurements of interesting coherent phenomena in turbid media, like the Enhanced Backscattering effect. This effect describes the enhancement of backscattering opposite to the direction of incidence of a field, due to the coherent addition of time-reversed counter-propagating wavelets scattered by the same sequence of scatterers in the turbid medium. Using

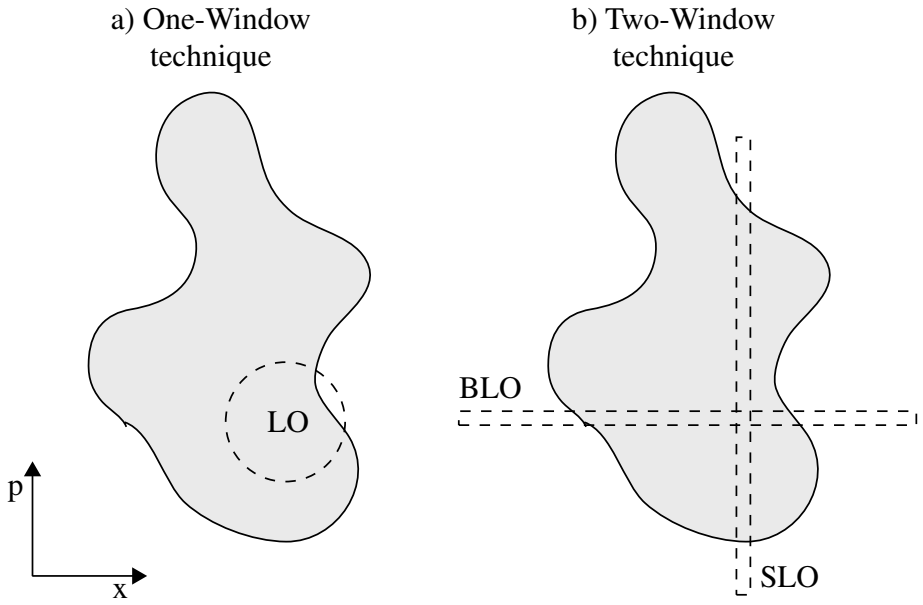

Figure 1.2: An electric field in phase-space (grey shaded shape) is measured by a heterodyne detection scheme. a) One-Window technique; the dashed circle shows the phase-space distribution of the LO. b) Two-Window technique, the dashed lines show the SLO and BLO which comprise the Dual-LO.

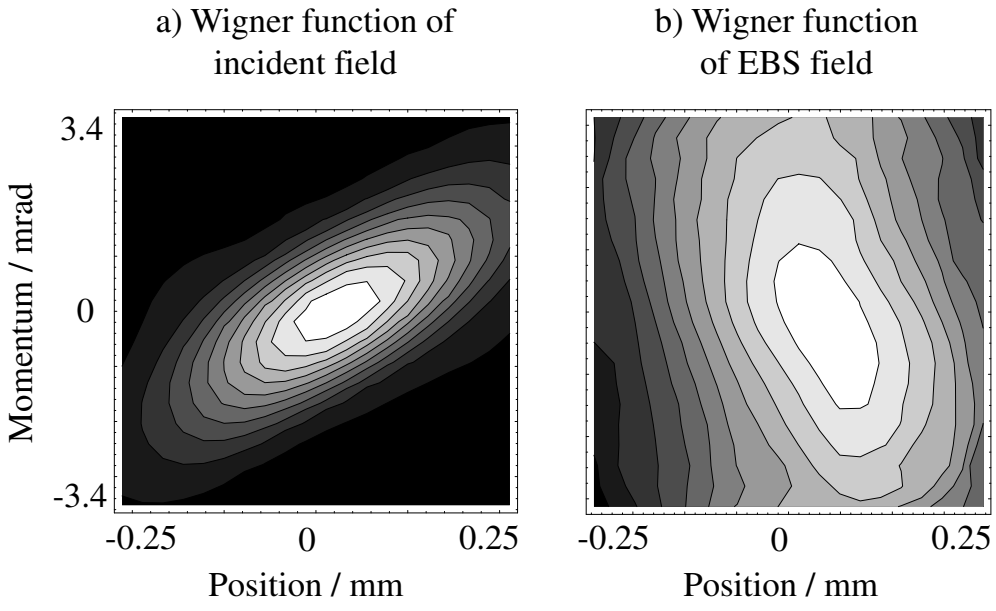

Figure 1.3: Wigner functions of fields incident on (a) and Enhanced-backscattered from (b) our turbid medium.

our two-window methods, we were for the first time able to show the reversal of sign of the radius of curvature of an incident wavefront. Figure 1.3 a) shows the Wigner function of a divergent field, incident on our turbid medium consisting of polystyrene spheres suspended in a solution. The tilt to the right indicates that the field is divergent, as will be explained in Chapter 3. In Figure 1.3 b), the Wigner function of the backscattered field is shown: The phase-space ellipse now tilts to the left, indicating a convergent field, confirming that the divergent incident field has reflected upon itself. The background which is broad in momentum, is the *incoherent background*, referring to the incoherent sum of intensities scattered regularly. This experiment is extremely challenging; various parts of the system have to be adjusted rapidly on a micrometer scale against the relatively strong and fast drift of our light source. It confirms for the first time ever the phase-conjugating properties of a turbid medium with respect to a curved wavefront. The phase-sensitivity of our Two-Window technique displayed in this experiment can refine optical tomographic measurements of scattering media in general. Enhanced Backscattering will be discussed further in Chapter 11 and Chapter 12.

Another interesting demonstration for the high resolution and phase sensitivity of our system is a small phase-space region in a single speckle field generated by a piece of glass containing air bubbles. Figure 1.4 shows the in-phase- and out-of-phase quadrature signals of the complex beat signal we measure, scanned over a phase-space region of just ± 0.25 mm and ± 0.625 mrad. The quadrature signals measured with our Two-Window technique are shown in a) and b); the resulting Wigner function is pictured in c). As a comparison, the bottom row shows the same phase-space region scanned by just the collimated LO (d) and the focused LO (e) by means of the One-Window technique. The latter detect two different stronger

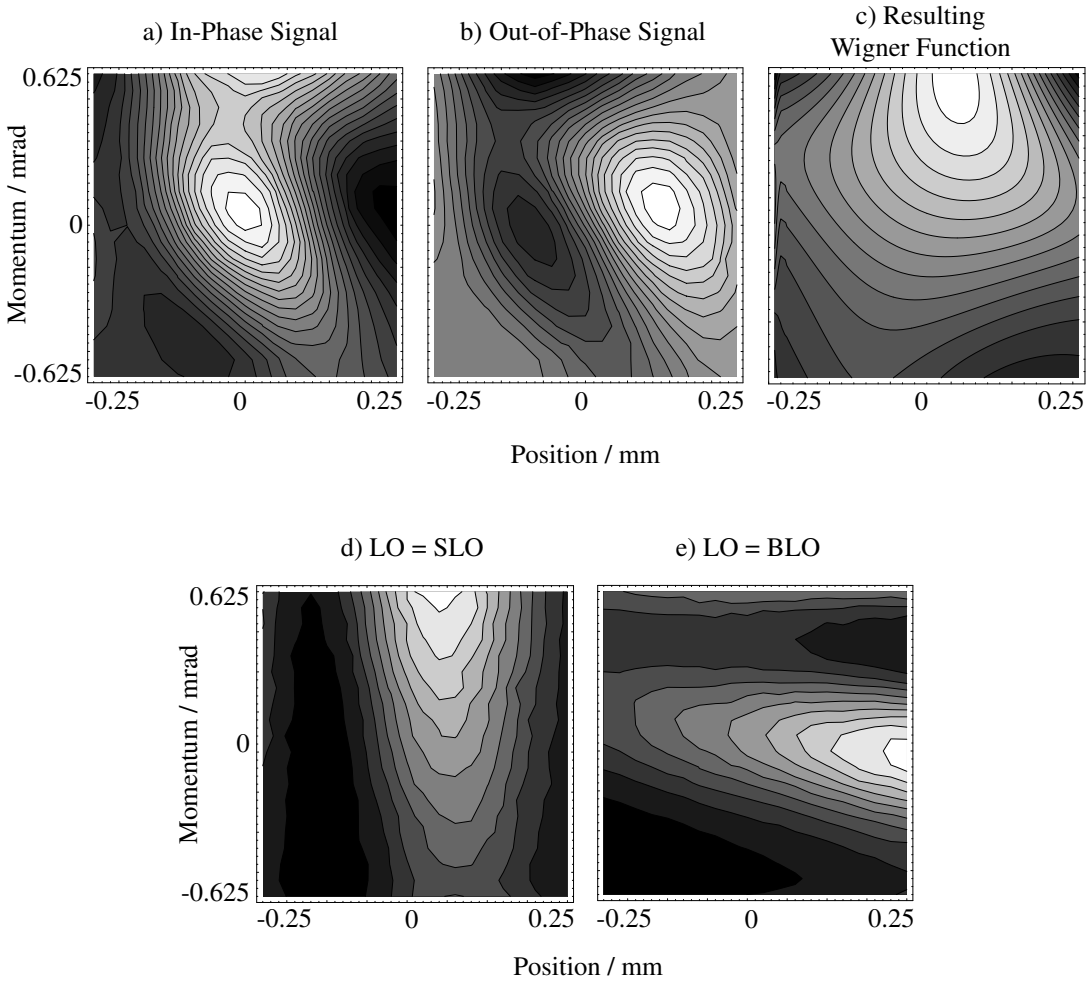

Figure 1.4: Single speckle measured by Two-Window (top row) and One-Window technique (bottom). a) In- and b) out-of-Phase quadrature signals, c) resulting Wigner function. Single-LO scan over the same part of phase-space with SLO only (d), and BLO only (e).

speckles outside the scanned region (as larger scans reveal) and yield insufficient information about the field inside the scanned region. The Two-Window technique, on the other hand, provides immediate phase-information of the field in the region and allows the retrieval of the true Wigner function, as seen in (c).

The low coherence length of 24.9 μm of our light source enables the selection of light having travelled a given path length. This is done by exploiting the fact that two fields from the same light source only interfere when the path travelled is equal within the longitudinal resolution Δl_B =21 μm. For scattering experiments in transmission, this allows the suppression of the ballistic (i.e., non-scattered) component through selection of a non-zero path-delay, which for dilute media is much stronger than the scattered components. Light backscattered and transmitted at various path delays also provide information about the properties of scatterers and medium. For example, in Enhanced Backscattering, the narrowing of the EBS cone with increasing path delay determines the scattering parameters such as the mean free path l and the transport mean free path l^*. Additional features, such as the momentum side-peaks of the EBS cone we observe, potentially hint towards aberrations from the diffusion regime. In transmission, time-resolution helps resolve the question about the contribution of various orders of scattering to the scattered field (see Chapter 13).

In summary, our Two-Window technique presents a new way to fully characterize a light field by measuring its Wigner function. A Wigner function contains all phase- and amplitude information contained in the field and obeys strict propagation laws. Our technique allows for the immediate distinction between coherent and incoherent parts of a light field, unlike the previously employed Single-Window technique. We apply the Two-Window technique to the determination of beam

parameters such as beam-size, curvature, and transverse and longitudinal coherence; the characterization of speckle, and to the study of propagation of light fields in turbid media.

1.2 Thesis organization

In Chapter 2 I will give an overview over the most important optical tomography methods. The two methods for path-resolved tomography, in the time- and in the frequency domain, are presented first. Thereafter, resolution enhancing techniques and those gaining information on chemical composition are briefly described. The chapter concludes with a section on Optical Coherence Tomography (OCT) and -Microscopy (OCM), which are related to our experiment.

In Chapter 3 we introduce the Wigner function. It basic properties, including both coherent and incoherent light, are presented, and its behavior during propagation through linear optical systems, in particular free space and lenses, are discussed.

The One-Window technique, which is the basis for the Two-Window technique, will be presented in Chapter 4. In addition to the experimental setup and its components we will discuss the measured mean square beat signal and its relation to the Wigner function as well as its shortcomings that triggered the development of the Two-Window technique. In Chapter 5 we present the Two-Window technique. Again, the experimental setup is described , the *complex* beat signal measured for ideal and non-ideal LOs and the retrieval of the *true* Wigner function are discussed. This chapter concludes with a description of essential parts of the Two-Window technique like the phase-locked loop and an overview of the complete system.

Chapter 6 presents the optical properties superluminescent diode (SLD) and its control gadgets used in our experiment: its power-supply and temperature-

stabilization. The generation of a collimated Gaussian beam from the SLD output field is described, as well as countermeasures against drift and beam instabilities.

Chapter 7 and Chapter 8 present the theoretical footing and the experimental results of the characterization of the transverse beam profile of the SLD using our Two-Window technique. Chapter 9 presents the corresponding results for the longitudinal beam characteristics of the SLD.

The second part of this thesis deals with scattering in turbid media. Chapter 10 describes the basics of scattering theory. The most important single-scattering models are discussed, which describe the amplitude of an electromagnetic wave scattering from a single particle for a range of special cases. In the second part of this chapter the most important models for the propagation of light in turbid media of various concentrations are presented.

In Chapter 11 and Chapter 12, theory and experimental results for our experiment on Enhanced Backscattering are presented. Chapter 11 discusses the basic principles of EBS to the complex beat signal measured for low-coherence light. Chapter 12 shows our experimental results for flat and curved incident beams.

Finally, Chapter 13 examines scattering in dilute media. The contributions of various orders of scattering as well as the preservation of coherence in scattered light are investigated. Chapter 14 concludes this thesis with a summary and discusses future directions.

Chapter 2

Optical Tomography Methods

2.1 Introduction

With the advent of technologies enabling the engineering of semiconductor light sources covering a spectrum from the far infrared to the far ultraviolet and almost arbitrary coherence properties and beam profiles, optical tomography of biological and non-biological materials has experienced a dramatic boost. This is especially true for time-resolved measurements which formerly depended on large and expensive femto-second lasers but can now be performed by small and inexpensive broadband superluminescent diodes (SLDs).

A field especially interesting for optical tomography is the medical field, where light backscattered from or generated in a sample provides insight about structural and chemical composition of biological tissue. A general feature of these samples is that the light experiences scattering and absorption between the surface and the tissue layer or object of interest. While some techniques contain ways to eliminate scattered or out-of-focus light, others collect that light for additional gain of information.

For example, a relatively common procedure these days is the examination of light backscattered from skin tissue to detect architectural abnormalities which can

be an indicator for cancer, in particular melanoma [6, 7]. Various methods which measure the way light diffuses through breast tissue enable the detection of tumors of less than 1 cm diameter before metastasis occurs and treatment becomes more difficult [8, 9].

Optical methods also provide a safe way to image cerebral oxygenation, blood volume by exploiting the characteristic absorption by hemoglobin, which acts as a natural contrast agent. But also artificial contrast agents like indocyanine have been administered for example to monitor blood flow optically [8].

Most optical techniques which examine the chemical composition of a sample make use of light generated in the sample by fluorescence, two- or multiple-photon processes or Raman scattering. The intensity, frequency composition or temporal profile of the response can be an indicator for the type and concentration of a chemical in question.

There are many approaches to push the spatial resolution for an optical method beyond the limit dictated by the wavelength of the used light. Two of the most important techniques are Near-field scanning optical microscopy (NSOM) and deconvolution which are presented in Section 2.5.1 and Section 2.5.2.

In the following sections I will give a brief overview over the most prominent optical tomography methods which are being developed today.

2.2 Time domain methods

Time domain methods use ultrashort light pulses or broadband light with a similar coherence time to obtain time-resolution, which in turn provides path-length resolution in the medium once the local speed of light is known. In the simplest case, femtosecond pulses of laser light are incident on a sample and the intensity of

the emerging light is measured by a streak camera [10–12]. [1] Ultra-fast Kerr gates provide another way of time-gating [14, 15]. Time-gating using broadband sources exploits the fact that two beams generated by the same light source only interfere if the difference in the paths they have travelled is within the coherence length of the light. By shining one beam onto the sample and superposing the emerging light with a second beam, only the parts of the field which match the path delay of the second beam contribute to interference, all other parts average out due to the random phase of broad band light. The interference signal can be measured by homo- or heterodyne detection. We postpone a more detailed explanation to Section 2.8, where we introduce Optical Coherence Tomography (OCT) which is a precursor to our experiment.

By varying the time delay of the trigger for the streak camera in case of the femtosecond laser setup or the path delay in case of a broadband source, light that has travelled a given additional path in the medium can be exclusively detected [10, 11]. In transmission, *ballistic*, i.e. non-scattered light can be selected, which arrives first at the opposite surface of the sample (path delay equals zero) [12]. This way scattered light can be suppressed, which enhances the visibility of objects hidden in the sample. The intensity of the ballistic light decreases exponentially with distance; the exponent is proportional to the sum of the absorption and scattering coefficients. For near-infrared light incident on most skin tissue, the ballistic component drops below the detection level after a few millimeters.

A deeper penetration into turbid media is possible by analyzing the scattered light component. In the transmission case, this component reaches the sample surface after the ballistic component, since it travels a longer path. Time gating

[1] A streak camera measures ultrafast light phenomena (resolution about 0.2 ps or 60 μm light advancement) and delivers intensity vs. time vs. position (or wavelength) information [13].

allows the selection of scattered light of a given path delay here as well; its amplitude or intensity as a function of path delay contain information about the concentration and properties of the scatterers in the sample. A more detailed treatment of light transmitted through turbid media is given in Chapter 13.

These time domain methods can also be used for fluorescence imaging methods [16], as described in Section 2.4.

2.3 Frequency domain methods

Frequency domain methods examine how light modulated at radio frequency propagates in a medium by measuring phase changes of the sideband frequencies with respect to the carrier frequency. A way to study how light diffuses in highly scattering media is to amplitude modulate the incident light and measure the resulting photon density waves in the medium [17]. These density waves have been shown to display refraction at boundaries [18], scattering and wavelength transduction [19] (*look up transduction*) as well as interference patterns [20]. This method has been used to locate breast tumors smaller than the critical size of 1 cm [21–23].

The aforementioned measurement of density waves is part of the wider field of modulation spectroscopy, which employs an amplitude- or frequency-modulated incident light field or combination thereof. For example, when a purely amplitude-modulated light field is passed through a medium that displays sufficiently strong frequency dependent propagation characteristics, the emerging field can be partially frequency-modulated [24]. This happens if the sidebands which are in phase for the incident light travel a different (optical) distance, leading to phase difference between them for the emerging field. From the degree of frequency modulation, information on narrow atomic states in the sample can be gained (i.e., trapping

defects in semiconductors or absorption states in gas).

2.4 Optical techniques using fluorescence

2.4.1 Multiphoton Fluorescence Microscopy

In Multiphoton Spectroscopy, femtosecond lasers serve as a light source for multiphoton excitation of organic fluorophores [2] [25] embedded in samples. Fluorophores can be designed so they are selectively absorbed in the specific area of a tissue under investigation [26]. The incident long-wavelength light (e.g., infrared) is projected onto the sample by a microscope objective. At high photon densities as in the focal spot, two or more photons can be simultaneously absorbed by mediation of a virtual state. The energies of those photons add up, leaving the fluorophore in an excited state. From this state, the fluorophore drops back into its original state by emitting a photon of higher energy than the exciting photons, generally in the visible spectrum. The resulting intensity of the fluorescence is measured as a function of the location of the focal spot.

As mentioned before, the required high photon density is only given in the focal point of the microscope objective (a micron thick at high numerical aperture), thereby diminishing background fluorescence and out-of-focus flare that typically limits the sensitivity in confocal microscopy. For the same reason, photodamage is minimized which is an important limiting factor in imaging living cells, thereby enabling the examination of thick living tissue specimen. By translating the focal point in all three dimensions and recording the intensity of the fluorescence, three-dimensional images with micron-resolution can be captured [25]. Two-photon

[2] an excited fluorescent molecule releases (part of) its energy by emitting a photon.

microscopy has developed into a standard technique of biomedical imaging.

2.4.2 Fluorescence Lifetime Imaging (FLIM)

In Fluorescence Lifetime Imaging Microscopy (FLIM), the temporal profile of the fluorescence is measured rather than the absolute intensity [16,27]. This is especially useful for greater depth, where the quantitative measurement of fluorescent intensity becomes increasingly difficult due to absorption and scattering in the tissue [26]. The fluorescence lifetime is a function of the fluorophore environment because the non-radiative decay rate depends on the interaction with the surrounding molecules. The fluorescence lifetimes can be measured by time-domain- and frequency-domain-methods. In time-domain methods, pulsed laser-light in combination with photon counting or other techniques described in Section 2.2 are used. In frequency-domain methods and and for decays on the order of nano-seconds, a light field modulated at a given radio-frequency experiences a characteristic phase-shift and attenuation caused by a specific life-time.

FLIM is already being used for the dynamic measurement of Ca^{2+} and oxygen concentrations as well as pH values with single-cell-resolution, for the characterization of impurities in metal samples and in combustion related studies [26, 27].

2.5 Resolution-enhancing techniques

2.5.1 Near-field Scanning Optical Microscopy (NSOM)

In almost all optical spectroscopy methods, the spatial resolution is limited by the wavelength of the light used. In Near-field Scanning Optical Microscopy (NSOM) a tapered single-mode optical fiber probe with an aperture of less than an optical

wavelength is placed within a fraction of wavelength of the surface which is to be examined [28]. The spatial resolution in this case is approximately the size of the tip diameter; resolutions of up to 20 times better than the best conventional microscope have been obtained. By collecting the light emitted in the near-field or by measuring the current induced by photo-excitation using a source with tunable wavelength, the composition and electronic structure of semiconductors or biomaterials can be examined. Also, evanescent phenomena in waveguides and couplers as well as temperature profiles of active devices can be studied.

2.5.2 Deconvolution Microscopy

The image observed at the focal plane of a microscope also contains out-of-focus contributions from sample regions above and below the focal plane. This flare is reversed by numerical deconvolution using the pointspread function (PSF) of the imaging system [29]. The measured image is the convolution of the PSF with the true image:

$$Image^{measured} = PSF * Image^{true}, \tag{2.1}$$

where $*$ represents the convolution operation. From the inverse PSF of the system, the true image can be calculated:

$$Image^{true} = Image^{measured} *^{-1} PSF, \tag{2.2}$$

where $*^{-1}$ denotes the deconvolution operation. Deconvolution can be performed by taking advantage of the fact that a convolution in position space corresponds to a product in momentum space: For two well-behaved functions $f(\vec{x})$ and $g(\vec{x})$

which might represent the intensity distribution of the image and the PSF of the imaging system,

$$\mathcal{F}[f(\vec{x}) * g(\vec{x})] = \hat{f}(\vec{p})\hat{g}(\vec{p}), \tag{2.3}$$

where $\mathcal{F}$ denotes the Fourier transformation with respect to x. $\hat{f}(\vec{p})$ and $\hat{g}(\vec{p})$ as a function of momentum $\vec{p}$ are the Fourier transforms of $f(\vec{x})$ and $g(\vec{x})$. $f(\vec{x})$ can then be solved for by inverse Fourier transformation:

$$f(\vec{x}) = \mathcal{F}\{\hat{f}(\vec{p})\} = \mathcal{F}^{-1}\left\{\frac{\mathcal{F}[(f * g)(\vec{x})]}{\hat{g}(\vec{p})}\right\} \tag{2.4}$$

The numerator in the braces is the narrower in momentum, the broader the convolution in of f and g in space is. For a broad $g(\vec{x})$, i.e. a PSF that does not discriminate well between two close points in space, the numerator becomes very small and therefore prone to noise for high spatial frequencies. The deconvolution, which manifests itself in the division by $\hat{g}(\vec{p})$ in momentum space, then results in a $\hat{f}(\vec{p})$ which is noisy for high spatial frequencies as well. The inverse Fourier transformation which yields $f(\vec{x})$ then contains this noise as well. These high-frequency contributions can be suppressed by adding a small constant in the denominator [5]:

$$f(\vec{x}) = \mathcal{F}^{-1}\left\{\frac{\mathcal{F}[(f * g)(\vec{x})]}{\hat{g}(\vec{p}) + \epsilon}\right\} \tag{2.5}$$

which has the disadvantage though that it smoothes the resulting distribution for $f(\vec{x})$.

2.6 Optical spectroscopy for chemical analysis

2.6.1 Infrared Spectroscopy

Infrared Spectroscopy measures the absorption spectrum of infrared light of various frequencies incident on a sample [30]. The absorption features, which are characteristic for a chemical, are the results of excitations of vibrational, rotational and bending modes of a molecule. The image contrast is solely dependent on the chemical nature of the sample. A requirement for excitation by infrared radiation is molecular asymmetry. Excitation of symmetric molecules is only possible if asymmetric stretching or bending transitions are possible. The wavelengths in Infrared Spectroscopy are usually in the near to mid-infrared; the wavelengths best suited for organic compounds are in the range from 2.5 to 16 μm [31].

2.6.2 Raman spectroscopy

Raman Spectroscopy is considered a complementary technique for Infrared Spectroscopy. It provides information about molecular vibrations that can be used for identification and quantification of a chemical contained in a sample. [32–34] A rather monochromatic laser beam is directed onto the sample and the scattered light detected by a spectrometer. While most of the scattered light will have the same frequency as the incident light, less than 10% is frequency shifted due to energy transfers between the incident field and vibrational energy levels of the molecules in the sample. The various frequency lines measured around the center frequency correspond to different functional group vibrations and are characteristic for a certain chemical. The lines with a frequency below the incident field frequency are called Stokes lines, the ones above anti-Stokes lines.

2.7 Confocal Microscopy

Confocal Microscopy is a technique for improving the contrast of microscope images, particularly in thick samples. By restricting the observed volume, the technique keeps scatterers close to the focal plane from contributing to the detected signal. The trade-off for this is that only one point at a time can be observed [35].

In this technique, a sample is scanned by a tightly focused laser beam while the reflected or fluoresced light is being collected by a high numerical aperture (≈ 1.4) objective lens [36]. The high-NA objective as well as a pinhole which is introduced into the path of light suppress out-of-focus glare which leads to improved contrast and sharpness. The intensity of the collected light is measured by a photomultiplier or a photo-diode. By moving the laser beam in a regular two-dimensional raster and repeating this procedure for various depths, a three-dimensional image of the sample can be created. The vertical resolution is on the order of 0.5 μm and the horizontal resolution on the order of 0.2 μm [37]. Confocal Microscopy provides a good technique for non-invasive, optical sectioning of thick living specimen.

There exist many more optical tomography methods, such as differential interference contrast (DIC) microscopy, Optical Staining microscopy, Hoffman Modulation Contrast Microscopy, Polarized Light Microscopy and Phase Contrast Microscopy, which will not be discussed in this thesis. Instead, we will conclude this chapter with the presentation of Optical Coherence Tomography, whose principle is the basis of our experiment.

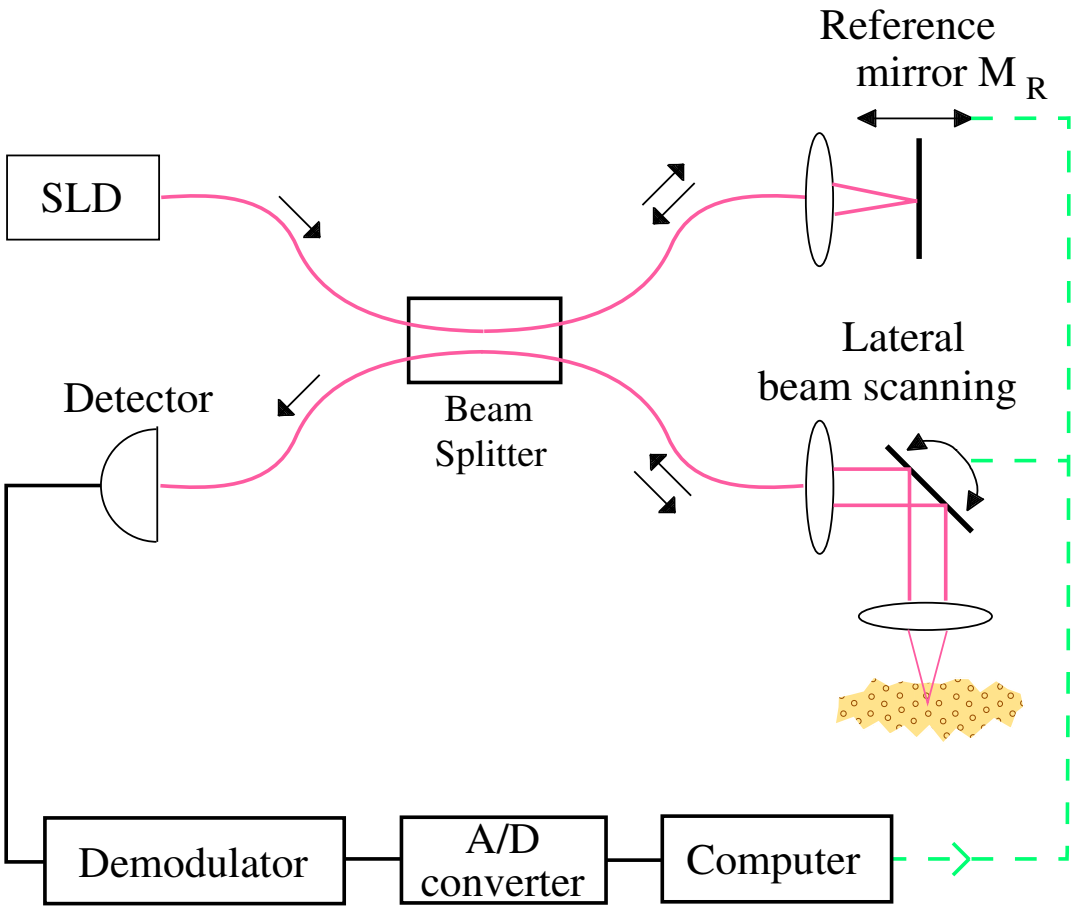

Figure 2.1: Setup for Optical Coherence Tomography (OCT).

2.8 Optical Coherence Tomography (OCT)

Optical Coherence Tomography (OCT) uses a combination of the principles of low-coherence tomography and confocal microscopy [38]. Figure 2.1 shows set setup: two beams are generated from a broadband (or pulsed laser) source (SLD); we will refer to them as *Signal*- and *Local Oscillator*- beam. The Signal beam is incident on the sample; the transmitted or scattered light is then superposed with the Local Oscillator beam. Due to the broad spectrum of the light, its longitudinal coherence length is small; typically on the order of tens of micrometers. The light coming from the sample and the Local Oscillator beam only interfere if their path-length is matched within the coherence length of the light. By changing the relative path-delay between the beams with the reference mirror (M_R) and detecting the interference signal of the beams at the same time, signal contributions from different regions in the sample can be selected. In the shown setup, a map of tissue reflectivity versus depth can be obtained (z-scan). By moving the laser beam in a two-dimensional raster and taking z-scans for each point, similar to the procedure described for Confocal Microscopy in Section 2.7, a three-dimensional image can be obtained.

The interference between the Signal- and Local Oscillator beam is usually measured by means of heterodyne detection. In the most straightforward way, the Doppler-shift introduced by the moving reference mirror M_R during a depth-scan is exploited: The interference signal will be centered at the Doppler frequency and can easily be extracted by a lock-in amplifier, while the parts of the signal that do not contribute to interference average out.

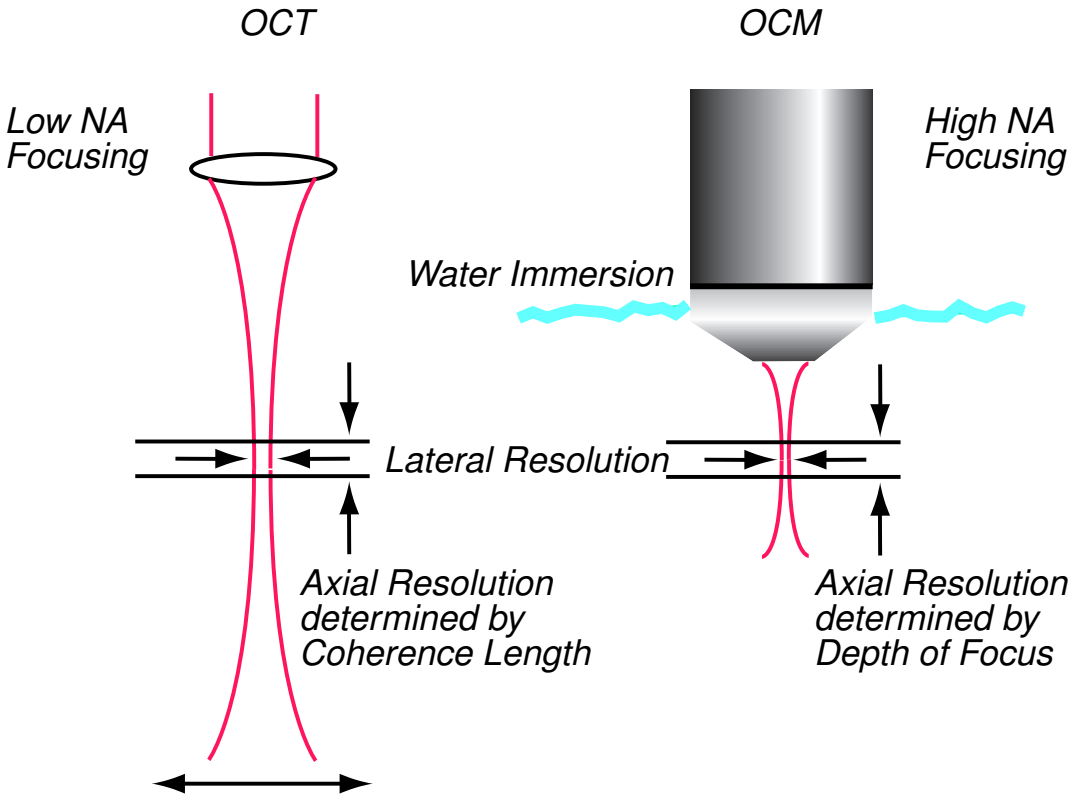

Figure 2.2: Optical Coherence Tomography (OCT, left) compared to Optical Coherence Microscopy (OCM, right).

2.8.1 Optical Coherence Microscopy (OCM)

Optical Coherence Tomography (OCM) directly combines OCT and Confocal Microscopy [38]. While its principle is the same as that of OCT, it adds a high NA objective in order to increase lateral and axial resolution due to the smaller focal spot size and Rayleigh length.[3] In addition the high NA objective provides enhanced rejection of out-of-focus or multiply scattered light. OCM can be used in case where there are no physical constraints with respect to the distance between the sample and the objective. Figure 2.2 demonstrates the differences between OCT

[3]The Rayleigh length is the distance after which a beam passing through its beamwaist grows to twice its area. It is inversely proportional to the area of the beamwaist.

and OCM. In the figure shown, the OCM objective is immersed in water where the wavelength is smaller, thereby enhancing the resolution.

Since the small Rayleigh length and the strong rejection of out-of-focus light in OCM determine the axial location of the examined plane, a longitudinal z-scan can not be performed as easily as for OCT, using the Doppler-shift introduced by the reference mirror, unless the focal plane of the objective is changed at the same rate.[4] This problem also arises when the reference mirror is moved stepwise and the heterodyne signal is generated by the beat frequency of the Signal- and Local Oscillator beams frequency-shifted by means of acousto-optic modulators.

Compared to Confocal Microscopy alone, the short coherence of the broadband light in OCM helps rejecting light coming from above and beneath the objective focal plane, where its point-spread function is broad.

2.8.2 Color Doppler Optical Coherence Tomography (CDOCT)

Color Doppler Optical Coherence Tomography measures the flow of objects in a sample by taking advantage of the additional Doppler-shift they introduce. This way, reflections from objects moving away and towards the incident Signal beam cause frequency components in the heterodyne signal below and above the Doppler-frequency generated by the reference mirror. Several groups have used this techniques for quantitative measurements of blood flow in tissue with micron-scale resolution [39, 40]. The spatial resolution in [39] is better than 45 μm in depth and 10 μm laterally, the velocity resolution on the order of 0.5 mm/s, the latter being

[4]This is non-trivial since the depth-dependent refractive index in the sample influences the depth of the focal plane which has to be taken into account when adjusting the relative path delay between the Signal- and Local Oscillator beam.

easily adjustable by varying the speed of the reference mirror.

Chapter 3

Wigner Functions

3.1 Introduction

A central feature of this thesis is the measurement of Wigner functions to characterize light fields. Wigner functions provide a convenient way to describe a light field is by means of the Wigner function [2, 3]. Wigner functions characterize the spatial and angular distribution of a field at the same time as well as its coherence properties. They obey simple transport equations in first-order systems such as thin lenses, magnifiers and free space [41] which are analogous to those in ray-optics.

A Wigner function is a real function which simultaneously describes a distribution in two conjugate variables, like time and frequency or space and momentum. In the first case it can be compared to a musical score, which tells a musician the frequencies of a song as a function of time. In the second case it can be considered the local spatial frequency spectrum of a signal. The Wigner function for a Gaussian beam closely resembles its ray-optical equivalent in geometrical optics [41]. For all other types of fields Wigner functions exhibit interference terms and negative features. Wigner functions belong to the group of so-called *quasi-propabilities*.

The Wigner function for a light field $\mathcal{E}(x)$ is

$$
\begin{aligned}
W(x,p) &= \frac{1}{2\pi}\int d\epsilon\ \exp(ip\epsilon)\ \langle \mathcal{E}^*(x+\frac{\epsilon}{2})\mathcal{E}(x-\frac{\epsilon}{2})\rangle \\
&= \int \frac{d\epsilon}{2\pi}\ \exp(ip\epsilon)\,\Gamma(x+\frac{\epsilon}{2}, x-\frac{\epsilon}{2}),
\end{aligned} \tag{3.1}
$$

where x is the transverse position and p the transverse momentum of the light field. The transverse momentum p is the wave-vector k times the angle of direction θ of a light field: $p = \theta k$. The angled brackets signifies temporal averaging for partially coherent light fields.

For a given transverse position x, $W(x,p)$ is the Fourier transform integral of the mutual coherence functions $\Gamma(x+\frac{\epsilon}{2}, x-\frac{\epsilon}{2}) = \langle \mathcal{E}^*(x+\frac{\epsilon}{2})\mathcal{E}(x-\frac{\epsilon}{2})\rangle$ centered around x. Similarly, for a given transverse momentum p, $W(x,p)$ is the Fourier transform integral of the angular cross-spectral densities $\Gamma(p+\frac{q}{2}, p-\frac{q}{2}) = \langle \mathcal{E}^*(p+\frac{q}{2})\mathcal{E}(p-\frac{q}{2})\rangle$ centered around p. The cross-spectral density becomes separable for coherent light, where the averaging becomes unnecessary.

Wigner functions contain *phase information* about a light field (as opposed to intensity measurements), which can easily be seen from its relationship to the mutual coherence function. Therefore, they offer an attractive framework in which to study the propagation of optical coherence through random media [42]. Previously, we have measured smoothed Wigner functions using a single beam heterodyne method [1–4]. In that technique, the position and momentum resolution were determined by the LO's size and angular spread, which are inversely proportional to each other and which mathematically manifests itself in an uncertainty product associated with Fourier transform pairs.

The novel two-window technique [1] presented in this thesis allows independent

control over the position and momentum resolution by using a phase-coupled set of LOs, thereby surpassing this uncertainty limit and permitting measurement of *true* (vs. smoothed) Wigner functions.

3.2 Basic properties of Wigner functions

In the following, some basic properties of Wigner functions will be discussed, which will be beneficial in understanding more complex experimental and theoretical results later on.

3.3 Wigner functions of spatially incoherent light

Spatially incoherent light, such as the broad background contribution of light experiencing large angle scattering in random media, can be described by the cross-spectral density $\Gamma(x+\frac{1}{2}\epsilon, x-\frac{1}{2}\epsilon) = c(x)\delta(\epsilon)$ with $c(x)$ being a non-negative function [41]. A Fourier-transformation with respect to ϵ yields the corresponding Wigner function $W(x,p) = c(x)$ which is independent of p. This is in agreement with the property of light to develop transverse coherence while travelling in a preferred direction: in order to be incoherent, the field has to be direction-independent.

3.4 Wigner functions of a (partially) coherent beam

Partially coherent Gaussian beams belong to the family of Gaussian Schell model light sources and can be described by the cross-spectral density [43]

$$\begin{aligned}\Gamma(x_1,x_2) &= \langle \mathcal{E}^*(x_1)\mathcal{E}(x_2)\rangle \\ &= \exp\left[-\frac{x_1^2+x_2^2}{4\sigma_s^2}\right]\exp\left[-\frac{(x_1-x_2)^2}{2\sigma_g^2}\right]\exp\left[\frac{ik}{2R}(x_1^2-x_2^2)\right]. \quad (3.2)\end{aligned}$$

The corresponding Wigner function is the Fourier transformation with respect to the difference between x_1 and x_2 (see Eq. (3.1)). Inserting Eq. (3.2) into Eq. (3.1) yields:

$$W^{part.coh}(x,p) = \frac{\pi}{\alpha}\exp\left[-\frac{x^2}{2\sigma_s^2}-\frac{(\frac{kx}{R}+p)^2}{4\alpha}\right] \quad (3.3)$$

with $\alpha = \frac{1}{8\sigma_s^2}+\frac{1}{2\sigma_g^2}$. The momentum spread of a light field in phase-space becomes larger with decreasing transverse coherence length σ_g which is consistent with the quintessence of Section 3.3. For finite radii of curvature, the spatial size of the field displays a similar σ_g-dependence, converging towards the size we would have for a flat wavefront. The momentum peaks at $p = -\frac{kx}{R}$.

Most laser beams can be viewed as transverse coherent, which implies $\sigma_g \gg \sigma_s$. In that case the exponential term in the middle of Eq. (3.2) is approximately unity. The resulting Wigner function reduces to:

$$W^{coh}(x,p) = \frac{1}{\pi^2}\exp\left[-\frac{x^2}{2\sigma_s^2}-2\sigma_s^2\left(\frac{kx}{R}+p\right)^2\right] \quad (3.4)$$

Figure 3.1: Ray-diagrams and their corresponding Wigner function for a Gaussian beam waist, and a divergent and convergent Gaussian beam.

Figure 3.1 shows ray-diagrams for a beam waist (a), divergent (b) and convergent (c) beams together with their correspondent Wigner functions.

For the beam waist ($R = \infty$), σ_s is both in the denominator of the x-prefactor and the numerator of the p-pre-factor, which confirms the inverse relationship between the size of the beam and its angular spread.

For $R \neq \infty$, i.e. a convergent or divergent beam, there exists a correlation between momentum and position: For a divergent beam (R positive), the momentum distribution is centered around positive values for positive x and around negative values for negative x. This is consistent with the physical picture of off-axis parts of a divergent beam moving away from the center. An opposite relationship between x and p exists for a convergent beam, seen on the right, as can easily be verified.

A Gaussian beam is the only field for which the Wigner distribution is positive throughout phase-space. Even the combination of two Gaussian beams separated by a distance displays negative features as part of an additional oscillating term in momentum [5].

3.5 Integrals of Wigner functions

The integrals

$$I(x) = \int dp\ W(x,p) \tag{3.5}$$

and

$$I(p) = \int dx\ W(x,p) \tag{3.6}$$

are the *positional* and the *directional intensity* of the light field, whereas

$$P = \int dp\ dx\ W(x,p) \tag{3.7}$$

is its total power.

3.6 Propagation through linear optical systems

A linear system in optics such as a thin lens or free space can be described by two equations which connect the position and momentum of an incident field with those of the emerging field. For the position distribution of both fields the relationship

$$\mathcal{E}_o^{coh}(x_o) = \int dx_i\, h_{xx}(x_o, x_i)\mathcal{E}_i^{coh}(x_i) \tag{3.8}$$

exists, where $h_{xx}(x_1, x_0)$ is the so-called *point-spread function* and $\mathcal{E}_0$ and $\mathcal{E}_1$ are the coherent incident and emerging field [41]. h_{xx} is the response of the system in the space domain when the input signal is a point source. Partially coherent light, which can be described by the cross-spectral density function, displays a similar relationship between emerging and incident field:

$$\Gamma_o(x_o, x_o') = \int\int dx\, dx'\, h_{xx}(x_o, x)\Gamma_i(x, x')h_{xx}^*(x_o', x'). \tag{3.9}$$

The Wigner function, which is Fourier-transform related to the mutual coherence function, can be directly calculated by inserting Eq. (3.9) into Eq. (3.1), which results in

$$W_o(x_o, p_o) = \int\int dx_i\, dp_i\, K(x_o, p_o, x_i, p_i)\, W_i(x_i, p_i). \tag{3.10}$$

K is called the *ray-spread function* of the system since it is the response to the hypothetical case of a single ray with the (impossible) Wigner function $W_i(x,p) = \delta(x-x_i)\delta(p-p_i)$ entering the system. K can be expressed as a function of the point-spread function h_{xx}:

$$\begin{aligned} K(x_o,p_o,x_i,p_i) &= \int\int dx'_o\, dx'_i\, h_{xx}(x_o+\frac{1}{2}x'_o, x_i+\frac{1}{2}x'_i) h^*_{xx}(x_o-\frac{1}{2}x'_o, x_i-\frac{1}{2}x'_i) \\ &\quad \times \exp[-i(p_o x'_o - p_i x'_i)]. \end{aligned} \tag{3.11}$$

This relation allows us to directly calculate the propagation of a Wigner function through linear media. For a **thin lens** in the paraxial approximation the point spread function takes the form

$$h_{xx}(x_1,x_0) = \exp\left(-\frac{ik}{2f}x_1^2\right)\,\delta(x_1-x_0) \tag{3.12}$$

which results in the transport equation for the Wigner function

$$W_1(x,p) = W_0(x,p+\frac{kx}{f}). \tag{3.13}$$

A **section of free space** in the Fresnel approximation has the point spread function

$$h_{xx}(x_1,x_0) = \sqrt{\frac{k}{2\pi i z}}\exp\left[\frac{ik}{2z}(x_1-x_0)^2\right]. \tag{3.14}$$

The corresponding Wigner function becomes:

$$W_1(x,p) = W_0(x-\frac{zp}{k},p). \tag{3.15}$$

Both Equations (3.13) and (3.15) are equivalent to the geometrical description of a ray propagating through a lens or a section of free space, respectively. It should be kept in mind though, that a Wigner function contains the full phase information of a field.

Another interesting property of the propagation of a Wigner function in free space is that the total time-derivative is zero, which has been verified for coherent electromagnetic fields [5]:

$$\frac{dW(\vec{x},\vec{p};t)}{dt} = \frac{\partial W(\vec{x},\vec{p};t)}{\partial t} + \vec{v}\cdot W(\vec{x},\vec{p};t) = 0. \tag{3.16}$$

This expression is equivalent to the Liouville's theorem of classical mechanics, which tells us that the density of a volume element we follow along a flow-line in phase-space is conserved [44]. This can easily be seen by looking at Eq. (3.15): For a given momentum p at a given distance z, the position-distribution $x(p)$ shifts by an offset $\frac{zp}{k}$, without otherwise changing its properties. A volume element containing an arbitrary part of the Wigner function remains constant in size, because in free space the field does not lose energy. Therefore, the Wigner function, which is the power *density* in phase-space, has to be constant as well, which proves Liouville's theorem in this particular case. By inspection of the corresponding expression for propagation through a lens (Eq. (3.13)), it is clear that Liouville's theorem should apply for that case, too.

3.6.1 General Luneburg's first order systems

Luneburg's first order systems [45] display a propagation behavior of

$$W_o(x_o,p_o) = W_i(Ax_i + Bp_i, Cx_i + Dp_i) \tag{3.17}$$

where the transformation parameters must obey the symplecticity condition on the determinant

$$\begin{vmatrix} A & B \\ C & D \end{vmatrix} = 1. \tag{3.18}$$

We have three free parameters here; the fourth one is determined by condition (3.18).

As we just have seen, Liouville's theorem holds for the first-order systems lens and free space. It is clear that it still holds for the similar, but more general cases where we replace the factors $-\frac{z}{k}$ and $\frac{k}{f}$ in Equations (3.15) and (3.13) with the arbitrary parameters B and C from Eq. (3.17). The $ABCD$ matrices for both cases are then

$$\begin{pmatrix} A & B \\ C & D \end{pmatrix}_{lens} = \begin{pmatrix} 1 & 0 \\ k/f & 1 \end{pmatrix} \tag{3.19}$$

$$\begin{pmatrix} A & B \\ C & D \end{pmatrix}_{free\,space} = \begin{pmatrix} 1 & -z/k \\ 0 & 1 \end{pmatrix}. \tag{3.20}$$

$$\tag{3.21}$$

B can even be negative, but in this case it does not represent the travel through free space anymore. Let us consider an arrangement of the generalized expressions for lens, a section of free space and another lens. It can then easily be verified that the resulting total $ABCD$-transformation matrix is symplectic and represents

a first-order Luneburg system itself:

We consider a Wigner function $W_1(x,p)$ incident on a lens. Right after lens L_1, the Wigner function is $W_2(x,p) = W_1(x, p+Cx)$. After travelling through the generalized space, $W_3(x',p') = W_2(x'+B'p', p')$ or

$$\begin{aligned} W_3(x,p) &= W_1[x + B'(p+Cx), p+Cx] \\ &= W_1[(1+B'C)x + B'p, Cx + p] \\ &= W_1(A''x + B''p, C''x + D''p). \end{aligned} \tag{3.22}$$

It can easily be verified that $A''D'' - B''C'' = 1$ which confirms that the combination of a lens and the distance of generalized space still represents a first-order system. After passing lens L_2, the Wigner function becomes

$$\begin{aligned} W_4(x'',p'') &= W_3(x'', p'' + C^{(3)}x'') \\ &= W_2[x' + B'p', p' + C^{(3)}(x' + B'p')] \\ &= W_1\{x(1+B'C) + B'p, [C + C^{(3)}(1+B'C)]x + (1 + c^{(3)}B')p\} \\ &= W_1(A^{(4)}x + B^{(4)}p, C^{(4)}x + D^{(4)}p). \end{aligned} \tag{3.23}$$

A^4, B^4, C^4 and D^4 are fully determined by C,B' and $C^{(3)}$ and fulfill the symplecticity condition (3.18) for every choice of them.

The relationship of A^4, B^4, C^4, D^4 and $C, B', C^{(3)}$ expressed in Eq. (3.23)

$$A^{(4)} = 1 + B'C \tag{3.24}$$

$$B^{(4)} = B' \tag{3.25}$$

$$C^{(4)} = C + C^{(3)}(1 + B'C) \tag{3.26}$$

$$D^{(4)} = 1 + C^{(3)}B' \tag{3.27}$$

can be solved for C,B' and $C^{(3)}$:

$$C = \frac{A^{(4)} - 1}{B^{(4)}} \tag{3.28}$$

$$B' = B^{(4)} \tag{3.29}$$

$$C^{(3)} = \frac{D^{(4)} - 1}{B^{(4)}} \tag{3.30}$$

where B' and $C^{(3)}$ can be uniquely derived from Equations (3.25) and (3.27); C results from Eq. (3.24) and either Eq. (3.25) or Eq. (3.26) together with the symplecticity requirement Eq. (3.18).

Since the Liouville expression holds for each one of the three-component system just described, it will also hold for their combination. Furthermore, Eq. (3.28) shows that an arbitrary Luneburg first-order system can be expressed as such a three-component system. Therefore we can draw the conclusion that the Liouville expression holds for all Luneburg first-order systems.

Chapter 4

The Single-Window technique

4.1 Introduction

In this section I will explain the experimental setup for the Single-Window technique that we have been using in the past to measure *smoothed* Wigner functions [46]. Its basic concept is the heterodyne measurement of a signal field by means of a single Local Oscillator (LO) beam. The Signal- and LO fields are frequency-shifted by different amounts and superposed on a detector. The detector measures a beat note which corresponds to the difference in frequencies of Signal- and LO fields. Its amplitude is proportional to the overlap integral of both fields at the area of coincidence. By stepwise changing the relative transverse position x and transverse momentum p of the LO with respect to the Signal field and recording the beat signal, the phase-space distribution of the Signal field can be determined. For maximum resolution, the LO itself must be as small as possible in phase-space, that means its diameter and angular spread must be minimal. The trade-off between small size and angular spread can best be met by using a Gaussian beam. A Gaussian beam of 'diameter' a has an angular spread of about $\frac{\lambda}{a}$. Therefore, the smallest features in the Signal field that can be measured are on the order of a in size and $\frac{1}{a}$ in transverse momentum. The finite x- and p resolution leads to a smoothing effect of

the measured signal. Therefore, we refer to the Single-LO technique as a technique for measuring 'smoothed' Wigner functions which will be explained in the following section Section 4.2.

In all of our experiments, we use a Superluminescent diode (SLD) as a light source. It has a longitudinal coherence of just 24.9 μm which enables time-resolved measurement of the signal field, as will be explained later. This short coherence length requires additional elements in the experimental setup. A detailed treatment will be given in Section 4.6.

The Single-LO technique used for the measurement of smoothed Wigner functions serves as a basis for the Two-Window technique, which enables the measurements of the true, i.e. non-smoothed Wigner function. This technique is the centerpiece of this thesis and will be described in Chapter 5.

In the following section, I start by explaining the experimental setup for the stationary measurement of smoothed Wigner functions, followed by a discussion of the balanced detection system (Section 4.3), the real-time noise suppression scheme (Section 4.4) and the automated data acquisition setup we use (Section 4.5). In Section 4.6 the modifications for time-resolved measurements using broadband light are discussed. The chapter is concluded in Section 4.7 with a description of the actual measurement of time-resolved Signal fields and the retrieval of Wigner functions for transversely coherent Signal fields.

4.2 Experimental setup with laser light source

Figure 4.1 shows the basic setup for the measurement of stationary smooth Wigner functions. For demonstrative purposes, the setup for transmission measurements is shown. Omitted for clarity are a $4f$-system used in the signal arm as well as several

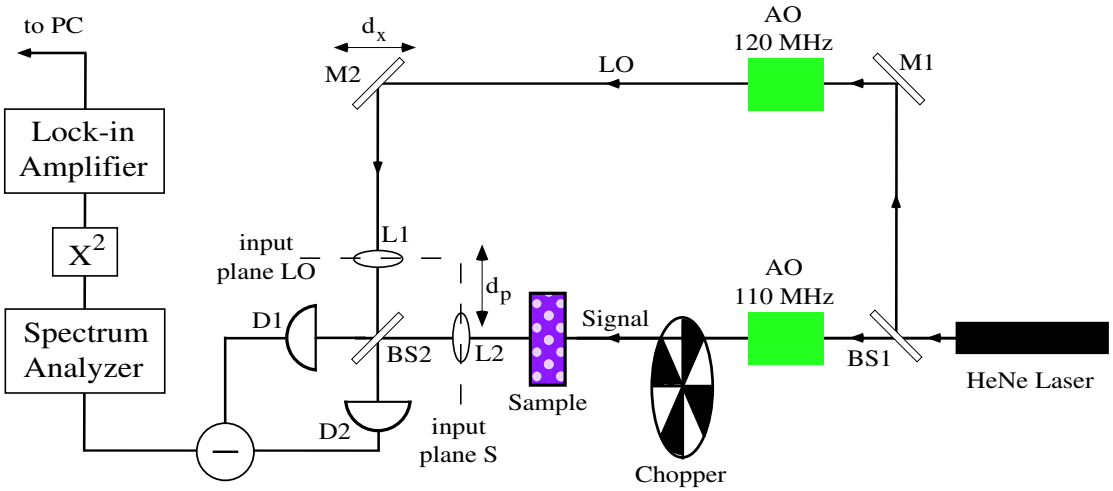

Figure 4.1: Experimental setup for measuring stationary smoothed Wigner functions using a HeNe as a light source

other optical elements which are not essential for understanding the functionality of the setup.

The HeNe beam is split at beam splitter BS_1 in a *signal arm S* and a *local oscillator arm LO*. Each beam is sent through an acousto-optic modulator crystal (AO); the Signal beam is shifted by 110 MHz and the Local Oscillator beam by 120 MHz. This results in a frequency difference of 10 MHz which will enable the detection of a beat signal. The Signal beam then passes through a chopper and through the cell containing the sample and reaches the input plane at the location of lens L_2. The LO passes a translating mirror M_2 and reaches the second input plane at lens L_1. The input planes are defined as the reference planes at which the incident Signal field and the Local Oscillator beam are compared to each other and where the Wigner function is measured. After passing the input planes, the Signal and the Local Oscillator fields are superposed in beam splitter BS_2 and the 10 MHz

beat signal is detected by a balanced detector, the workings of which are described in Section 4.3. L_1 and L_2 are at a distance of their focal length $f = 6$ cm from the detector for three reasons: Firstly, the incident fields are usually rather more collimated than focused; by passing them through a lens and placing the detector in the focal plane, all light can be collected into the detector. Secondly, the translation of one of the lenses, in our case L_2, can be used to change the relative angle between the Signal- and the LO field, which will be explained below. Finally, when mirror M_2 is translated, the position of the focus of the LO in the detector plane does not change.

The light of the superposed Signal and Local Oscillator field generate - among other terms - a 10 MHz beat note current in the photodiodes, which is proportional to the spatial overlap of their electric field amplitudes in the detector planes. The total photodiode current is transformed into a voltage and fed into a spectrum analyzer where the beat note is detected. The output voltage of the spectrum analyzer is then squared using a low noise multiplier and fed into a Lock-in amplifier, which detects the squared beat signal using the chopper frequency as a reference. The squaring of the beat signal allows measurement of the Wigner function and real time noise suppression, which will be explained in Section 4.4.

In order to generate smoothed Wigner function plots of the Signal field, we scan the LO relative to it in position and momentum and simultaneously record the mean square beat signal. The relative position of the LO to the Signal field S can be changed by an amount d_x via translation of mirror M_2. The relative angle between S and LO is modified via translation of lens L_2 by an amount d_p. These translations are performed by linear actuators holding M_2 and L_2 on their moving table, respectively. These actuators are controlled by a LabView program

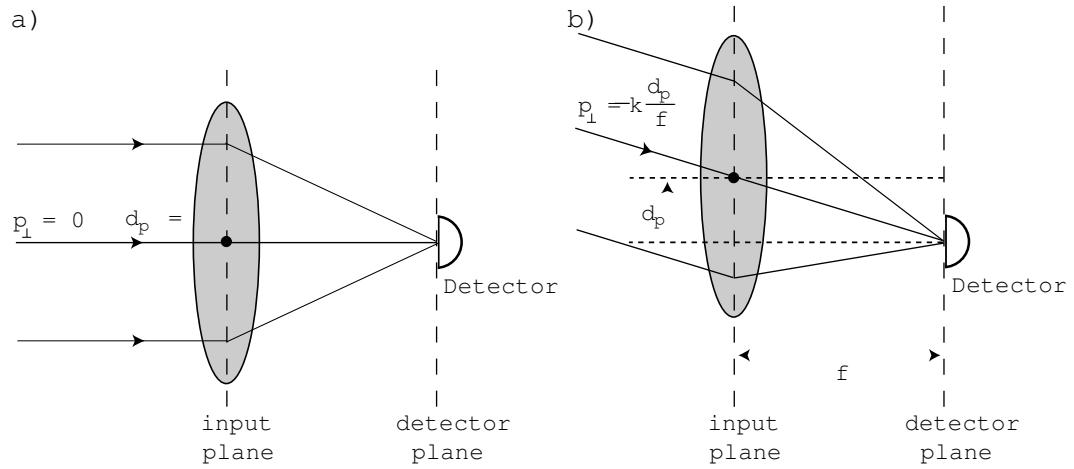

Figure 4.2: Selection of transverse momenta of Signal field being detected. The LO (not shown) is focused onto the detector, fixing the Signal field sampling the region in the detector plane. a) lens is centered with respect to detector; field contributions with $p = 0$ are detected at the focus. b) lens is off-center by d_p; field contributions with $p = -k\frac{d_p}{f}$ are detected at the focus.

on a PC and are described in more detail in Section 4.5. The scanning process is performed line by line in phase-space; for each momentum, the signal is measured for a recurring set of positions.

It is apparent that a translation of M_2 by d_x corresponds to a translation of the LO with respect to the Signal beam by the same amount. The translation of lens L_2 by an amount d_p on the other hand changes the angle of the transmitting field in its focal plane by $\theta_p = \frac{d_p}{f}$ as depicted in Figure 4.2. This corresponds to a change in transverse momentum of $k\theta_p$, where k is the wavenumber of the field. A detailed treatment as well as the measurement of smoothed Wigner functions using the experimental setup just described will be the subject of Section 4.7. That section also describes the more general case of broadband light measurements. In the following I will explain the features of some of the systems we use in the experiment.

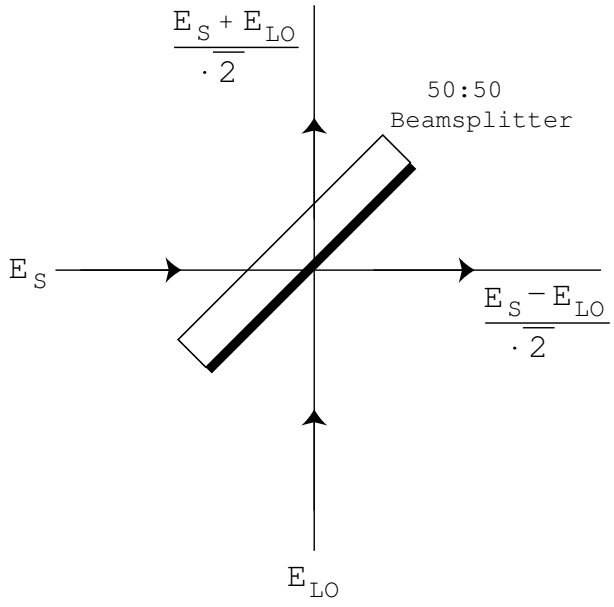

Figure 4.3: $\mathcal{E}_S$ and $\mathcal{E}_{LO}$ are incident on a 50:50 beamsplitter and add with different signs due to a 180 degree phase-shift for the LO at the reflecting surface.

4.3 Balanced detection scheme

A balanced detector allows the detection of a signal field down to the shot-noise level by subtracting classical noise that is present in both beams and which does not contribute to the beat signal. Figure 4.3 shows how the scheme works. A Signal and a Local Oscillator field are superposed by a 50 : 50 beam splitter. The reflected fraction of one of the beams experiences a 180 degree phase-shift, while the corresponding fraction of the other beam and both transmitted components do not. This phase shift is due to the reflection off a medium with higher index of refraction. Assuming for the moment perfect matching of S and LO transversely and longitudinally, the resulting intensities I_1 and I_2 at the outputs of the beam splitter are:

$$I_1 = (\frac{\mathcal{E}_S}{\sqrt{2}})^2 + (\frac{\mathcal{E}_{LO}}{\sqrt{2}})^2 + \mathcal{E}_S\mathcal{E}_{LO} \tag{4.1}$$

$$I_2 = (\frac{\mathcal{E}_S}{\sqrt{2}})^2 + (\frac{\mathcal{E}_{LO}}{\sqrt{2}})^2 - \mathcal{E}_S\mathcal{E}_{LO} \tag{4.2}$$

where the suffices S and LO denote the respective beams.

The photodiodes in the balanced detector are connected in series with same polarity with the output current being measured at the connecting point. This way the currents generated in each diode are subtracted from each other. Therefore, the intensities of each beam cancel, while the intensity contribution generated by the interference of S and BLO add, due to their opposite sign. The resulting total photo current is therefore

$$J_B \propto \mathcal{E}_S\mathcal{E}_{LO} = \sqrt{P_S P_{LO}} \tag{4.3}$$

where P denotes the power of the respective beams.

Hence, this method suppresses the classical noise, which contains not only intensity fluctuations but also the modulation frequency components of all AOs, while the beat note is measured. For an ideal balanced detection system, the signal to noise ratio up to the detection by the photodiodes is limited by shot-noise.

4.4 Real time noise suppression

While the balanced detection scheme enables the suppression of optical noise, the following scheme allows the subtraction of noise entering the system after the detection by the photodiodes, i.e., electronic noise. The output voltage of the spectrum

analyzer is proportional to the RMS voltage at the selected spectrum analyzer frequency. Including the remaining noise, this voltage is

$$V_{RMS} = \sqrt{V_{signal}^2 + V_{noise}^2} \tag{4.4}$$

where $V_{noise} = \sqrt{V_{noise1}^2 + V_{noise2}^2 + ...}$ contains all noise sources. The squared terms add since they are statistically independent. By squaring V_{RMS} from the spectrum analyzer using an analog multiplier one receives a sum of quadratic terms. The squared signal voltage due to the optical beat signal, which is modulated by the chopping frequency, can now be extracted by a Lock-in amplifier using that chopping frequency as a reference. The noise terms on the other hand simply subtract; hence the lock-in output is proportional to V_{signal}^2.

4.5 Automated data acquisition

In the experiment, the translation of mirror M_2 and lens L_2 and the simultaneous data acquisition is controlled by a LabView program on a PC (Figure 4.4). The PC controls linear actuators (443 Series by Newport) for the translation of M_2 and L_2 by means of an external controller (MM 2000 by Newport). This controller allows the simultaneous control of up to 4 actuators or similar devices. Linear actuators are step-motor-controlled sliding benches. They allow the positioning along a given direction in 50 nanometer increments. The reproducibility for our actuators is approximately 1 micron. During the scanning process, the beat signal coming from the Lock-In amplifier is recorded by an A/D-converter (BNC-2090 by National Instruments). The A/D-converter output is fed back into the PC and written into a file, together with the actuator positions.

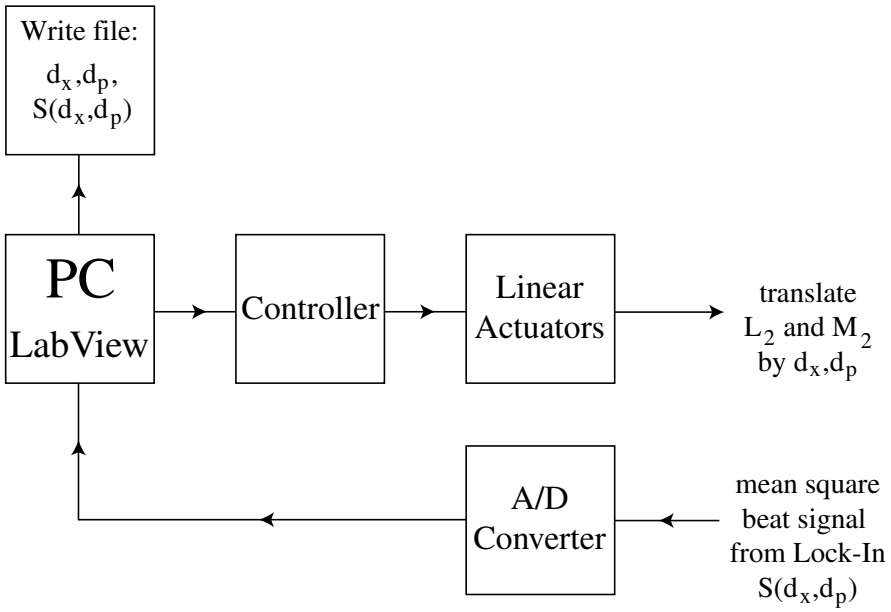

Figure 4.4: Block diagram for the automated data acquisition

In the following chapter I will describe necessary modifications to the experiment when using broad-band light instead of coherent light.

4.6 Experimental setup with SLD light source

The usage of broadband light in our experiment enables the time-resolved measurement of Wigner functions. This is because in order for S and LO to interfere, their path lengths must match within a coherence length l_c of the light used. This path difference requirement translates into a time-difference requirement, when we consider the coherence time $t_c = \frac{l_c}{c}$ instead of the coherence length itself, where c is the speed of light in the sample. In our experiments, we are mainly interested in the selection of path-lengths, in particular in the experiments involving a random medium. Broadband light requires a number of modifications to the experimental setup for coherent light.

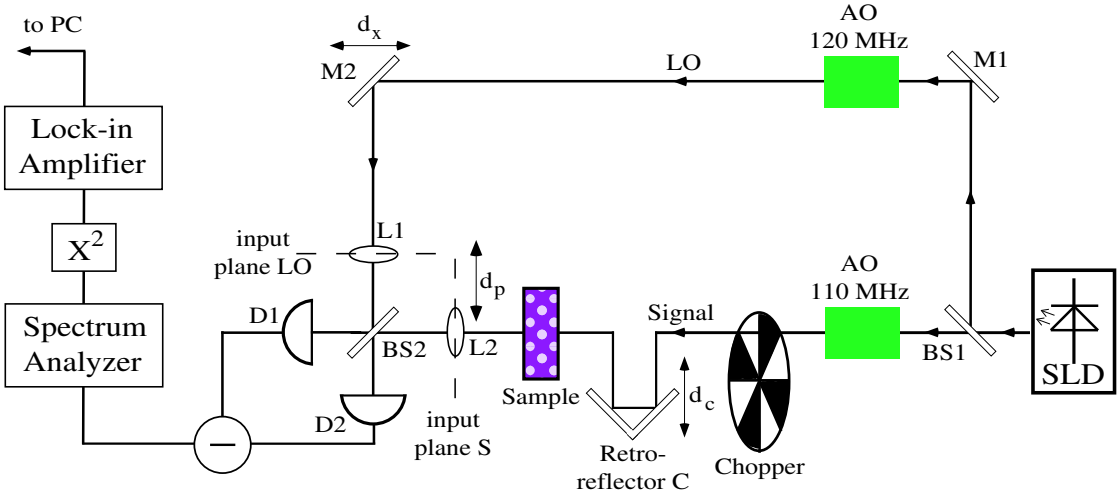

Figure 4.5: Experimental setup for measuring time-resolved smoothed Wigner functions using an SLD as a light source

The light source used in all our experiments is a superluminescent diode (SLD), which provides broadband light with a center wavelength of 678.3 nm and a longitudinal coherence length of 24.9 μm. Its properties are described in detail in Chapter 6. The light emerging from the SLD has a wide angular spread and an intensity profile the shape of a sickle. By means of a high-numerical-aperture collimation lens and a telescope, the light field is transformed into a collimated beam with a diameter of about 2 mm. The intricacies of this procedure are discussed in Section 6.3. The short longitudinal coherence length of the SLD requires the addition of a retro-reflector into the Signal arm to equalize the path lengths of S and LO during the adjustment process (see Figure 4.5). It also enables the selection of a path delay offset Δl in experiments involving turbid media, and it counterbalances changes in the relative path-delay between S and LO due to the movement of M_2 and L_2 during the scanning process. For given displacements d_x and d_p, the

correction will be given by the last three terms of Eq. (4.5):

$$\Delta l = 2d_c + d_x + \frac{d_p^2}{2f} - \frac{d_p d_x}{2f} \tag{4.5}$$

f is the focal length of the detector input lenses L_1 and L_2. The derivation of this correction factor is outlined in the following section Section 4.7.

4.7 Measurement of smoothed Wigner functions

In this section I will describe how smoothed Wigner functions can be measured using the experimental setup outlined in the previous section. The calculations will be done for the more general case of partially coherent light of a broadband source, since this light is used in all our experiments. The expressions for coherent light can usually be directly deduced from those for partially coherent light. In most cases they simplify considerably. In other parts of the calculation, I use transformations for partially coherent light usually reserved for coherent light, but only when the frequency dependency of the elements involved is negligible (lenses, short distances of free space). The calculation of the squared beat signal and its connection to the Wigner function of the Signal field will be the center part of this section. During the calculation, the path-delay compensation necessary for broadband light and to be performed by the retro-reflector will become evident.

For the following calculations, Figure 4.6 shows the notation regarding the different planes under consideration. The subscript 0 denotes the field right before the input lens in the input plane, the prime $'$ the field right behind it. The subscript D denotes the field at the location of the detector.

In the derivation of the voltage output of the balanced detection scheme in

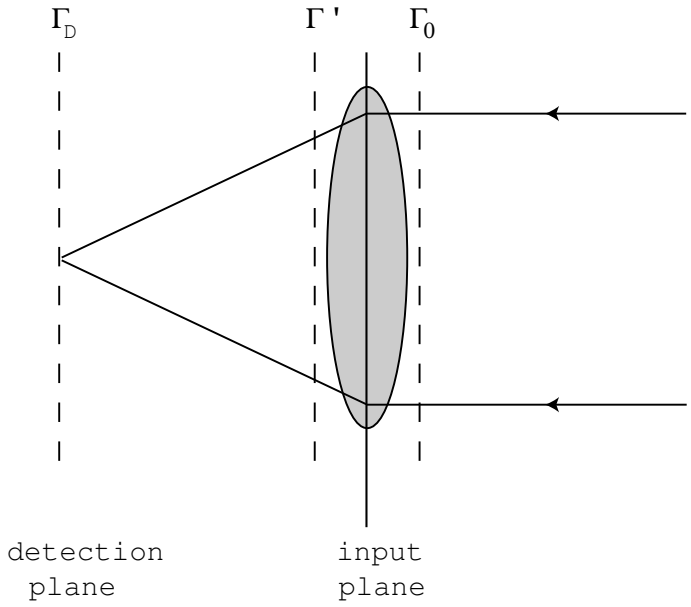

Figure 4.6: Notation of the cross-spectral density Γ in different planes

Section 4.3 we assumed coherent light and a perfect match of S and LO on the detection surface. The general amplitude of the beat signal for partially coherent light is proportional to the integrated *spectral density* of the superposed field of S and LO, $\Gamma_D(x,x) = \langle \mathcal{E}^*_{LO}(x)\mathcal{E}_S(x)\rangle$ in the detector plane (see Figure 4.6), where $\langle ...\rangle$ denotes the average over the source:

$$V_B \propto \int dx\, \Gamma_D(x,x). \tag{4.6}$$

The spectral density is just the cross-spectral density for the special case when its spatial coordinates coincide. The y-component remains constant during the scanning process and only adds an overall pre-factor; therefore it is suppressed in the integration. It is also assumed that $\mathcal{E}_{LO}$ and $\mathcal{E}_S$ are phase-matched longitudinally, when d_x and $d_p = 0$. For a given set of translations d_x, d_p of mirror M_2 and lens L_2

the input fields $\mathcal{E}_S$, $\mathcal{E}_{LO}$ right behind the input lenses are[1]

$$\mathcal{E}'^{*}_{LO}(x) = \mathcal{E}^{*}_{LO}(x - d_x) \exp\left(-i\frac{k}{2f}x^2\right) \tag{4.7}$$

$$\mathcal{E}'_{S}(x) = \mathcal{E}_{S}(x) \exp\left[-i\frac{k}{2f}(x - d_p)^2\right]. \tag{4.8}$$

The first term in Eq. (4.7) is due to the translation of M_2 which shifts the LO relative to S by a distance d_x. The following position dependent phase factor is the paraxial approximation for the wavefront passed through input lens L_1. A similar transformation occurs in Eq. (4.8): S itself does not translate, but its input lens L_2 does by a factor d_p, thereby introducing a position dependent quadratic phase factor, shifted by d_p. Even though $\mathcal{E}_S$ and $\mathcal{E}_{LO}$ superpose only in the beam splitter and not yet in the input planes, we treat the problem as such in the following, because we consider the input planes of the detection system as our reference. This is perfectly valid, since both $\mathcal{E}_S$ and $\mathcal{E}_{LO}$ undergo the same linear transformations after the input planes and before they superpose at the detectors.

The cross-spectral density of the superposed field behind the input lens is then:

$$\Gamma'(x, x') = \langle \mathcal{E}'^{*}_{LO}(x) \mathcal{E}'_{S}(x') \rangle \tag{4.9}$$

$$= \Gamma_0(x - d_x, x') \exp\left\{ i\frac{k}{2f}[x^2 - (x' - d_p)^2] \right\}, \tag{4.10}$$

where $\Gamma_0(x - d_x, x') = \langle \mathcal{E}^{*}_{LO}(x - d_x) \mathcal{E}_S(x') \rangle$ is the cross-spectral density before the

[1]Since the SLD light is partially coherent, the cross-spectral density $\Gamma(x_1, x_2)$ should actually be used instead of $\mathcal{E}(x)$. But, as pointed out at the beginning of this section, in cases where the coherence properties have a negligible effect, I treat the field as if it were coherent since it simplifies the calculations.

lens. From there, both fields travel a distance f to the photodiodes, where f is the focal length of the input lenses. The cross-spectral density at that location can be calculated by propagating the cross-spectral density of $\mathcal{E}_S$ and $\mathcal{E}_{LO}$ with the point-spread function for travel through free space (see Equations (3.9), (3.14)):

$$\Gamma_D(x_1, x_1') = \int\int dx\, dx'\, h_{xx}(x_1, x)\, \Gamma'(x, x')\, h_{xx}^*(x_1', x') \tag{4.11}$$

where, according to Eq. (3.14),

$$h_{xx}(x_1, x_0) = \sqrt{\frac{k}{2\pi i z}}\, \exp\left[\frac{ik}{2z}(x_1 - x_0)^2\right]. \tag{4.12}$$

By inserting Equations (4.9) and (4.12) into Eq. (4.11), the cross-spectral density at the detector results:

$$\begin{aligned} \Gamma_D(x, x') &= \frac{k}{2\pi f} \exp\left[\frac{ik}{2f}(x^2 - x'^2 - d_p^2)\right] \\ &\times \int\int d\eta\, d\eta'\, \Gamma_0(\eta - d_x, \eta') \\ &\times \exp\left\{\frac{ik}{f}[\eta^2 - \eta'^2 - x(\eta - \eta') + \eta' d_p]\right\}. \end{aligned} \tag{4.13}$$

Inserting Eq. (4.13) into Eq. (4.6), the complex beat voltage for partially coherent light results:

$$V_B \propto \exp(-i\frac{k}{2f}d_p^2) \int d\eta\, \Gamma_0(\eta - d_x, \eta)\, \exp(i\frac{k}{f}\eta d_p). \tag{4.14}$$

The phase factors are due to path contributions when d_p is off-center. They indicate an additional path delay of

$$l' = -\frac{d_p^2}{2f} + \frac{d_p \eta}{f} \tag{4.15}$$

during the integration which introduces an attenuation factor of $\exp(-\frac{l'}{l_c})$ due to the short coherence length l_c of the light source. By compensating those path delays by means of the retro-reflector, the attenuating term vanishes. The second term in Eq. (4.15) can not be compensated directly since it changes with integration over the detector plane, but it can be minimized for certain types of fields. For signal fields which are broad in position, as is the case for fields emerging from a turbid medium, $\Gamma(\eta - d_x, \eta)$ is centered around d_x. The phase factor inside the integral in Eq. (4.14) can then be approximated by replacing η with d_x, which results in a correction factor

$$-\frac{d_p^2}{2f} + \frac{d_p d_x}{f}. \tag{4.16}$$

Another path delay that needs to be taken into consideration is introduced by the translation of M_2 by d_x. Together with Eq. (4.16) the total correction term amounts to

$$2d_c = d_x - \frac{d_p^2}{2f} + \frac{d_p d_x}{f}. \tag{4.17}$$

The factor 2 in front of d_c accounts for the fact that for a translation d_c of the retro-reflector the path length changes by $2d_c$, as can easily be seen. The attenuation due to the varying path difference is now reduced to almost zero and the mean square voltage is

$$\mid V_B(d_x, d_p) \mid^2 \propto \left| \int d\eta \, \Gamma_0(\eta - d_x, \eta) \, \exp(i\frac{k}{f}\eta d_p) \right|^2 \tag{4.18}$$

4.7.1 Mean square beat signal for transversely coherent light

For longitudinally coherent light, S and LO will interfere regardless of relative path length difference. No correction by the retro-reflector is necessary. For transversely coherent light, Γ_0 separates into a product of $\mathcal{E}^*_{LO}$ and $\mathcal{E}_S$ due to the infinite transverse coherence length (see Eq. (3.2)):

$$\Gamma_0^{Coh}(x_1, x_2) = \mathcal{E}^*_{LO}(x_1)\mathcal{E}_S(x_2) \tag{4.19}$$

without the requirement to average over fluctuations inherent only to partially coherent light, so that Eq. (4.18) can be written as

$$\begin{aligned} \mid V_B^{coh}(d_x, d_p) \mid^2 &\propto \left| \int d\eta\, \mathcal{E}^*_{LO,0}(\eta - d_x)\mathcal{E}_{S,0}(\eta) \exp(-i\frac{k}{f}\eta d_p) \right|^2 \\ &= \int d\eta\, \mathcal{E}^*_{LO,0}(\eta - d_x)\mathcal{E}_{S,0}(\eta) \exp(-i\frac{k}{f}\eta d_p) \\ &\times \int d\eta'\, \mathcal{E}_{LO,0}(\eta' - d_x)\mathcal{E}^*_{S,0}(\eta') \exp(i\frac{k}{f}\eta' d_p). \end{aligned} \tag{4.20}$$

In the following we replace η and η' by the relative coordinates $x = \frac{1}{2}(\eta + \eta')$ and $x' = \eta - \eta'$. The Jacobian in this case is unity, so $d\eta\, d\eta' = dx\, dx'$. The substitution yields:

$$\begin{aligned} \mid V_B^{coh}(d_x, d_p) \mid^2 &\propto \int dx \int dx'\, \mathcal{E}^*_{LO,0}(x + \frac{x'}{2} - d_x))\mathcal{E}_{LO,0}(x - \frac{x'}{2} - d_x) \\ &\times \mathcal{E}^*_{S,0}(x + \frac{x'}{2})\mathcal{E}_{S,0}(x - \frac{x'}{2}) \exp(-i\frac{k}{f} d_p x'). \end{aligned} \tag{4.21}$$

A product of fields $\mathcal{E}^*(x + \frac{\epsilon}{2})\mathcal{E}(x - \frac{\epsilon}{2})$ can be expressed in terms of their Wigner

function by inverse Fourier-transformation of expression Eq. (3.1):

$$\mathcal{E}^*(x+\frac{\epsilon}{2})\mathcal{E}(x-\frac{\epsilon}{2}) = \int dp\, \exp(-i\epsilon p)\, W(x,p). \tag{4.22}$$

Replacing $\mathcal{E}^*_{S,0}(x+\frac{x'}{2})\mathcal{E}_{S,0}(x-\frac{x'}{2})$ in Eq. (4.21) yields

$$\begin{aligned} \mid V_B^{coh}(d_x,d_p)\mid^2 \;&\propto\; \int dx \int dx'\, \mathcal{E}^*_{LO,0}(x+\frac{x'}{2}-d_x)\mathcal{E}_{LO,0}(x-\frac{x'}{2}-d_x) \\ &\times\; \int dp\, \exp(ix'p)\, W_S(x,p) \exp(-i\frac{k}{f}d_p x') \end{aligned} \tag{4.23}$$

where $W_S(x,p)$ is the Wigner function of the Signal field.

Using Eq. (3.1) again, we can express the remaining terms in Eq. (4.23) together with the integral over dx' as a Wigner function:

$$\begin{aligned} W_{LO}(x_0-d_x,p+\frac{k}{f}d_p) \;&=\; \int \frac{dx'}{2\pi} \exp[ix'(p+\frac{k}{f}d_p)] \\ &\times\; \mathcal{E}^*_{LO,0}(x+\frac{x'}{2}-d_x)\mathcal{E}_{LO,0}(x-\frac{x'}{2}-d_x). \end{aligned} \tag{4.24}$$

Replacing this expression in Eq. (4.23) we get as a final expression for the mean square beat signal for coherent light:

$$\mid V_B^{coh}(d_x,d_p)\mid^2 \propto \int dx\, dp\, W_{LO}(x-d_x,p+p_x)\, W_S(x,p) \tag{4.25}$$

with $p_x = \frac{k}{f}d_p$.

This is a convolution of the Wigner functions of the Signal- and the Local Oscillator field which shows that the measured distribution is indeed a smoothed Wigner

function. For identical Signal- and Local Oscillator beams, such a convolution broadens the phase-space profile by a factor $\sqrt{2}$, as can easily be verified (also see Section 5.4.4). For a finite transverse coherence length Γ_0 does not separate into $\mathcal{E}_{LO}$ and $\mathcal{E}_S$; in that case $\mid V_B(d_x, d_p) \mid^2$ can not be expressed in terms of the individual Wigner functions as in Eq. (4.25).

4.7.2 Averaging over fields

There are several types of averaging of interest in our experiments. First, there is the averaging process in the Lock-In amplifier which extracts a weak signal from a noisy background. Secondly, for experiments involving turbid media, the signal field displays speckle, which are due to the interference of parts of the field taking different paths in the medium. This effect is noticeable stronger for coherent light than for partially coherent light. Speckle is considered noise in the type of experiments we do and can shield weaker features of the field we are interested in. In our experiment, we use polystyrene spheres floating in a water-glycerol mixture as a turbid medium (see Section 12.1.1). These spheres are subject to Brownian motion; therefore the speckle pattern changes with time. By ensemble averaging over the sample, i.e. either spatial or temporal averaging over the signal field emerging from the sample, speckle average out. Ensemble averaging in turbid media is also necessary to make sure all possible arrangements of scatterers contribute to the measured signal. The different techniques we apply for spatial averaging will be the subject of Section 12.1.1. Temporal averaging is performed by the Lock-In amplifier in our experiment. Ensemble averaging over a turbid medium is necessary for both coherent and incoherent light probing the sample. For coherent light, it is often more convenient to calculate the Wigner function of the ensemble averaged Signal

field and the LO field separately and use Eq. (4.25) to calculate the mean square beat signal.

For partially coherent light on the other hand, a third type of averaging makes it necessary to perform the averaging at the plane where S and LO interfere: Partially coherent light of frequency ω, which has a bandwidth of $\Delta\omega$, fluctuates temporally at a rate of about $\Delta\omega$. In our experiment we measure the average of the fluctuating product of S and LO which is not equal to the product of the averaged S and LO itself, at least for partially coherent light:

$$\langle \mathcal{E}_{LO}^{*} \mathcal{E}_S \rangle \neq \langle \mathcal{E}_{LO}^{*} \rangle \langle \mathcal{E}_S \rangle \tag{4.26}$$

4.7.3 Resolution of the Single-Window technique

The resolution of the measured signal field is determined by the size of the LO in phase-space, namely its spatial width and its angular spread. For a Gaussian beam with a diameter of $2\sigma_s$ the angular spread is about $\frac{\lambda}{2\sigma_s}$, i.e. $\Delta k = \frac{1}{2\sigma_s}$, so that $\Delta x \Delta k = 1$.

There is obviously a trade-off between good position- and momentum resolution: A small diameter σ_s of the LO provides good position resolution, but its resulting high momentum spread decreases the momentum resolution. The opposite relationship holds for a wide collimated beam. This uncertainty relation associated with Fourier transform pairs can be surpassed by using a combination of two LOs with small and big diameter, as will be described in the next chapter.

Chapter 5

The Two-Window technique

5.1 Introduction

The last chapter which treated the experimental setup for the Single-Window technique showed that there is a trade-off between position and momentum resolution if a single LO is used. Therefore, the measured signal is a smoothed Wigner function rather then the true Wigner function. In the following, we present a Two-Window technique which employs a combination of two phase-coupled LOs, which enables the measurement of un-smoothed Wigner functions. The set of phase-coupled LOs consists of an LO which is narrowly focused to allow high spatial resolution (*small* LO or *SLO*), and a second LO which is highly collimated which provides high angular resolution (*big* LO or *BLO*). Both LOs are frequency-shifted by 120 and 120.003 MHz, respectively; their frequency-difference of 3 kHz is locked to an external oscillator by means of a phase-locked loop. The signal field S, which is frequency-shifted by 110 MHz as in the Single-Window experimental setup, is superposed with the dual-LO in the detector plane. This time, the beat note contains two frequency components, one from the superposition of S and BLO at 10 MHz, the other from S and SLO at 10.003 MHz.

The beat-signals are detected by a spectrum analyzer and squared as in the

Single-Window case. The signal exiting the squarer oscillates at the frequency difference of SLO and BLO of 3 kHz and is detected in the Lock-In amplifier which uses the 3 kHz external oscillator as a reference. The quadrature outputs of the Lock-In amplifier contain all the information about the true Wigner function, as we will see below.

In the following section, the experimental setup for the Two-Window technique will be described. In Section 5.3 and Section 5.3.1 we will derive the mathematical expression for the signal we measure and show how to retrieve the true Wigner function of the field from it. Also, a derivation of the direct relation between mean square beat signal and the distribution of the Signal field in position and momentum will be presented. In Section 5.4 we discuss the physical meaning of the measured complex beat-signal for an ideal and non-ideal dual-LO.

I will conclude the chapter by short descriptions of the Acousto-optic modulators (Section 5.5), the phase-locked loop I developed for this experiment (Section 5.6), the $4f$-system (Section 5.7), and an overview over the complete system (Section 5.8).

5.2 Experimental Setup

As already mentioned in the Introduction, the Two-Window technique employs a pair of phase-coupled LO's instead of a single LO as in the Single-Window case. This pair consists of a large collimated beam (*'Big LO'* or *BLO*) providing high momentum resolution and a small focused beam (*'Small LO'* or *SLO*) providing high spatial resolution. Figure 5.1 shows the experimental setup. Again, a $4f$-system as well as other optical components which are not crucial for grasping the concept of this technique were omitted in the figure. Electronic connections are displayed as dashed lines, optical pathways as solid lines. While the Signal arm has

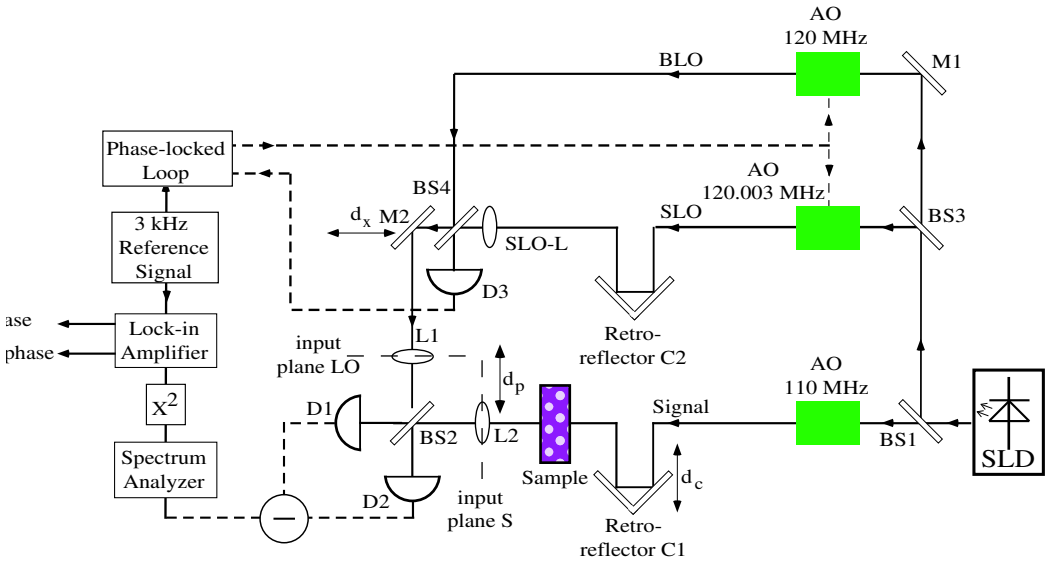

Figure 5.1: Two-Window technique experimental setup for measuring true Wigner functions

lost the chopper, the LO arm is split up by beam splitter BS_3. The SLO beam is shifted by 120.003 MHz and reaches the lens $SLO-L$ (f=25 cm), which focuses the beam onto the LO-input plane. The BLO is shifted by 120 MHz and superposed with the SLO at beamsplitter BS_4. In order to match the path length of BLO and SLO, a second retro-reflector is introduced in BLO. The 3 kHz frequency difference between SLO and BLO is kept constant by means of a phase-locked loop (PLL) and detector D_3: The PLL compares a 3 kHz reference signal with the beat signal of SLO and BLO at detector D_3. It multiplies both signals and adjusts the voltage controlled SLO-AO by an error voltage in order to keep the averaged product zero, which is *only* the case when reference- and beat-frequency are equal and out of phase by 90 degrees. The PLL is discussed in greater detail in in Section 5.6. The phase-coupled LO-pair is, as in the Single-LO setup, mixed with the Signal field and detected by a balanced detector. The beat notes of 10 and 10.003 MHz are detected by a spectrum analyzer, squared, and fed into a Lock-in amplifier which

uses the 3 kHz reference signal as a reference as opposed to the chopper used in the Single-Window setup. The Lock-in amplifier produces two quadrature voltages: an *In-phase* signal which is proportional to the signal component which is in phase with respect to the reference signal, and an *out-of-phase* signal which is proportional to the component which is 90 degrees shifted to it. In combination they contain the complete amplitude- and phase information of the detected signal. In the next section I show how the true Wigner function of a signal field can be measured using this setup.

5.3 Measurement of true Wigner functions

For sufficiently high global coherence, the Wigner function of a Signal field can be directly measured. In our experiment, this condition is met to a very good degree with a global coherence of more than 7 (see Section 8.1). In the following we show how the true Wigner function is measured and retrieved.

The LO in the dual-LO scheme is a phase-coupled pair of a *small LO* (*SLO*) and a *big LO* (*BLO*), as already mentioned. Its electric field can be written as: [1]

$$\mathcal{E}_{LO}(x) = \mathcal{E}_{LO,0}\left[\exp(-\frac{x^2}{2a^2}) + \beta e^{i\omega t}\exp(-\frac{x^2}{2A^2})\right], \tag{5.1}$$

where $e^{i\omega t}$ denotes the relative phase of the BLO with respect to the SLO determined by the phase-locking at $\omega = 2\pi \times 3$ kHz and β its relative amplitude. a and A are the beam intensity e^{-2} radii for the SLO and BLO, respectively. The Wigner function for this LO is then:

[1] In the following calculation, a and A denote characteristic widths of SLO and BLO. In all other calculations in this thesis a and A are dimensionless scaling factors. We only choose to stray from this habit here to enhance the readability of the formulae.

$$
\begin{aligned}
W_{LO}(x,p) &= \int \frac{d\epsilon}{2\pi}\, e^{ip\epsilon}\mathcal{E}^*_{LO}(x+\frac{\epsilon}{2})\mathcal{E}_{LO}(x-\frac{\epsilon}{2}) \\
&= \mathcal{E}^2_{LO,0}\int \frac{d\epsilon}{2\pi} e^{ip\epsilon}\left\{\exp\left[-\frac{(x+\frac{\epsilon}{2})^2}{2a^2}\right] + \beta e^{-i\omega t}\exp\left[-\frac{(x+\frac{\epsilon}{2})^2}{2A^2}\right]\right\} \\
&\times \left\{\exp\left[-\frac{(x-\frac{\epsilon}{2})^2}{2a^2}\right] + \beta e^{i\omega t}\exp[-\frac{(x-\frac{\epsilon}{2})^2}{2A^2}]\right\}. \qquad (5.2)
\end{aligned}
$$

Since the Lock-in amplifier locks on to the reference frequency used to phase-lock the LO's, only the cross terms $\propto \exp(\pm i\omega t)$ in Eq. (5.2) are detected; the other terms cancel. The cross terms are

$$
\begin{aligned}
W_{aA}(x,p) &= \beta E_0^2 \int \frac{d\epsilon}{2\pi}\, e^{ip\epsilon}\left\{e^{i\omega t}\exp\left[-\frac{(x+\frac{\epsilon}{2})^2}{2a^2} - \frac{(x-\frac{\epsilon}{2})^2}{2A^2}\right]\right. \\
&+ \left. e^{-i\omega t}\exp\left[-\frac{(x+\frac{\epsilon}{2})^2}{2A^2} - \frac{(x-\frac{\epsilon}{2})^2}{2a^2}\right]\right\} \\
&\propto e^{-i\omega t}I + e^{i\omega t}I^* \qquad (5.3)
\end{aligned}
$$

where

$$
I = \int \frac{d\epsilon}{2\pi}\exp\left[-\frac{(x+\frac{\epsilon}{2})^2}{2a^2} - \frac{(x-\frac{\epsilon}{2})^2}{2A^2}\right] e^{i\epsilon p}. \qquad (5.4)
$$

I can be transformed the following way:

$$
\begin{aligned}
I &= \int \frac{d\epsilon}{2\pi} \exp\left[-\frac{A^2(x+\frac{\epsilon}{2})^2 + a^2(x-\frac{\epsilon}{2})^2}{2a^2A^2}\right] e^{i\epsilon p} \\
&= \int \frac{d\epsilon}{2\pi} \exp\left\{-\frac{1}{2}\left[(\frac{1}{a^2}+\frac{1}{A^2})(x^2+\frac{\epsilon^2}{4}) + (\frac{1}{a^2}-\frac{1}{A^2})x\epsilon\right]\right\} e^{i\epsilon p} \\
&= \exp\left[-\frac{1}{2}(\frac{1}{a^2}+\frac{1}{A^2})x^2\right] \\
&\times \int \frac{d\epsilon}{2\pi} \exp\left\{-\left[\frac{1}{8}(\frac{1}{a^2}+\frac{1}{A^2})\epsilon^2 + \frac{1}{2}(\frac{1}{a^2}-\frac{1}{A^2})x\epsilon - ip\epsilon\right]\right\} \\
&= \exp(-\frac{\alpha}{2}x^2) \int \frac{d\epsilon}{2\pi} \exp\left[-\left(\frac{\alpha}{8}\epsilon^2 + \frac{\beta}{2}x\epsilon - ip\epsilon\right)\right] \qquad (5.5)
\end{aligned}
$$

where

$$
\begin{aligned}
\alpha &= \frac{1}{a^2} + \frac{1}{A^2} \\
\beta &= \frac{1}{a^2} - \frac{1}{A^2}. \qquad (5.6)
\end{aligned}
$$

Solving the integral in Eq. (5.5) yields:

$$
\begin{aligned}
I &= \frac{4}{\alpha} \exp(-\frac{\alpha}{2}x^2) \exp\left[\frac{2}{\alpha}\left(\frac{\beta^2}{4}x^2 - p^2 - i\beta xp\right)\right] \\
&= \frac{4}{\alpha} \exp\left[-(\frac{\alpha}{2} - \frac{\beta^2}{2\alpha})x^2 - \frac{2}{\alpha}p^2 - 2i\frac{\beta}{\alpha}xp\right]. \qquad (5.7)
\end{aligned}
$$

Replacing α and β according to Eq. (5.6), one gets

$$
I \propto \frac{A^2a^2}{A^2+a^2} \exp\left(-2x^2\frac{1}{A^2+a^2} - 2p^2\frac{A^2a^2}{A^2+a^2} - 2i\frac{A^2-a^2}{A^2+a^2}xp\right) \qquad (5.8)
$$

which reduces to

$$I \propto \exp\left(-\frac{2x^2}{A^2} - 2a^2p^2 - 2ixp\right) \tag{5.9}$$

for $A \gg a$. This is always the case in our experiment, where we choose the BLO to have a much larger diameter than the focused SLO. When we choose the diameters of BLO and SLO so that A is much bigger than the position x range of the Signal field and $\frac{1}{a}$ much bigger than the momentum p range of the Signal field we measure, the exponential terms in Eq. (5.9) reduce to unity and we get:

$$I \propto \exp(-2ixp). \tag{5.10}$$

With Equations (5.9) or (5.10) we can calculate the Wigner function of the LO in Eq. (5.3):

$$\begin{aligned} W_{aA}(x,p) &\propto e^{-i\omega t}I + e^{\omega t}I^* \\ &= \exp\left(-\frac{2x^2}{A^2} - 2a^2p^2\right)[\exp(i\omega t - 2ixp) + \exp(-i\omega t + 2ixp)] \\ &= 2\exp\left(-\frac{2x^2}{A^2} - 2a^2p^2\right)\cos(2xp - \omega t) \qquad (5.11) \\ &\approx 2\cos(2xp - \omega t). \qquad (5.12) \end{aligned}$$

Now that we have the Wigner function for our dual-LO beam, we can calculate the *in-phase* signal we measure, using Eq. (4.25)

$$\begin{aligned} S_B^{IP}(x,p) &= \int dx'\,dp'\,W_{LO}(x'-x,p'-p)\,W_S(x',p') \\ &\propto \int dx'\,dp'\,\cos[2(x'-x)(p'-p)]\,W_S(x',p'). \qquad (5.13) \end{aligned}$$

The second quadrature of the Lock-In amplifier, which is referred to as *out-of-phase signal*, measures the signal field component that is 90 degrees out of phase with respect to the reference signal and can be found by subtracting a phase of 90 degrees from ωt in Eq. (5.13). This manipulation just changes cosine into sine:

$$S_B^{OP}(x,p) \propto \int dx'\, dp'\, \sin[2(x'-x)(p'-p)]\, W_S(x',p'). \tag{5.14}$$

The combined in-phase and out-of-phase signals can be written more elegantly using complex notation:

$$\begin{aligned} S_B(x,p) &= S_B^{IP}(x,p) + iS_B^{OP}(x,p) && (5.15)\\ &= \frac{1}{\pi}\int dx'\, dp'\, \exp[2i(x'-x)(p'-p)]\, W_S(x',p'). && (5.16) \end{aligned}$$

$S(x,p)$ is a Margenau-Hill transformation of the true Wigner function $W_S(x,p)$ of the field. We will refer to $S_B(x,p)$ as the *complex beat signal*.

5.3.1 Extraction of the true Wigner function from $S_B(x,p)$

In order to retrieve the Wigner function $W_S(x',p')$ of the signal field, the expression in Eq. (5.16) must be inverted. A reasonable guess would be that

$$W_S(x,p) = \frac{1}{\pi}\int dx'\, dp'\, \exp[-2i(x-x')(p-p')]\, S_B(x',p'). \tag{5.17}$$

That this is indeed the case can be shown very straightforwardly by integrating Eq. (5.16) from both sides according to the right side of Eq. (5.17):

$$
\begin{aligned}
& \frac{1}{\pi}\int dx\,dp\,S_B(x,p)\exp[-2i(x''-x)(p''-p)] \\
= \;& \frac{1}{\pi^2}\int\int\int\int dx\,dp\,dx'\,dp'\;\exp[-2i(x''-x)(p''-p)+2i(x'-x)(p'-p)] \\
\times \;& W_S(x',p') \\
= \;& \frac{1}{\pi^2}\int\int\int\int dx\,dp\,dx'\,dp'\;\exp[2i(x'p'-x''p''+x(p''-p')+p(x''-x')] \\
\times \;& W_S(x',p') \\
= \;& \frac{1}{\pi^2}\int\int\exp[2i(x'p'-x''p'')]\,W_S(x',p') \\
& \times\int dx\,dp\;\exp[2i(x(p''-p')+p(x''-x)]. \qquad (5.18)
\end{aligned}
$$

The last integral on the left reduces to a product of delta functions:

$$
\int dx\,dp\;\exp[2i(x(p''-p')+p(x''-x)] = \pi^2\delta(p''-p')\delta(x''-x') \qquad (5.19)
$$

so that Eq. (5.18) becomes:

$$
\begin{aligned}
\pi^2\frac{1}{\pi^2}\int\int\exp[2i(x'p'-x''p'')]\,W_S(x',p')\delta(p''-p')\delta(x''-x') \\
= W_S(x'',p''). \qquad (5.20)
\end{aligned}
$$

Summarizing Equations (5.18)-(5.20), it was shown that $W_S(x,p)$ can indeed be retrieved from the complex beat signal $S_B(x,p)$ by means of the inverse Margenau-Hill transformation

$$W_S(x,p) = \frac{1}{\pi}\int dx'\,dp'\,\exp[-2i(x-x')(p-p')]\,S_B(x',p'). \tag{5.21}$$

Eq. (5.21) shows that the Two-Window technique enables the retrieval of the true Wigner function without the smoothing effect of a convolution with the Wigner function of a Single-LO. The spatial and momentum resolution with which the Wigner function is measured is limited by the size of the small LO and collimation of the big LO.

In practice, we use a C++ program program to perform the inverse Margenau-Hill transformation in Eq. (5.21) for the data we measure. The program code and description can be found in Appendix C.

5.3.2 Relation between $S_B(x,p)$ and the Signal field

Another interesting relation between the measured complex beat signal $S_B(x,p)$ and the Signal field as a function of position and momentum will be demonstrated in the following.

When we replace $W_S(x,p)$ in Eq. (5.16) by its expression in terms of the cross-spectral density in Eq. (3.1), we get

$$
\begin{aligned}
S_B(x,p) &= \frac{1}{\pi}\int dx'\,dp'\,\exp[2i(x'-x)(p'-p)] \\
&\times \int d\epsilon\,\exp(i\epsilon p)\,\langle \mathcal{E}^*(x'+\frac{\epsilon}{2})\,\mathcal{E}(x'-\frac{\epsilon}{2})\rangle \\
&= \frac{1}{\pi}\int dx' \int d\epsilon\,\langle \mathcal{E}^*(x'+\frac{\epsilon}{2})\,\mathcal{E}(x'-\frac{\epsilon}{2})\rangle \\
&\times \int dp'\,\exp(i\epsilon p')\,\exp[2i(x'-x)(p'-p)] \\
&= \frac{1}{\pi}\int dx' \int d\epsilon\,\langle \mathcal{E}^*(x'+\frac{\epsilon}{2})\,\mathcal{E}(x'-\frac{\epsilon}{2})\rangle \\
&\times \exp[2i(x-x')p] \int dp'\,\exp(i\epsilon p')\exp[2i(x'-x)p']. \qquad (5.22)
\end{aligned}
$$

The last integral in Eq. (5.22) reduces to a delta function:

$$
\int dp'\,\exp(i\epsilon p')\exp[2i(x'-x)p'] = 2\pi\delta[\epsilon + 2(x'-x)] \qquad (5.23)
$$

so that Eq. (5.22) becomes

$$
S_B(x,p) = 2\langle \mathcal{E}^*(x)\exp(2ixp)\int dx'\,\mathcal{E}(2x'-x)\exp(-2ix'p)\rangle. \qquad (5.24)
$$

If we replace $2x'-x$ by the variable u, Eq. (5.24) becomes:

$$
\begin{aligned}
S_B(x,p) &= \langle \mathcal{E}^*(x)\exp(2ixp)\int du\,\mathcal{E}(u)\exp[-i(u+x)p]\,\rangle \\
&= \langle \mathcal{E}^*(x)\exp(ixp)\int du\,\mathcal{E}(u)\exp(-iup)\rangle \\
&= \langle \mathcal{E}^*(x)\,\mathcal{E}(p)\rangle\exp(ixp). \qquad (5.25)
\end{aligned}
$$

The measured signal $S_B(x,p)$ is the averaged correlation of the Signal field at a given

position $\mathcal{E}(x)$ and the Signal field at given momentum $\mathcal{E}(p)$, times a phase-factor. A much shorter derivation in terms of the electric fields as well as a discussion of the phase-factor will be given in Section 5.4. We note that this expression only holds for Signal fields which are sufficiently broad in space and momentum, which is the case for all our experiments involving turbid media. In other words, the results for an *ideal* Dual-LO must be very close to those for the Dual-LO we employ. In our experiments involving the characterization of the Signal beam itself, we have to take into account the finite size of the BLO and the non-zero size of the SLO we use. This will be discussed for a transverse coherent beam in Section 5.4.3; the complete derivation for a finite coherence area of a beam will be performed in Section 7.2.

5.4 Interpretation of the measured beat signals

In the Two-window scheme, the balanced detection system isolates two beat notes from the frequency components of $\mathcal{E}_S$, $\mathcal{E}_{BLO}$ and $\mathcal{E}_{SLO}$ which oscillate with 110, 120 and 120.003 MHz. Between the SLO and BLO, there is no 180 degree phase-shift since they take the same paths through the detector beam splitter. Therefore, their beat amplitude at a relative frequency of 3 kHz cancels in the balanced detector. The relative phase-shift exists only between the Signal field on one side and the SLO and BLO on the other side. The measured beat notes have therefore frequencies of 10 and 10.003 MHz. The bandwidth on the spectrum analyzer has to be chosen so that both frequencies can pass without experiencing attenuation or frequency-dependent phase-shifts. In our experiment, the bandwidth was set to at least ten times the frequency difference.

The beat note of a superposed LO and S can be written as (see Eq. (4.6)):

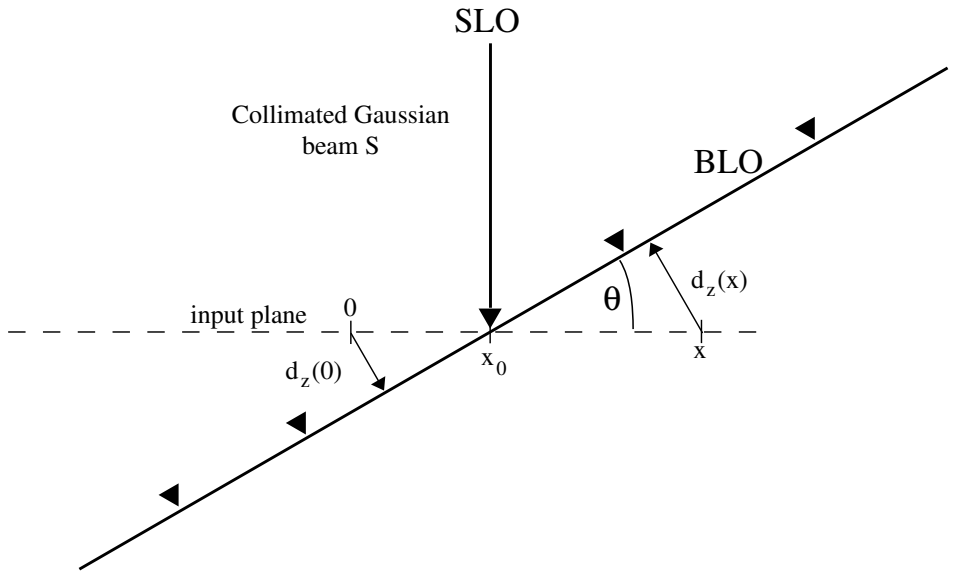

Figure 5.2: Ideal SLO (Delta function) incident at x_0 and BLO (plane wave tilted at $\theta = \frac{p_0}{k}$) interfere with a collimated beam S. $d_z(x)$ is the path difference of the BLO's wavefront with respect to the input-plane, introduced by the tilt.

$$V_B \propto \exp(i\Delta\omega t) \int dx \, \langle \mathcal{E}_S^*(x) \, \mathcal{E}_{LO}(x) \rangle \tag{5.26}$$

where the integral is again performed over the detection plane. Here we have explicitly written the exponential oscillating a the beat frequency $\Delta\omega$, near 10 MHz.

For a dual-LO consisting of a SLO and a BLO the beat signal becomes

$$\begin{aligned} V_B &\propto V_B^{SLO} + V_B^{BLO} \\ &= \exp(i\Delta\omega_S t) \int dx \, \langle \mathcal{E}_{SLO}^*(x) \, \mathcal{E}_S(x) \rangle + \exp(i\Delta\omega_B t) \int dx \, \langle \mathcal{E}_{BLO}^*(x) \, \mathcal{E}_S(x) \rangle \end{aligned} \tag{5.27}$$

where $\Delta\omega_S$ and $\Delta\omega_B$ are the beat frequencies due to SLO and BLO, respectively.

5.4.1 Ideal Dual-LO

An ideal SLO has the shape of a Delta function in space, while an ideal BLO is a tilted plane wave (i.e. Delta function in momentum); both are shifted by a distance x_0 relative to S:

$$\mathcal{E}_{SLO} \propto \delta(x - x_0) \tag{5.28}$$

$$\mathcal{E}_{BLO} \propto \exp[i\phi_b(x)] \tag{5.29}$$

where $\phi_b(x)$ linearly changes with x. Figure 5.2 clarifies these statements: S is a Gaussian beam centered at $x = 0$. The SLO is a delta function centered at $x = x_0$. The BLO is tilted by an angle $\theta = \frac{p_0}{k}$ and, like the SLO, crosses the input plane at $x = x_0$.[2] p_0 is the transverse wave vector and k is the total wave vector. The tilt introduces a phase change $\phi_b(x)$ between S and BLO [3] for all $x \neq x_0$ which is the wave vector times the additional path length $d_z(x)$:

$$\begin{aligned} \phi_b(x) &= k d_z(x) = k(x - x_0)\theta = k(x - x_0)\frac{p_0}{k}. \\ &= (x - x_0)p_0 \end{aligned} \tag{5.30}$$

By using Equations (5.28) and (5.29) with Eq. (5.30) in Eq. (5.27), we get:

[2] Here we used again the small-angle approximation $\sin\theta \approx \theta$ for $\theta \ll 1$.

[3] In the experiment, the SLO is tilted as well relative to S, but its momentum spread is so large due to its small size that we can neglect all effects resulting from that tilt.

$$
\begin{aligned}
V_B &= V_B^{SLO} + V_B^{BLO} \\
&\propto \exp(i\Delta\omega_S t) \int dx \, \langle \delta(x - x_0)\mathcal{E}_S(x) \rangle \\
&+ \exp(i\Delta\omega_B t) \int dx \, \langle \exp[-i(x - x_0)p_0]\mathcal{E}_S(x) \rangle \\
&= \mathcal{E}_S(x_0)\exp(i\Delta\omega_S t) + \mathcal{E}_S(p_0)\exp(ix_0p_0)\exp(i\Delta\omega_B t) \qquad (5.31)
\end{aligned}
$$

where $\mathcal{E}_S(p_0)$ is the Fourier transform of $\mathcal{E}_S(x_0)$. The mean square signal is then

$$
\begin{aligned}
|\, V_B \,|^2 &= |\, V_B^{SLO} + V_B^{BLO} \,|^2 \\
&= |\, V_B^{SLO} \,|^2 + |\, V_B^{BLO} \,|^2 + V_B^{SLO*}V_B^{BLO} + V_B^{SLO}V_B^{BLO*} \\
&= |\, \mathcal{E}_S(x_0) \,|^2 + |\, \mathcal{E}_S(p_0) \,|^2 \\
&+ \mathcal{E}_S^*(x_0)\mathcal{E}_S(p_0)\exp(ix_0p_0)\exp[i(\Delta\omega_B - \Delta\omega_S)t] \\
&+ \mathcal{E}_S(x_0)\mathcal{E}_S^*(p_0)\exp(-ix_0p_0)\exp[-i(\Delta\omega_B - \Delta\omega_S)t]. \qquad (5.32)
\end{aligned}
$$

The first cross-term is the complex conjugate of the second cross-term. As explained in Section 5.2, we detect the complex beat signal by means of a Lock-In amplifier using the frequency difference between SLO and BLO, $\Delta\omega_B - \Delta\omega_S$, as a reference. Therefore, we detect only the cross-terms in Eq. (5.32) and the measured complex mean square beat signal can be written as one of the cross-terms:

$$
\begin{aligned}
S_B(x_0, p_0) &\propto V_B^{SLO*} V_B^{BLO}\big|_{\Delta\omega_B - \Delta\omega_S} \\
&\propto \langle \mathcal{E}_S^*(x_0)\rangle \langle \mathcal{E}_S(p_0)\rangle \exp(i x_0 p_0) \\
&= \langle \mathcal{E}_S^*(x_0)\mathcal{E}_S(p_0)\rangle \exp(i x_0 p_0) \qquad (5.33)
\end{aligned}
$$

where the ensemble averaging can be performed over the product of $\mathcal{E}_S^*(x_0)$ and $\mathcal{E}_S(p_0)$ since the individual fields are uncorrelated and therefore statistically independent. This result is identical with expression Eq. (5.25) which was derived using Wigner functions.

We now see that the phase factor $\exp(ix_0p_0)$ is just due to the additional relative path difference $d_z(0) = -\frac{p_0}{k}x_0$ caused by the shift x_0 in connection with a tilt p_0 of the BLO relative to S (see Figure 5.2). In the following section Section 5.4.2, we will use this model to explain the shape of the quadrature signals in phase-space.

5.4.2 The quadrature signals

Let us consider the quadrature signals for a simple Signal field - a flat Gaussian beam. In that case, both $\mathcal{E}(x_0)$ and $\mathcal{E}(p_0)$ are real and Gaussian. According to Eq. (5.33), the in-phase and out-of-phase quadrature signals, which are the real and imaginary parts of $S_B(x_0, p_0)$, are just Gaussians, modulated by a cosine or sine function respectively. Figure 5.3 shows a plot of Eq. (5.33) for a typical flat Gaussian beam.

The particular shape of the quadrature signals becomes evident when we go back to Section 5.4.1 and look at the phase-factor BLO introduces due to its displacement and tilt relative to S. This phase-factor $\exp(ix_0p_0)$ is equal to $\exp[i\phi_b(0)] =$

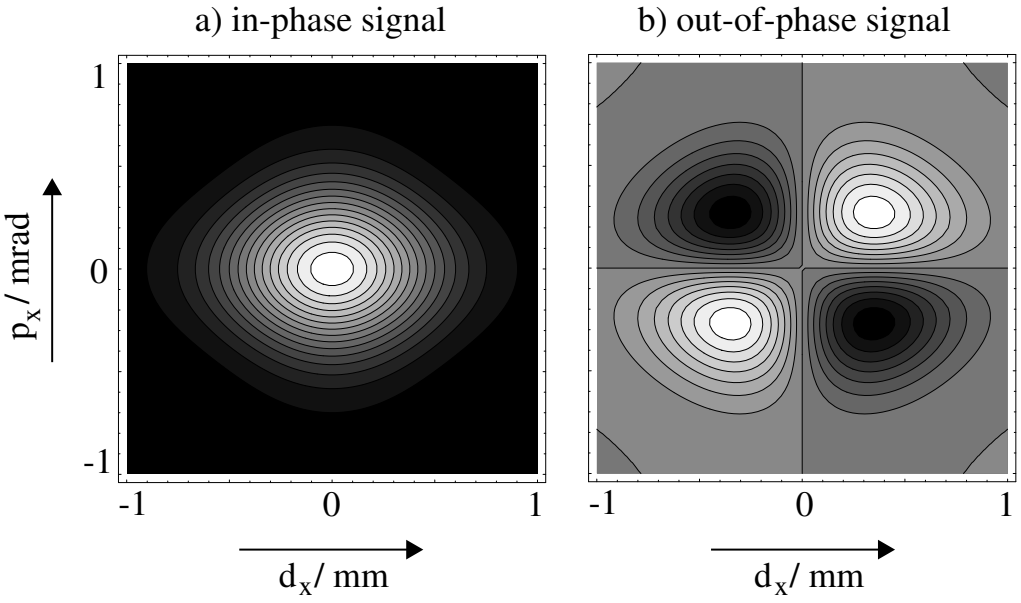

Figure 5.3: Simulation of real part (a) and imaginary part (b) of $S_B(d_x, p_x)$, which correspond to the measured in-phase- and out-of-phase signal of a typical Gaussian Schell Signal beam.

$\exp[ikd_z(0)]$ as stated in Eq. (5.30). We remember that $d_z(x)$ is the additional path-difference at between S and BLO at a given position on the input plane relative to the center of S. $d_z(0)$ is shown in Figure 5.2. We therefore get:

$$S_B^{IP}(x_0, p_0) = \langle \mathcal{E}_S(x_0)\mathcal{E}_S(p_0)\rangle \cos(x_0 p_0) \tag{5.34}$$

$$= \langle \mathcal{E}_S(x_0)\mathcal{E}_S(p_0)\rangle \cos(-kd_z(0)) \tag{5.35}$$

$$S_B^{OP}(x_0, p_0) = \langle \mathcal{E}_S(x_0)\mathcal{E}_S(p_0)\rangle \sin(x_0 p_0) \tag{5.36}$$

$$= \langle \mathcal{E}_S(x_0)\mathcal{E}_S(p_0)\rangle \sin(-kd_z(0)) \tag{5.37}$$

When we keep x_0 constant we see in Figure 5.2 that when we tilt the BLO to the other side by the same amount ($p_0 \to -p_0$), $d_z(0)$ changes its sign. The in-phase

part does not see the sign of $d_z(0)$ here; its amplitude which is maximal for $p_0 = 0$ becomes smaller in each case by the same amount. The out-of-phase signal on the other hand which is proportional to the sine of $-kd_z(0)$, switches its sign. The same happens when we keep the momentum of BLO constant and change the location of the LOs from x_0 to $-x_0$, where $d_z(0)$ changes its sign as well. This behavior of these phase-terms, together with the Gaussian dependence of the beat-signals amplitude, explains the spade-like shape of the in-phase signal (Figure 5.3a) as well as the clover-like appearance of the out-of-phase signal (Figure 5.3b).

5.4.3 Non-ideal Dual-LO

The requirements for an SLO to be infinitely small and a BLO to be a perfect plane wave can of course not be realized. In fact, both SLO and BLO have a Gaussian beam profile. While the SLO has a diameter of about 100 μm, the BLO has approximately the same size as the Signal beam. As already mentioned, most Signal fields measured in our experiment have position- and momentum distributions which are much larger than those of the SLO or the BLO, respectively. In those cases, the Dual-LO can be considered perfect, to a good approximation. When we try do determine the beam parameters of the Signal input beam *itself* (Chapter 7) on the other hand, we must take into account that its momentum distribution is equal to that of the BLO and the BLO also becomes position-dependent due to its finite size. The SLO on the other hand can still be considered perfect, with its beam size smaller than the Signal beam by an order of magnitude.

In the following we will briefly outline the corrections for the beat signal of a finite size BLO and a similar Signal beam. The expression for an ideal BLO on the right of Eq. (5.29) is multiplied by a Gaussian term:

$$\mathcal{E}_{realBLO}(x, A) \propto \exp[i\phi_b(x)] \exp(-\frac{x^2}{2A^2}) \tag{5.38}$$

For an ideal BLO, $A \to \infty$ and the second exponential becomes unity. We express the Signal beam in the Gaussian-Schell model as a product of a Gaussian term and a phase term $\mathcal{E}'_S(x)$ describing the curvature of the field:

$$\mathcal{E}_S(x) \propto \exp(-\frac{x^2}{2B^2})\mathcal{E}'_S(x) \tag{5.39}$$

B is usually on the order of half a millimeter. Again we assume the transverse coherence length to be sufficiently large to be neglected. The beat signal for the BLO in line 3 of Eq. (5.31) then becomes:

$$\begin{aligned} V_B^{realBLO}(x_0, p_0, A, B) &\propto \int dx\ \exp[-i(x - x_0)p_0] \exp[-\frac{(x - x_0)^2}{2A^2}] \exp(-\frac{x^2}{2B^2})\mathcal{E}'_S(x) \\ &\propto \exp(ix_0p_0) \exp[-\frac{x_0^2}{2(A^2 + B^2)}] \\ &\times \int dx \exp(-ixp_0) \exp\left[-\frac{1}{2}(\frac{1}{A^2} + \frac{1}{B^2})(x - \frac{x_0}{1 + \frac{A^2}{B^2}})^2\right] \mathcal{E}'_S(x) \end{aligned} \tag{5.40}$$

where we omitted the exponential containing the beat frequency which will not be affected by the following calculations. There is no general solution to the above integral. For a plane wavefront ($\mathcal{E}'_S(x) \equiv 1$), Eq. (5.40) becomes

$$V_B^{realBLO}(x_0, p_0, A, B, R=\infty) \propto \exp\left[-\frac{x_0^2}{2(A^2+B^2)}\right] \exp\left[-\frac{p_0^2}{2(\frac{1}{A^2}+\frac{1}{B^2})}\right] \times \exp\left[ix_0p_0\left(\frac{1}{1+\frac{B^2}{A^2}}\right)\right]. \quad (5.41)$$

Compared to the the beat signal for an ideal BLO ($A \to \infty$)

$$V_B^{idealBLO}(x_0, p_0, B, R=\infty) \propto \exp(-\frac{B^2}{2}p_0^2)\exp(ix_0p_0) \quad (5.42)$$

the pre-factor of both x_0 and p_0 change by a factor $\sqrt{1+\frac{B^2}{A^2}}$, as can easily be seen:

$$V_B^{realBLO}(x_0, p_0, A, B, R=\infty) = V_B^{idealBLO}(\frac{x_0}{\sqrt{1+\frac{B^2}{A^2}}}, \frac{p_0}{\sqrt{1+\frac{B^2}{A^2}}}, R=\infty). \quad (5.43)$$

In our experiment, $B = A$, so Eq. (5.43) reduces to:

$$V_B^{realBLO}(x_0, p_0, A=B, R=\infty) = V_B^{idealBLO}(\frac{x_0}{\sqrt{2}}, \frac{p_0}{\sqrt{2}}, R=\infty) \quad (5.44)$$

which is the expected result for the convolution of two equal-sized beams, as in the Single-LO technique. The above expressions is only exact for $R = \infty$; for finite R we need to replace $\frac{1}{2B^2}$ by $\frac{1}{2B^2} - \frac{ik}{2R} = \frac{1}{2B^2}(1 - i\frac{kB^2}{R})$. Eq. (5.44) is still a good approximation as long as $R \gg kB^2$ which is usually on the order of 5 meters.

For completeness we mention the result for $V_B^{realBLO}$ for the other extreme where the radii of curvature $R \ll kB^2$:

$$V_B^{realBLO}(x_0, p_0, A, B, R_{small}) \propto \exp\left[-\frac{1}{2A^2}(x_0 - \frac{R}{k}p_0)^2 - \frac{R^2}{2B^2k^2}p_0^2\right] \times \exp\left\{i\left[xp + \frac{2R}{k}\left(\frac{x^2}{(2A^2)^2} + p^2\right)\right]\right\} \quad (5.45)$$

The derivation is shown in Appendix B.

5.4.4 Measurement of Gaussian beams for ideal and real Dual-LO

While a real Dual-LO comes very close to an ideal LO in most experiments involving turbid media, in measurements of Signal fields which are small in phase-space the true properties of BLO and SLO have to be taken into account. For a flat Gaussian Signal field of the form

$$\mathcal{E}_S(x) \propto \exp(-\frac{x^2}{2B^2}), \quad (5.46)$$

an ideal Dual-LO will measure a complex beat signal of

$$S_B^{ideal}(x_0, p_0) \propto \mathcal{E}_S(x_0)\mathcal{E}_S(p_0)\exp(ix_0p_0) \propto \exp(-\frac{x^2}{2B^2})\exp(-\frac{B^2}{2}p^2)\exp(ix_0p_0) \quad (5.47)$$

as shown in Eq. (5.33), where we omitted the averaging brackets again since we consider a transverse coherent beam. Also, the electric fields are real because the wavefront is flat.

For the Dual-LO in our experiment on the other hand, which uses practically

an ideal SLO but a BLO the size of the Signal beam (A=B), the measured signal is

$$\begin{aligned} S_B^{real}(x_0,p_0) &= \exp\left[-\frac{x^2}{2}\left(\frac{1}{B^2}+\frac{1}{A^2+B^2}\right)\right]\exp\left(-\frac{B^2}{2(\frac{1}{A^2}+\frac{1}{B^2})}p_0^2\right) \\ &\times \exp\left[ix_0p_0\left(1-\frac{1}{1+\frac{B^2}{A^2}}\right)\right] \\ &= \exp[-\frac{x^2}{2B^2(\frac{2}{3})}]\exp(-\frac{B^2}{4}p_0^2)\exp(\frac{i}{2}x_0p_0). \end{aligned} \tag{5.48}$$

It can easily be seen that the measured position distribution is narrower by a factor $\sqrt{\frac{2}{3}}$ compared to a perfect BLO, while the momentum distribution is broader by a factor $\sqrt{2}$ (convolution of two beams with identical momentum distribution).

In Chapter 7 we will characterize the Signal beam of the SLD we use, which requires the incorporation of the finite transverse coherence length into the calculation of the beat signals.

In the following I will give an overview over some of the integral building blocks of the experimental setup.

5.5 Acousto-optic modulators (AO)

In our experiment we use three AO-Drivers and -crystals by IsoMET Co. with driver shifting frequencies of 110 and 120 MHz and a third 120 MHz tunable-one. The crystals are made from Lead Molybdate ($PbMoO_4$) and have an active aperture of 1 mm. The tunable AO-driver contains a VCO with a voltage range between 4 and 17 V, which corresponds to a frequency range of 80 to 130 MHz. The frequency-voltage dependency is approximately linear.

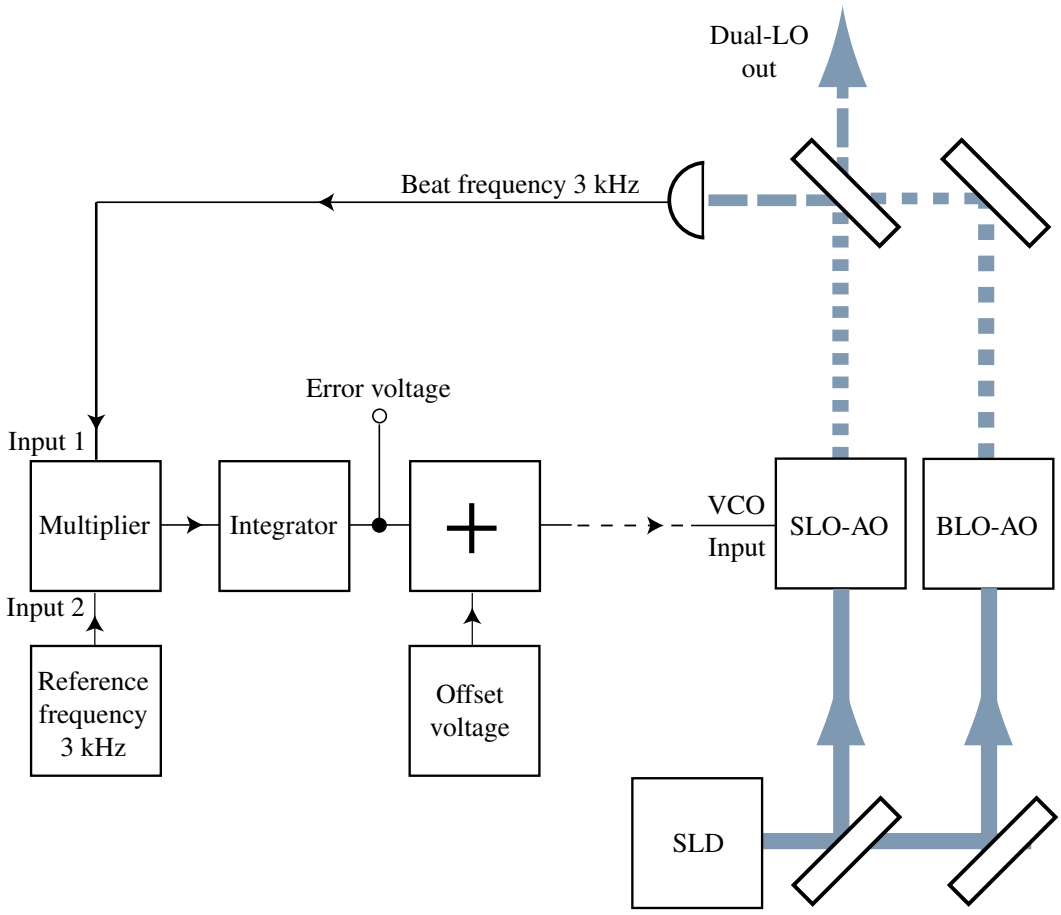

Figure 5.4: Block diagram of the PLL system. The SLO and BLO beams on the right are shifted by 120 and 120.003 MHz respectively. Its frequency difference is phase-locked with respect to the reference frequency.

5.6 Phase-locked loop

I developed the phase-locked loop to phase-couple the SLO to the BLO at a fixed low frequency. Its circuit diagram can be found in Appendix A. Figure 5.4 shows the block diagram: A photo-detector measures the beat signal of the small and the big LO and feeds it to input 1 of the multiplier. A 3 kHz reference signal provided by the Lock-in amplifier is applied at input 2. The product of both signals will be an alternating voltage which is fed into an integrator. If and only if the signals

at input 1 and 2 are 90 degrees out of phase, which implies they have the same frequency as well, will the product average and therefore the integrated output signal of the multiplier be zero. The integrator produces an error voltage which controls the frequency of the BLO. When the phase of either of the LOs drifts, the average output voltage takes on a positive or negative values depending on whether the relative phase of the BLO with respect to the SLO becomes bigger or smaller. Subsequently, this error voltage increases or decreases at the VCO of the BLO-AO-Driver, changing the frequency until the relative phase shift is back to 90 degrees. The offset voltage which is provided by a 22.5 V-battery just serves to adapt the voltage output of the PLL to the range of the VCO of the adjustable AO-Driver, which is 4-17 V. The offset voltage for an AO frequency of 120 MHz is about 10.17 V. A battery has an extremely low noise level compared to regular power supplies which makes it an ideal choice to provide the offset voltage in this case. Given the high input impedance of the AO-driver, which is on the order of 100 kΩ, the battery has a life-time of about a month.

For low difference frequencies between the BLO and the SLO, the bandwidth of the spectrum analyzer measuring the output of the balanced detector can be kept to a minimum which improves the S/N-ratio (for the frequencies detected see Section 5.4). The minimum frequency that can be realized depends on the noise-level in the feed-back loop. The variable AO has a voltage to frequency dependence of about 4 $\frac{\mathrm{MHz}}{\mathrm{V}}$. In order to stabilize the AOs at a given relative frequency f, the electronic noise level $V_{noise}(f)$ must be

$$V_{noise}(f) \ll \frac{f}{4\frac{MHz}{V}} \tag{5.49}$$

For a locking frequency of 1 kHz, $V_{noise} \ll 250\ \mu$V. This condition requires high-

frequency shielding and -blocking of the electronics and good grounding. Also, ground-loops which pick up magnetic fields (e.g. from the monitor) and high-impedance inputs in combination with unshielded wires which pick up electrical fields from the surroundings, have to be carefully avoided. As it turns out, even a common electronic multimeter connected in parallel to the feedback loop to the adjustable AO introduces enough noise to increase the smallest possible locking frequency to more than 10 kHz. Other noise sources are in the optical part of the system. Small fluctuations of the beam in position or momentum due to temperature changes of the SLD or noise in its power source can introduce considerable noise to the system. Especially when the two interfering beams are slightly misaligned, noise due to spatial fluctuations becomes stronger since the spatial derivative of the electric field of a Gaussian beam is larger off-center. An unstable phase-locked loop is therefore a reliable indicator that the alignment of the Local Oscillator beams has deteriorated due to drift and needs readjustment. A similar procedure works for the combination of Signal- and LO-field in the balanced detector.

An advantage of higher locking frequencies on the other hand is that the Lock-in amplifier provides a more stable signal for a given averaging time. Similarly, the PLL produces a more stable error voltage for a given time period since it can average over more cycles. From experience, a good coupling frequency, which counterbalances the described trade-off between low- and high-frequency operation, seems to be on the order of 3 kHz. A circuit diagram of the PLL is shown in Appendix A.

5.7 4f-system

A signal field emerging, for example, from a sample cell containing a turbid medium will change its transverse profile while travelling the distance to the input plane in

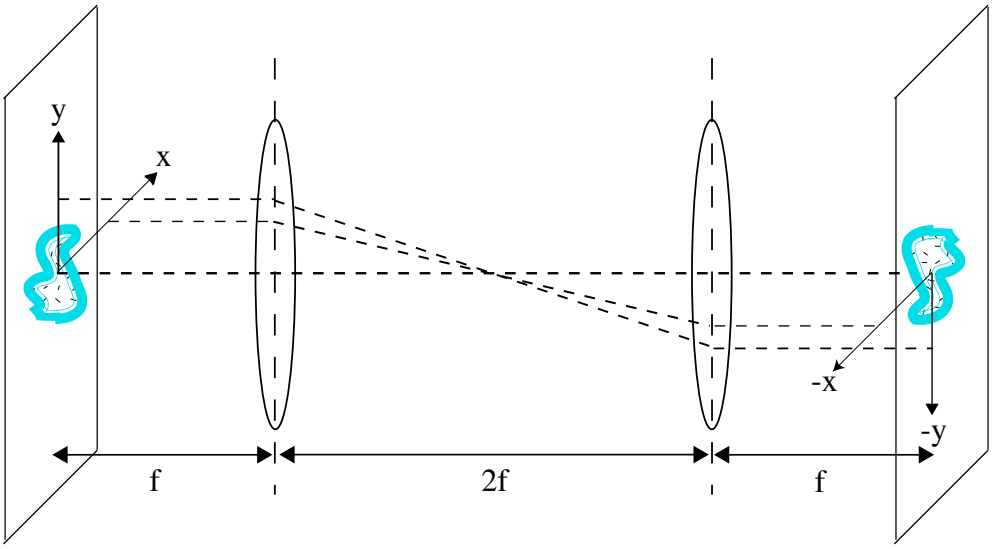

Figure 5.5: A 4f-system reproduces a field in the outer focal plane of one of its lenses in the outer focal plane of its other lens. The coordinates of the reproduced field as well as its momentum distribution are inverted.

our experiment. In most cases, the field will diverge; in which case the measured Wigner function will display a characteristic tilt to the right (see Figure 3.1). In all our experiments we therefore introduce a 4f-system that projects the light at the sample surface directly into the input plane. A 4f-system consists of two lenses of equal focal length f at a mutual distance of $2f$ (see Figure 5.5). A light field in the outer focal plane of one lens will be exactly reproduced in the outer focal plane of the other lens, but with the spatial and momental coordinates inverted. This becomes clear from the fact that a single lens Fourier-transforms the field in its focal plane into its other focal plane, which is also the focal plane of the second lens. The second lens Fourier transforms this field again, which reproduces the original field. The lenses have to have the same focal length in order for the magnification to be unity. In our 4f-system, we use achromatic lenses with a high

numerical aperture. Each lens consists of a convex lens glued to a concave lens made from a material with higher refractive index. This combination corrects spherical aberration to a good degree, thereby allowing high-numerical aperture applications without distortions [47].

In our experiment, the 4f-system is one of the most sensitive parts. Even small tilts of the lenses with respect to each other, misalignments perpendicular to the direction of the beam or regarding the mutual distance of the lenses will lead to distortions in the measured Signal, due to the high phase-sensitivity of the Two-Window technique.

In all our experiments we use a 4f-system right before the input lens in the Signal arm in order to project the output field from the sample directly into the input plane, as can be seen in the following section.

5.8 Overview of complete system

We conclude this chapter with the presentation of the complete experimental setup, which includes all optical elements which have been omitted for clarity in the previous sections. Figure 5.6 shows the scheme.

The preparation of a collimated beam from the SLD light is performed by the optical elements between the SLD and beam splitter BS_1. This is discussed in more detail in Chapter 6. The three lenses and the aperture collimate the beam; the mirrors M_{13} and M_{14} serve to adjust the transverse location and the angle of the beam entering the system. The $\lambda/2$-plate turns the polarization to vertical in order to avoid polarization effects in the system.

All three AOs are situated in the focal planes of 4f-systems built from lenses with a focal length of 30 cm (L_6-L_{11}). Focusing a beam before sending it through

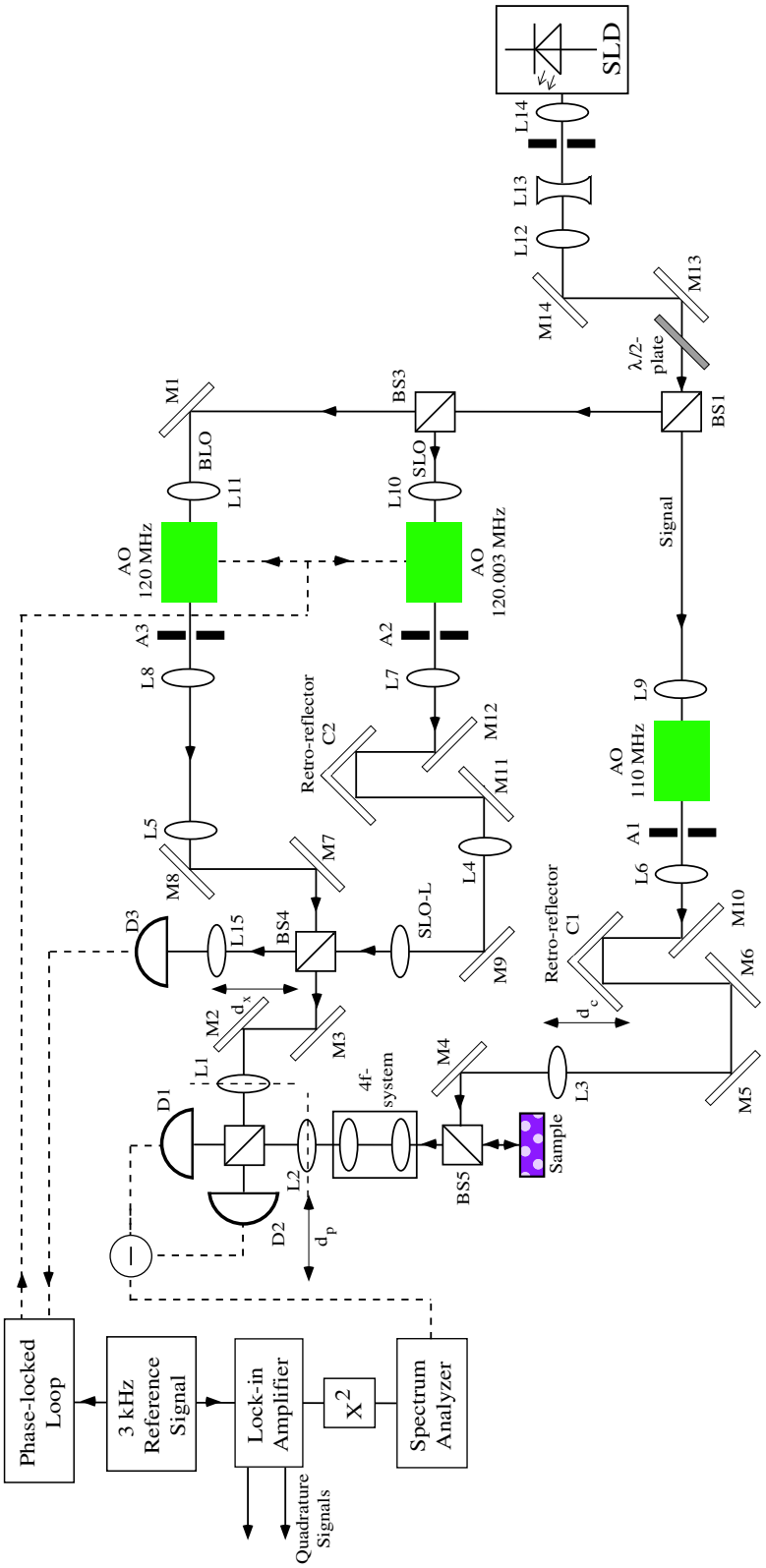

Figure 5.6: Complete experimental setup for the Two-Window technique.

an AO crystal is necessary to ensure that the beam hits a region in the AO crystal where the phase of the acoustic wave is approximately uniform, which guarantees uniform deflection. A beam diameter on the order of 0.5 mm is recommended by IsoMET. In order to minimize random differences of the beam profiles of both LOs and S, the distances between each AO and the initial beam splitter BS_1 are set to be equal.

There are additional lenses with a focal lens of 100 cm in each beam close to the detector (L_3-L_5) which allow the fine-tuning of the wavefronts in the input planes. Transversely partially coherent light has a stronger tendency to diverge than coherent light. The Two-Window technique is especially sensitive to the radii of curvature of each beam, which requires a careful alignment of all three correction lenses.[4] A more detailed treatment about the properties of partially coherent light in this context can be found in Section 6.3.

The Signal beam arm shows the setup for backscatter measurements. The incoming Signal beam from M_4 is reflected onto the sample by beam splitter B_5. The light backscattered from the sample is projected onto the Signal field input plane at L_2 by the 4f-system. The sample surface is in the first focal plane, the Signal field input plane in the second focal plane of the 4f-system. The adjustment of the Signal arm for the measurement of the enhanced backscattering effect will be explained in detail in Section 12.1.

For transmission experiments, beam splitter BS_5 will be replaced by a mirror and the sample be placed between this mirror and the 4f-system. As before, the sample surface must be located in the focal plane of the first lens of the 4f-system (see Section 13.1).

[4]Even though the SLO has an additional convex lens with a shorter focal lens ($SLO - L$), the correction lens L_4 is still useful for initial alignment of the SLO.

Chapter 6

The Superluminescent diode

6.1 Introduction

In nearly all of our experiments, a superluminescent light emitting diode *SLD* by Superlum Co. serves as a light source. An SLD is an emitter based on stimulated emission with amplification but insufficient feedback for laser oscillation to build up [48]. It can be viewed as a semiconductor laser diode with angled cleaved surfaces. Consequently, the free spectral range is relatively high, resulting in a broad spectra width on the order of 10 nm. A laser diode on the other hand has typically a spectral width of just 2-3 nm. Due to the angled structure of the emitter, the emerging light field is usually non-Gaussian and has an intensity distribution the shape of a sickle. Its angular spread is on the order of tens of degrees. Therefore the losses for beam-collimation can be expected to be high; they were measured to be about 70-80% which coincides with data from Superlum Co. The intricacies of the collimation of the SLD light and its collimation will be dealt with in Section 6.3.

The SLD is very sensitive to static electricity and other voltage spikes which might damage its depletion area. Because of its exponential $I-V-$characteristics, it requires a current source for operation. Due to the relatively small size of the emitting area the current density in the emitter can be on the order of tens of

$\frac{\text{kA}}{\text{cm}^2}$. This makes it vulnerable to current spikes and optical feedback which can lead to local overheating resulting in dopant diffusion or even destruction of the semiconductor crystal. The power supply and its safety measures regarding the operation of the SLD will be explained in Section 6.6.

SLDs from Superlum Co. which operate in the visible spectrum use a relatively new technology which make them very temperature-sensitive. Therefore temperature stabilization is required. A thermistor in combination with a peltier element which are mounted in the SLD casing keep the temperature constant down to milli-Kelvins. A brief description of the temperature stabilization will be given in Section 6.5

6.2 General parameters of the SLD

In this section we present the intrinsic parameters of the SLD we use as well as the properties of the collimated beams. The following table shows the most important parameters of the SLD provided by Superlum Co.:

Spectral center	678.3 nm
Spectral bandwidth	8.1 nm
Spectral ripple	0.5%
Maximum output power	18 mW
Maximum current	210 mA
Beam divergence vertical (e^{-2}-width intensity)	28 deg.
Beam divergence horizontal (e^{-2}-width intensity)	9 deg.

The global coherence, which is the ratio of the transverse coherence length σ_g to the beam size σ_s, changes during the collimation process due to the presence of apertures and lenses with insufficient numerical aperture. The global coherence of the light exiting our collimating system will be determined in Section 8.1 and also briefly discussed in Section 6.3. In the next section, the experimental determination of the longitudinal coherence will be presented.

6.2.1 Determination of the SLD's longitudinal coherence length

The longitudinal coherence l_c is a measure of the bandwidth of the light. It is usually defined as the path difference between perfect match of two equal beams, where the intensity of their interference is maximal, to the mutual distance where that intensity drops to half its maximal value.

In our experiment, the path-length dependency of the intensity of two interfering

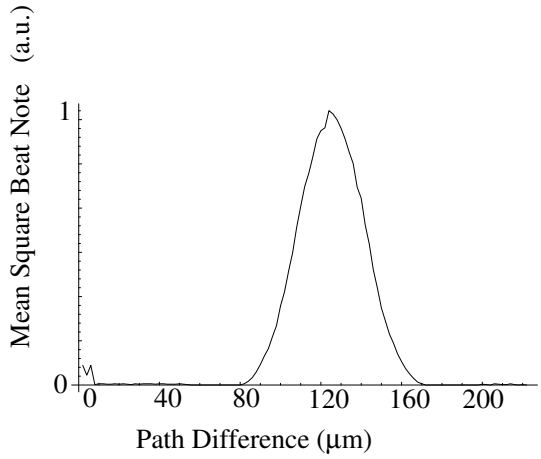

Figure 6.1: The mean square beat signal as a function of path difference between the Signal- and LO beams yields the longitudinal coherence length.

beams is proportional to the beat voltage $|V_B(z)|$:

$$|V_B(z)| \propto \exp\left[-\frac{1}{2}\left(\frac{z}{\Delta l_B}\right)^2\right], \tag{6.1}$$

where Δl_B is defined as the longitudinal spatial resolution. Δl_B can be shown to be $2/(\Delta k_{1/e})$, where Δk is the half width at e^{-1} of the wave-number distribution of the broadband light (compare Eq. (5.15) in [5]). Using $\Delta k_{1/e} = (2\pi/\lambda^2)\Delta\lambda_{1/e}$ and a straightforward transformation between $\Delta\lambda_{1/e}$ and its FWHM, the relation between Δl_B and the FWHM of the optical spectrum follows:

$$\Delta l_B = \frac{\sqrt{2\ln 2}}{\pi}\frac{\lambda^2}{\Delta\lambda_{FWHM}}. \tag{6.2}$$

From the values for the FWHM spectral width of $\Delta\lambda_{FWHM} = 8.1$ nm and center wavelength of $\lambda = 678.3$ nm provided by Superlum Co., we get a value of

$$\Delta l_B = 21.3\,\mu\text{m}. \tag{6.3}$$

According to the definition for l_c, $|V_B(z)|$ will drop to 1/2 of its maximal value at $z = l_c$, which determines the relation of Δl_B and l_c:

$$l_c = \sqrt{2\ln 2}\Delta l_B \approx 1.177 \times \Delta l_B \tag{6.4}$$

$$= \frac{2\ln 2}{\pi}\frac{\lambda^2}{\Delta\lambda_{FWHM}} = 25.0\,\mu\text{m}. \tag{6.5}$$

In our One-Window technique z-scans of the Signal beam itself we measure

$$|V_B(z)|^2 \propto \exp\left[-\left(\frac{z}{\Delta l_B}\right)^2\right] \tag{6.6}$$

l_c can easily be determined by first maximizing the overlap of Signal- and BLO beam and then measuring $|V_B(z)|^2$ as a function of path-delay by translating the retro-reflector, as shown in Figure 6.1. The shape of $|V_B(z)|^2$ is approximately Gaussian, dropping to e^{-1} of its maximal value at $z = \Delta l_B$ =21 μm, which yields a longitudinal coherence length, according to Eq. (6.4), of l_c ≈24.7 μm, which agrees well with the value derived from the spectrum in Eq. (6.5).

6.3 Collimation of SLD light

The collimating system as shown in Figure 6.2 consists of an achromatic high-numerical aperture lens L_{14} with a focal length of 8 mm with the SLD light emitting substrate approximately in its focal plane, followed by a Galilean telescope (L_{13} and L_{12}).

A Galilean telescope can partially or completely correct spherical aberration, which becomes important for beam diameters approaching the limits for the paraxial

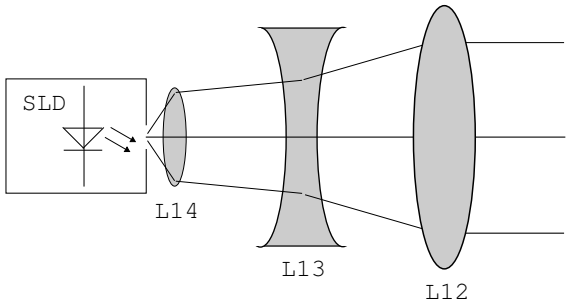

Figure 6.2: Collimator for the SLD

approximation [47]. This effect results from the combination of undercorrection of spherical aberration by the convex lens and overcorrection by the concave lens.

After installing the achromatic collimator lens L_{14} the telescope will be set up so that the beam diameter of near- and far-field (20 feet) are of similar size. As mentioned above, our SLD usually produces a field with sickle-shaped intensity distribution and an angular intensity profile of approximately 35 degrees. Due to the limited numerical aperture of L_{14} and the irregular shape of the SLD intensity distribution, the light field behind L_{14} will be neither Gaussian nor collimated. While the latter can be corrected by the ensuing telescope, the non-Gaussian features are partially corrected by a range of measures: First, an aperture close to the SLD will clip the curved parts of the sickle which allows for a reasonable preliminary collimation of the beam. Then, once the beam is approximately collimated, the distance between L_{14} and the SLD are carefully adjusted by means of a micrometer bench, until the phase-profile emerging from the telescope will result in a Gaussian far-field. For a less than optimal distance the light field can exhibit two off-center peaks. By the repeated interchanging adjustment of L_{14} and the telescope, a collimated beam with a good beam profile can be achieved.

As already mention in Section 5.8, the large distance between the telescope

and the input planes of the detector will lead to a considerable divergence at the detector for the beam size we use. The additional spread due to the finite transverse coherence is negligible in our case: With a global coherence $\sigma_{glob} = \sigma_g/\sigma_s$ of 7.05 (see Section 8.1), the angular spread θ_s increases by about 4% according to the relation below [43]:

$$\theta_s = \frac{1}{\sqrt{2}\sigma_s k}\sqrt{1 + \frac{4}{\sigma_{glob}^2}} \tag{6.7}$$

6.4 Drift

The Superlum SLD is based on a relatively new technology which enables the production of low-cost, red-light high-power SLDs. One trade-off though is the relatively high sensitivity towards temperature changes and backscattered light.

The SLD casing contains a peltier element and a thermistor which are part of an electronic temperature stabilization.

During experimental runs I have noticed that the airstream as a result of a person passing by could already change the direction of the beam considerably. A cardboard windshield around the SLD an the sealing of the foil curtains around the optical table with duct tape reduced this kind of drift by 80%.

Even small amounts of light reflecting back into the SLD can lead to changes in power output and temporal oscillations. In particular, this effect was observed with light reflecting off an acousto-optic modulator crystal in the signal beam arm. A brief reflection, e.g. coming from the glass surface of our sample container during adjustment, usually changes the direction of the output beam for hours.

The remaining drift can not be sufficiently controlled at the moment and presents a major challenge. Necessary readjustments due to changes in direction as well as

the phase- and intensity distribution of the beam generated by the SLD, require about 99% of the time allocated to experimental work. Drifts over a time period of minutes to hours necessitate rapid readjustment of all elements involved, and a comprehensive knowledge of especially drift-sensitive parts of the system which need frequent readjustments. Furthermore, the ability to quickly interpret and correct drift-induced aberrations visible in the measured phase-space distribution is imperative: Misalignments of various components in the $x-$ and $y-$directions display characteristic distortions in the phase-space diagram. Extremely sensitive measurements, as the 'curvature flipping'-experiment presented in Section 12.2.2, could only be accomplished by fully exploiting all drift countermeasures. In addition, taking those scans at night proved beneficial, probably due to less air turbulence and vibrations. With the advancement of SLD technology, these light sources, and especially those using the novel technology that is employed in our SLD, should hopefully become more stable.

6.5 Temperature stabilization

The temperature stabilization controller keeps the temperature of the SLD at 25 degrees Celsius in our experiments. This is done by a feedback loop: The controller measures the temperature of the SLD by means of a temperature-sensitive resistor and adjusts it by heating or cooling of a thermoelectric cooler (TEC) which holds the SLD.

The temperature-sensitive resistor is an NTC thermistor (temperature dependent resistor with a negative temperature coefficient) also placed close to the SLD in its casing.

This thermistor is part of a Wien bridge in the temperature controller, whose

voltage output will be adjusted to zero for the value thermistor's resistance at 25 degrees C. For other temperatures, the Wien bridge will then generate a positive or negative voltage, depending on whether the measured temperature is higher or lower than 25 degrees. This voltage is amplified using operational amplifiers and passed through low-pass filters in order to adjust the time constant of the temperature control: If the time constant is too fast, the feedback loop and with it the temperature will oscillate. If the time constant is too slow, it can not keep up with temperature fluctuations.

The operational amplifiers control a pair of two transistors in push-pull configuration which are connected to the TEC in the SLD casing. The error voltage generated by the Wien bridge is also used to trigger an alarm to sound in case the temperature deviates from the selected value by more than a degree. A circuit diagram of the temperature stabilization is shown in Appendix A.

6.6 SLD power supply

The power supply for the SLD is a stabilized current source. It consists of a MOSFET which is controlled by a stabilized, but variable voltage at the gate. The output circuit contains an internal feedback loop: In the source side of the MOSFET, a low-ohm resistor is in series with the SLD across which the voltage is measured and fed back into an OP Amp which controls the MOSFETs gate. This way fluctuations in the source current can be compensated.

The power supply also has protective measures against current overload as resistors. Diodes in forward and reverse parallel to the SLD shortcut voltage spikes. In the current setup, the maximum current is limited to 160 mA and the maximum voltage to 2.7 V. A circuit diagram of the SLD power supply is shown in

Appendix A.

Chapter 7

Characterization of a transverse beam profile - Theory

The spatial- and coherence properties of the Signal beam S can easily be determined using the Two-Window technique: The phase-space profile $S_B(d_x, p_x)$ and the longitudinal profile $S_B(z)$ of the Signal beam itself are measured, which then determine all beam parameters of interest for our experiment. In this chapter we show how to extract from a transverse scan the beam size σ_s, the *transverse* coherence length σ_g, and the radius of curvature R of the Signal beam. We use the theory developed here in the experimental part in Chapter 8. Chapter 9 completes the characterization of all beams in this experiment with the measurement of the *longitudinal* coherence length and the spectral characteristics of our light source. Also in that chapter, a model for determining the spot-size and Rayleigh length of the small LO (SLO) as well as a model for mapping the location and frequency-shifts of transverse modes are introduced.

In the past, we have used the Single-Window technique to characterize the Signal- and LO-beams. In this technique, the Signal- and the LO-beam are prepared equally in size and radius of curvature. Then, the phase-space profile of the Signal beam is measured using the identical LO-beam. This technique requires knowledge about the preparation of the Signal field to be measured so that the LO can be pre-

pared the same. This information is not always available. Also, the Single-Window technique does not allow for the detection of misalignments below a level that is necessary for some of the beam parameters to have a reasonable margin of error: For a radius of curvature of both beams on the order of a meter, a 20% difference of radius of curvature and beam size in one of the beams, which is difficult to detect in a convolution of similar beams, can lead to a 50% error in measured beam-size and 20% error in the transverse coherence length of the beam pair. For a larger misalignment of more than 25% the measured transverse coherence length goes towards infinity, after that it becomes imaginary. The beam-size on the other hand goes towards zero.

Using flat wavefronts for the determination of the transverse coherence length σ_g has several advantages. Firstly, it is easier to give both the LO- and Signal beam a nearly flat wavefront than any other finite value which has to be equal for both beams. Secondly, it turns out that the measured beam parameters then become much less dependent on differences in beam-size between the beams than for finite radii of curvature. This is also of importance for the Two-Window technique, where the *big* LO (BLO)- and Signal (S) beam are of equal size. Generally, mismatches in radius of curvature and beam size decrease the measured beam size and increase the transverse coherence length.

The Two-window uses flat wavefronts for both SLO and BLO, regardless of the Signal field to be measured.[1] In the following sections we show how to determine two beam parameters while a third is known. For the determination of σ_s and σ_g of the Signal beam as described in Section 7.2, I collimate the Signal beam in order to make the measurement less dependent on misalignments, as mentioned above. From

[1]The Single-Window technique could theoretically also be modified so that the preparation of only one beam is required, but small misalignments have a larger effect in that case.

the measured beam properties we can determine the global coherence $\sigma_{glob} = \sigma_g/\sigma_s$ which is the same for all beams. In Section 7.3 I show how to determine σ_s and R from a transversely coherent beam, which applies to our system very well, given the high transverse coherence of the light we employ. In Chapter 8 I use the theory derived in the current chapter to determine the beam parameters in our experiment. In Chapter 9 I present the experimental results and a discussion of phase-sensitive z-scans, i.e., scans which measure the complex beat signal as a function of path-delay Δl. We examine the origin and potential applications of a phase-gradient in the complex beat signal that we observe in these experiments.

7.1 Introduction

7.1.1 Single-Window method

Previously, we have measured the parameters of an identically prepared set of Signal- and LO beam, using the Single-LO method [2, 3]. In this section, we will briefly describe the workings of this technique.

From Eq. (4.14) we know the beat voltage for a the superposed Signal- and LO beams as a function of relative displacement d_x and momentum d_p to be

$$\begin{aligned} V_B &\propto \int d\eta \, \exp\left(i\frac{k}{f}\eta d_p\right) \Gamma(\eta - d_x, \eta) \\ &= \int d\eta \, \exp(i\eta p_x) \, \langle \mathcal{E}^*_{LO}(\eta - d_x)\mathcal{E}_S(\eta)\rangle \end{aligned} \tag{7.1}$$

where $\langle ... \rangle$ denotes the temporal averaging over the source light. We omitted the phase-factor $\exp(-i\frac{k}{2f}d_p^2)$ which is identical for SLO and BLO and will cancel when

we multiply V^{SLO*} and V^{BLO} later on (see Eq. (5.33)). We also abbreviated the transverse momentum $\frac{k}{f}d_p$ by p_x.

The cross-spectral density of the combined field for *identical* S and LO beam is given by Eq. (3.2). For two equal-sized beams with a different radius of curvature, this expression becomes:

$$\begin{aligned}
\Gamma(x_1, x_2) &= \langle \mathcal{E}^*(x_1)\mathcal{E}(x_2)\rangle \\
&= \exp\left(-\frac{x_1^2 + x_2^2}{4\sigma_s^2}\right)\exp\left[-\frac{(x_1 \pm x_2)^2}{2\sigma_g^2}\right]\exp\left(\frac{ik}{2R_1}x_1^2 - \frac{ik}{2R_2}x_2^2\right) \\
&= \exp\left(-\frac{x_1^2}{4\sigma_s^2} + \frac{ik}{2R_1}x_1^2\right)\exp\left(-\frac{x_2^2}{4\sigma_s^2} - \frac{ik}{2R_2}x_2^2\right)\exp\left[-\frac{(x_1 \pm x_2)^2}{2\sigma_g^2}\right] \qquad (7.2) \\
&= \langle \mathcal{E}^*(x_1)\rangle\langle \mathcal{E}^*(x_2)\rangle \exp\left[-\frac{(x_1 \pm x_2)^2}{2\sigma_g^2}\right]. \qquad (7.3)
\end{aligned}$$

We also replaced the minus in the term containing the transverse coherence length with a $\pm$. The $\pm$ is "$-$" when the beam profiles of S and LO match, and "$+$" when they are inverted with respect to each other. Such an inversion only affects the relative position of the coherence areas, necessitating the change in sign of one of the spatial variables in the σ_g-term. In the Single-LO technique, which, as stated earlier, employs identical beams, $x_1 - x_2 = d_x$, where d_x is again the perpendicular translation between the beams. If the beam profiles of S and LO are matched ("$-$"), the last term in Eq. (7.3) can be simplified accordingly, leading to the following relation between the cross-spectral density for a partially transversely coherent beam $\Gamma(x_1, x_2)$ and a fully transversely coherent beam $\langle \mathcal{E}(x_1)\rangle\langle \mathcal{E}(x_2)\rangle$:

$$\Gamma(x - d_x, x) = \exp\left(-\frac{d_x^2}{2\sigma_g^2}\right)\langle \mathcal{E}^*(x - d_x)\rangle\langle \mathcal{E}^*(x)\rangle. \qquad (7.4)$$

Inserting this expression into Eq. (7.1) yields

$$\begin{aligned} V_B^{part.coh.}(d_x, p_x) &= \exp\left(-\frac{d_x^2}{2\sigma_g^2}\right) \int d\eta \, \exp(i\eta p_x) \, \langle \mathcal{E}^*(x - d_x)\rangle \langle \mathcal{E}^*(x)\rangle \\ &= \exp\left(-\frac{d_x^2}{2\sigma_g^2}\right) V_B^{coh}(d_x, p_x) \end{aligned} \tag{7.5}$$

and consequently

$$|V_B^{incoh}(d_x, p_x)|^2 = \exp\left(-\frac{d_x^2}{\sigma_g^2}\right) |V_B^{coh}(d_x, p_x)|^2. \tag{7.6}$$

This demonstrates the simple relationship between the beat voltages of pairs of equally-sized beams with different transverse coherence: A finite transverse coherence length narrows the position width of the phase-space profile of $|V_B(d_x, p_x)|^2$ by a Gaussian factor. Note that even though the beams have to be equal in size, their individual radii of curvature can be arbitrary.

Previously, we identically prepared the Signal and the LO beam before determining their beam parameters. Using relation (7.6) we can readily derive the mean square beat signal for two arbitrary but equal beams. From Eq. (3.4) we know the Wigner function of a coherent Gaussian beam to be

$$W^{coh}(x, p) \propto \exp\left[-\frac{x^2}{2\sigma_s^2} - 2\sigma_s^2(\frac{kx}{R} + p)^2\right]. \tag{7.7}$$

For transversely coherent light, $|V_B(d_x, p_x)|^2$ is just the convolution of the identical Wigner functions of S and LO, according to Eq. (4.25). This convolution causes a broadening of $|V_B(d_x, p_x)|^2$ in x and p by a factor of $\sqrt{2}$ (see Section 5.4.4), resulting in

$$
\begin{aligned}
|V_B^{coh}(d_x, p_x)|^2 &\propto \propto \int dx\, dp\, W_{LO}(x - d_x, p + p_x)\, W_S(x, p) \\
&= \exp\left[-\frac{x^2}{4\sigma_s^2} - \sigma_s^2(\frac{kx}{R} + p)^2\right]. \qquad (7.8)
\end{aligned}
$$

The mean square beat signal for *finite* transverse coherence length then follows immediately from Eq. (7.6):

$$
|V_B^{part.coh}(d_x, p_x)|^2 = \exp\left[-d_x^2\left(\frac{1}{4\sigma_s^2} + \frac{1}{\sigma_g^2}\right)\right] \exp\left[-\sigma_s^2\left(p_x + d_x\frac{k}{R}\right)^2\right] \qquad (7.9)
$$

which reproduces the result in [3]. In this paper, we measured the position-, momentum- and position-integrated momentum distribution to determine σ_s, σ_g and R of the equally prepared beam pair.

7.1.2 Two-Window method

In the Two-Window technique we prepare the Dual-LO as usual; the BLO collimated and the SLO focused. The Signal beam can have an arbitrary Gaussian wavefront. The fact that no two beams are prepared to be equal leads to a more complex interplay between the beam parameters. We adapt the expression for the cross-spectral density in Eq. (7.2) by including beam size scaling factors a, A and B and different radii of curvature R_1, $R_2 = \infty$ for S and LO:

$$\Gamma(x_1,x_2) = \exp\left[-x_1^2\left(\frac{1}{4\sigma_s^2A^2}+\frac{ik}{2R_1A^2}\right)\right]\exp\left[-x_2^2\left(\frac{1}{4\sigma_s^2B^2}-\frac{ik}{2R_2B^2}\right)\right] \times \exp\left[-\frac{(\frac{x_1}{A}\pm\frac{x_2}{B})^2}{2\sigma_g^2}\right]. \quad (7.10)$$

a, A and B are dimensionless scaling parameters which relate the size ratio of a (potentially modified) beam at the detection input plane to its original size $2\sigma_s$. For the BLO and S beam, A and B are usually close to 1, while for the SLO a is on the order of 0.1. Note that the definition of a, A and B is different than in Section 5.3, where they denoted the respective beam-sizes itself.

In the following sections, we will calculate the complex beat signal for the two most important cases: a flat Signal beam of finite transverse coherence length (Section 7.2) and a transversely coherent beam with a finite radius of curvature (Section 7.3). For both cases, we will show how to extract the remaining unknown parameters.

7.2 $R{=}\infty$, σ_s and σ_g unknown

In this section, we will show how to determine σ_s and σ_g of a flat Signal beam of arbitrary transverse coherence. We first derive the general expression for the beat voltage between the Signal beam and an LO (Section 7.2.1), followed by the beat voltage for a close-to perfect SLO (Section 7.2.2) and a BLO about the size of the Signal beam (Section 7.2.3) as used in our experiment. From the complex beat signal calculated in Section 7.2.4 we show how to extract σ_s and σ_g from either quadrature signal (Section 7.2.5).

7.2.1 General beat voltage

Inserting Eq. (7.10) into Eq. (7.1) and setting $R_1 = \infty$ (flat LO) and $R_2 = \infty$ (flat Signal beam), we get for the beat voltage of the S and BLO beams:

$$\begin{aligned} V_B(d_x, p_x) &\propto \int d\eta \exp(i\eta p_x) \\ &\times \exp\left\{ -\frac{1}{4\sigma_s^2}\left[\frac{(\eta - d_x)^2}{A^2} + \frac{\eta^2}{B^2}\right] - \frac{1}{2\sigma_g^2}\left(\frac{\eta - d_x}{A} \pm \frac{\eta}{B}\right)^2 \right\} \\ &= \exp\left\{ -dx^2 \left[\frac{1}{A^2}\left(\frac{1}{4\sigma_s^2} + \frac{1}{2\sigma_g}\right)\right]\right\} \\ &\times \int d\eta \exp\left\{ -\eta^2 \left[\frac{1}{4\sigma_s^2}\left(\frac{1}{A^2} + \frac{1}{B^2}\right) + \frac{1}{2\sigma_g^2}\left(\frac{1}{A^2} + \frac{1}{B^2} \pm \frac{2}{AB}\right)\right] \right. \\ &+ \left. 2\eta \left[i\frac{p_x}{2} + \frac{d_x}{2\sigma_g^2}\left(\frac{1}{A^2} \pm \frac{1}{AB}\right)\right]\right\}. \end{aligned} \tag{7.11}$$

By defining $\rho = \frac{1}{4\sigma_s^2} + \frac{1}{2\sigma_g^2}$ we get

$$\begin{aligned} V_B(d_x, p_x) &\propto \exp(-d_x^2 \frac{\rho}{A^2}) \\ &\times \int d\eta \exp\left\{ -\eta^2 \left[\rho\left(\frac{1}{A^2} + \frac{1}{B^2}\right) \pm \frac{1}{\sigma_g^2 AB}\right] \right. \\ &+ \left. 2\eta \left[i\frac{p_x}{2} + d_x\left(\frac{\rho^2}{A^2} \pm \frac{1}{2\sigma_g^2 AB}\right)\right]\right\} \\ &\propto \exp(-d_x^2 \frac{\rho}{A^2}) \exp\left\{ \frac{[i\frac{p_x}{2} + d_x(\frac{\rho}{A^2} \pm \frac{1}{2\sigma_g^2 AB})]^2}{\rho(\frac{1}{A^2} + \frac{1}{B^2}) \pm \frac{1}{\sigma_g^2 AB}} \right\} \\ &= \exp(-d_x^2 \frac{\rho}{A^2}) \\ &\times \exp\left\{ \frac{1}{\rho(\frac{1}{A^2} + \frac{1}{B^2}) \pm \frac{1}{\sigma_g^2 AB}} \left[-d_x^2 \left(\frac{\rho}{A^2} \pm \frac{1}{2\sigma_g^2 AB}\right)^2 - \frac{p_x^2}{4} + i d_x p_x \left(\frac{\rho}{A^2} \pm \frac{1}{2\sigma_g^2 AB}\right)\right]\right\}. \end{aligned} \tag{7.12}$$

While the pre-factors for p_x and $d_x p_x$ can not be simplified any further, the prefactor d_x can be transformed as follows:

$$\begin{aligned} -pref_{d_x} &= \frac{\rho}{A^2} + \frac{(\frac{\rho}{A^2} \pm \frac{1}{2\sigma_g^2 AB})^2}{(\frac{1}{A^2} + \frac{1}{B^2}) \pm \frac{1}{\sigma_g^2 AB}} \\ &= \frac{\rho}{A^2} - \frac{\frac{\rho^2}{A^4} \pm \frac{\rho}{A^2}\frac{1}{\sigma_g^2 AB} + \frac{1}{4\sigma^4 A^2 B^2}}{\frac{\rho}{A^2} + \frac{\rho}{B^2} \pm \frac{1}{\sigma_g^2 AB}} \\ &= \frac{\rho}{A^2} - \frac{\rho}{A^2}\frac{\frac{\rho}{A^2} \pm \frac{1}{\sigma_g^2 AB} + \frac{1}{4\rho\sigma^4 B^2}}{\frac{\rho}{A^2} + \frac{\rho}{B^2} \pm \frac{1}{\sigma_g^2 AB}}. \end{aligned} \tag{7.13}$$

For simplicity we define $\xi = \frac{\rho}{A^2} \pm \frac{1}{\sigma^2 AB}$:

$$\begin{aligned} -pref_{d_x} &= \frac{\rho}{A^2} - \frac{\rho}{A^2}\frac{\xi + \frac{1}{4\rho\sigma^4 B^2}}{\xi + \frac{\rho}{B^2}} \\ &= \frac{\rho}{A^2}\left[1 - \frac{\xi + \frac{1}{4\rho\sigma_g^4 B^2}}{\xi + \frac{\rho}{B^2}}\right] \\ &= \frac{\rho}{A^2}\left[\frac{\xi + \frac{\rho}{B^2} - \xi - \frac{1}{4\rho\sigma_g^4 B^2}}{\xi + \frac{\rho}{B^2}}\right] \\ &= \frac{\rho}{A^2}\left[\frac{\frac{\rho}{B^2} - \frac{1}{B^2(\sigma_g^4/\sigma_s^2 + 2\sigma_g^2)}}{\rho(\frac{1}{A^2} + \frac{1}{B^2}) \pm \frac{1}{\sigma_g^2 AB}}\right] \\ &= \frac{\rho}{A^2 B^2}\left\{\frac{\rho - \frac{\sigma_s^2/\sigma_g^2}{\sigma_g^2 + 2\sigma_s^2}}{(\frac{1}{A^2} + \frac{1}{B^2})[\rho \pm \frac{1}{\sigma_g^2(\frac{B}{A} + \frac{A}{B})}]}\right\}. \end{aligned} \tag{7.14}$$

The numerator can be simplified even further:

$$
\begin{aligned}
& \rho\left(\rho - \frac{\sigma_s^2/\sigma_g^2}{\sigma_g^2 + 2\sigma_s^2}\right) \\
= & \left(\frac{1}{4\sigma_s^2} + \frac{1}{2\sigma_g^2}\right)\left(\frac{1}{4\sigma_s^2} + \frac{1}{2\sigma_g^2} - \frac{\sigma_s^2/\sigma_g^2}{\sigma_g^2 + 2\sigma_s^2}\right) \\
= & \left(\frac{1}{4\sigma_s^2} + \frac{1}{2\sigma_g^2}\right)^2\left[1 - \frac{\sigma_s^2/\sigma_g^2}{(\frac{1}{4\sigma_s^2} + \frac{1}{2\sigma_g^2})(\sigma_g^2 + 2\sigma_s^2)}\right] \\
= & \left(\frac{1}{4\sigma_s^2} + \frac{1}{2\sigma_g^2}\right)^2\left[1 - \frac{1}{\frac{\sigma_g^4}{4\sigma_s^4} + \frac{\sigma_g^2}{\sigma_s^2} + 1}\right] \\
= & \left(\frac{1}{4\sigma_s^2} + \frac{1}{2\sigma_g^2}\right)^2\left[1 - \frac{1}{(\frac{\sigma_g^2}{2\sigma_s^2} + 1)^2}\right] \\
= & \left(\frac{1}{4\sigma_s^2} + \frac{1}{2\sigma_g^2}\right)^2\left[1 - \frac{1}{4\sigma^4(\frac{1}{4\sigma_s^2} + \frac{1}{2\sigma_g^2})^2}\right] \\
= & \left(\frac{1}{4\sigma_s^2} + \frac{1}{2\sigma_g^2}\right)^2 - \frac{1}{\sigma_g^4} \\
= & \rho^2 - \frac{1}{4\sigma_g^4} = \left(\rho - \frac{1}{2\sigma_g^2}\right)\left(\rho + \frac{1}{2\sigma_g^2}\right). \qquad (7.15)
\end{aligned}
$$

Inserting this expression into Eq. (7.14) and also simplifying the first two terms in the denominator of Eq. (7.14) finally yields:

$$
pref_{d_x} = \frac{1}{A^2 + B^2}\,\frac{(\rho - \frac{1}{2\sigma_g^2})(\rho + \frac{1}{2\sigma_g^2})}{\rho \pm \frac{1}{\sigma_g^2(\frac{B}{A} + \frac{A}{B})}}. \qquad (7.16)
$$

The complete expression for $V_B(d_x, d_p)$ then becomes:

$$
\begin{aligned}
V_B(d_x,p_x) \;\propto\; & \exp\left\{ -d_x^2 \,\frac{1}{A^2+B^2}\,\frac{(\rho-\frac{1}{2\sigma_g^2})(\rho+\frac{1}{2\sigma_g^2})}{\rho \pm \frac{1}{\sigma_g^2(\frac{B}{A}+\frac{A}{B})}} \right. \\
& - \; p_x^2 \,\frac{1}{4[\rho(\frac{1}{A^2}+\frac{1}{B^2}) \pm \frac{1}{\sigma_g^2 AB}]} \\
& + \; id_x p_x \,\frac{\rho/A^2 \pm \frac{1}{2\sigma_g^2 AB}}{\rho(\frac{1}{A^2}+\frac{1}{B^2}) \pm \frac{1}{\sigma_g^2 AB}} \left. \right\} \qquad (7.17)
\end{aligned}
$$

Using this general expression we now calculate the $V_B(d_x, d_p)$ for our SLO ($A \ll B$) and the special BLO we use ($A = B$).

7.2.2 Beat voltage for a close-to perfect SLO ($A \ll B$)

For a close-to perfect SLO, i.e., $A \ll B$, the expression in Eq. (7.17) simplifies considerably:

$$
\begin{aligned}
V_B^{SLO}(d_x,p_x) \;\propto\; & \exp\left\{ -\frac{d_x^2}{B^2}\,\frac{\rho^2-\frac{1}{4\sigma_g^4}}{\rho} - \frac{p_x^2}{4[\rho/A^2]} + id_x p_x \,\frac{\frac{\rho}{A} \pm \frac{1}{2\sigma_g^2 B}}{\frac{\rho}{A} \pm \frac{1}{\sigma_g^2 B}} \right\} \\
=\; & \exp\left\{ -\frac{d_x^2}{B^2}\left[\rho - \frac{1}{\frac{\sigma_g^4}{\sigma_s^2}+2\sigma_g^2}\right] - p_x^2\frac{A^2}{4\rho} + ip_x d_x \right\}. \qquad (7.18)
\end{aligned}
$$

The prefactor for p_x^2 goes towards zero as expected for an SLO, which has a big momentum spread. The prefactor for d_x simplifies as shown below:

$$
\begin{aligned}
pref_{d_x} &= \frac{1}{4\sigma_s^2} + \frac{1}{2\sigma_g^2} - \frac{1}{\frac{\sigma_g^4}{\sigma_s^2} + 2\sigma_g^2} \\
&= \frac{1}{4\sigma_s^2} + \frac{1}{2\sigma_g^2}\left(1 - \frac{2\sigma_g^2}{\frac{\sigma_g^4}{\sigma_s^2} + 2\sigma_g^2}\right) \\
&= \frac{1}{4\sigma_s^2} + \frac{1}{2\sigma_g^2}\left(1 - \frac{1}{\frac{\sigma_g^2}{2\sigma_s^2} + 1}\right) \\
&= \frac{1}{4\sigma_s^2} + \frac{1}{2\sigma_g^2}\left(\frac{1}{1 + \frac{2\sigma_s^2}{\sigma_g^2}}\right) \\
&= \frac{1}{4\sigma_s^2} + \frac{1}{2\sigma_g^2 + 4\sigma_s^2}. \qquad (7.19)
\end{aligned}
$$

Inserting Eq. (7.19) into Eq. (7.18) yields the final expression for the beat voltage for the SLO:

$$
V_B^{SLO}(d_x, p_x) \propto \exp\left[-\frac{d_x^2}{B^2}\left(\frac{1}{4\sigma_s^2} + \frac{1}{2\sigma_g^2 + 4\sigma_s^2}\right) + i d_x p_x\right] \qquad (7.20)
$$

which is independent of a potential inversion between SLO and S.

7.2.3 Beat voltage for our special BLO ($A = B$)

For a BLO the same size as the Signal beam ($A = B$), Eq. (7.17) simplifies as well:

$$
\begin{aligned}
V_B^{BLO}(d_x, p_x) \;\propto\; & \exp\left[-\frac{d_x^2}{2B^2}\,\frac{(\rho - \frac{1}{2\sigma_g^2})(\rho + \frac{1}{2\sigma_g^2})}{\rho \pm \frac{1}{2\sigma_g^2}} - \frac{p_x^2}{\frac{4}{B^2}(\frac{1}{2\sigma_s^2} + \frac{1}{\sigma_g^2} \pm \frac{1}{\sigma_g^2})}\right. \\
& + \left. i d_x p_x\,\frac{\frac{1}{B^2}(\frac{1}{4\sigma^2} + \frac{1}{2\sigma_g^2} \pm \frac{1}{2\sigma_g^2})}{\frac{1}{B^2}(\frac{1}{2\sigma_s^2} + \frac{1}{\sigma_g^2} \pm \frac{1}{\sigma_g^2})}\right]. \qquad (7.21)
\end{aligned}
$$

Depending on the sign which signifies an inversion between BLO and S, we get two different results. If the beam profiles are matched, we get

$$\begin{aligned} V_B^{BLO(-)}(d_x, p_x) &\propto \exp\left[-\frac{d_x^2}{2B^2}\left(\rho + \frac{1}{2\sigma_g^2}\right) - \frac{p_x^2 B^2}{4(\frac{1}{2\sigma_s^2})} + i d_x p_x \frac{\frac{1}{4\sigma_s^2}}{\frac{1}{2\sigma_g^2}}\right] \\ &= \exp\left[-\frac{d_x^2}{B^2}\left(\frac{1}{8\sigma_s^2} + \frac{1}{2\sigma_g^2}\right) - p_x^2 \frac{B^2\sigma_s^2}{2} + i\frac{d_x p_x}{2}\right]. \end{aligned} \quad (7.22)$$

In case BLO is inverted with respect to S, expression (7.21) becomes:

$$\begin{aligned} &V_B^{BLO(+)}(d_x, p_x) \\ &\quad \propto \exp\left[-\frac{d_x^2}{2B^2}\left(\rho - \frac{1}{2\sigma_g^2}\right) - p_x^2 \frac{B^2}{4\left(\frac{1}{2\sigma_s^2} + \frac{2}{\sigma_g^2}\right)} + i d_x p_x \frac{\frac{1}{B^2}\left(\frac{1}{4\sigma_s^2} + \frac{1}{\sigma_g^2}\right)}{\frac{1}{B^2}\left(\frac{1}{2\sigma_s^2} + \frac{2}{\sigma_g^2}\right)}\right] \\ &\quad = \exp\left[-\frac{d_x^2}{8B^2\sigma_s^2} - p_x^2 \frac{B^2}{\frac{2}{\sigma_s^2} + \frac{8}{\sigma_g^2}} + i\frac{d_x p_x}{2}\right]. \end{aligned} \quad (7.23)$$

Notice that for matched beam profiles the position distribution depends on $\frac{1}{8\sigma_s^2} + \frac{1}{2\sigma_g^2}$, while the momentum distribution only on σ_s^2. For inverted beam profiles, it is exactly the other way around.

7.2.4 Complex beat signal $S_B(d_x, p_x)$

Now that we know the beat voltages for both SLO and BLO, we can calculate the complex beat voltage which - as stated in Section 5.4.1 - consists of the cross terms from $|V_B^{SLO} + V_B^{BLO}|^2$ as seen in Eq. (5.33):

$$S_B(d_x, d_p) \propto V_B^{SLO*} V_B^{BLO} \quad (7.24)$$

where we omitted the frequency-dependent factor. The resulting complex beat signals for non-inverted (−) and inverted (+) Dual-LO are:

$$S_B^{(-)}(d_x, p_x) \propto \exp\left[-d_x^2\left(\frac{3}{8\sigma_s^2}+\frac{1}{2\sigma_g^2}+\frac{1}{4\sigma_s^2+2\sigma_g^2}\right)-p_x^2\frac{\sigma_s^2}{2}-i\frac{d_x p_x}{2}\right] \quad (7.25)$$

$$S_B^{(+)}(d_x, p_x) \propto \exp\left[-d_x^2\left(\frac{3}{8\sigma_s^2}+\frac{1}{4\sigma_s^2+2\sigma_g^2}\right)-p_x^2\frac{1}{2\left(\frac{1}{\sigma_s^2}+\frac{4}{\sigma_g^2}\right)}-i\frac{d_x p_x}{2}\right]. \quad (7.26)$$

Figure 5.3 in Section 5.4.2 shows a numerical simulation of the in-phase and out-of-phase quadrature signals, which are the real and imaginary part of the complex beat signal, of a collimated partially coherent Gaussian beam for typical values of σ_s and σ_g, according to Eq. (7.25) or Eq. (7.26).

7.2.5 Extraction of σ_s and σ_g from the quadrature signals

From the complex beat signal $S_B(d_x, p_x)$ measured in our experiment, the coefficients of d_x and p_x in Equations (7.25) and (7.26) can be determined. We can then solve for the beam size σ_s and the transverse coherence length σ_g. In the following, we will abbreviate the coefficients as follows:

$$(d_x^e)^2 = \left(\frac{3}{8\sigma_s^2}+\frac{1}{2\sigma_g^2}+\frac{1}{4\sigma_s^2+2\sigma_g^2}\right)^{-1} \quad (7.27)$$

$$(p_x^e)^2 = \frac{2}{\sigma_s^2} \quad (7.28)$$

for the non-inverted Dual-LO, and

$$(d_x^e)^2 = \left(\frac{3}{8\sigma_s^2} + \frac{1}{4\sigma_s^2 + 2\sigma_g^2}\right)^{-1} \tag{7.29}$$

$$(p_x^e)^2 = 2\left(\frac{1}{\sigma_s^2} + \frac{4}{\sigma_g^2}\right) \tag{7.30}$$

for the inverted Dual-LO, so that

$$S_B(d_x, p_x) \propto \exp\left[-\frac{d_x^2}{(d_x^e)^2} - \frac{p_x^2}{(p_x^e)^2} - i\frac{d_x p_x}{2}\right]. \tag{7.31}$$

Both the in-phase- and out-of-phase quadrature signal contain all information about σ_s and σ_g. When we use the in-phase signal, we measure the e^{-1}-width of its x- and $p-$ distribution individually holding its respective conjugate coordinate at zero. In this case the term containing the variable held at zero as well as the phase in Eq. (7.31) cancels.[2] For example, if we set $d_x \equiv 0$, the d_x^2 and $d_x p_x$ terms cancel. $S_B(d_x \equiv 0, p_x)$ is then maximal at $p_x = 0$ and drops to e^{-1} of that value at a momentum p_x^e which can be measured. The extraction of d_x^e works similarly, when we set $p_x \equiv 0$.

The out-of-phase signal also contains the beam parameters for example in the distance of its four peaks from another (see Figure 5.3). In the following we will derive how σ_s and σ_g determine the location of those peaks.

The out-of-phase signal, which is the imaginary part of the complex beat signal (see Eq. (5.16)), is of the form

$$f(x, p) = \exp(-ax^2 - bp^2) \sin\frac{xp}{2} \tag{7.32}$$

[2]One has to keep in mind that this is only true when $R = \infty$ for all beams, as is the case here. For finite radii, S_B contains additional phase factors which shift the phase of both quadrature signals. This will be subject of Section 7.3.

where $x = d_x$, $p = p_x$ and

$$a = \frac{1}{(d_x^e)^2} \tag{7.33}$$

$$b = \frac{1}{(p_x^e)^2}. \tag{7.34}$$

At the location (x_m, p_m) of the extrema, the derivatives of $f(x,p)$ with respect to both variables must be zero:

$$\left.\frac{df(x,p)}{dx}\right|_{x_m,p_m} = \left[\frac{p_m}{2}\cos\left(\frac{x_m p_m}{2}\right) - 2ax_m \sin\left(\frac{x_m p_m}{2}\right)\right]\exp(-ax_m^2 - bp_m^2)$$
$$= 0 \tag{7.35}$$

$$\left.\frac{df(x,p)}{dp}\right|_{x_m,p_m} = \left[\frac{x_m}{2}\cos\left(\frac{x_m p_m}{2}\right) - 2bp_m \sin\left(\frac{x_m p_m}{2}\right)\right]\exp(-ax_m^2 - bp_m^2)$$
$$= 0 \tag{7.36}$$

which requires the terms in squared brackets to vanish. Regrouping its terms yields:

$$\frac{p_m}{4ax_m} = \tan\left(\frac{x_m p_m}{2}\right) \tag{7.37}$$

$$\frac{x_m}{4bp_m} = \tan\left(\frac{x_m p_m}{2}\right). \tag{7.38}$$

Solving for a and b and replacing them with $\frac{1}{(d_x^e)^2}$ and $\frac{1}{(p_x^e)^2}$ then leads to the final expressions

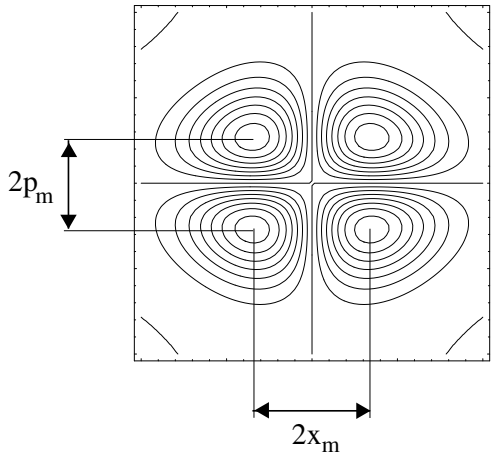

Figure 7.1: The distances in position and momentum between the peaks of the out-of-phase signal yield x_m and p_m for the calculation of d_x^e and p_x^e in Equations (7.39) and (7.40).

$$d_x^e = \sqrt{\frac{4x_m}{p_m}\tan\left(\frac{x_m p_m}{2}\right)} \tag{7.39}$$

$$p_x^e = \sqrt{\frac{4p_m}{x_m}\tan\left(\frac{x_m p_m}{2}\right)}. \tag{7.40}$$

The inverted expression for x_m and p_m are

$$x_m = \sqrt{2\frac{d_x^e}{p_x^e}\tan^{-1}\left(\frac{d_x^e p_x^e}{4}\right)} \tag{7.41}$$

$$p_m = \sqrt{2\frac{p_x^e}{d_x^e}\tan^{-1}\left(\frac{d_x^e p_x^e}{4}\right)} \tag{7.42}$$

as shown in Appendix B.

For practical purposes, the easiest way to retrieve d_x^e and p_x^e is to measure the distance in position and momentum between two opposite maxima or minima in

the out-of-phase phase-space diagram, as shown in Figure 7.1, divide by 2 to get x_m and p_m and calculate d_x^e and p_x^e using the expressions (7.39) and (7.40). From there we solve for σ_s and σ_g as shown below.

The advantage of using the out-of-phase signal to extract the beam parameters is that the procedure only requires measuring a distance as opposed to fitting a Gaussian to a curve to measure its width as in the case for the in-phase part.

Now that we know d_x^e and p_x^e, either from the measured in-phase or out-of-phase quadrature signal for the Signal beam, we need to calculate an expression for σ_s and σ_g in terms of those parameters, in order to extract them from the measurements.

Let us first consider the case for non-inverted S and Dual-LO, expressed in Eq. (7.25). We have:

$$[p_x^e]^2 = \frac{2}{[\sigma_s^{(-)}]^2} \tag{7.43}$$

Solving for σ_s yields

$$\sigma_s^{(-)meas} = \frac{\sqrt{2}}{p_x^e}. \tag{7.44}$$

We added *meas* to the superscript to emphasize that σ_s was determined from the measured value of p_x^e.

Again, according to Eq. (7.25), we have for $[d_x^e]^2$:

$$[d_x^e]^2 = \left[\frac{3}{8[\sigma_s^{meas(-)}]^2} + \frac{1}{2\sigma_g^2} + \frac{1}{4[\sigma_s^{meas(-)}]^2 + 2\sigma_g^2}\right]^{-2} \tag{7.45}$$

We already know $\sigma_s^{meas(-)}$ so we solve for $\sigma_g^{meas(-)}$:

$$\sigma_g^{meas(-)} = \sigma_s \sqrt{\frac{7 - 8\sigma_s^2/[d_x^e]^2 \pm \sqrt{25 - 48\sigma_s^2/[d_x^e]^2 + 64\sigma_s^4/[d_x^e]^4}}{-3 + 8\sigma_s^2/[d_x^e]^2}} \tag{7.46}$$

where we omitted the superscript *meas(-)* of σ_s for the sake of visual clarity. The procedure for extracting $\sigma_s^{meas(+)}$ and $\sigma_g^{meas(+)}$ is similar. Equations (7.47) and (7.48) show the results:

$$\sigma_s^{meas(+)} = \sqrt{-\frac{8/[d_x^e]^2 - \frac{5}{2}[p_x^e]^2 \pm \sqrt{64/[d_x^e]^4 - 24[p_x^e]^2/[d_x^e]^2 + \frac{25}{4}[p_x^e]^4}}{8[p_x^e]/[d_x^e]}} \tag{7.47}$$

$$\sigma_g^{meas(+)} = \sqrt{\frac{8/[d_x^e]^2 - \frac{7}{2}[p_x^e]^2 \pm \sqrt{64/[d_x^e]^4 - 24[p_x^e]^2/[d_x^e]^2 + \frac{25}{4}[p_x^e]^4}}{4[p_x^e]^2/[d_x^e]^2 - \frac{3}{4}[p_x^e]^4}}. \tag{7.48}$$

There are obviously two sets of solutions for both parameters σ_s and σ_g, but only one set where both parameters are real. From $\sigma_s^{meas(\pm)}$ and $\sigma_g^{meas(\pm)}$ the global coherence

$$\sigma_{glob}^{meas(\pm)} = \frac{\sigma_g^{meas(\pm)}}{\sigma_s^{meas(\pm)}}. \tag{7.49}$$

can be calculated, which does not change during propagation through free space or first-order optical systems as lenses [43]. We will apply this theory to the determination of σ_s and σ_g of a flat Gaussian Signal beam in Section 8.1.

7.3 σ_g=∞, σ_s and R unknown

In this section we will show how to extract the beam size σ_s and the radius of curvature R from a transversely coherent Signal beam. We again assume the SLO to be close to perfect. For the BLO, we consider two frequently encountered cases in our experiment; where the BLO is close to the size of the Signal beam ($A = B$), and where it is much larger.

First, we will derive the beat voltage for a LO of arbitrary size in Section 7.3.1. We use this result to derive the beat voltages for a perfect SLO (Section 7.3.2), a BLO the size of the Signal beam (Section 7.3.3) and an ideal BLO (Section 7.3.4). Using these results, we calculate the complex beat signal (Section 7.3.5) and an approximation of the complex beat signal for small R which we frequently use (Section 7.3.6). We conclude this theory chapter by showing how to extract σ_s and R from the measured complex beat signal (Section 7.3.7).

7.3.1 General beat voltage

Inserting Eq. (7.10) into Eq. (7.1) again we can write the beat voltage of the Signal-with a general LO beam for this case ($\sigma_g \to \infty$, $R_2 = R_{LO} \to \infty$) as

$$V_B(d_x, p_x) = \int dx \exp(ixp) \exp\left[-\frac{(x-d_x)^2}{4\sigma_s^2 A^2} - \frac{x}{4\sigma_s^2 B^2} - i\frac{k}{2R}\frac{x^2}{B^2}\right]. \tag{7.50}$$

Solving the integral yields

$$V_B(d_x, p_x) \quad \propto \quad \exp\left(-\frac{d_x^2}{4\sigma_s^2 A^2}\right) \exp\left[\frac{(\frac{d_x}{4\sigma_s^2 A^2} + i\frac{p_x}{2})^2}{\frac{1}{4\sigma_s^2 A^2} + \frac{1}{4\sigma_s^2 B^2} + i\frac{k}{2RB^2}}\right]. \tag{7.51}$$

Transformation of the denominator results in

$$\frac{1}{\frac{1}{4\sigma_s^2 A^2}+\frac{1}{4\sigma_s^2 B^2}+i\frac{k}{2RB^2}} = 4\sigma_s^2 A^2 \frac{1+\frac{A^2}{B^2}-i2\sigma_s^2\frac{A^2}{B^2}\frac{k}{R}}{(1+\frac{A^2}{B^2})^2+4\sigma_s^4\frac{A^4}{B^4}(\frac{k}{R})^2}. \tag{7.52}$$

Combining Equations (7.51) and (7.52) yields

$$\begin{aligned} V_B(d_x,p_x) &\propto \exp\left(-\frac{d_x^2}{4\sigma_s^2 A^2}\right) \\ &\times \exp\left[\left(\frac{d_x^2}{4\sigma_s^2 A^2}-p_x^2\sigma_s^2 A^2+ip_x d_x\right)\frac{1+\frac{A^2}{B^2}-i2\sigma_s^2\frac{A^2}{B^2}\frac{k}{R}}{(1+\frac{A^2}{B^2})^2+4\sigma_s^4\frac{A^4}{B^4}(\frac{k}{R})^2}\right]. \end{aligned} \tag{7.53}$$

Let us abbreviate the size ratio of BLO and S as well as the denominator in the second exponential as follows:

$$g \equiv \frac{A}{B} \tag{7.54}$$

$$m(g,R) \equiv (1+g^2)^2+4\sigma_s^4 g^4(\frac{k}{R})^2. \tag{7.55}$$

Regrouping the terms according to the order of d_x and p_x, we can then rewrite Eq. (7.53) as

$$
\begin{aligned}
V_B(d_x, p_x) \;&\propto\; \exp\left\{-\frac{d_x^2}{4\sigma_s^2 A^2}\left[1-\frac{1+g^2}{m(g,R)}-i\frac{k}{2RB^2}\frac{1}{m(g,R)}\right]\right. \\
&\times\; -\frac{p_x^2}{m(g,R)}\left[\sigma_s^2 A^2(1+g^2)+i2\sigma_s^4 g^4\frac{k}{R}\right] \\
&\times\; \left.\frac{p_x d_x}{m(g,R)}\left[2\sigma_s^2 g^2\frac{k}{R}+i(1+g^2)\right]\right\}. \qquad (7.56)
\end{aligned}
$$

Using this general expression we can calculate the beat voltages for three types of LOs: $g \ll 1$ (SLO), $g = 1$ (our BLO which is the size of the Signal beam) and $g \to \infty$ (ideal BLO). $g = 1$ does not necessarily represent the case of identical LO and S as in Section 7.2, where we used a collimated Signal beam: the preparation of a divergent or convergent Signal beam by means of a lens changes the beam width in the detection input plane, provided there is a non-zero distance between lens and input-plane.

7.3.2 Beat voltage for a perfect SLO ($A \ll B$)

For $g \ll 1$, all terms except for the d_x^2-terms and the $ip_x d_x$-term are negligible. The beat signal for the SLO is then:

$$
V_B^{SLO}(d_x, p_x) \;\propto\; \exp\left\{-\frac{d_x^2}{4\sigma_s^2 A^2}\left[1-\frac{1+g^2}{(1+g^2)^2+4\sigma_s^4 g^4(\frac{k}{R})^2}\right]-i\frac{d_x^2}{B^2}\frac{k}{2R}+ip_x d_x\right\}. \qquad (7.57)
$$

The real pre-factor of $-d_x^2$ simplifies as shown below:

$$
\begin{aligned}
& \frac{1}{4\sigma_s^2 A^2}\left[1-\frac{1+g^2}{(1+g^2)^2+4\sigma_s^4 g^4(\frac{k}{R})^2}\right] \\
\approx\ & \frac{1}{4\sigma_s^2 A^2}\left[1-\frac{1+\frac{A^2}{B^2}}{(1+\frac{A^2}{B^2})^2}\right] \approx \frac{1}{4\sigma_s^2 A^2}\left(1-\frac{1+\frac{A^2}{B^2}}{1+2\frac{A^2}{B^2}}\right) \\
=\ & \frac{1}{4\sigma_s^2 A^2}\frac{\frac{A^2}{B^2}}{1+2\frac{A^2}{B^2}} \\
\approx\ & \frac{1}{4\sigma_s^2 B^2}. \qquad (7.58)
\end{aligned}
$$

The complete expression for V_B^{SLO} is thus

$$
V_B^{SLO}(d_x, p_x) \propto \exp\left(-\frac{d_x^2}{4\sigma_s^2 B^2} - i\frac{d_x^2}{2B^2}\frac{k}{R} + ip_x d_x\right). \qquad (7.59)
$$

$V_B^{SLO}(d_x, p_x)$ is therefore directly proportional to the amplitude and phase of the curved Signal field, given by the first two terms in Eq. (7.59). The third term is just due to the fact that we change the relative momentum p_x between S and SLO in the Signal arm rather than the LO-arm: If we replace the x in $\exp(ixp_x)$ in Eq. (7.50) by $x - d_x$, which would correspond to tilting the respective LO rather than S, this phase-factor cancels, but will then turn up in the BLO beat signal.

7.3.3 Beat voltage for our special BLO ($A = B$)

For $g = 1$,

$$
m(g, R) \to 4 + 4\sigma^4(\frac{k}{R})^2. \qquad (7.60)
$$

Eq. (7.56) then simplifies to:

$$
\begin{aligned}
V_B^{g=1}(d_x,p_x) \quad \propto \quad & \\
& \exp\left\{ -d_x^2 \left[\frac{1}{4\sigma_s^2 B^2} \left(1 - \frac{2}{4+4\sigma_s^4(\frac{k}{R})^2} \right) - i \frac{1}{B^2} \frac{\frac{k}{2R}}{4+4\sigma_s^4(\frac{k}{R})^2} \right] \right. \\
& -p_x^2 \left[\sigma_s^2 B^2 \frac{2}{4+4\sigma_s^4(\frac{k}{R})^2} + iB^2 \frac{2\sigma_s^4 \frac{k}{R}}{4+4\sigma_s^4(\frac{k}{R})^2} \right] \\
& \left. +2p_x d_x \left[\frac{\sigma_s^2 \frac{k}{R}}{4+4\sigma_s^4(\frac{k}{R})^2} + i \frac{2}{4+4\sigma_s^4(\frac{k}{R})^2} \right] \right\}. \qquad (7.61)
\end{aligned}
$$

The real exponentials can be simplified even further:

$$
\begin{aligned}
& -\frac{d_x^2}{4\sigma_s^2 B^2} \left[\frac{2+4\sigma_s^4(\frac{k}{R})^2}{4+4\sigma_s^4(\frac{k}{R})^2} \right] - p_x^2 \left[\sigma_s^2 B^2 \frac{2}{4+4\sigma_s^4(\frac{k}{R})^2} \right] + 2p_x d_x \left[\frac{\sigma_s^2 \frac{k}{R}}{4+4\sigma_s^4(\frac{k}{R})^2} \right] \\
= \quad & -\frac{d_x^2}{4\sigma_s^2 B^2} \left[\frac{2+2\sigma_s^4(\frac{k}{R})^2}{4+4\sigma_s^4(\frac{k}{R})^2} \right] \\
- \quad & d_x^2 \frac{\sigma_s^2(\frac{k}{R})^2}{2B^2[4+4\sigma_s^4(\frac{k}{R})^2]} - p_x^2 \left[\sigma_s^2 B^2 \frac{2}{4+4\sigma_s^4(\frac{k}{R})^2} \right] + 2p_x d_x \left[\frac{\sigma_s^2 \frac{k}{R}}{4+4\sigma_s^4(\frac{k}{R})^2} \right] \\
= \quad & -\frac{d_x^2}{8\sigma_s^2 B^2} - \frac{(d_x \frac{k}{R} \frac{\sigma_s}{\sqrt{2}B} - p_x \sigma_s \sqrt{2} B)^2}{4+4\sigma_s^4(\frac{k}{R})^2}. \qquad (7.62)
\end{aligned}
$$

The final expression for $V_B^{g=1}$ then reads:

$$
\begin{aligned}
V_B^{g=1}(d_x,p_x) \quad \propto \quad & \exp\left[-\frac{d_x^2}{8\sigma_s^2 B^2} - \frac{(d_x \frac{k}{R} \frac{\sigma_s}{\sqrt{2}B} - p_x \sigma_s \sqrt{2} B)^2}{4+4\sigma_s^4(\frac{k}{R})^2} \right] \\
\times \quad & \exp\left[\frac{i}{4+4\sigma_s^4(\frac{k}{R})^2} \left(-d_x^2 \frac{k}{2B^2 R} + 2B^2 p_x^2 \sigma_s^4 \frac{k}{R} + 2d_x p_x \right) \right]. \qquad (7.63)
\end{aligned}
$$

7.3.4 Beat voltage for a perfect BLO ($A \gg B$)

For $g \to \infty$, i.e., for a perfect BLO,

$$m(g,R) \to g^4 \left[1 + 4\sigma_s^4 (\frac{k}{R})^2\right]. \tag{7.64}$$

All pre-factors in Eq. (7.56), except for those of p_x^2, vanish. We get

$$\begin{aligned} V_B^{g\to\infty} &\propto \exp\left\{-p_x^2\sigma_s^2\left[\frac{A^2(1+\frac{A^2}{B^2})}{\frac{A^4}{B^4}[1+4\sigma_s^4(\frac{k}{R})^2]} - i\frac{2\sigma_s^2\frac{k}{R}\frac{A^4}{B^2}}{\frac{A^4}{B^4}[1+4\sigma_s^4(\frac{k}{R})^2]}\right]\right\} \\ &= \exp\left\{-p_x^2\sigma_s^2\left[\frac{\frac{A^4}{B^2}}{\frac{A^4}{B^4}[1+4\sigma_s^4(\frac{k}{R})^2]} - i2B^2\frac{\sigma_s^2\frac{k}{R}}{1+4\sigma_s^4(\frac{k}{R})^2}\right]\right\} \\ &= \exp\left\{-p_x^2\sigma_s^2B^2\left[\frac{1}{1+4\sigma_s^4(\frac{k}{R})^2} - i2\frac{\sigma_s^2\frac{k}{R}}{1+4\sigma_s^4(\frac{k}{R})^2}\right]\right\}. \end{aligned} \tag{7.65}$$

7.3.5 Complex beat signal $S_B(d_x, p_x)$

Using the beat voltages calculated in the previous sections (Section 7.3.2-Section 7.3.4), we can calculate the complex beat signal we expect. In all of our experiments involving the characterization of the divergent or convergent Signal beam itself, the BLO generally has a larger diameter than the Signal beam, so that we can approximate the BLO to a very good degree to be perfect, i.e. infinitely wide. The remaining scaling factor B then becomes meaningless and we can set it to unity.

Using the results for $V_B^{g\ll1}$ (Eq. (7.59)) and $V_B^{g\to\infty}$ (Eq. (7.69)) to describe the beat voltages for SLO and BLO, we get for the complex beat signal:

$$
\begin{aligned}
S_B(d_x, p_x) &\propto V_B^{SLO*}(d_x, p_x) V_B^{BLO}(d_x, p_x) \\
&\propto \exp\left[-\frac{d_x^2}{4\sigma_s^2} - p_x^2 \frac{\sigma_s^2}{1 + 4\sigma_s^4 (\frac{k}{R})^2} \right] \\
&\times \exp\left\{ i \left[\frac{d_x^2}{2} \frac{k}{R} + 2\sigma_s^2 p_x^2 \frac{\sigma_s^2 \frac{k}{R}}{1 + 4\sigma_s^4 (\frac{k}{R})^2} - p_x d_x \right] \right\}. \qquad (7.66)
\end{aligned}
$$

It can readily be seen that, unlike Single-LO beat signals, for curved Signal beams (see Eq. (7.9)), there is no correlation between position and momentum in the *magnitude* of the beat signal. All information on the radius of curvature is contained in the *phase* of $S_B(d_x, p_x)$. [3]

7.3.6 Approximation of $S_B(d_x, p_x)$ for small R

If, for a given σ_s and k, the radius of curvature of the Signal beam is sufficiently small, Eq. (7.66) can be simplified even further. Let us assume the phase-difference between the center of the beam and the transverse position $2\sigma_s$ where the relative field amplitude drops to e^{-1}, is large compared to unity, i.e.

$$
\frac{k}{2|R|} (2\sigma_s)^2 \gg 1, \qquad (7.67)
$$

where R can be positive or negative. Squaring both sides yields

$$
4\sigma_s^4 \frac{k^2}{R^2} \gg 1 \qquad (7.68)
$$

[3] For a less than ideal Dual-LO on the other hand, there is a correlation between position and momentum in the amplitude due to the finite and non-zero size and angular spread of the LOs.

For a typical σ_s in our experiment of about 0.4 mm, the left-hand side exceeds 10 for radii of curvature smaller than 1 m. Using relation (7.68) we can neglect the 1 in the denominators $1 + 4\sigma_s^4(\frac{k}{R})^2$ appearing in Eq. (7.66), thereby simplifying this expression considerably:

$$\begin{aligned} S_B(d_x, p_x, R < 1m) \;\; &\rightarrow \;\; \exp\left[-\frac{d_x^2}{4\sigma_s^2} - p_x^2 \frac{1}{4\sigma_s^2(\frac{k}{R})^2}\right] \\ &\times \;\; \exp\left[i\left(\frac{d_x^2}{2}\frac{k}{R} + p_x^2 \frac{}{2}\frac{R}{k} - p_x d_x\right)\right] \\ &= \;\; \exp\left[-\frac{1}{4\sigma_s^2}\left(d_x^2 - p_x^2\frac{R^2}{k^2}\right)\right] \\ &\times \;\; \exp\left[\frac{ik}{2R}\left(d_x - p_x\frac{R}{k}\right)^2\right]. \end{aligned} \tag{7.69}$$

It can easily be seen and verified that for R < 1m, the error introduced by this approximation is smaller than 10%. For R = 10 cm, which is in the range of interest for our Enhanced Backscatter experiments in Chapter 12, the error is less than 1%. Figure 7.2 shows the in-phase- (a) and out-of-phase quadrature signal of a typical divergent beam, according to the expression in Eq. (7.69) or Eq. (7.66).

7.3.7 Extraction of R and σ_s from the quadrature signals

The radius of curvature can be extracted most easily from the out-of-phase quadrature signal. The clover-like peaks that -for a perfectly flat Signal beam- are located between the axes and vanish for zero momentum and position (see Figure 5.3), cross both axes for finite radii of curvature, as can be seen in Figure 7.2. From the location of the crossings we can extract the size σ_s and the radius of curvature of

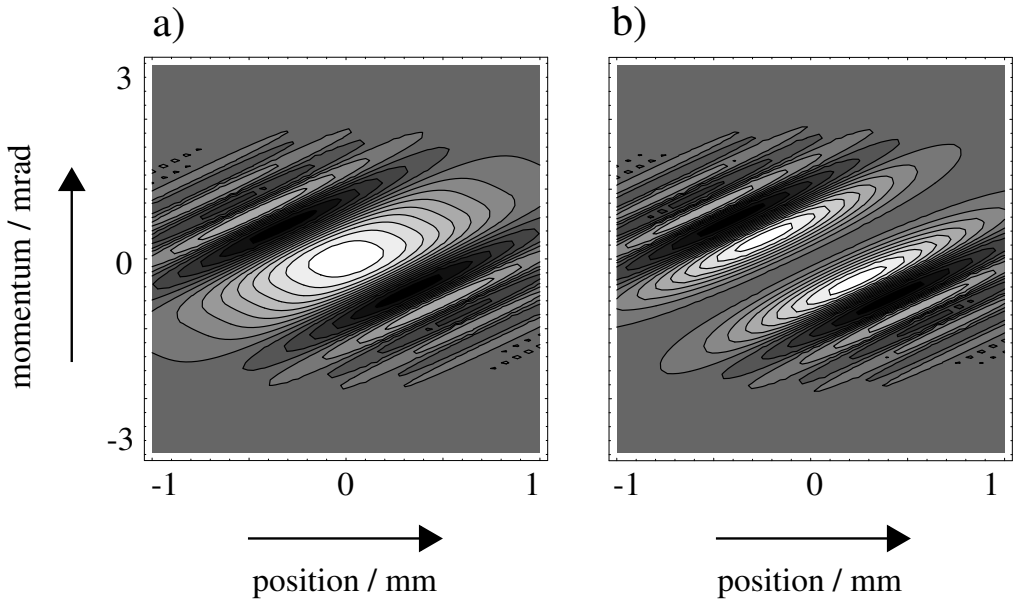

Figure 7.2: In-phase- (a) and out-of-phase quadrature signal (b) of $S_B(d_x, p_x)$ for a typical divergent Gaussian beam as given in Eq. (7.69) or Eq. (7.66).

the Signal beam, as we will see in the following.

For zero momentum, Eq. (7.66) as well as its approximation Eq. (7.69) reduce to:

$$S_B(d_x, p_x) \propto \exp\left[-d_x^2\left(\frac{1}{4\sigma_s^2} + i\frac{k}{2R}\right)\right] \tag{7.70}$$

which is proportional to and only to the beat voltage picked up by the SLO: the amplitude of the Signal beam's electrical field (first term) and its phase-distribution determined by its curvature (second term).

The out-of-phase quadrature signal is then given by

$$S_B^{OP}(d_x, p_x) \propto \exp\left(-\frac{d_x^2}{4\sigma_s^2}\right)\sin\left(d_x^2\frac{k}{2R}\right). \tag{7.71}$$

A plot of this expression is shown in Figure 7.3(a). At the position d_x^m of the closest

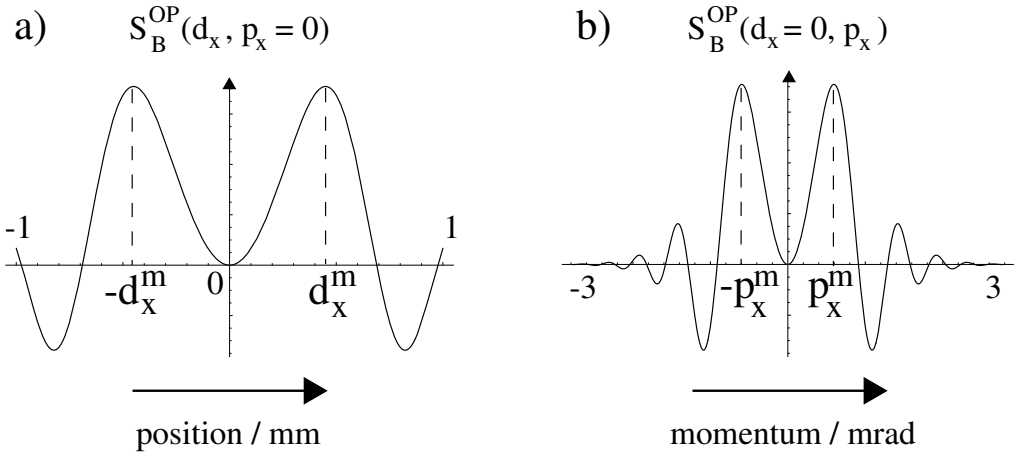

Figure 7.3: The position distribution for zero momentum (a) and the momentum distribution at the beam center (b) of the out-of-phase quadrature part of $S_B(d_x, p_x)$ are used to extract σ_s and R.

peaks, which correspond to the intersection of the clover peaks in phase-space with the d_x-axis, the derivative of $S_B^{OP}(d_x, p_x)$ with respect to d_x must vanish:

$$\begin{aligned} \left.\frac{dS_B^{OP}(d_x,0)}{d(d_x)}\right|_{d_x^m} &= 0 \\ &= \left\{ -\frac{d_x^m}{2\sigma_s^2}\sin\left[(d_x^m)^2\frac{k}{2R}\right] + d_x^m\frac{k}{R}\cos\left[(d_x^m)^2\frac{k}{2R}\right]\right\} \\ &\times \exp\left[-\frac{(d_x^m)^2}{4\sigma_s^2}\right] \end{aligned} \tag{7.72}$$

which requires the term in the braces to vanish. Rearranging and solving for σ_s yields

$$\sigma_s = \sqrt{\frac{R}{2k}\tan\left[(d_x^m)^2\frac{k}{2R}\right]}. \tag{7.73}$$

The next step is to find the crossings of the clover peaks with the p-axis (Figure 7.3(b)). We use the approximate expression in Eq. (7.69) here since in our

experiment we are exclusively concerned with radii of curvature $\ll 1$ m, and we can express R and σ_s in a closed form. If we used the full expression in Eq. (7.66) we would have to rely on iterative numerical methods.

For $x \equiv 0$, Eq. (7.69) reduces to

$$S_B(d_x, p_x) \propto \exp\left[-p_x^2\left(\frac{1}{4\sigma_s^2}\frac{R^2}{k^2} - i\frac{R}{2k}\right)\right] \tag{7.74}$$

with the out-of-phase part being

$$S_B^{OP}(d_x, p_x) \propto -\exp\left[-p_x^2\left(\frac{R}{2\sigma_s k}\right)^2\right]\sin\left(p_x^2\frac{R}{2k}\right). \tag{7.75}$$

Again, the derivative of $S_B^{OP}(d_x, p_x)$, this time with respect to p_x, has to be zero at the intersection p_x^m between the clover peaks and the p-axis:

$$\begin{aligned}\left.\frac{dS_B^{OP}(0,p_x)}{d(p_x)}\right|_{p_x^m} &= 0 \\ &= -\left\{p_x\frac{R}{k}\cos\left[(p_x^m)^2\frac{R}{2k}\right] - \frac{(p_x^m)}{2}\left(\frac{R}{\sigma_s k}\right)^2\sin\left[(p_x^m)^2\frac{R}{2k}\right]\right\} \\ &\times \exp\left[-(p_x^m)^2\left(\frac{R}{2\sigma_s k}\right)^2\right].\end{aligned} \tag{7.76}$$

As before, the term in braces has to be zero in order for the equation to hold. Rearranging and solving for σ_s yields

$$\sigma_s = \sqrt{\frac{R}{2k}\tan\left[(p_x^m)^2\frac{1}{2}\frac{R}{k}\right]}. \tag{7.77}$$

By comparing Eq. (7.77) to Eq. (7.73) it is clear that the arguments of their respective tangent have to be equal, resulting in an expression for R:

$$(p_x^m)^2 \frac{R}{2k} = (d_x^m)^2 \frac{k}{2R} \tag{7.78}$$

$$\boxed{\mathrm{R} = \pm \frac{d_x^m}{p_x^m} k.} \tag{7.79}$$

The "+" holds if the phase-space profile is tilted in the direction where d_x and p_x have the same sign, and "−" for different signs; which is the reasoning outlined in Section 3.4. The above expression is identical to the one we use to determine R from the plot of Wigner function itself, when we consider $\frac{p_x^m}{d_x^m}$ its slope in phase-space.

We use the R extracted in Eq. (7.79) to determine σ_s in either Eq. (7.77) or Eq. (7.73):

$$\boxed{\sigma_s = \sqrt{\frac{1}{2} \frac{d_x^m}{p_x^m} \tan\left(\frac{d_x^m p_x^m}{2}\right)}.} \tag{7.80}$$

We will apply this theory to the determination of R and σ_s for a divergent Gaussian Signal beam in Section 8.2.

Chapter 8

Characterization of a transverse beam profile - Experiment

The Signal beam can most easily be measured in the transmission setup by omitting the sample, as shown in Figure 13.1. In backscatter experiments, the setup of which is shown in Figure 5.6, the Signal beam can be measured using the specular reflection of the sample container surface, or for more accurate measurements, by replacing the sample container with a mirror.

In the following, we measure the beam parameters in the transmission setup. Due to the 4f-system in addition to the even number of mirrors and beam-splitters for each beam, the Signal beam is inverted with respect to the Dual-LO. In Section 8.1, we determine the beam size σ_s and the transverse coherence length σ_g of a collimated beam. From σ_s and σ_g we can calculate the global coherence σ_g/σ_s which is preserved in all beams, independent of the their configuration. In Section 8.2 we determine σ_s and the radius of curvature R of a transversely coherent beam.

8.1 $R{=}\infty$, σ_s and σ_g unknown

In this section we are going to determine σ_s and σ_g of a flat Signal beam. Figure 8.1 shows the measured quadrature signals. As mentioned in Section 7.2.5, we only need

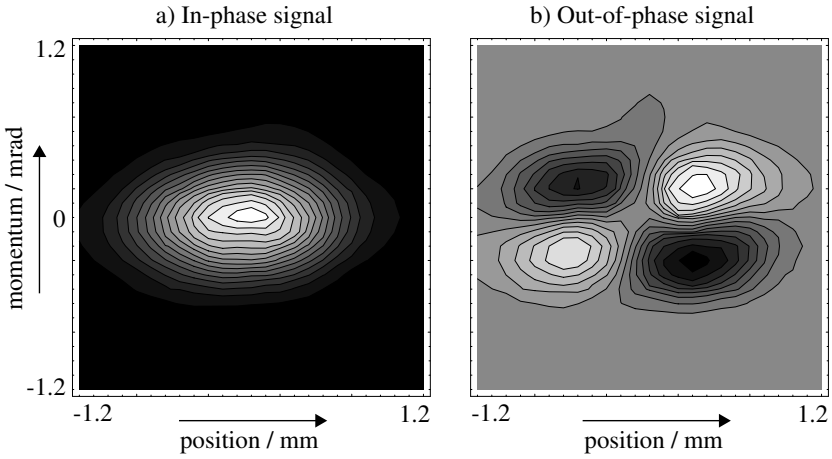

Figure 8.1: Measured in-phase- (a) and out-of-phase quadrature signal (b) of the complex beat signal for a collimated Gaussian beam.

one of the quadrature signals to determine σ_s and σ_g. We are going to compare the results using both quadrature signals.

8.1.1 Extraction of beam parameters from in-phase signal

Figure 8.2 shows the position distribution for $p_x = 0$ and the momentum distribution for $d_x = 0$, which is just a subset of the data for the in-phase part along its axes. From this data we measure values of

$$d_x^e = 0.675\,\text{mm} \tag{8.1}$$

$$p_x^e = 3.52\,\text{mm}^{-1}. \tag{8.2}$$

Using the expressions for σ_s and σ_g in Equations (7.47) and (7.48) we get

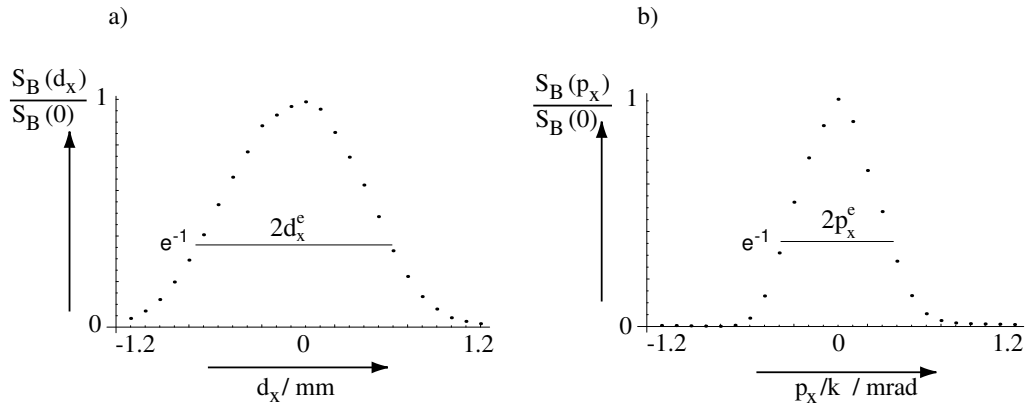

Figure 8.2: (a) Measured position distribution for $p = 0$ and (b) momentum distribution for $x = 0$ of the in-phase part of S_B in Figure 8.1.

$$\sigma_s = 0.42\,\text{mm} \tag{8.3}$$

$$\sigma_g = 2.82\,\text{mm} \tag{8.4}$$

and therefore a global coherence for our SLD light leaving the collimating system of

$$\sigma_{glob} = \frac{\sigma_g}{\sigma_s} = 7.05. \tag{8.5}$$

8.1.2 Extraction of beam parameters from out-of-phase signal

The measurement of d_x^e and p_x^e from the out-of-phase signal is done by measuring the distance between the peaks and using Equations (7.39) and (7.40), as discussed in Section 7.2.5. In Figure 8.1b, x_m and p_m are measured as shown in Figure 7.1:

$$x_m = 0.425\,\mathrm{mm} \tag{8.6}$$

$$p_m = 2.22\,\mathrm{mm}^{-1}. \tag{8.7}$$

Using again Equations (7.47) and (7.48), these values yield d_x^e and d_p^e of

$$d_x^e = 0.625\,\mathrm{mm} \tag{8.8}$$

$$p_x^e = 3.26\,\mathrm{mm}^{-1}, \tag{8.9}$$

which differs by 7% from the values determined by the in-phase part. This might partly be due to the slight divergence of the Signal beam which manifests itself in the tilt to the right, seen especially in the out-of-phase part.

σ_s can be retrieved from Eq. (7.35):

$$\sigma_s = 0.36\,\mathrm{mm} \tag{8.10}$$

which is 14% smaller than the value extracted from the in-phase signal. Eq. (7.36) produces an imaginary value for σ_g, which is due to the fact that the solution to Eq. (7.36) has surpassed the value for $\sigma_g = \infty$, $1/\sigma_g^2 = 0$ for a fully coherent beam. This is not surprising, since differences in the properties of a perfect transversely coherent Gaussian beam and one with a global coherence of 7 are very hard to detect. Even a small variation in d_x and p_x for beams with a high degree of transverse coherence will consequently have a large effect on the measured beam parameters. Therefore, we conclude that the global coherence of beam is

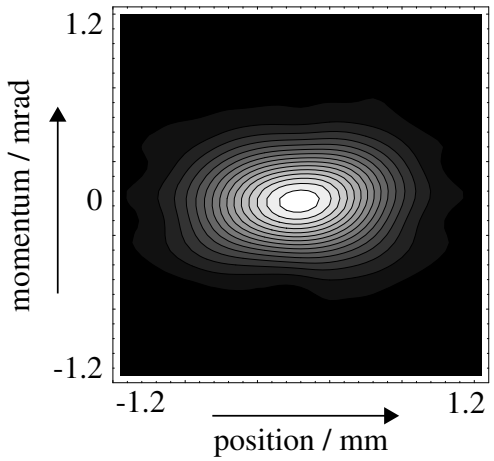

Figure 8.3: Wigner function retrieved by an inverse Margenau-Hill transformation from the measured quadratures signals depicted in Figure 8.1.

$$\sigma_{glob} \geq 7.05. \tag{8.11}$$

8.1.3 Wigner function of Signal beam

The fact that $\sigma_g \gg \sigma_s$ allows us to derive the Wigner function from the quadrature signals, as explained in Section 5.3.1. The inverse Margenau-Hill transformation is performed by a C++ program, the source code of which can be found in Appendix C.

Figure 8.3 shows the Wigner function derived from the quadrature signals in Figure 8.1. As expected for a flat Gaussian wavefront, the Wigner function is elliptical and not tilted.

8.1.4 Discussion

The value of 0.42 mm for σ_s determined from the in-phase quadrature signal agrees well with that determined by the e^{-2} intensity profile using the reticon, which leads to a value of 0.45 mm $\pm$ 0.025 mm. The value of 0.36 mm retrieved from the

out-of-phase signal on the other hand is off by 20 % from the reticon value, which might be due to a slight curvature in the Signal beam wavefront which affects the out-of-phase signal more than the in-phase signal.

The measured values for the transverse coherence length of $\sigma_g \geq 2.82$ mm in the in-phase signal and $\sigma_g \to \infty$ in the out-of-phase signal can not as easily be verified. A good indicator to support the result that $\sigma_g \gg \sigma_s$ is that in our experiments the beat signal is almost invariant with respect to an inversion of the beam profile by insertion of a 4f-system. Such an inversion affects not only the $x-$ but also the $y-$distribution of the field which most likely has a different global coherence length due to the different collimation process in this direction.

The emitting area of our SLD is only 5×1 μm (width $\times$ height) [49] which leads to a large angle of radiation. An estimate of the transverse coherence length can be done using the Cittert-van Zernike theorem, assuming incoherent radiation from the emitting area of the SLD, and taking into account the clipping of the field by apertures: Light emitted from the emitting area of a width of w=5 μm propagates approximately d=8 mm before entering the first collimation lens. At that distance, the width of the coherence area is

$$\sigma_g \approx \frac{\lambda}{w} d \approx 1.1\,\mathrm{mm}. \tag{8.12}$$

An aperture with a diameter of less than a millimeter clips the beam further in order to improve the beam profile (see Section 6.3); therefore the transverse part of the beam we use is well within its coherence area.

The fact that $\sigma_g \gg \sigma_s$ is very convenient since it allows us to neglect the $\exp\left[-\frac{(x_1-x_2)^2}{2\sigma_g^2}\right]$-term in Eq. (3.2) which couples the Signal- and LO-fields due to its cross-terms in the heterodyne scheme and makes it impossible to use their in-

dividual Wigner functions. Using the procedures outlined in Section 5.3.1 we can then determine the Wigner function of the Signal field by inverse Margenau-Hill transformation of the complex beat signal.

8.2 σ_g=∞, σ_s and R unknown

In this section, we are going to determine the radius of curvature and beam size of a divergent Signal beam, using the out-of-phase quadrature signal as described in Section 7.3.7. We detect and measure the beam reflected off the polished surface of the sample container used in an experiment in Section 12.2.2 where we demonstrate the change in sign of the radius of curvature of a field backscattered from a random medium. The incident field, partially reflected from the surface of the sample cell, serves as a reference in that experiment. The set-up modifications in the Signal arm for the measurement of backscattered and reflected light are displayed in Figure 12.1.

The divergent beam is generated by placing a lens with a focal length of f=20 cm at a distance of 27 cm from the sample surface. The top row of Figure 12.5 shows the measured in-phase part, out-of-phase part and resulting Wigner function of this field, reflected off the sample container. The rest of the figures shall not concern us at the moment.

We extract the points of intersection d_x^m and p_x^m of the tilted peaks in the out-of-phase signals by plotting the momentum distribution at $d_x = 0$ and the position distribution at $p_x = 0$, as demonstrated in Section 7.3.7. Figure 8.4 shows both plots.

We measure:

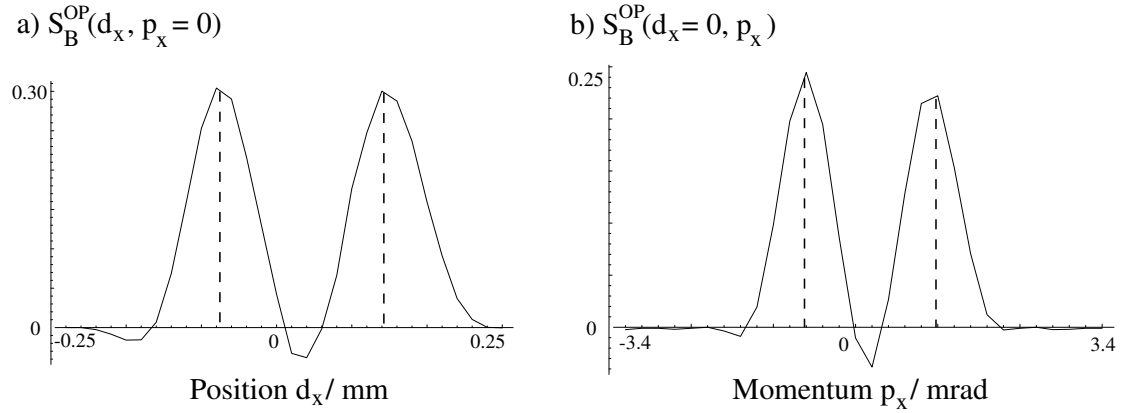

Figure 8.4: Position distribution at $p_x = 0$ (a) and momentum distribution at $d_x = 0$ (b), yielding d_x^m and p_x^m.

$$d_x^m = 90\,\mu\text{m} \tag{8.13}$$

$$p_x^m = 1.02\,\text{mrad} \times \text{k} = 9.45\,\text{mm}^{-1} \tag{8.14}$$

yielding, according to Eq. (7.79), a radius of curvature of

$$R = \frac{d_x^m}{p_x^m} k = +8.8\,\text{cm}. \tag{8.15}$$

The sign of R is positive because of the tilt to the right of the quadrature signals in Figure 12.5.

The beam size σ_s follows from Eq. (7.80):

$$\sigma_s = \sqrt{\frac{1}{2}\frac{d_x^m}{p_x^m}\tan\left(\frac{d_x^m p_x^m}{2}\right)} = 47\,\mu\text{m}. \tag{8.16}$$

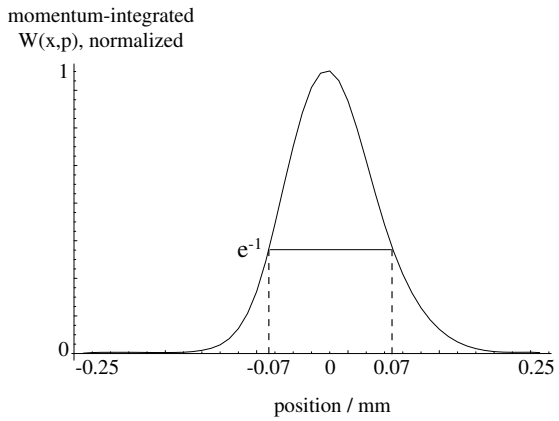

Figure 8.5: Measured momentum-integrated Wigner function of the divergent Gaussian beam shown in the top row of Figure 12.5.

8.2.1 Discussion

According to Gaussian beam optics, a lens of 20 cm focal length at a distance of 27 cm subjected to a collimated incident beam of σ_s=305 μm produces a divergent field with a radius of curvature of about 7.8 cm at the sample surface. The radius of curvature of 8.8 cm measured with the Two-Window technique is reasonably close to that value (12.8% larger).

The measured beam size σ_s of 47 μm can be compared to the value retrieved from the Wigner function calculated from the quadrature signals. From Eq. (3.4) we know the Wigner function of a Gaussian beam:

$$W^{coh}(x,p) = 8\pi\sigma_s^2 \exp\left[-\frac{x^2}{2\sigma_s^2} - 2\sigma_s^2\left(\frac{kx}{R}+p\right)^2\right]. \tag{8.17}$$

If we momentum-integrate the Wigner function, the second exponential integrates out and we get

$$\hat{W}^{coh}(x) = \int dp\, W^{coh}(x,p) \propto \exp\left(-\frac{x^2}{2\sigma_s^2}\right). \tag{8.18}$$

From the spatial width of $\hat{W}^{coh}(x)$ we can determine σ_s. Figure 8.5 shows the measured $\hat{W}^{coh}(x)$, retrieved from the measured Wigner function in Figure 12.5. We measure $\sigma_s = 50$ μm, which agrees very well with the value of 47 μm determined by the intersection points of the peaks in the out-of-phase quadrature signal.

8.3 Summary

The Two-Window technique enables the determination of the beam size σ_s, the transverse coherence length σ_g and the radius of curvature R of the Signal beam by means of either quadrature of the complex beat signal $S_B(d_x, p_x)$. For a collimated Signal beam, σ_s and σ_g can be extracted by determining the width of the in-phase signal in position and momentum and also, more easily, from the location of the clover-like peaks of the out-of-phase signal. From σ_s and σ_g the global coherence σ_{glob} can be derived which is invariant for propagation through first-order optical systems, in particular lenses and free space.

The measured beam sizes of $\sigma_s = 0.42$ mm (from in-phase signal) and 0.36 mm (from out-of-phase signal) are in reasonable agreement with the value determined by the reticon (0.45 mm $\pm$ 0.025 mm). A value for the transverse coherence length of σ_g=2.82 mm was determined by the in-phase signal, the out-of-phase signal yields a value of $\sigma_g \rightarrow \infty$, resulting in a global coherence of σ_{glob} >7.05. Due to the indistinguishability of beams with different but large global coherence, the determination of an exact value for σ_g proves challenging.

For a Signal beam with finite radius of curvature and $\sigma_g \gg \sigma_s$, R and σ_s have been determined from the locations of the clover-like peaks in phase-space for zero position and momentum. The radius of curvature determined this way agrees with the value calculated with Gaussian optics to within 13%. The beam-size σ_s was

measured to be 47 μm, which agrees very well with the value of 50 μm determined by the spatial width of the momentum-integrated measured Wigner function of the beam.

Unlike the One-Window technique previously used, the Two-Window technique does not require the preparation of two identical beams. It employs a Dual-LO consisting of a phase-locked set of a flat focused and a flat collimated LO which enables the fast and accurate determination of beam-size, transverse coherence length and radius of curvature of a Signal beam.

Chapter 9

Characterization of a longitudinal beam profile

We conclude the characterization of the Signal beam by performing longitudinal z-scans using the Two-Window technique. z-scans record the complex beat signal (or mean square beat signal) as a function of path delay between the LO and the Signal field. While the amplitude of the beat voltage formerly measured by the One-Window technique can be easily explained (see Section 6.2.1), we observe a phase-gradient in the Two-Window technique which is not fully understood yet. In the following, we will present the experimental data, followed by a discussion of several models which try to explain the data.

9.1 Experimental Results

The quadrature signals as a function of the path-delay Δl are measured in the same set-up as in Chapter 8. The z-scans are performed for a variety of focal lengths of the SLO lens; with and without detector input lenses, the reason of which will become clear soon. In all scans, a flat Signal beam and big LO (BLO) of beam radius $w = 2\sigma_s = 600$ μm are used. Figure 9.1 shows a scan taken for a focal lens of 15 cm of the SLO lens with the detector input lenses present. The top row shows the

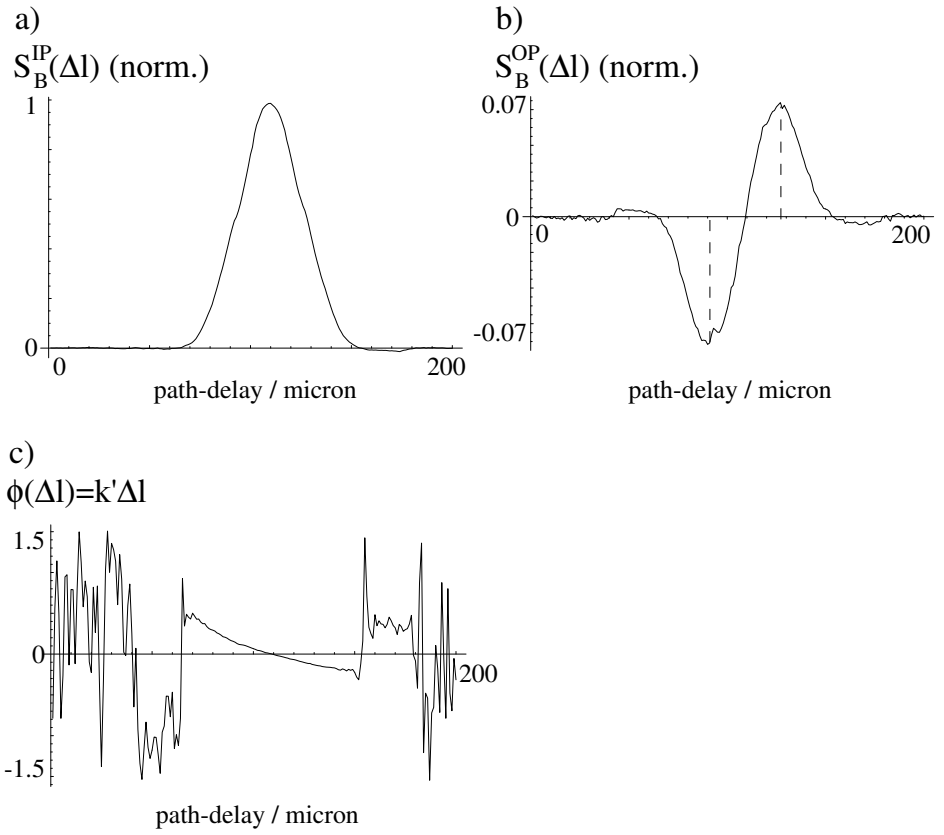

Figure 9.1: Dual-LO z-scan of a Gaussian beam with all lenses present in the experimental setup. a) In-phase-, b) out-of-phase quadrature signal. Both quadrature signals are normalized with respect to the in-phase signal for zero path-delay. c) phase of complex beat signal. The rapid phase changes in sign left and right to the smooth center region are due to noise for low beat signal levels.

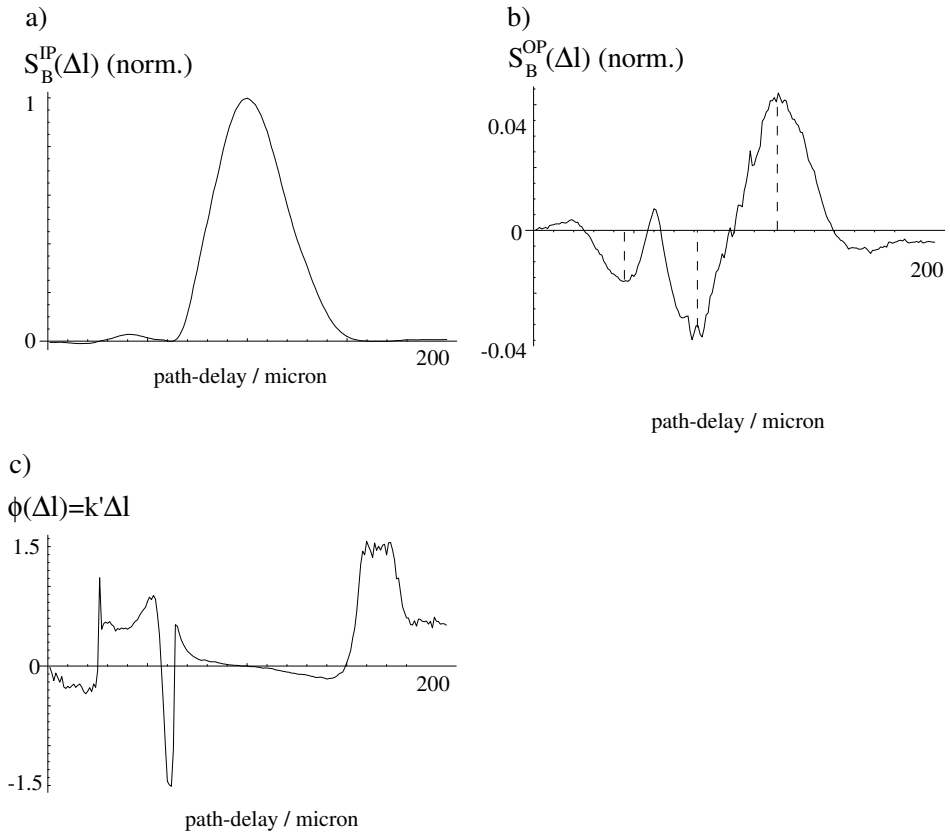

Figure 9.2: Dual-LO z-scan of a Gaussian beam with SLO-lens present and both input lenses removed. a) In-phase-, b) out-of-phase quadrature signal. Both quadrature signals are again normalized with respect to the in-phase signal for zero path-delay. c) phase of complex beat signal.

in-phase- (a) and out-of-phase quadrature signal (b), normalized to the maximum amplitude of the in-phase signal at zero path delay, over a path-delay range of 200 microns. c) shows the phase of the complex beat signal. The in-phase part looks almost Gaussian, with an e^{-1} half-width of about Δl_B, as in the Single-LO z-scan (Section 6.2.1).

Additional measurements without the input lenses and SLO-lenses of different focal lengths yield results where the location of the out-of-phase peaks and amplitude relative to the in-phase signal is similar to those measured in the first scan.

One example, which is shown in Figure 9.2, is a z-scan taken with the SLO-lens present and both detector input lenses removed.

9.1.1 Discussion

The quadrature signals observed in Figure 9.1 and Figure 9.2 can be modelled by the sum of a Gaussian amplitude and a phase gradient along the scanning direction; i.e., a phase-difference between V_B^{SLO} and V_B^{BLO} that changes linearly with the path-difference Δl between the respective LO and the Signal beam. In this case, the beat voltages of the LOs can be written as

$$V_B^{BLO}(\Delta l) \propto \exp\left[-\frac{\Delta l^2}{2(\Delta l_B)^2}\right]\exp(ik\Delta l + ik_1'\Delta l) \tag{9.1}$$

$$V_B^{SLO}(\Delta l) \propto \exp\left[-\frac{\Delta l^2}{2(\Delta l_B)^2}\right]\exp(ik\Delta l + ik_2'\Delta l). \tag{9.2}$$

The first terms in both beat voltages in Equations (9.1) and (9.2) describe the amplitude dependence; in the Single-Window technique this term is squared and reproduces Eq. (6.1). The second term contains the phase contributions from the path difference Δl between the Signal beam and the respective LO and by the additional phase gradients k_1' and k_2', which contribute to V_B^{BLO} and V_B^{SLO}. The complex beat signal is then:

$$\begin{aligned} S_B(\Delta l) &= V_B^{SLO*}V_B^{BLO} \\ &= \exp\left[-\frac{\Delta l^2}{(\Delta l_B)^2}\right]\exp\left[i(k_1' - k_2')\Delta l\right] \end{aligned} \tag{9.3}$$

with the in-phase signal

$$S_B^{IP}(\Delta l) = \exp\left[-\frac{\Delta l^2}{(\Delta l_B)^2}\right]\cos(\Delta k'\Delta l) \tag{9.4}$$

and the out-of-phase signal

$$S_B^{OP}(\Delta l) = \exp\left[-\frac{\Delta l^2}{(\Delta l_B)^2}\right]\sin(\Delta k'\Delta l) \tag{9.5}$$

where we abbreviated $k_1' - k_2'$ by $\Delta k'$. Weak side peaks on the slopes of the in-phase signal seen especially well in Figure 9.1 bear witness of the cosine factor in Eq. (9.4). The out-of-phase signals displays the phase-factor in Eq. (9.5) of course more distinctively.

Judging from the small relative amplitude of the out-of-phase part in both scans, the phase-gradient is very small. In this case, we can approximate the $\sin(\Delta k'\Delta l)$ in Eq. (9.5) by $\Delta k'\Delta l$ and neglect the cosine in Eq. (9.4):

$$S_B^{IP}(\Delta l) \approx \exp\left[-\frac{\Delta l^2}{(\Delta l_B)^2}\right] \tag{9.6}$$

$$S_B^{OP}(\Delta l) \approx \Delta k'\Delta l \exp\left[-\frac{\Delta l^2}{(\Delta l_B)^2}\right]. \tag{9.7}$$

Figure 9.3 shows a plot of the quadrature signals in Eq. (9.6) (a) and Eq. (9.7) (b) for an arbitrary value of $\Delta k = 4.2 \times 10^{-5}$ μm^{-1}. The location and relative amplitude of the peaks in the out-of-phase part can be used to retrieve the value of the phase gradient. The peaks are located where the derivative of $S_B^{OP}(\Delta l)$ is zero:

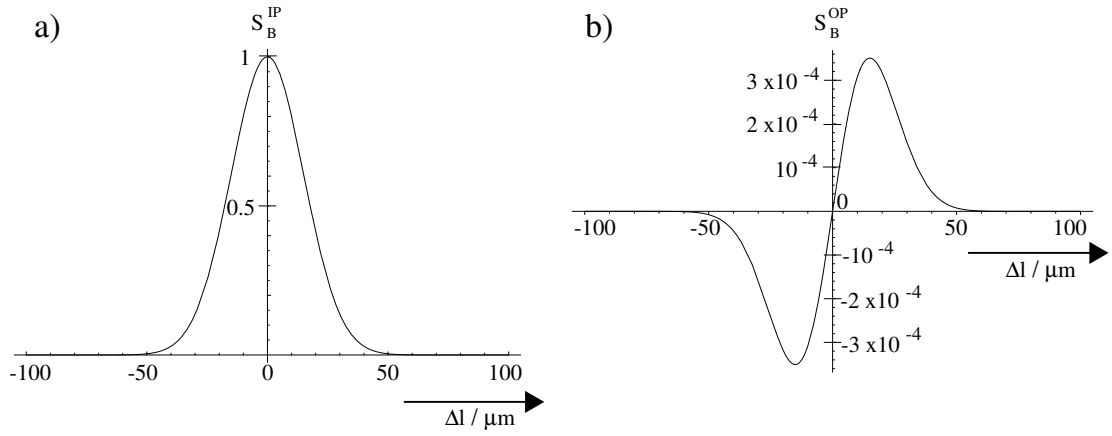

Figure 9.3: Plot o of the quadrature signals for $\Delta k' \ll k$ in a longitudinal scan by our Two-Window method, according to Equations (9.6) and (9.7). a) in-phase signal; b) out-of-phase signal.

$$\begin{aligned} \frac{d}{d\Delta l} S_B^{OP}(\Delta l) &= 0 \\ &= \left[1 - \Delta l \frac{2\Delta l}{(\Delta l_B)^2}\right] \Delta k' \exp\left[-\frac{\Delta l^2}{(\Delta l_B)^2}\right] \end{aligned} \tag{9.8}$$

which requires the terms in brackets to vanish. Solving for Δl yields:

$$\Delta l_{1,2} = \pm \frac{\Delta l_B}{\sqrt{2}}. \tag{9.9}$$

The distance between the peaks [1] is therefore just the longitudinal spatial resolution (Section 6.2.1) times a pre-factor, which directly leads to the coherence length of the light:

[1] This refers to the difference of Δl_1 and Δl_2. The *sum* of Δl_1 and Δl_2 can be shown to be the distance between the Δl-position where we set the phase to zero at the beginning of the scan, and the Δl-position where the beat signal is maximal, which is helpful for the alignment process. For a symmetric peak arrangement as in Figure 9.3, this sum is zero.

$$\Delta l_1 - \Delta l_2 = \sqrt{2}\Delta l_B = \frac{l_c}{\sqrt{\ln 2}} \tag{9.10}$$

$$l_c = \sqrt{\ln 2}(\Delta l_1 - \Delta l_2). \tag{9.11}$$

The difference $\Delta l_1 - \Delta l_2$ between the minimum and maximum in is Figure 9.1 is 36 μm, which corresponds to a longitudinal resolution of

$$\Delta l_B = 25.0\,\mu\text{m}, \tag{9.12}$$

according to Eq. (9.10) and a longitudinal coherence length of

$$l_c = 29.4\,\mu\text{m}, \tag{9.13}$$

according to Eq. (9.11). Our measurements with a single LO (Section 6.2.1) as well as data provided by Superlum Co. suggest a coherence length of $l_c = 25.0$ μm, according to Eq. (6.5), which agrees reasonably well with the value in Eq. (9.13). Inserting the values for $z_{1,2}$ from Eq. (9.9) into Eq. (9.7) yields the peak amplitudes of $S_B^{OP}(\Delta l)$, normalized to 1:

$$S_B^{OP}(\Delta l_{1,2}) = \pm\frac{\Delta l_B}{\sqrt{2}}\Delta k' e^{-\frac{1}{2}} \tag{9.14}$$

Solving for $\Delta k'$ and expressing Δl_B in terms of $\Delta l_1 - \Delta l_2$ as in Eq. (9.10), the phase-gradient follows

$$\Delta k' = \frac{2}{e^{-\frac{1}{2}}}\left|\frac{S_B^{OP}(\Delta l_1)}{\Delta l_1 - \Delta l_2}\right|. \tag{9.15}$$

From the relative peak amplitudes of $S_B^{OP}(\Delta l_1)$ and $S_B^{OP}(\Delta l_2)$ of ≈ 0.04 (Figure 9.1)

and ≈ 0.07 (Figure 9.2), phase-gradients of

$$\Delta k_1' = 6.3 \times 10^{-3}\,\mu m^{-1} \tag{9.16}$$

and

$$\Delta k_2' = 4.0 \times 10^{-3}\,\mu m^{-1} \tag{9.17}$$

follow.

As mentioned before, the origin of these phase gradients is not quite clear yet. In the following we will discuss two possible explanations for its origin.

Phase gradients by curved wavefronts

As is well known, Gaussian beams undergo an additional phase-change of π when going through their beam waist [50]:

$$\phi(z) = tan^{-1}\frac{z}{z_0} \tag{9.18}$$

This phase-change occurs over a distance which solely depends on the beam's Rayleigh length z_0 ([50], Eq. 14.5.21):

$$z_0 = \frac{\pi w_0^2}{\lambda} \tag{9.19}$$

where $w_0 = 2\sigma_s$ is the e^{-2} intensity radius of the beam waist and λ the wavelength of the beam.

The observed phase-gradient could therefore be due to passing through a beam waist during the longitudinal scan of either the SLO which is narrow in the detection input plane, or the BLO which is narrow in the detection plane due to the focusing

by the detector input lens. Since the latter produces the bigger phase-gradient due to the shorter focus length of $f = 6$ cm of the detection lens, we will consider it in the following. The SLO which is already focused in the detection input plane is not focused any further by the detection input lenses, but instead diverges because of diffraction. The size and shape of the (Gaussian) Signal beam in this case are irrelevant since its longitudinal phase contributes equally to both beat voltages V_{BLO} and V_{SLO}.

Since the peak width of $S_B(\Delta l)$ in all scans is much smaller than the Rayleigh length, we can approximate $tan^{-1}\frac{z}{z_0}$ in Eq. (9.18) by $\frac{z}{z_0}$ so that

$$\Delta k' = z_0^{-1}. \tag{9.20}$$

According to this relation, the phase-gradient of $\Delta k' = 6.3 \times 10^{-3}\,\mu m^{-1}$ determined in the last section from Figure 9.1 where both detector input lenses are present, then corresponds to a Rayleigh length of $z_0 = 158$ μm and, according to Eq. (9.19), a beam waist size of $w_0 = 5.8$ μm.

But, according to asic Gaussian optics theory the BLO, which has a size of $w = 600$ μm, is focused by the detector input lens to a beam waist in the focal plane of $w_0 = 21.6$ μm with a Rayleigh length of $z_0 = 2.2$ mm. Both values are not consistent with the beam size and Rayleigh length of the BLO retrieved from Eq. (9.20). All other lenses in the local oscillator arms can be excluded as a possible source as well: their focal lengths are much longer so the beam size and Rayleigh lengths in their focal planes are even larger.

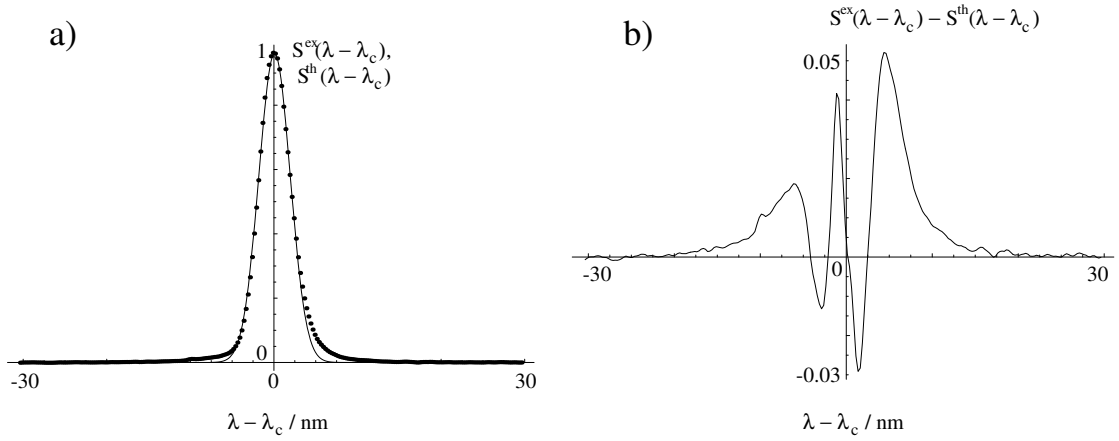

Figure 9.4: a) Measured power spectrum (dots) of SLD, relative to its center frequency of $\lambda_c = 676.5$ nm, and a Gaussian fit (solid line). Both are normalized with respect to their maximum value. b) The difference between measured spectrum and its Gaussian fit reveals a spectral modulation.

Phase gradients through spectral ripple

In the previous section we unsuccessfully tried to explain the observed phase-gradient by passing through a small beam waist in either SLO and BLO. The phase-difference due to this effect turned out to be too small though. A stronger z-dependent phase-difference between the LOs could be generated if the SLO and the BLO, due to their different transverse geometry, interfered with different frequency components of the Signal beam. This would not be surprising in laser diodes, where different transverse modes exhibit slightly different frequencies: In this case, a focused SLO would interfere almost exclusively with low-order modes close to the optical axis, while a collimated BLO would also interfere with higher-order modes. The resulting phase-difference of the beat signals V_{SLO} and V_{BLO} would then result in a phase-gradient seen in the complex beat signal according to Equations (9.1) and (9.2).

The phase gradient of $\Delta k_1' = 6.3 \times 10^{-3}\,\mu m^{-1}$ seen in Figure 9.1 could be

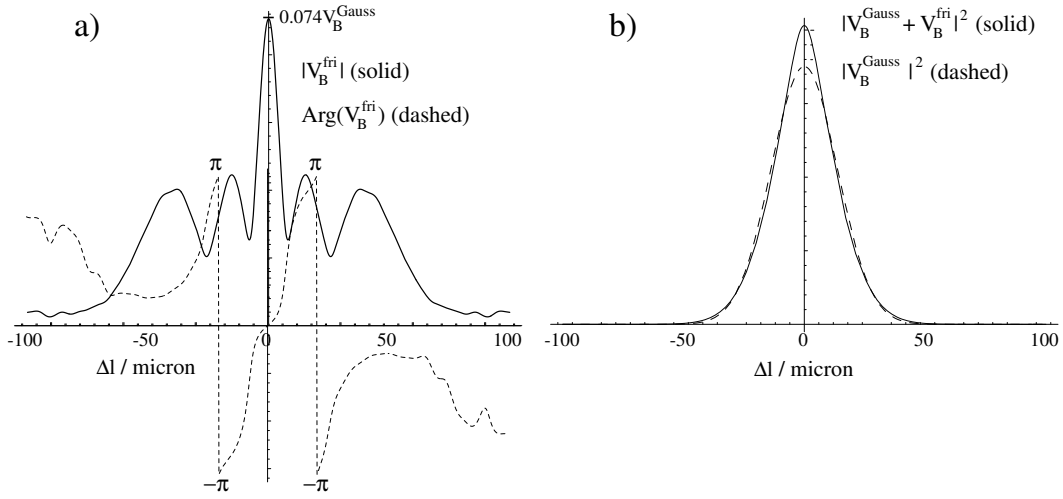

Figure 9.5: a) The additional beat voltage $|V_B^{fri}|$ with its magnitude (solid line) and argument (dashed line) due to the ripple in the spectrum is proportional to the longitudinal correlation function of the light field and was calculated according to Eq. (9.21) by Fourier transformation of S(ν) in Figure 9.4b). b) $|V_B(\Delta l)|^2$ with (solid line, measured) and without ripple (dashed line, from Gaussian fit in Figure 9.4).

generated by a prominent frequency peak in the spectrum shifted by $\nu = ck'/(2\pi)$ = 300 GHz with respect to the center frequency. This frequency shift corresponds to a shift in wavelength of $\Delta\lambda = \lambda^2/c\,\Delta\nu = 0.46$ nm, which can be resolved by standard optical spectrum analyzers. In the following, we measure the optical power spectrum using an optical spectrometer (EPP 2000 from StellarNet Inc.) with a resolution of 0.5 nm.[2] The measured power spectrum, relative to the measured center wavelength of 676.5 nm, is shown in Figure 9.4a). It is normalized with respect to its maximum. The dots show the measured values, the solid line its Gaussian fit. In Figure 9.4b), the difference between the measured power spectrum and its Gaussian fit is shown. It shows a fringe pattern superposed on a Gaussian with peaks at a distance of -11, -7.2, -2.3 and 4.5 nm from the center frequency. Its zeroes reveal a period of

[2]A measurement of a HeNe-laser line confirms this value.

$\Delta\lambda \approx 4.4$ nm, which corresponds to frequency shifts of $\Delta\nu^{(n)} \approx nc\,\Delta\lambda/\lambda^2 \approx n\times$ 2.90 THz and phase gradients of $k_{Spec}^{(n)} = \frac{2\pi}{c} n\Delta\nu \approx n\times 60.7\times 10^{-3}\mu\mathrm{m}^{-1}$. [3] Obviously the phase-gradient caused by this spectral ripple is an order of magnitude stronger than the one measured in our Two-Window longitudinal scans.

In the following we will compare the optical spectrum directly with the measured beat voltage. The optical power spectrum of a light field and its longitudinal correlation function are Fourier-transform related. With the knowledge of the spectrum, we can calculate the expected beat voltage $V_B(\Delta l)$ between a local oscillator beam and a Signal beam, which is directly proportional to the longitudinal correlation function:

$$V_B(\Delta l) \propto \gamma(\Delta l) \propto \int d\nu S(\nu) \exp(-2\pi i\nu\Delta l/c) \tag{9.21}$$

where $\gamma(\Delta l)$ is the longitudinal correlation function, $S(\nu)$ the optical power spectrum, and ν the optical frequency.

Figure 9.5a) shows the magnitude of the additional beat voltage $|V_B^{fri}(\Delta l)|$ (solid line) and its argument (dashed line) as a result of the ripple shown in Figure 9.4b). The amplitude of center-peak $|V_B^{fri}(0)|$ is a little more than 7% of the (not shown) Gaussian resulting from the Gaussian fit of the spectrum shown in Figure 9.4a). Obviously, for a given path-delay $\Delta l'_B$, $V_B(\Delta l')$=$V_B^*(-\Delta l')$ in order for

$$S(\nu) \propto \int d\Delta l V_B(\Delta l) \exp(2\pi i\nu\Delta l/c) \tag{9.22}$$

to be real. This means that the phase is an antisymmetric function of Δl_B, which

[3] The resolution of 0.5 nm is probably too small to reveal fringes of that order by deconvolution with the power spectrum of the HeNe-line, which, with its approx. 10^{-3} nm width, maps the response function of the Optical Spectrum Analyzer very accurately.

leads to a phase gradient close to zero path-delay, while its amplitude magnitude is symmetric. Even though the phase-gradient is obviously much stronger than the one observed in the z-scans, it might be possible that BLO and SLO interfere with two parts of the Signal beam which have a slightly different spectral composition, thereby causing a small phase-gradient in the complex beat signal $S_B(\Delta l) \propto V^*_{SLO} V_{BLO}$.

Figure 9.5b) shows the mean square beat signal $|V_B(\Delta l)|^2$ calculated from the measured spectrum with (solid line) and without (dashed line) ripple in the spectrum. From the e^{-1}-amplitude of the Gaussian fit of $|V_B(\Delta l)|^2$ a value of Δl_B=19.5 μm follows which is about 8% smaller than the values of 21.3 μm and 21.0 μm, determined by the spectral values provided by Superlum Co. and a single-LO z-scan in Section 6.2.1. This is probably due to the too small resolution of the optical spectrometer of 0.5 nm which broadens the measured spectrum and thereby decreases the resulting Δl_B.

9.2 Summary

The measurement of the longitudinal distance between the peaks in the out-of-phase signal, seen in Figure 9.1, enables the determination of the longitudinal coherence to within 17.6%. This method requires a linear phase-gradient but is independent of its magnitude as long as the phase-gradient is much smaller than the wavenumber of the light. The origin of the phase gradient observed in our experiment is unknown. It can not be explained by a narrow beam waist in either LO: The smallest values in our experiment for the Rayleigh length z_0 and the size of the beam waist w_0 are still an order of magnitude greater than those which would would cause the observed phase gradient.

A much stronger phase gradient could be caused by spectral ripple pattern. The phase-gradient we observe corresponds to a secondary peak in the spectrum of 0.46 nm next to the center peak. A measurement with an optical spectrometer with 0.5 nm resolution does not give any indication of such a peak though, but reveals a ripple spectrum with spacings of about 4.4 nm. The corresponding phase gradient, which is an order of magnitude larger than that measured by the z-scans, would only be observed if the LOs would interfere with two different peaks in the spectrum. Most likely though both LOs will interfere with parts of the Signal field of almost the same spectral composition, except for a small difference which could possibly cause the small phase gradient in the complex beat signal we observe.

The origin of the ripple in the spectrum itself is unknown; Superlum Co. gives a value of 1% for the residual spectral modulation, and a maximum of 5%. Judging from the peaks close to the center wavelength, the spectral modulation we measure is about 4%. Transverse modes in the SLD could be a possible explanation, in case the optical feedback is sufficiently high. Transverse modes differ by their spatial and angular profile, so that LO beams with different beam profiles would interfere with each mode to various extents, resulting in an overall phase-shift between the respective beat voltages. But, in order to avoid stimulated emission, optical feedback in SLDs is suppressed by anti-reflective coatings (reflectivity usually <0.01%, [51]) and a tilted or curved geometry of the active channel.

The pattern could also be caused by a parasitic Fabry-Perot interferometer of an optical length of $L = \frac{c}{2\Delta\nu}$=52 μm within (reflections in the semiconductor crystal) or immediately after the SLD itself (SLD glass window). The frequency-selection by a Fabry-Perot interferometer depends on the the angle of incidence, so that LOs with different angular spectra will interfere with different frequency-components of

the Signal beam, also resulting in a approximately linear phase-gradient parallel to scanning direction.

A more thorough investigation in a modified set-up could clarify the situation: A measurement with a high-resolution optical spectrum analyzer space-integrated over the beam profile should detect all side-peaks. Also, z-scans performed with two *small* local oscillator beams at a variable, pre-selected transverse distance, superposed with a collimated Signal beam, could potentially enable the mapping of the spatial distribution of spectral features. In lasers, such a measurement could be used to map the spatial profile and frequencies of transverse modes.

Chapter 10

Scattering theory

10.1 Introduction

Scattering in random media plays an important part in many fields of science. In meteorology, electromagnetic waves are used to measure the properties of the atmosphere by investigating the reflection off turbulent layers of air, rain, hail and snow. In oceanography, particles in the ocean and fish swarms can be detected and analyzed. In astronomy, scattering theory of light is used to model asteroid belts, the rings and outer layers of the gas planets in our solar system and the interior of stars. Another field where scattering theory plays an important role is biophysics, where many optical techniques exist to characterize biological tissue, in particular in-vivo, as described in Chapter 2. In some cases, scattering by cells is an unwelcome byproduct that can be suppressed by certain techniques. In other cases the scattered light is detected and analyzed in order to gain information about the scatterers themselves. In particular, the spatial and angular distribution of a field scattered from a skin layer can provide useful information about an architectural atypia of its skin cells, which is an indicator for or, for mild abnormalities, a potential precursor to skin cancer. This provides the grounds for a new diagnostic tool which might potentially replace the time-consuming and invasive biopsy of today. Scattering

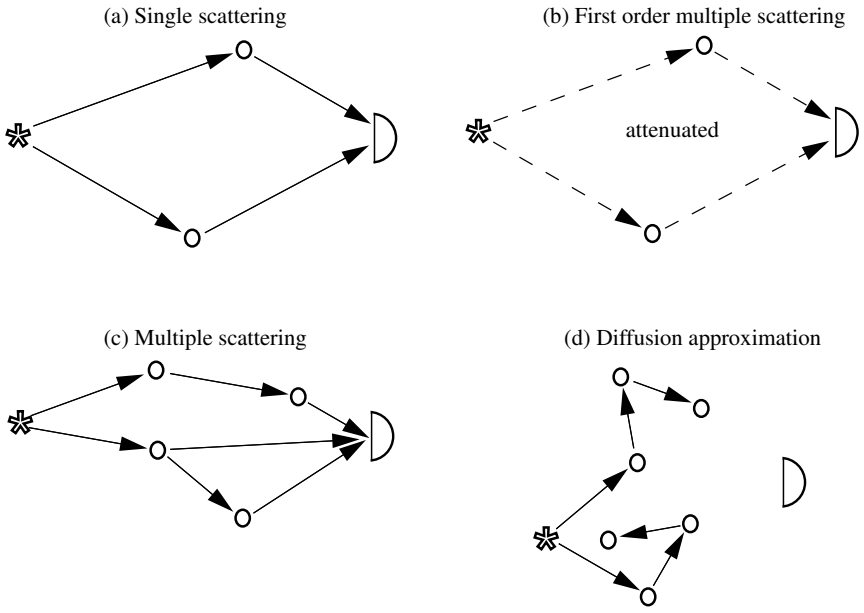

Figure 10.1: The various scattering regimes in random media. The light source is denoted by a star; the detector by a semi-circle.

theory is a vast and complex field and there exists no unique theory to describe and model all scenarios. Depending on the density and physical and geometrical properties of the scatterers and the surrounding medium, several approximations exist that provide exact results in many practical cases. Due to the advance of sufficiently fast computers, most of today's modelling in scattering theory has shifted to numerical calculations, in particular Monte Carlo computations.

Different types of scattering in random media are displayed in Figure 10.1. The scattering and propagation of waves in a tenuous distribution of scatters can be described by the *single scattering theory* (a). As the name indicates, one assumes that the light wave undergoes only one scattering event in the medium, which is oftentimes the case in the atmosphere or the ocean. This theory will be the subject of Section 10.2.

For tenuous to intermediate concentrations, the propagation of light can be

approximated by first-order multiple scattering (b) where also only one scattering event is considered but with the path to and from the scatterer weighted by an attenuation factor.

For intermediate concentrations, multiple scattering events are taken into account (c). One approach for this very complex problem is the *Transfer theory*, also called *theory of radiative transfer*, which focuses on the propagation of intensities at intermediate densities and provides a good approximation for many situations. This theory will be the described in Section 10.3.1. Another approach is the *Multiple Scattering theory*, which approximates the electric field by recursively integrating over a number of scattering events while omitting unlikely scattering sequences. This theory will be briefly summarized in Section 10.3.2.

For sufficiently dense distributions of scatterers and a scattering coefficient with low angular dependence, the propagation of photons can be approximated by a Markovian random-walk which means the intensity distribution is described by the isotropic diffusion equation (d). This diffusion theory will be presented in Section 10.4. Most practical examples in the diffusion-approximation regime display an incoherent light field emerging from the random medium, due to the rapid randomization of the fields phase and amplitude. There are some interesting coherent phenomena though, which have gained increasing attention since their realization in optical experiments in the beginning of the 1980s. They base on interference of waves counter-propagating through identical paths in the medium. The most important examples of this kind are *Anderson localization* and *Enhanced backscattering*, the latter of which is an important part of this thesis. They are described in Chapter 11.

10.2 Single-scatter theory

Most scatterers can be approximated by spheres, especially when they appear in great numbers and random orientations. All single-scattering approximations presented in the following calculate the far-field of the secondary field generated in a sphere by an incident flat wave. Depending on the size and relative index of refraction of the sphere there are many approximations. A good reference for a detailed treatment is [52]. In the following I will briefly describe the idea and the most important results of each approximation.

10.2.1 Rayleigh scattering

Rayleigh scattering describes the case where the size of a particle is much smaller than a wavelength. Let us again assume this particle to be a dielectric sphere. In that case, at each instant in time the electric field within and near the particle can be approximated by an electrostatic field. The scattered field then corresponds to that of regular dipole. The differential cross-section is proportional to the square of the volume and inversely proportional to the fourth power of the wavelength. The latter is responsible for the blue sky, because blue light scatters more than red light. Contrary to early beliefs, the molecules of air itself contribute to Rayleigh scattering, not only water and ice particles. The Rayleigh scattering cross section approximation is exact within 4% of the true value if the size of the particle is smaller then 0.05λ [53].

10.2.2 Born approximation

The Born approximation, also known as Raleigh-Debye scattering, applies to scatterers whose relative dielectric constant is close to unity:

$$[\epsilon_r(\vec{r}) - 1]kD \ll 1, \tag{10.1}$$

where D is the diameter of the particle and k the wavenumber. In this case the electric field inside the particle is approximated by the incident field. The resulting scattering amplitude takes on a very simple form; it is directly proportional to the Fourier transform of $\epsilon_r(\vec{r}) - 1$ as a function of the change in momentum during the scattering process.

10.2.3 WKB interior wave number approximation

In the WKB approximation the field inside the particle is approximated as the incident field propagating with the medium's propagation constant without changing direction on entry into the medium. The transmission coefficient is assumed to be that for normal incidence. The necessary conditions for this approximation are

$$[\epsilon_r(\vec{r}) - 1]kD \gg 1 \tag{10.2}$$

$$\epsilon_r(\vec{r}) - 1 < 1. \tag{10.3}$$

The calculated absorption cross sections in this approximation are usually a little larger than the true value.

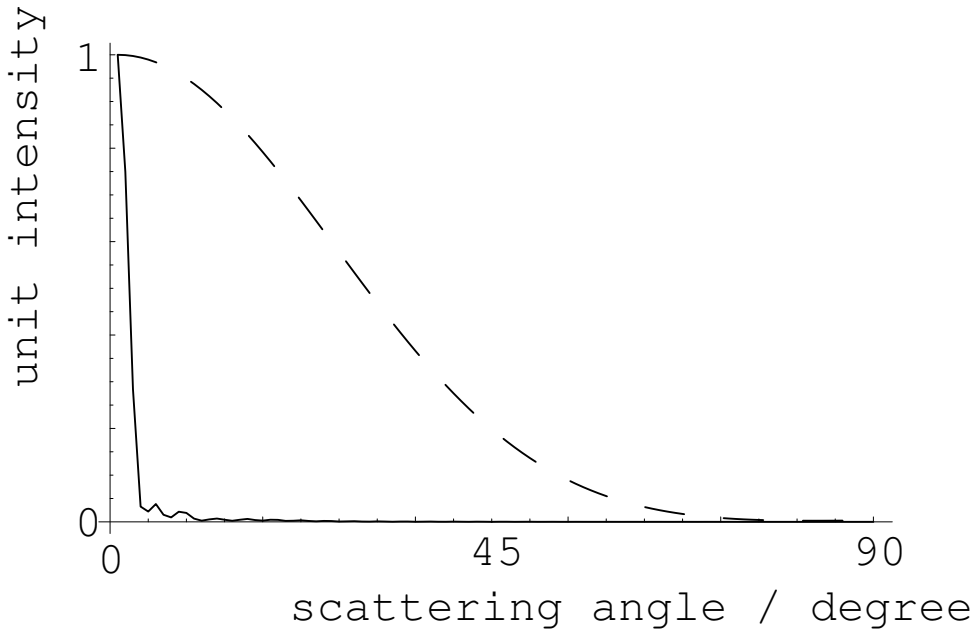

Figure 10.2: Scattered normalized intensity as a function of angle for λ=678.3 nm. Solid line: 9.9 μm diameter spheres, dashed line: 0.5 diameter μm spheres.

10.2.4 Mie Theory

The Mie theory is the exact solution for scattering of a plane electromagnetic wave by an isotropic, homogeneous sphere. It calculates the electric and magnetic fields inside the sphere using the Maxwell equations together with the appropriate boundary conditions. The calculations and resulting expressions are quite lengthy; for practical calculations of scattering parameters of our polystyrene spheres, we use a Fortran program from the book 'Absorption and Scattering of Light by Small Particles' by Bohren and Huffman (p. 477, [54]).

Figure 10.2 shows the scattered intensity as a function of angle for the two types of spheres we use. The 0.5 μm diameter spheres are on the order of a wavelength of the light we use (678.3 nm), therefore the angular spread of the scattered light is much larger than for the 10 μm spheres. The average cosine of the angular spread

for a 0.5 μm sphere is $\langle \cos\theta \rangle = 0.805$, for a 10 μm sphere it is $\langle \cos\theta \rangle = 0.901$.

Due to diffraction, the scattering cross-section of our spheres deviates from the 'classical' cross-section that would be expected for particles. This is taken into account by a correction factor Q_{sca} so that the true cross section is $Q_{sca}\pi r_{sph}^2$. For 0.5 μm diameter spheres, $Q_{sca} = 0.515$, resulting in a scattering cross-section of σ_s=0.101 μm^2, for 10 μm diameter spheres $Q_{sca} = 1.993$, leading to a cross-section of σ_s=156.5 μm^2.

10.3 Multiple Scattering

10.3.1 Transfer theory

Transfer theory, also called radiative transfer theory, is appropriate in the multiple-scattering regime (see Figure 10.1(c)). It deals with the transport of energy in random media containing particles and does not include interference or diffraction effects, except for those affecting the single particle scattering characteristics. Also, no correlation between fields is assumed, allowing for the superposition of intensities. Transfer theory produces a differential equation, commonly referred to as *equation of transfer*, which is equivalent to Boltzmann's equation. The specific intensity $I(\vec{r}, \hat{s})$ is the quantity propagated in Transfer theory; it is the intensity per solid angle and frequency at a given position and is measured in $\frac{W}{m^2\, sr\, Hz}$.

The general form of the equation of transfer is

$$\frac{dI(\vec{r}, \hat{s})}{ds} = -\rho\sigma_t I(\vec{r}, \hat{s}) + \frac{\rho\sigma_t}{4\pi}\int_{4\pi} p(\hat{s}, \hat{s}')I(\vec{r}, \hat{s})d\omega + \epsilon(\vec{r}, \hat{s}) \tag{10.4}$$

which describes the change of $I(\vec{r}, \hat{s})$ as it travels along a path ds. The first term on the right-hand side describes the attenuation, which is proportional to the den-

sity of scatterers ρ and their total cross-section σ_t, which includes absorption and scattering. The second term describes light scattered into the path of propagation from all directions. It is proportional to $\rho\sigma_s$ since it is the scatterers in the path of propagation that deflect the light. It is also proportional to the integral over the specific intensities coming from all directions weighted by the *phase-function* $p(\hat{s}, \hat{s'})$ which is the probability for a photon to be scattered from direction $\hat{s}'$ into direction $\hat{s}$. The final term describes a potential source term. An exact analytical solution is possible only for certain simple geometries and phase-functions. In cases where the volume density is less then 0.1%, the second term can be simplified by assuming that the light going to be scattered into the path $\hat{s}$ has to come from the reduced incident intensity itself, rather than from diffuse light coming from all directions.

10.3.2 Twersky's theory

Twersky's integral is an iterative method where the field incident on a scatterer is expressed as the field incident on the sample plus the field scattered from all other scatterers [52]. The field scattered from that scatterer is in turn used to calculate the field incident on all other scatterers. In order to simplify the iteration procedure, certain unlikely scattering sequences are neglected. For practical calculations, the sums are replaced by integrals.

10.4 Diffusion theory

For volume densities much greater than 1%, which is the case for all samples we use for enhanced backscattering, the diffusion approximations provides good results. The assumption here is that the diffuse intensity is scattered almost uniformly in

all directions, with a small overall flux in a direction $\hat{s}$. This can be expressed as

$$I_d(\vec{r},\hat{s}) \propto U_d(\vec{r}) + c\vec{F}_d(\vec{r})\cdot\hat{s}, \tag{10.5}$$

where $U_d(\vec{r}) = \frac{1}{4\pi}\int_{4\pi} d\omega\, I_d(\vec{r},\hat{s})$ is the average diffuse intensity and $\vec{F}_d(\vec{r}) = \int_{4\pi} d\omega\,\hat{s}\, I_d(\vec{r},\hat{s})$ is the diffuse flux vector. From the equation of transfer, the diffusion equation can then be derived:

$$\nabla^2 U_d(\vec{r}) + 3\rho^2\sigma_{tr}[\sigma_s U_{ri}(\vec{r}) - \sigma_a U_d(\vec{r})] = -\frac{3}{4\pi}\rho\sigma_{tr}E(\vec{r}) + \frac{3}{4\pi}\nabla\cdot\int_{4\pi} d\omega\,\epsilon(\vec{r},\hat{s})\,\hat{s}, \tag{10.6}$$

where σ_{tr} is the absorption cross section σ_a plus the scattering cross-section σ_s corrected for anisotropic scattering and the ratio of the volume occupied by scatterers to the total volume. $E(\vec{r})$ is the angle-integrated source-function and $\epsilon(\vec{r},\hat{s})$ the source-terms due to the ballistic part of the incident field as well as additional sources. Since the diffusion equation only holds if the light if sufficiently diffuse, it is valid only far from the boundary and the source. Mathematically, this manifests itself as follows: The boundary condition at a surface of a dense turbid medium, $I_d(\vec{r},\hat{s}) = 0$ when $\hat{s}$ is pointed inwards can not be fulfilled because the diffusion equation describes the scalar field U rather then a vector field. Therefore, this boundary condition needs to be replaced by one of the many approximations that exist in that case. One of them requires that the total diffuse flux inwards be zero:

$$\int_{2\pi} d\omega\, I_d(\vec{r},\hat{s})\,(\hat{s}\cdot\hat{n}) = 0 \tag{10.7}$$

where $\hat{n}$ is a unit vector normal to the surface and pointing inwards. Depending on the anisotropy of the scatterers, this boundary condition takes on different forms for

the average diffuse intensity U. For special practical cases this boundary condition simplifies. One example is the so-called Milne problem: For a semi-infinite slab containing isotropic scatterers, an exact solution can be derived [52]. We will discuss the time-dependent diffusion equation and present a solution for the Milne case in Section 11.3. This section deals with the probability density for photon migration which is proportional to the intensity of the light field.

In the following chapter I will describe *Enhanced backscattering*, which manifests itself in the diffusion approximation regime but is nevertheless a coherent effect.

Chapter 11

Enhanced Backscattering (EBS) Theory

11.1 Introduction

Random media can display unusual phenomena regarding the transport of particles, such as electrons and photons, caused by their wave nature. The best known might be Anderson localization. In solid-state physics, this is a disorder-induced phase transition in the electron-transport behavior from the classical diffusion regime, in which the Ohm's law holds, to a localized state in which the material behaves as an insulator [55]. The same effect can be observed for photons in very dense random media, in which case the localization is not disturbed by mutual interaction between the particles as in the case for electrons. Figure 11.1 visualizes the effect for the latter case: From a light source in a random medium, denoted by a star, a wavelet travels along a path through several scattering events back to the source. Another wavelet, travelling the same path from the opposite direction, will have the same phase and therefore interfere constructively with the first wavelet at the position of the light source. As a consequence, the probability of the wave-field propagating away from the light source will be decreased compared to the probability of returning to it. For strong enough scattering, light incident on a slab of random media will be

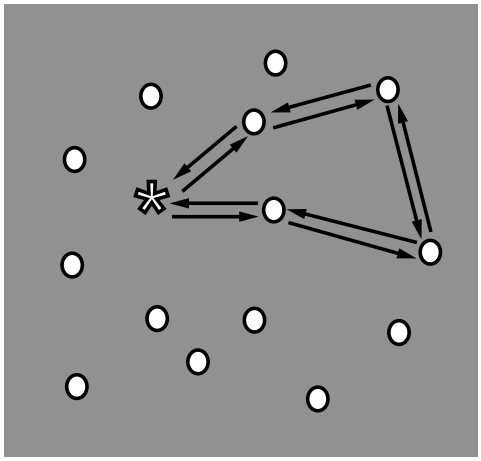

Figure 11.1: Anderson localization in a random medium. A random light path beginning and ending at the light source (denoted by a star) is followed in two opposite directions, leading to constructive interference of the counter-propagating wavelets. This effect inhibits diffusion away from the light source: it causes localization of the light field.

almost entirely reflected. While the diffusive light intensity in the classical regime decreases linearly with the the thickness of such a slab, it decreases exponentially in the localized regime. In the transition between the regimes, the dependence might be quadratic [56, 57]. According to the (modified) Ioffe-Regel criterion, localization is expected for $kl \leq 1$ [58], where k is the wave-vector of the light field and l the mean free path in the random medium. In this case, the field can not perform a single oscillation before being scattered again.

Enhanced backscatter is a precursor to Anderson localization and is often called 'weak localization' [59,60]. It can be observed for much less dense random media, in our case on the order of $kl \approx 8$, which is still in the classical diffusion regime. Figure Figure 11.2 illustrates the enhanced backscattering effect: A light beam is incident on a highly scattering random medium. As in the case of Anderson localization, two wavelets travelling the same path in the medium, but from opposite directions,

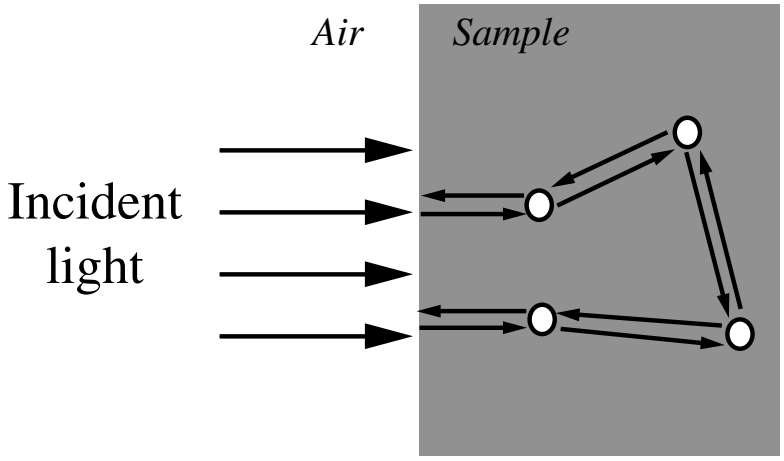

Figure 11.2: Enhanced backscattering in a random medium. The backscattered light is twice as intense in the direction of the beam, due to constructive interference of counter-propagating wavelets along a path in the random medium.

interfere constructively, resulting in an reflective intensity in the opposite direction of the incoming beam twice as high as in other directions. This is due to the fact that the amplitudes of the counter-propagating wavelets add up rather than the intensities.

11.2 Wigner function of an EBS field

In this section we will first derive the Enhanced Backscattered field as a function of the incident field in terms of mutual coherence functions in momentum Section 11.2.1. After discussing basic properties (Section 11.2.2) and the circumstances where breakdown of EBS occurs (Section 11.2.3), we will derive the corresponding time-resolved Wigner functions of the EBS field, which are Fourier-transform related to the mutual coherence functions derived in Section 11.2.1.

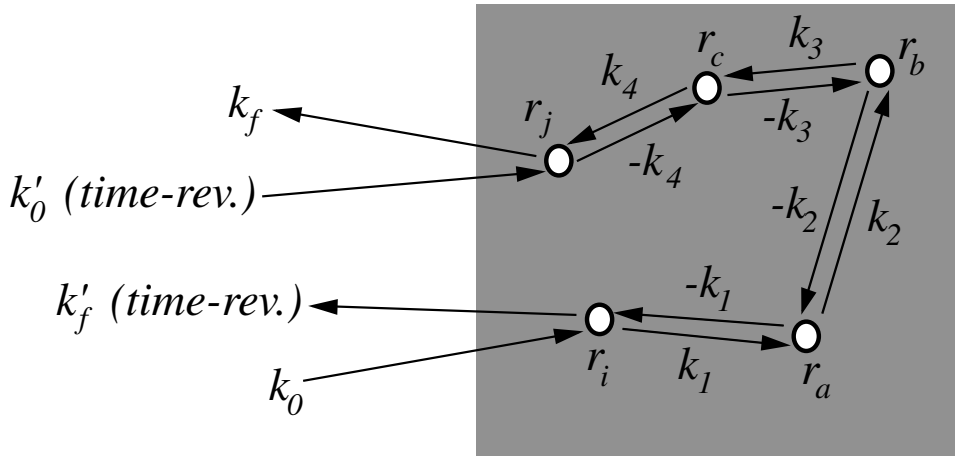

Figure 11.3: Random path and its time-reversed counterpart in a random medium for an arbitrary incident wave: the rays $\vec{k}_0$ and $\vec{k}_0'$ which are incident on $\vec{r}_i$ and $\vec{r}_j$ are no longer parallel, their amplitude is no longer equal. The outgoing field $\vec{k}_f$ and $\vec{k}_f'$ becomes space-dependent and can no longer be fully described by a momentum-dependent intensity only.

11.2.1 Mutual coherence function of an EBS field

Figure 11.3 shows the intricacies of enhanced backscattering in more detail: the incoming field with wave-vector $\vec{k}_0$ is incident on scatterers located at $\vec{r}_i$ and $\vec{r}_j$ in a sample of random medium. We assume all scatterers in the sample to be point-like and lossless. The relation between the momentum component of the field scattered by a single scatterer $\vec{k}$ and of the incident field $\vec{k}'$ can be described by a scattering matrix.[1] For the simple case of elastic scattering off a point scatterer at position $\vec{r}$, the scattering matrix $S_{k,k'}(r)$ can be approximated by a position dependent phase shift, weighted by a term describing the angular dependence:

$$S_{\vec{k},\vec{k}'}(\vec{r}) = S_{\vec{k},\vec{k}'} e^{i(\vec{k}'-\vec{k})\cdot\vec{r}} \tag{11.1}$$

[1]Here and in the following a prime $'$ will mark fields and rays before scattering.

$S_{\vec{k}',\vec{k}}=S_{-\vec{k},-\vec{k}'}$ is time-reversal invariant, which means that the scattering characteristics remain unchanged if we interchange incoming and outgoing wavevectors. The amplitude of the field following a ray path with wavevector $\vec{k}_0$ which scatters first at $\vec{r}_i$ and exits with wavevector $\vec{k}_f$ after scattering at $\vec{r}_j$ is therefore given by

$$\begin{aligned} A_j &= S_{\vec{k}_f\vec{k}_4}S_{\vec{k}_4\vec{k}_3}S_{\vec{k}_3\vec{k}_2}S_{\vec{k}_2\vec{k}_1}S_{\vec{k}_1\vec{k}_0} \\ &\times e^{i\vec{r}_j\cdot(\vec{k}_4-\vec{k}_f)+i\vec{r}_c\cdot(\vec{k}_3-\vec{k}_4)+i\vec{r}_b\cdot(\vec{k}_2-\vec{k}_3)+i\vec{r}_a\cdot(\vec{k}_1-\vec{k}_2)+i\vec{r}_i\cdot(\vec{k}_0-\vec{k}_1)}A'_i \qquad (11.2) \\ &= \mathcal{P}_{i,j}(\alpha)e^{i(\vec{k}_0\cdot\vec{r}_i-\vec{k}_f\cdot\vec{r}_j)}A'_i \qquad (11.3) \end{aligned}$$

where A'_i and A_j are the complex amplitudes of the ray incident at $\vec{r}_i$ and exiting at $\vec{r}_j$,

$$\mathcal{P}_{j,i}(\alpha) = S_{\vec{k}_f\vec{k}_4}S_{\vec{k}_4\vec{k}_3}S_{\vec{k}_3\vec{k}_2}S_{\vec{k}_2\vec{k}_1}S_{\vec{k}_1\vec{k}_0}e^{i\vec{k}_4\cdot(\vec{r}_j-\vec{r}_c)+i\vec{k}_3\cdot(\vec{r}_c-\vec{r}_b)+i\vec{k}_2\cdot(\vec{r}_b-\vec{r}_a)+i\vec{k}_1\cdot(\vec{r}_a-\vec{r}_i)}. \quad (11.4)$$

and α denotes the sequence of scatterers at locations $\vec{r}_i$, $\vec{r}_a$...$\vec{r}_c$, $\vec{r}_j$ that determine the path and the direction of travel in the medium. $\mathcal{P}_{j,i}(\alpha) = |\mathcal{P}_{j,i}(\alpha)|\exp(i\phi_{j,i})$ is called an probability *amplitude* by some authors [61] since it is a measure for the probability that a given loop between $\vec{r}_i$ and $\vec{r}_j$ has acquired a phase $\phi_{i,j}$ and its square magnitude enters the intensity.

Similarly, the ray entering at $\vec{r}_j$ and exiting at $\vec{r}_i$, i.e. the ray counter-propagating the one in Eq. (11.3) is given by

$$
\begin{aligned}
A_i &= S_{\vec{k_f}-\vec{k}_1} S_{-\vec{k}_1-\vec{k}_2} S_{-\vec{k}_2-\vec{k}_3} S_{-\vec{k}_3-\vec{k}_4} S_{-\vec{k}_4\vec{k_0}} \\
&\times e^{i\vec{r_i}\cdot(-\vec{k}_1-\vec{k_f})+i\vec{r_a}\cdot(-\vec{k}_2+\vec{k_1})+i\vec{r_b}\cdot(-\vec{k}_3+\vec{k_2})+i\vec{r_c}\cdot(-\vec{k}_4+\vec{k_3})+i\vec{r_j}\cdot(\vec{k_0}+\vec{k_4})} A'_j \qquad (11.5) \\
&= \mathcal{P}_{i,j}(\alpha_T) e^{i(\vec{k_0}\cdot\vec{r_j}-\vec{k_f}\cdot\vec{r_i})} A'_j \qquad (11.6)
\end{aligned}
$$

where A_i, A'_j and $\mathcal{P}_{i,j}(\alpha_T)$ are defined accordingly, with α_T denoting the same scatterer sequence as α, travelled from the opposite direction. By comparison of the phase-terms defining $\mathcal{P}_{i,j}$ and $\mathcal{P}_{j,i}$ it can be seen that $\mathcal{P}_{i,j}(\alpha_T)$=$\mathcal{P}_{j,i}(\alpha)$.

The mutual coherence function in momentum space resulting from all loops is the sum of Equations (11.3) and (11.6), summed over all possible starting points, paths and incident wavevectors:

$$
\begin{aligned}
\langle \mathcal{E}^*(\vec{k}_{f1}) \mathcal{E}(\vec{k}_{f2}) \rangle &= \sum_{i,j,\alpha,\vec{k}_{01}} \mathcal{P}_{j,i}(\alpha) \mathcal{E}_0(\vec{k_{01}}) e^{i(\vec{k_{01}}\cdot\vec{r_i}-\vec{k_{f1}}\cdot\vec{r_j})} \\
&\times \sum_{l,m,\alpha',\vec{k}_{02}} \mathcal{P}^*_{l,m}(\alpha') \mathcal{E}^*_0(\vec{k_{02}}) e^{-i(\vec{k_{02}}\cdot\vec{r_m}-\vec{k_{f2}}\cdot\vec{r_l})} \qquad (11.7) \\
&= \sum_{i,j,\alpha,\vec{k}_{01}} \sum_{l,m,\alpha',\vec{k}_{02}} \langle \mathcal{P}_{j,i}(\alpha) \mathcal{P}^*_{l,m}(\alpha') \rangle \langle \mathcal{E}_0(\vec{k_{01}}) \mathcal{E}^*_0(\vec{k_{02}}) \rangle \\
&\times \exp\{i(\vec{k}_{01}\cdot\vec{r}_i - \vec{k}_{f1}\cdot\vec{r}_j) - i(\vec{k}_{02}\cdot\vec{r}_m - \vec{k}_{f2}\cdot\vec{r}_l)\} \qquad (11.8)
\end{aligned}
$$

where we replaced the vectors A by electric fields $\mathcal{E}$(k). $\mathcal{E}(k_{01})$ and $\mathcal{E}(k_{02})$ describe the incoming field, $\mathcal{E}(k_{f1})$ and $\mathcal{E}(k_{f2})$ the outgoing field. The incoherent part represents the case where both electrical fields undergo the same sequence of scattering in the same direction, i.e. $i = m$, $j = l$, $\alpha = \alpha'$. In this case Eq. (11.8) reduces to

$$\langle \mathcal{E}^*(\vec{k}_{f1})\mathcal{E}(\vec{k}_{f2})\rangle_{incoh} = \sum_{i,j,\alpha,\vec{k}_{01},\vec{k}_{02}} \langle|\mathcal{P}_{j,i}(\alpha)|^2\rangle\langle|\mathcal{E}_0^*(\vec{k}_{01})\mathcal{E}_0(\vec{k}_{02})\rangle \times \exp\{i[(\vec{k}_{02}-\vec{k}_{01})\cdot\vec{r}_i-(\vec{k}_{f2}-\vec{k}_{f1})\cdot\vec{r}_j]\} \quad (11.9)$$

For the coherent part, the electrical fields go exactly opposite directions so that $i = l$, $j = m$ and $\mathcal{P}_{ij}(\alpha_T) = \mathcal{P}_{ji}(\alpha)$, so that

$$\langle \mathcal{E}^*(\vec{k}_{f1})\mathcal{E}(\vec{k}_{f2})\rangle_{coh} = \sum_{i,j,\alpha,\vec{k}_{01},\vec{k}_{02},\alpha} \langle|\mathcal{P}_{j,i}(\alpha)|^2\rangle\langle|\mathcal{E}_0^*(\vec{k}_{01})\mathcal{E}_0(\vec{k}_{02})\rangle \times \exp\{i[(\vec{k}_{02}+\vec{k}_{f1})\cdot\vec{r}_i-(\vec{k}_{f2}+\vec{k}_{01})\cdot\vec{r}_j]\}. \quad (11.10)$$

All other contributions for arbitrary i, j, l, m, excluding Equations (11.9) and (11.10), are responsible for a speckle pattern, which can be observed for stationary scatterers and masks the enhanced backscatter peak. The speckle have a characteristic width $\Delta\theta_{Sp} \propto \lambda/L_0$, where L_0, for limited-sized beams, is on the order of the size of the coherence area or illuminated area, whichever is smaller. In the introduction to this thesis, Chapter 1, we showed the Wigner function of a single speckle coming from a piece of glass containing air bubbles. In the current setup, the scattering polystyrene spheres which are suspended in a solution, are subject to Brownian motion, so the speckle averages out and can therefore be neglected.

Before we go on with this calculation, let us consider the special case where a plane wave is incident normal to the surface ($\vec{k}_{01} = \vec{k}_{02} \equiv \vec{k}_0$) and we measure the intensity as a function of angle ($\vec{k}_{f1} = \vec{k}_{f2} \equiv \vec{k}_f$). In this case, Equations (11.9) and (11.10) reduce to

$$\langle|\mathcal{E}(\vec{k_f})|^2\rangle_{incoh} = \sum_{\alpha,i,j}\langle|\mathcal{P}_{j,i}(\alpha)|^2\rangle\langle|\mathcal{E}_0(\vec{k}_0)|^2\rangle \tag{11.11}$$

$$\langle|\mathcal{E}(\vec{k_f})|^2\rangle_{coh} = \sum_{\alpha,i,j}\langle|\mathcal{P}_{j,i}(\alpha)|^2\rangle\langle|\mathcal{E}_0(\vec{k}_0)|^2\rangle\cos[(\vec{k}_0+\vec{k}_f)\cdot\vec{r}_i-(\vec{k}_f+\vec{k}_0)\cdot\vec{r}_j], \tag{11.12}$$

yielding a total squared field of

$$\begin{aligned}\langle|\mathcal{E}(\vec{k_f})|^2\rangle &= \sum_{\alpha,i,j}\langle|\mathcal{P}_{j,i}(\alpha)|^2\rangle\langle|\mathcal{E}_0(\vec{k}_0)|^2\rangle \\ &\times \quad (1+\cos[(\vec{k}_0+\vec{k}_f)\cdot\vec{r}_i-(\vec{k}_f+\vec{k}_0)\cdot\vec{r}_j]),\end{aligned} \tag{11.13}$$

which displays the well known $(1+\cos[(\vec{k}_0+\vec{k}_f)\cdot\vec{r}_i-(\vec{k}_f+\vec{k}_0)\cdot\vec{r}_j])$-factor observed in intensity measurements of collimated beams [59, 62, 63]. This factor becomes 2 when $k_0{=}{-}k_f$.

The width and length of the sample as well as the spatial characteristics of the incident beam are generally large compared to the mean free path, so we can treat the medium as semi-infinite. Then it is convenient to replace the sums in Eq. (11.8) by integrals. For a given set of scatterers close to the surface at $\vec{r}_i$ and $\vec{r}_j$, the sum of the probabilities $\langle|\mathcal{P}_{i,j}(\alpha)|^2\rangle$ over all possible loops $\alpha(\vec{r}_i,\vec{r}_j)$ joining these scatterers can be replaced by an integral over a probability density $P(\vec{r}_j-\vec{r}_i,t)$:[2]

[2]We directly assume P to be a function of the difference between $\vec{r}_j$ and $\vec{r}_i$, which is justified in a semi-infinite random medium with homogeneous concentration of scatterers.

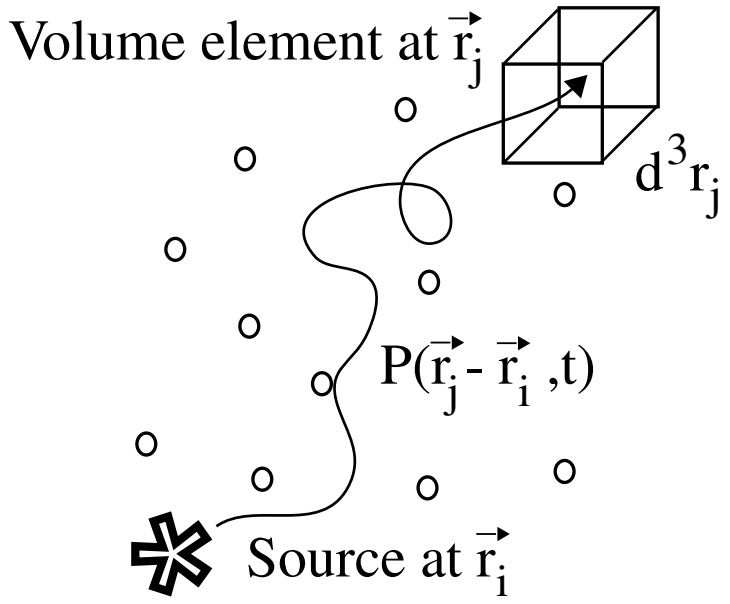

Figure 11.4: $P(\vec{r}_j - \vec{r}_i, t)d^3r_j$ is the probability for a photon emitted by a source at $\vec{r}_i$ to reach the volume element at $\vec{r}_j$ in time t.

$$\sum_\alpha \langle |\mathcal{P}_{i,j}(\alpha)|^2 \rangle \rightarrow$$
$$P(\vec{r}_j - \vec{r}_i, t)\, d^2\vec{r}_{j\perp}\, dz_j \times \tfrac{n_{Scatt}(\vec{r}_{i\perp}, z_i)}{N}\, d^2\vec{r}_{i\perp}\, dz_i \times \exp(-\tfrac{z_j}{\mu_j l} - \tfrac{z_i}{\mu_i l}). \tag{11.14}$$

$P(\vec{r}_j - \vec{r}_i, t)\, d^2\vec{r}_j\, dz_j$ is the probability of a photon that was at $(\vec{r}_i, z_i)$ at time t=0 to reach $(\vec{r}_j, z_j)$ at time t, as depicted in Figure 11.4. The probability that a photon is emitted in volume element $d^2r_i\, dz_i$ at $(\vec{r}_i\, z_i)$ is proportional to the number of scatters in that element, which is $n_{Scatt}(\vec{r}_i, z_i)d^2r_i\, dz_i$, where $n_{Scatt}(\vec{r}_i, z_i)$ is the local density of scatterers.

The factor $\exp(-\frac{z_j}{\mu_j l})$ describes the probability of a photon to not scatter until it reaches depth z_i, $\exp(-\frac{z_j}{\mu_i l})$ is the corresponding probability until the photon

reaches the surface after scattering at depth z_j. l is the scattering mean free path and μ_j and μ_i are the projections of the direction unit vectors of k_j and k_i on the z-axis, assuming close to perpendicular incidence and emergence of the beam[3]. We will incorporate this factor into P later on and therefore neglect displaying it for now.

We will postpone the derivation of an expression for $P(\vec{r}_j - \vec{r}_i, t)$ to Section 11.3. The quantitatively exact integral form of Eq. (11.8), i.e., the correct prefactor, is still subject to debate. The qualitatively correct expression follows from combining Equations (11.8) and (11.14):

$$\begin{aligned}
\langle \mathcal{E}^*(\vec{k}_{f1}) \mathcal{E}(\vec{k}_{f2}) \rangle_{Back} &= \int d^3 r_i \, d^3 r_j \, P(\vec{r_j} - \vec{r_i}, t) \\
&\times \int d^3 k_{01} \, d^3 k_{02} \, \langle \mathcal{E}_0^*(\vec{k}_{01}) \mathcal{E}(\vec{k}_{02}) \rangle \\
&\times \Big\{ \exp\left[i(\vec{k}_{02} + \vec{k}_{f1}) \cdot \vec{r_i} - i(\vec{k}_{f2} + \vec{k}_{01}) \cdot \vec{r_j} \right] \\
&+ \exp\left[i(\vec{k}_{02} - \vec{k}_{01}) \cdot \vec{r_i} - i(\vec{k}_{f2} - \vec{k}_{f1}) \cdot \vec{r_j} \right] \Big\} \quad (11.15)
\end{aligned}$$

where we omitted constant prefactors.

11.2.2 Basic properties of an EBS field

The angular distribution of the intensity of the backscattered field as shown in Eq. (11.13) is centered around the opposite direction of incidence ($\vec{k}_f = -\vec{k}_i$), where the cosine is one. In this direction, the intensity is twice as big as the incoherent

[3]Actually the distance travelled by the wavelets before and after the scattering events differs for a given path and its time-reversed counterpart [64], which is negligible in the small angle regime we are interested in. Therefore we just take one set of $\mu_{i,j}$ for both parts. Later on, we assume $\mu \approx 1$.

background. The angular width of the Enhanced Backscatter peak depends on the path lengths in the medium contributing to the enhanced backscatter effect and is, for a given path length, approximately [62]

$$\theta_c = \frac{\lambda}{2\pi\sqrt{Dt}} \tag{11.16}$$

Here, D is the diffusion constant of the photon migrating in the medium and t the time passed after its incidence; $\sqrt{Dt}$ therefore is the typical distance of diffusion.

11.2.3 Breakdown of Enhanced Backscattering

There are many ways enhanced backscattering can break down. When the scatterers move so fast that during the time the light needs to travel a given path, the path-length changes by more than half the light's wavelength, the wavelets coming from opposite directions will not interfere constructively. In that case the EBS effect is no longer observable. This does not pose a problem in our experiment though; even with our smallest scatterers the comparably slow Brownian motion would require a path length of the light in the medium of 3 meters [62] in order to destroy the symmetry between counter-propagating wavelets, which is orders of magnitude more than the submillimeter path-length we employ.

Other methods of destroying the Enhanced Backscatter effect break the symmetry between co- and counter-propagating waves. This works for example for electrons, which are subjected to a magnetic field [55], but they have also been experiments in the optical regime exploiting the Faraday effect [65].

11.2.4 Time-resolved Wigner function of an EBS field

The Wigner function formalism offers an attractive framework to describe Enhanced Backscattering since it includes angular- and position information as well as phase information. In this section, the time-resolved Wigner function of the backscattered scalar field for a given incident light field will be derived. We again assume the case of a light beam incident on the surface of a semi-infinite random medium. This time we employ broadband light though, which enables us to selectively measure the contributions by paths in the medium of a given length. The random medium shall again consist of non-absorbing point-like scatterers.

We can transform the relation between the mutual coherence functions for the incident and exiting fields in Eq. (11.15) into a relation between Wigner functions, since the angular mutual coherence function is Fourier-transform related to the Wigner function, as pointed out in Chapter 3:

$$W(\vec{x},\vec{p}) = \int \frac{d^3q}{(2\pi)^3}\ \exp(i\vec{x}\cdot\vec{q})\ \langle \mathcal{E}^*(\vec{p}+\frac{\vec{q}}{2})\mathcal{E}(\vec{p}-\frac{\vec{q}}{2})\rangle \tag{11.17}$$

Solving for the mutual coherence function in momentum space yields:

$$\langle \mathcal{E}^*(\vec{p}+\frac{\vec{q}}{2})\mathcal{E}(\vec{p}-\frac{\vec{q}}{2})\rangle = \int d^3x\ \exp(-i\vec{q}\cdot\vec{x})W(\vec{x},\vec{p}). \tag{11.18}$$

We then define $\vec{k}_{01} = \vec{p}_1 - \vec{q}_1/2$, $\vec{k}_{02} = \vec{p}_1 + \vec{q}_1/2$ for the incident field and $\vec{k}_{f1} = \vec{p}_2 - \vec{q}_2/2$, $\vec{k}_{f2} = \vec{p}_2 + \vec{q}_2/2$ for the backscattered field in Eq. (11.15). This transformation has a Jacobian of unity so that $d^3k_{01}\,d^3k_{02} = d^3p_1\,d^3q_1$ and $d^3k_{f1}\,d^3k_{f2} = d^3p_2\,d^3q_2$. Replacing $\langle \mathcal{E}^*(\vec{k}_{01})\mathcal{E}(\vec{k}_{02})\rangle$ in Eq. (11.15) and integrating both sides according to Eq. (11.17) yields

$$
\begin{aligned}
W_{Back}(\vec{x},\vec{p}) &= \int d^3\vec{r}_i\, d^3\vec{r}_j\, P(\vec{r_j}-\vec{r_i},t) \\
&\times \int \frac{d^3q_2}{(2\pi)^3}\, \exp(i\vec{x}\cdot\vec{q_2}) \\
&\times \int d^3p_1\, d^3q_1 \int d^3x'\, \exp(-i\vec{q_1}\cdot\vec{x}')W_0(\vec{x}',\vec{p}_1) \\
&\times \{\exp(i\vec{q_1}\cdot\vec{r_i}-i\vec{q_2}\cdot\vec{r_j}) \\
&+ \exp\left[i\left(\vec{p_1}+\vec{p_2}+\frac{\vec{q_1}-\vec{q_2}}{2}\right)\cdot\vec{r_i}-i\left(\vec{p_1}+\vec{p_2}+\frac{\vec{q_2}-\vec{q_1}}{2}\right)\cdot\vec{r_j}\right]\Big\}
\end{aligned}
\tag{11.19}
$$

with the first exponential in the bottom line still the coherent and the second exponential the incoherent part. The integrals with respect to $\vec{q_1}$ and $\vec{q_2}$ contain only complex exponentials and can be directly solved, yielding delta functions for the incoherent part (Equations (11.20),(11.21)) and coherent part (Equations (11.22),(11.23)):

$$
\int d^3q_2\, \exp[i\vec{q_2}\cdot(\vec{x}-\vec{r_j})] = (2\pi)^3\delta(\vec{r_j}-\vec{x}) \tag{11.20}
$$

$$
\int d^3q_1\, \exp[i\vec{q_1}\cdot(\vec{r_i}-\vec{x}')] = (2\pi)^3\delta(\vec{r_i}-\vec{x}') \tag{11.21}
$$

$$
\int d^3q_2\, \exp\left[i\vec{q_2}\cdot\left(\vec{x}-\frac{\vec{r_i}+\vec{r_j}}{2}\right)\right] = (2\pi)^3\delta\left(\vec{x}-\frac{\vec{r_i}+\vec{r_j}}{2}\right) \tag{11.22}
$$

$$
\int d^3q_1\, \exp\left[i\vec{q_1}\cdot\left(-\vec{x}'+\frac{\vec{r_i}+\vec{r_j}}{2}\right)\right] = (2\pi)^3\delta\left(\vec{x}'-\frac{\vec{r_i}+\vec{r_j}}{2}\right) \tag{11.23}
$$

By replacing the integrals in Eq. (11.19) with those delta functions the incoherent and coherent parts of the Wigner function of the backscattered field result:

$$W_{Back}^{Incoh}(\vec{x},\vec{p}) = \int d^3x'\, d^3p_1\, P(\vec{x}'-\vec{x},t) W_0(\vec{x}',\vec{p}_1)$$
$$= \int d^3x'\, P(\vec{x}'-\vec{x},t)\tilde{W}_0(\vec{x}') \qquad (11.24)$$

where $\tilde{W}_0(\vec{x}')$ is the momentum-integrated incident Wigner function[4], and

$$W_{Back}^{Coh}(\vec{x},\vec{p}) = \int d^3r'\, d^3p_1\, P(\vec{r}',t) \exp[-i(\vec{p}_1+\vec{p})\cdot\vec{r}'] W_0(\vec{x},\vec{p}_1). \qquad (11.25)$$

Even though the probability distribution P is not yet known, there are already some interesting features discernible. The incoherent contribution W_{Back}^{Incoh} in Eq. (11.24) depends only on x and not an p, as is expected from incoherent fields. The spatial characteristics of W_{Back}^{Coh} in Eq. (11.25) are identical to W_0. Its angular characteristics are determined by P. In the next section we will derive an expression for P in the diffusion approximation, which allows us to solve the integrals in Equations (11.24) and (11.25) analytically.

11.3 The probability density P for photon migration

There exist many approximations for the probability density P, describing the stationary as well as the time-resolved behavior of photons in random media. The stationary case has already been discussed in Section 10.4. As already pointed out there, for sufficiently small size and large density of scatterers in the medium the

[4]Note that $\tilde{W}$ has the unit power times momentum space volume = [Watt/m^3], while the unit of W is just [Watts].

transport of the light can be described by the isotropic diffusion equation, at least for distances from the surface large compared to the mean free path, where the photons are sufficiently randomized. The Green's function in the time-dependent diffusion approximation regime has to obey [62]

$$(D\nabla_r^2 + \frac{\partial}{\partial t})P(\vec{r}, \vec{r'}; t) = \delta(\vec{r} - \vec{r'})\delta(t) \tag{11.26}$$

where D is the diffusion constant. $P(\vec{r}, \vec{r'}; t)$ is then the probability distribution for a photon to perform a random walk from $\vec{r}$ to $\vec{r'}$ in time t without crossing the surface. It would appear that the latter condition could be satisfied by requiring $P(\vec{r}, \vec{r'}; t)$ to cancel at the surface. But, depending on the approach, P will cancel at different surfaces outside the medium: For the exact solution of the Milne problem, which treats the stationary mean-density of energy $U(z)$ of a semi-infinite medium containing isotropic scatterers as outlined in Section 10.4, P will cancel on the plane $z = -z_0$ with $z_0 = 0.7104...l$. Within the more general stationary diffusion approximation on the other hand, P will cancel on the plane $z = -z_0$ with $z_0 = \frac{2}{3}l$ which is also valid for the time-dependent case. In this case, one obtains for P [62]:

$$P(\vec{r}, \vec{r'}; t) = \frac{1}{(4\pi Dt)^{\frac{3}{2}}} \exp\left(-\frac{\rho^2}{4Dt}\right) \left\{ \exp\left[-\frac{(z-z')^2}{4Dt}\right] - \exp\left[-\frac{(z+z'+2z_0)^2}{4Dt}\right] \right\}. \tag{11.27}$$

It can readily be seen that the terms in brackets becomes zero for $z = z' = -z_0$. Also, P depends only on $\rho = \mid (\vec{r} - \vec{r'})_\perp \mid$ as expected from a semi-infinite medium with translational invariance.

In our experiment, we measure the emerging field at the output plane, where $z = z' = 0$. Eq. (11.27) then reduces to

$$P(\rho;t) = \frac{1}{(4\pi Dt)^{\frac{3}{2}}} \exp\left(-\frac{\rho^2}{4Dt}\right)\left[1 - \exp\left(-\frac{z_0^2}{Dt}\right)\right]. \tag{11.28}$$

For $\sqrt{Dt} \gg z_0$, which means that the light has diffused over much more than a mean free path, the exponential can be expanded and the term in brackets becomes approximately $\frac{z_0^2}{Dt}$, so that Eq. (11.28) simplifies to:

$$P(\rho;t) = \frac{z_0^2}{(4\pi)^{\frac{3}{2}}(Dt)^{\frac{5}{2}}} \exp\left(-\frac{\rho^2}{4Dt}\right). \tag{11.29}$$

In this expression and in the following we neglect the attenuation in z-direction expressed by the last term in Eq. (11.14); we assume that the distance between the sample surface and the first scatterer can be neglected.

In Section 11.4, the Wigner function for the backscattered field in the diffusion approximation regime will be discussed, using the probability distribution for photon migration in Eq. (11.29).

Note regarding the dimensionality of Wigner functions

Scattering in a bulk medium is a three-dimensional problem and needs to be treated as such. On the other hand, we only detect the light field on the surface of the sample, which is a two-dimensional problem.

For close to perpendicular incidence on and emission from a random medium, the transverse mutual coherence function of the scattered field is determined by the transverse properties of the incident beam but also by the path delay in z, as discussed in the previous sections. The longitudinal mutual coherence function of the backscattered field depends on the longitudinal properties of the incident beam but also on the transverse location; inside the EBS cone it is different than out-

side. That means, that unlike for a Gaussian beam, the transverse and longitudinal mutual coherence functions are not separable.

We extract the transverse Wigner function by keeping z constant, thereby defining the transverse plane we are interested in:

$$W^{(3D)}(\vec{r},\vec{p}) \rightarrow W_{\perp}(\vec{r}_{\perp},\vec{p}_{\perp}, z = const, p_z = \frac{\omega}{c}) \tag{11.30}$$

We can therefore use all results for three-dimensional Wigner functions from the previous sections and just assume all vectors to be two-dimensional surface vectors.

11.4 EBS in the diffusion approximation regime

When we combine the result for the probability distribution P for photon migration from Eq. (11.29) and the general expression for the Wigner function of the backscattered field in Equations (11.24) and (11.25), we get

$$W^{Incoh}_{Back}(\vec{x},\vec{p}) \;\propto\; \frac{z_0^2}{(4\pi)^{\frac{3}{2}}(Dt)^{\frac{5}{2}}} \int d^2x' \exp\left[-\frac{(\vec{x}-\vec{x}')^2}{4Dt}\right] \tilde{W}_0(\vec{x}') \tag{11.31}$$

$$W^{Coh}_{Back}(\vec{x},\vec{p}) \;\propto\; \frac{z_0^2}{Dt} \int d^2p' \exp[-Dt(\vec{p}+\vec{p}')^2] W_0(\vec{x},\vec{p}'). \tag{11.32}$$

We now have an expression for the Wigner function of the backscattered field as a function of the Wigner function of the incident field alone. For the case of a Gaussian beam incident on the sample, Equations (11.31) and (11.32) yield relatively simple analytic expressions, as will be shown in Section 11.4.1.

In addition to the features of W_{Back}^{Incoh} and W_{Back}^{Coh} for general probability distributions P already pointed out in Section 11.2.4, some other interesting properties become visible for this special P: W_{Back}^{Incoh} is the convolution of the incident Wigner function and a Gaussian broadening term. It becomes broader with time as diffusion progresses. For the hypothetical case of $\tilde{W}_0 = \delta(\vec{x})$, W_{Back}^{Incoh} would be proportional to $P(\vec{x}, \vec{x}_0, t)$.

For the coherent part $W_{Back}^{Coh}(\vec{x}, \vec{p})$, the incident Wigner function is convolved with a Gaussian term, which, unlike its counterpart in the incoherent term, becomes narrower with time, which causes the momentum distribution of the Enhanced Backscatter Wigner function also to narrow with time. This Gaussian term is maximal for $\vec{p} = -\vec{p}'$, which agrees with the physical picture that enhanced backscattering is most intense in the direction exactly opposite of the incident field.

11.4.1 EBS field for Gaussian incident beam

The Wigner function for the backscattered field with Gaussian transversely coherent incident beam can be calculated straightforwardly by replacing the $W_0(\vec{x}, \vec{p})$ in Equations (11.31) and (11.32) by Eq. (3.4):

$$W_0^{coh}(\vec{x}, \vec{p}) \propto \exp\left[-\frac{\vec{x}^2}{2\sigma_s^2} - 2\sigma_s^2\left(\frac{\vec{k}\cdot\vec{x}}{R} + \vec{p}\right)^2\right] \tag{11.33}$$

where the vectors denote transverse components; we omit the $\perp$ subscript for simplicity. After some lines of straight-forward transformations we get for the incoherent part

$$W_{Back}^{Incoh,Gaussian}(\vec{x},\vec{p}) = \frac{z_0^2}{(4\pi)^{\frac{3}{2}}(Dt)^{5/2}}\int d^2x'd^2p' \exp\left[-\frac{(\vec{x}-\vec{x}')^2}{4Dt}\right] W_0^{coh}(\vec{x}',\vec{p}')$$
$$= \frac{\sqrt{\pi}}{2}\frac{z_0^2}{(Dt)^{3/2}}\frac{1}{2\sigma_s^2+4Dt}\exp\left(-\frac{\vec{x}^2}{2\sigma_s^2+4Dt}\right) \quad (11.34)$$

and for the coherent part

$$W_{Back}^{Coh,Gaussian}(\vec{x},\vec{p}) = \frac{z_0^2}{Dt}\int d^2p' \exp[-Dt(\vec{p}+\vec{p}')^2] W_0^{coh}(\vec{x},\vec{p}')$$
$$= \frac{z_0^2}{Dt}\frac{\pi^2}{2\sigma_s^2+Dt}\exp\left[-\frac{\vec{x}^2}{2\sigma_s^2}-\frac{\left(\frac{\vec{k}\cdot\vec{x}}{R}-\vec{p}\right)^2}{\frac{1}{Dt}+\frac{1}{2\sigma_s^2}}\right]. \quad (11.35)$$

The combined Wigner function is then:[5]

$$W_{Back}^{tot,Gaussian}(\vec{x},\vec{p}) = W_{Back}^{Incoh,Gaussian}(\vec{x},\vec{p}) + W_{Back}^{Coh,Gaussian}(\vec{x},\vec{p})$$
$$= \frac{z_0^2}{(Dt)^{3/2}}\left\{\frac{\sqrt{\pi}/2}{2\sigma_s^2+4Dt}\exp\left(-\frac{\vec{x}^2}{2\sigma_s^2+4Dt}\right)\right.$$
$$\left. + \frac{\pi^2\sqrt{Dt}}{2\sigma_s^2+Dt}\exp\left[-\frac{\vec{x}^2}{2\sigma_s^2}-\frac{\left(\frac{\vec{k}\cdot\vec{x}}{R}-\vec{p}\right)^2}{\frac{1}{Dt}+\frac{1}{2\sigma_s^2}}\right]\right\} \quad (11.36)$$

[5]For both W, $W\to\infty$ for $t\to 0$ which is non-physical. This happens because our assumption that $Dt \gg z_0^2$ is violated so the approximation leading to Eq. (11.29) breaks down and we need to replace $\frac{z_0^2}{Dt}$ with $1-\exp\left(-\frac{z_0^2}{Dt}\right)$.

11.5 Measured signal for the backscattered field

11.5.1 General expression for S_B^{incoh} and S_B^{coh}

Now that we have an expression for the Wigner function of the backscattered field we can calculate the mean square beat signal in the Single-Window technique and the complex beat signal in the Two-Window technique that we expect to measure. In Section 11.5.2 we will discuss the Single-Window case where all beams have a circular Gaussian beam profile of the same size and the same radius of curvature. Afterwards, the results can easily be adapted to the more general case. In Section 11.5.3 we will derive the complex beat signal for the Two-Window technique. All two-dimensional integrals in the following integrate over the transverse field. For simplicity we will again omit the $\perp$-subscript after each vector.

According to Eq. (4.25), the signal we measure is the convolution of the Wigner function of the signal field, in the following denoted as W_{Back}, and the Wigner function of the local oscillator field, W_{LO}:

$$S_B(\vec{d_x}, \vec{d_p}) = \int d^2x\, d^2p\, \langle W_{LO}(\vec{x} - \vec{d_x}, \vec{p} - \vec{p_x}) W_{Back}(\vec{x}, \vec{p}, t)\rangle. \tag{11.37}$$

As shown in Eq. (3.1), the Wigner function of the LO can be directly expressed in terms of the corresponding electric field:

$$\begin{aligned} W_{LO}(\vec{x} - \vec{d_x}, \vec{p} + k\frac{\vec{d_p}}{f_0}) &= \int \frac{d^2\epsilon}{(2\pi)^2} \exp\left[i\vec{\epsilon}\left(\vec{p} + \vec{k}\cdot\frac{\vec{d_p}}{f_0}\right)\right] \\ &\times \mathcal{E}^*_{LO}(\vec{x} + \frac{\vec{\epsilon}}{2} - \vec{d_x})\, \mathcal{E}_{LO}(\vec{x} - \frac{\vec{\epsilon}}{2} - \vec{d_x}). \end{aligned} \tag{11.38}$$

Here we just replaced $(\vec{x}, \vec{p})$ by the coordinates shifted in phase-space $(\vec{x} - \vec{d_x}, \vec{p} + k\frac{\vec{d_p}}{f_0})$

which describe the phase-space location of the LO relative to the Signal beam.

Incoherent part

We now insert Equations (11.34) and (11.38) into Eq. (11.37) and replace $W_0^{coh}(\vec{x},\vec{p}')$ in Eq. (11.34) according to Eq. (3.1), which yields

$$\begin{aligned} S_B^{incoh} &= \frac{1}{(2\pi)^4}\frac{z_0^2}{(4\pi)^{3/2}(Dt)^{5/2}}\int d^2x\, d^2p\, d^2x' d^2p' d^2\epsilon\, d^2\epsilon' \exp[i\vec{\epsilon}\cdot(\vec{p}+\vec{p}_x)] \\ &\times \exp\left[-\frac{(\vec{x}-\vec{x}')^2}{4Dt}\right]\exp(i\vec{\epsilon}'\cdot\vec{p}') \\ &\times \langle\mathcal{E}_{LO}^*(\vec{x}+\frac{\vec{\epsilon}}{2}-\vec{d}_x)\mathcal{E}_{LO}(\vec{x}-\frac{\vec{\epsilon}}{2}-\vec{d}_x)\mathcal{E}_0^*(\vec{x}'+\frac{\vec{\epsilon}'}{2})\mathcal{E}_0(\vec{x}'-\frac{\vec{\epsilon}'}{2})\rangle. \end{aligned} \tag{11.39}$$

As explained in Section 4.7, for heterodyne detection with transversely partially coherent light it is necessary to ensemble average over $\mathcal{E}_{LO}^*(x)\mathcal{E}_S(x')$ rather than $\mathcal{E}_S^*(x)\mathcal{E}_S(x')$ and $\mathcal{E}_{LO}^*(x)\mathcal{E}_{LO}(x')$ itself. Therefore we group the angled brackets in Eq. (11.39) so that this is achieved. The integrals for p and p' can be solved right away:

$$\int d^2p \exp(i\vec{\epsilon}\cdot\vec{p}) = (2\pi)^2\delta(\vec{\epsilon}) \tag{11.40}$$

$$\int d^2p' \exp(i\vec{\epsilon}'\cdot\vec{p}') = (2\pi)^2\delta(\vec{\epsilon}') \tag{11.41}$$

$$\tag{11.42}$$

so that Eq. (11.39) becomes

$$
\begin{aligned}
S_B^{incoh}(\vec{d}_x,\vec{d}_p) &= \frac{z_0^2}{(4\pi)^{3/2}(Dt)^{5/2}}\int d^2x\, d^2x' \exp\left[-\frac{(\vec{x}-\vec{x}')^2}{4Dt}\right] \\
&\times \langle\mathcal{E}_{LO}^*(\vec{x}-\vec{d}_x)\mathcal{E}_0(\vec{x}')\rangle\langle\mathcal{E}_{LO}(\vec{x}-\vec{d}_x)\mathcal{E}_0^*(\vec{x}')\rangle \\
&= \frac{z_0^2}{(4\pi)^{3/2}(Dt)^{5/2}}\int d^2x\, d^2x' \exp\left[-\frac{(\vec{x}-\vec{x}')^2}{4Dt}\right] |\langle\mathcal{E}_{LO}^*(\vec{x}-\vec{d}_x)\mathcal{E}_0(\vec{x}')\rangle|^2.
\end{aligned}
\tag{11.43}
$$

Coherent part

For the coherent part we proceed similar to the incoherent part, except that we now insert Equations (11.35) and (11.38) into Eq. (11.37). We get:

$$
\begin{aligned}
S_B^{coh}(\vec{d}_x,\vec{d}_p) &= \frac{1}{16\pi^4}\frac{z_0^2}{Dt}\int d^2x\, d^2\epsilon\, d^2\epsilon' \\
&\times \langle\mathcal{E}_{LO}^*(\vec{x}+\frac{\vec{\epsilon}}{2}-\vec{d}_x)\mathcal{E}_{LO}(\vec{x}-\frac{\vec{\epsilon}}{2}-\vec{d}_x)\mathcal{E}_0^*(\vec{x}+\frac{\vec{\epsilon}}{2})\mathcal{E}_0(\vec{x}-\frac{\vec{\epsilon}'}{2})\rangle \\
&\times \int d^2p\, d^2p_0 \exp\left[i\vec{\epsilon}\cdot\left(\vec{p}+k\frac{\vec{d}_p}{f_0}\right)\right]\exp(i\vec{\epsilon}'\cdot\vec{p}_0)\exp[-Dt(\vec{p}+\vec{p}_0)^2].
\end{aligned}
\tag{11.44}
$$

The integrals over p and p_0 can be solved right away:

$$
\begin{aligned}
&\int d^2p\, d^2p_0 \exp(i\vec{\epsilon}\cdot\vec{p})\exp(i\vec{\epsilon}'\cdot\vec{p}_0)\exp[-Dt(\vec{p}+\vec{p}_0)^2] \\
&= \exp(i\vec{p}_x\cdot\vec{\epsilon})\int d^2p \exp(i\vec{\epsilon}\cdot\vec{p})\exp(-i\vec{\epsilon}'\cdot\vec{p})\int d^2p_0\exp(i\vec{\epsilon}'\cdot\vec{p}_0)\exp[-Dt\vec{p}_0^2] \\
&= \frac{4\pi^3}{Dt}\exp(i\vec{p}_x\cdot\vec{\epsilon})\exp\left(-\frac{\vec{\epsilon}'^2}{4Dt}\right)\delta(\vec{\epsilon}-\vec{\epsilon}').
\end{aligned}
\tag{11.45}
$$

Inserting Eq. (11.45) into Eq. (11.44) and switching the angled brackets as in the incoherent case, we get

$$\begin{aligned} S_B^{coh}(\vec{d_x},\vec{d_p}) &= \frac{z_0^2}{4\pi(Dt)^2}\int d^2x\, d^2\epsilon \exp\left[-\frac{\vec{\epsilon}^2}{4Dt} - i\vec{\epsilon}\cdot\vec{d_p}\frac{k}{f_0}\right] \\ &\times \langle \mathcal{E}^*_{LO}(\vec{x}-\vec{d_x}+\frac{\vec{\epsilon}}{2})\mathcal{E}_0(\vec{x}-\frac{\vec{\epsilon}}{2})\rangle \\ &\times \langle \mathcal{E}_{LO}(\vec{x}-\vec{d_x}-\frac{\vec{\epsilon}}{2})\mathcal{E}^*_0(\vec{x}+\frac{\vec{\epsilon}}{2})\rangle. \end{aligned} \tag{11.46}$$

Equations (11.43) and (11.46) are the basis for the calculations of the mean square beat signal in the Single-Window technique and the complex beat signal in the Dual-Window technique.

11.5.2 Single-Window technique

The mean square beat signal for the special case that LO and incident Signal beam have an identical beam profile, has already been derived in [4, 5]. Since then, we corrected the prefactor of the probability density P we use so that the mean square signal now reads:

$$S_B^{SingleLO}(d_x,d_p,t) \propto \frac{\sqrt{4\pi}\delta^2 z_0^2}{(Dt)^{3/2}}\exp\left(-\frac{d_x^2}{a'^2}\right) + \frac{\delta'^2 z_0^2}{(Dt)^2}\exp\left(-\frac{d_x^2}{a^2} - \delta'^2 p_x^2\right), \tag{11.47}$$

where $1/a^2 = 1/(4\sigma_s^2) + 1/\sigma_g^2$, $1/\delta^2 = 1/(Dt) + 4/a^2$, $a'^2 = a^2(Dt/\delta^2)$, and $1/\delta'^2 = 1/\delta^2 + 4k^2\sigma_s^2/R^2$. As in previous chapters, σ_s is the beam size, σ_g the transverse coherence, and R the radius of curvature.

Since this thesis deals primarily with the Two-Window technique, we will not

get into the details of the Single-Window technique results and instead refer to the aforementioned papers.

11.5.3 Dual-Window technique

The calculations of the mean square beat signal for the Dual-Window technique are rather lengthy and not very instructional. I will therefore just mention the most important steps and refer to Appendix B for details.

Incoherent part

For the incoherent part, we take Eq. (11.43) and adapt it to the dual-LO case. The electric fields for LO and incident light are, as already shown in Eq. (5.1):

$$\mathcal{E}_{LO}(\vec{x}) \propto \exp\left(-\frac{\vec{x}^2}{4\sigma_s^2 a^2}\right) + \beta e^{i\theta} \exp\left(-\frac{\vec{x}^2}{4\sigma_s^2 A^2}\right) = \mathcal{E}_{LO}^{a}(\vec{x}) + \beta e^{i\theta} \mathcal{E}_{LO}^{A}(\vec{x}) \quad (11.48)$$

with $\theta = \omega t$ denoting the 3 kHz-phase-lock frequency between the LOs and β the relative amplitude of the big LO with respect to the small LO; and the incident beam is

$$\mathcal{E}_0(\vec{x}) \propto \exp\left(-\frac{\vec{x}^2}{4\sigma_s^2 B^2} + \frac{ik}{2RB^2}\vec{x}^2\right). \quad (11.49)$$

A, a and B denote again the scaling factors of the big LO, small LO and signal beam relative to the initial beam radius $2\sigma_s$. The squared product of the electric fields in Eq. (11.43) is then:

$$
\begin{aligned}
|\langle \mathcal{E}^*_{LO}(\vec{x}_1)\mathcal{E}_0(\vec{x}_2)\rangle|^2 &= (\langle \mathcal{E}^{a*}_{LO}(\vec{x}_1)\mathcal{E}_0(\vec{x}_2)\rangle + \beta e^{i\theta}\langle \mathcal{E}^{A*}_{LO}(\vec{x}_1)\mathcal{E}_0(\vec{x}_2)\rangle) \\
&\times (\langle \mathcal{E}^{a}_{LO}(\vec{x}_1)\mathcal{E}^*_0(\vec{x}_2)\rangle + \beta e^{-i\theta}\langle \mathcal{E}^{A}_{LO}(\vec{x}_1)\mathcal{E}^*_0(\vec{x}_2)\rangle) \quad (11.50)
\end{aligned}
$$

with $\vec{x}_1{=}\vec{x} - \vec{d_x}$ and $\vec{x}_2{=}\vec{x}'$. Again, we detect the cross-terms only:

$$
\beta e^{i\theta}\langle \mathcal{E}^{A*}_{LO}(\vec{x}_1)\mathcal{E}_0(\vec{x}_2)\rangle\langle \mathcal{E}^{a}_{LO}(\vec{x}_1)\mathcal{E}^*_0(\vec{x}_2)\rangle + \beta e^{-i\theta}\langle \mathcal{E}^{A}_{LO}(\vec{x}_1)\mathcal{E}^*_0(\vec{x}_2)\rangle\langle \mathcal{E}^{a*}_{LO}(\vec{x}_1)\mathcal{E}_0(\vec{x}_2)\rangle, \quad (11.51)
$$

the other terms average to zero. The second term in Eq. (11.51) is the complex conjugate of the first, so we need to calculate the first term only. The *in-phase* mean square beat signal will be twice the real part of the ensuing calculation; the *out-of-phase* signal twice the imaginary part. The ensuing calculation is explicitly shown in Appendix B; we will just show the result here. The complex beat signal S_B^{incoh} is then:

$$
\begin{aligned}
S_B^{incoh}(d_x) &= \sqrt{\frac{\pi}{4}}\frac{z_0^2}{(Dt)^{3/2}}\frac{1}{(v_B + v_B^*)(v_A + v_a)} \\
&\times \exp\left(-\frac{d_x^2}{\frac{1}{v_A+v_a} + \frac{1}{v_B+v_B^*} + 4Dt}\right). \quad (11.52)
\end{aligned}
$$

where

$$v_A = \frac{1}{4\sigma_s^2 A^2} \tag{11.53}$$

$$v_a = \frac{1}{4\sigma_s^2 a^2} \tag{11.54}$$

$$v_B = \frac{1}{4\sigma_s^2 B^2} - \frac{ik}{2RB} \tag{11.55}$$

$$\tag{11.56}$$

The complex beat signal for the incoherently backscattered field is real. Therefore, the out-of-phase quadrature signal is zero throughout phase-space. In reality, the measured out-of-phase signal is never at exactly at 90 degree phase-shift with respect to the center of the EBS cone in Signal phase-space, which leads to small contributions from the incoherent background for the out-of-phase part as well.

The imaginary part of v_B which contains the radius of curvature R of the Signal field, cancels. This means that the properties of the incoherent background are independent of the radius of curvature of the incident field, at least for an ideal turbid medium.

Coherent part

For the calculation of the coherent part of the mean square beat signal, S_B^{coh}, we start with Eq. (11.46), using the same expressions for $\mathcal{E}_0$ (Eq. (11.49)) and $\mathcal{E}_{LO}$ (Eq. (11.48)) as for the incoherent part. The detailed calculation is shown in Appendix B. The resulting integral for S_B^{coh} is

$$
\begin{aligned}
S_B^{coh}(d_x, d_p) &= \frac{z_0^2}{4(Dt)^2} \frac{\alpha}{v_A + v_B + \beta} \\
&\times \exp\left\{ -d_x^2(v_A + v_a) + \alpha(v_A d_x - i\frac{p_x}{2})^2 \right. \\
&+ \left. \frac{\left[(v_a + \frac{v_A \alpha}{4Dt})d_x + i2Dt\beta p_x\right]^2}{v_a + v_B + \beta} \right\}
\end{aligned} \tag{11.57}
$$

where

$$
\alpha = \frac{1}{\frac{1}{4Dt} + v_A + v_B^*} \tag{11.58}
$$

$$
\beta = \frac{1}{4Dt + \frac{1}{v_A + v_B^*}}. \tag{11.59}
$$

The v-variables are declared in the previous section. Unlike for the incoherent background, the imaginary part of the complex beat signal for the coherent part is not zero. As usual, the in-phase quadrature signal is the real part of $S_B^{coh}(d_x, d_p)$ in Eq. (B.44), the out-of-phase signal is its imaginary part.

11.5.4 Generalization for arbitrary Gaussian beams

While the previous derivations of the single- and two-window mean square beat signal are for the case where all beams are circular and Gaussian with the same radius of curvature, in the more realistic case the beams have different beam profiles in x- and y-direction, e.g. they might be elliptically shaped and have different radii of curvature. In some of our experiments we choose different radii of curvature on purpose.

For beams with a different beam profile in y- than in x-direction, the exponentials

in the final results remain the same, but the pre-factor $pref$ must be replaced by $\sqrt{pref_x pref_y}$, where $pref_x$ and $pref_y$ contain the direction-specific beam parameters in x and y.

Misalignments in y-direction, both angular and positional, can be also be included into the model simply by introducing equivalent expressions for d_y and $d_{p(y)}$ as for d_x and d_p.

Chapter 12

Enhanced Backscattering (EBS) Experiments

This chapter presents a study of measured time-resolved Wigner functions of Enhanced Backscattering from a turbid medium. In the first section we briefly describe the adaptations to the experimental setup for the measurement of backscattered light. Also we are going to discuss the properties and limitations of the turbid medium we use: It consists of polystyrene spheres of 0.5 micron diameter suspended in a neutral buoyancy solution.

In the second section we are going to present our experimental results; for a collimated as well as a convergent and divergent incident beam and at various path lengths in the medium. The Enhanced Backscatter cone for a curved incident wavefront shows a reversal of radius of curvature, confirming for the first time directly the phase-conjugating properties of a Enhanced Backscattering from a turbid medium. In the third section we study the momentum distribution of the EBS peak as a function of path-delay. We conclude this chapter with the discussion of the experimental results, the comparison to the theoretical predictions outlined in Chapter 11, and the summary.

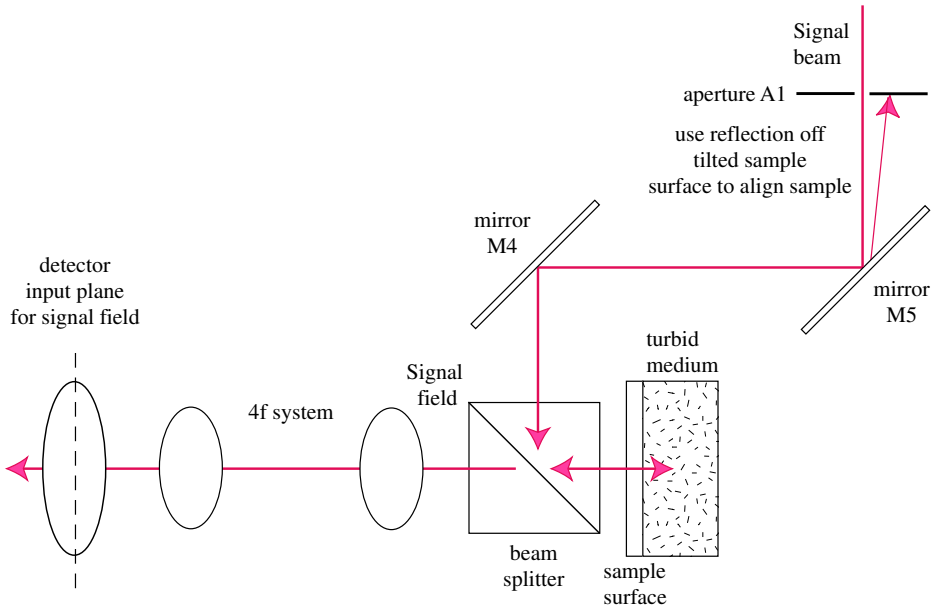

Figure 12.1: Experimental setup close to the sample container for the measurement of Enhanced Backscattering.

12.1 Experimental Setup

The complete experimental setup modified for the detection of Enhanced Backscattering is shown in Figure 5.6. In Figure 12.1 the setup close to the sample container is shown in more detail, with Signal beam wavefront correction lens L_3 omitted. The Signal beam is reflected by a beam-splitter onto the sample container which contains the turbid medium. The backscattered field at the sample surface is collected by a $4f$-system and projected onto the detector input lens. The $4f$-system reproduces the field at the sample surface exactly in the detector input plane; without it the field would have to bridge the distance through free space between those planes and subsequently change its characteristics according to Eq. (3.15).

In order to be able to observe Enhanced Backscattering, the detection system must collect the light that goes in the opposite direction of the incident Signal beam.

Without proper alignment, one can take a large phase-space scan and hope that the Enhanced Backscatter cone shows up somewhere. Then the actuators that select the measured position and momentum can be moved to that location in phase-space and defined to be the origin for all measurements to follow. This procedure has the disadvantage that the Signal field as well as the Local Oscillator beam pass through a range of lenses off-center, which can introduce distortions in the phase front caused by lens aberrations that can be picked up by this very phase-sensitive technique. Also, the lack of a reference light spot close to the detector makes it difficult to counteract the drift of our superluminescent diode (SLD) (see Section 6.4).

We therefore use the fact that the reflective outer surface of the sample container is to a good degree parallel to the inner surface and therefore to the surface of the turbid medium: If the beam reflected from the outer surface generates a light spot close to the opening of an aperture $A1$ that the Signal beam has passed through earlier, it must reflect upon itself to a good degree. The Enhanced Backscattering cone will consequently point into this direction. Apart from this constraint the reflected beam must also be located at the phase-space coordinates $(\vec{x},\vec{p})$=(0,0), defined by the initial, lens-concentric alignment of the system. A third requirement is that the path-length of the reflected beam and the LO match within the longitudinal spatial resolution Δl_B which is 21 μm for our light source (Section 6.2.1).

These three requirements can be met by adjusting M_4, M_5 (see Figure 12.1 or Figure 5.6), the sample container and retro-reflector C_1 (see Figure 5.6), in an iterative manner: First the beat signal is maximized using M_5 and the sample container. Then C_1 is adjusted to counter changes in path-length of S introduced by the adjustment of M_5 and C_1. Then, the beam reflected off the sample surface is brought back close to the opening of aperture A_1, ideally directly above or below

the opening since we want to optimize the alignment primarily parallel to the table. Thereafter, the beat signal is maximized again, followed again by the adjustment of the reflected beam spot on the aperture, and so on. This iterative procedure converges reasonably fast.

During the adjustment it should be avoided to reflect the beam *through* the hole of aperture $A1$, since it might re-enter the SLD and therefore shorten its lifespan. During scans, the sample container needs to be tilted in order to turn the specular reflection from the sample surface away from the detector. This reflection is orders of magnitude brighter than the Enhanced Backscatter cone and can add considerable noise to the signal. [1]

12.1.1 Turbid medium

The turbid medium we use in our backscatter experiments consists of polystyrene spheres with a diameter of 0.5 μm (1.9% variance) suspended in a neutral buoyancy solution of water (80%) and glycerol (20%). The mixture has a refractive index of n_{Sol}=1.36, the spheres n_{Sph}=1.59, resulting in a relative refractive index of the spheres of 1.17. These spheres are a little smaller than the wavelength of our SLD, which means their angular scattering distribution is relatively large. The exact optical properties of such a sphere can be calculated by means of the Mie solution (Section 10.2.4). It yields an average cosine of the scattering angle of $\langle \cos\theta \rangle = 0.805$ which corresponds to an angle of 36.39 degree. Since the size of a sphere is on the order of the wavelength λ of the light, diffraction differs from that expected

[1] Ideally, the container should be tilted up- or downwards, in order to minimize the 'wandering wave'-effect associated with Enhanced Backscattering. This effect exists when a parts of a tilted plane wave hit the sample at different times. Our elliptical beam profile is smaller in y-direction, therefore this effect is smaller along this direction.

from objects much larger than λ. This is taken into account by a multiplicative correction factor Q_{sca}, as already mentioned in Section 10.2.4. Q_{sca} is 0.515 for 0.5 μm-spheres at our wavelength λ=678.3 nm, according to the Mie solution. The resulting cross section is $Q_{sca}\pi r_{Sph}^2 = 0.101\ \mu\text{m}^2$.

Since there is only a finite number of scatterers in the medium, there is as well only a finite number of paths in the medium suitable for enhanced backscattering. For rigid media, the EBS effect can oftentimes not be seen, because it is masked by an overlaying speckle pattern as already discussed in Section 11.2. The EBS effect is only visible if we ensemble-average over the medium, in which case the speckle-pattern washes out and the averaged intensity remains. For rigid media, this averaging process is either done by rotation or translation or a combination thereof of the sample relative to the incident beam. In the case of scatterers suspended in liquids like our medium (Section 12.1.1), the Brownian motion of the spheres in the solution provides a convenient way of attaining ensemble averaging for the backscattered light. In some cases, the ensemble averaging by Brownian motion is too slow to meet the time constraints for data taking imposed by the slow drift of the SLD. In these cases, improved ensemble averaging can be achieved by shaking or stirring the sample. Shaking of the sample container has been performed by mounting the container to the center of a loudspeaker, which was then subjected to a sinusoidal current at about 13-18 Hz. The resulting elongation was on the order of a millimeter. This method is very stable and improves the ensemble averaging of backscatter- and transmission signals in particular from larger spheres, which -due to their slower Brownian motion- otherwise produces slow moving speckle that is impossible to average out electronically.

Mainly due to space limitations, the loudspeaker shaking device has been re-

places by a magnetic stirrer. It consists of a piece of plastic with embedded magnets, which is placed into the sample container. A magnet, mounted on a slowly rotating electric motor, is placed close to the sample container and causes the magnetic pebble inside to stir the solution.

12.2 Experimental Data

12.2.1 Collimated incident beam

Figure 12.2 shows the experimental data gained by our Two-Window technique and the theoretical predictions for the Wigner functions of the Enhanced Backscattered field for a path delay of the Signal beam relative to the Dual-LO of 150 μm (150 μm/1.36=110 μm in the medium). a) and b) are the measured in-phase and out-of-phase signals comprising the complex beat signal, c) is the resulting Wigner function. d) is the theoretical prediction of the Wigner function. The concentration of the sample is 1.2×10^{12} spheres/cm^3, which yields a scattering mean free path of 8.3 μm and a transport mean free path of l^*=42.3 μm, according to Mie theory. σ_s for the BLO and the incident beam are 343 μm (e^{-2} intensity width 1370 μm), and of the SLO 25 μm (e^{-2} intensity width 100μm). Figure 12.3 shows the corresponding data for a path delay of 250 μm (185 μm in the medium).

The bright spot in the center is due the Enhanced Backscatter peak, while the bands extending in momentum are the incoherent background. As can clearly be seen, the Enhanced Backscatter peak is narrowing in momentum with increasing path delay. The position distribution remains unaffected.

The origin of the momentum side peaks which are seen in Figure 12.3c) is unknown; but it could be related to phase aberrations from the usual

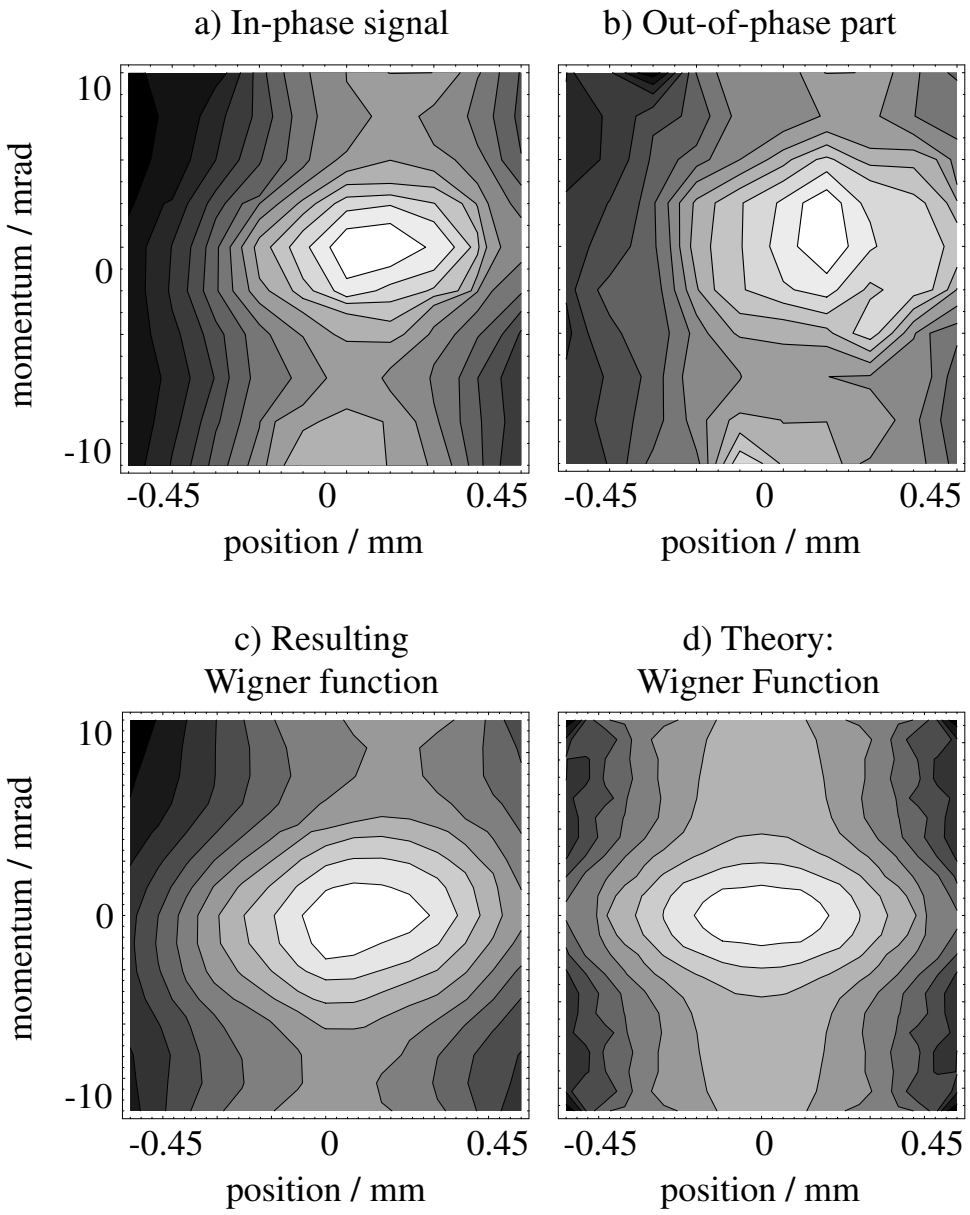

Figure 12.2: Two-Window measurement of EBS from a flat incident beam, 150 μm path-delay (110 μm in the medium). Measured in-phase (a) and out-of-phase (b) quadrature signals, resulting Wigner function (c), theory for Wigner function (d).

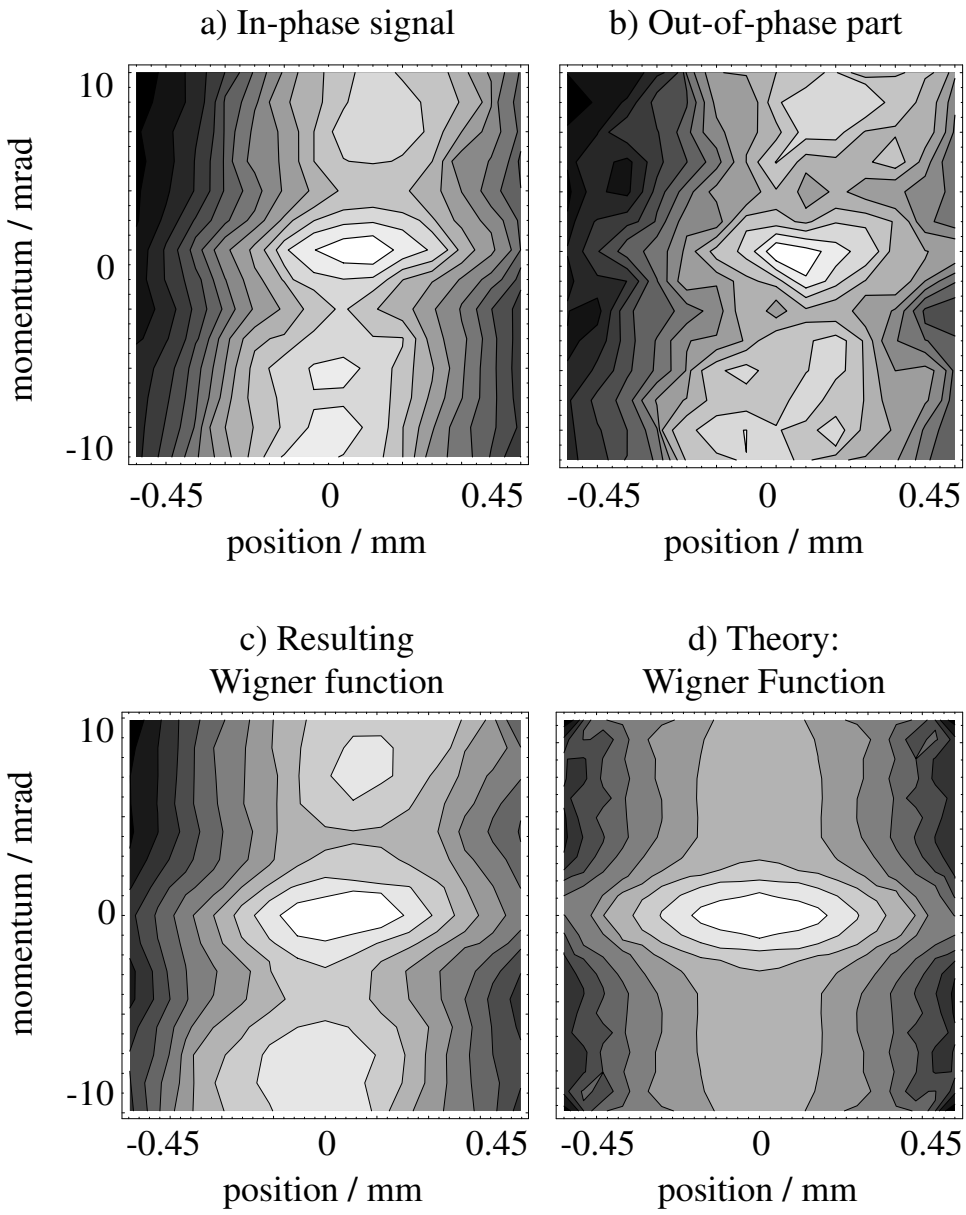

Figure 12.3: Two-Window measurement of EBS from a flat incident beam, 250 μm path-delay (185 μm in the medium). Measured in-phase (a) and out-of-phase (b) quadrature signals, resulting Wigner function (c), theory for Wigner function (d).

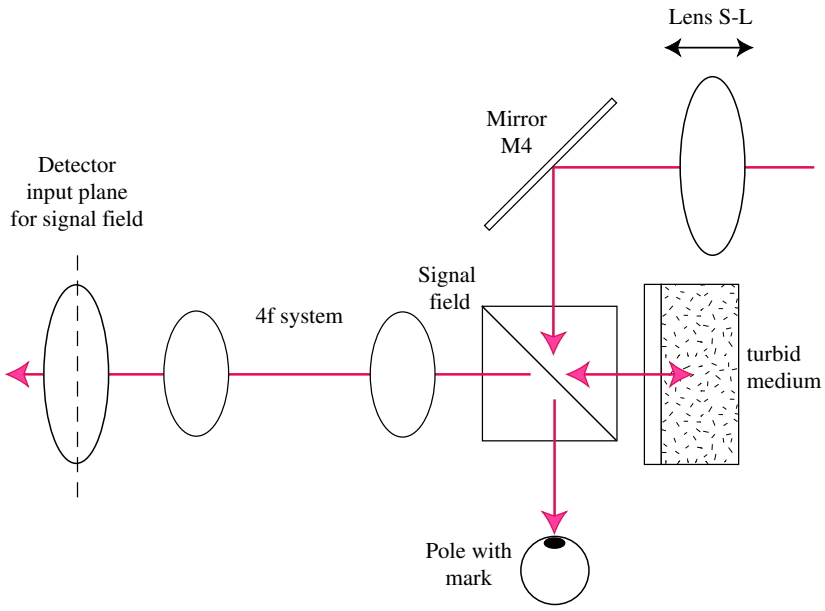

Figure 12.4: Setup modification for introducing a finite radius of curvature into the incident beam.

$1 + \cos[(\vec{k}_0 + \vec{k}_f)(\vec{r}_i - \vec{r}_j)]$ behavior for the mutual coherence function for larger momenta, due to imperfections of the turbid medium in combination with the non-ideal Dual-LO. For an ideal turbid medium in conjunction with perfect LOs, theory predicts the phase-terms in the Wigner function to cancel (see Section 11.2.4), resulting in just a single Enhanced Backscattering peak.

12.2.2 Diverging incident beam

In this section, the experimental results for the backscattered light for both convergent and divergent incident beam are presented. The experimental realization is the most challenging of the experiments in this thesis. The change in setup is shown in Figure 12.4. First of all, the set-up has to be aligned as for a flat incident wavefront, using the reflection of the sample container. Then, a pole with a mark is added next to the beam-splitter, which marks the position of the Signal beam. Then, a

convex lens $S-L$ is introduced into the path of the Signal beam. Depending on whether the distance between the sample and the lens is more or less than its focal length, the beam incident onto the sample is divergent or convergent. The lens has to be very carefully adjusted horizontally and vertically, using the mark on the pole. Since the lens increases the optical path of the Signal beam due to its refractive index, retro-reflector C_1 (see Figure 5.6) has to be readjusted with the help of the beat signal. Afterwards, the position of lens $S-L$ and the retro-reflector have to be optimized iteratively, again using the beat signal.

Then, the Wigner function of the beam reflected off the sample surface is measured. After that, retro-reflector C_1 is moved by about a millimeter to bridge the wall of the sample cell, plus the wished path length in the medium.[2]
Figure 12.5 shows the experimental results for a divergent incident input field with a radius of curvature of 8.8 cm (compare Section 8.1). It was generated by placing a lens with f=20 cm at a distance of 27 cm. σ_s is then 240 μm (e^{-2} intensity width 960 μm) and therefore smaller than before.

The top row shows the signal beam incident on the sample, measured as the beam reflected off the polished surface of the sample container. From left to right: the in-phase and out-of-phase quadrature signals at 3 kHz, scanned over $\pm$0.25 mm and $\pm$3.4 mrad. On the right is the corresponding Wigner function that is obtained from an inverse Margenau-Hill transformation of the in- and out-of-phase parts as described above. The divergence of the incident beam manifests itself in the tilted elliptic shape of the depicted Wigner function. The second row shows the enhanced backscattered field at a path-delay of 300 μm (220 μm in the medium). The slope of the phase-space ellipse has changed its sign: The enhanced backscatter cone is

[2]It has to be kept in mind that a given change in position Δz of the retro-reflector causes a change in the optical path-length of $2\Delta z$ in air and $2\Delta z/n_0$ in the medium.

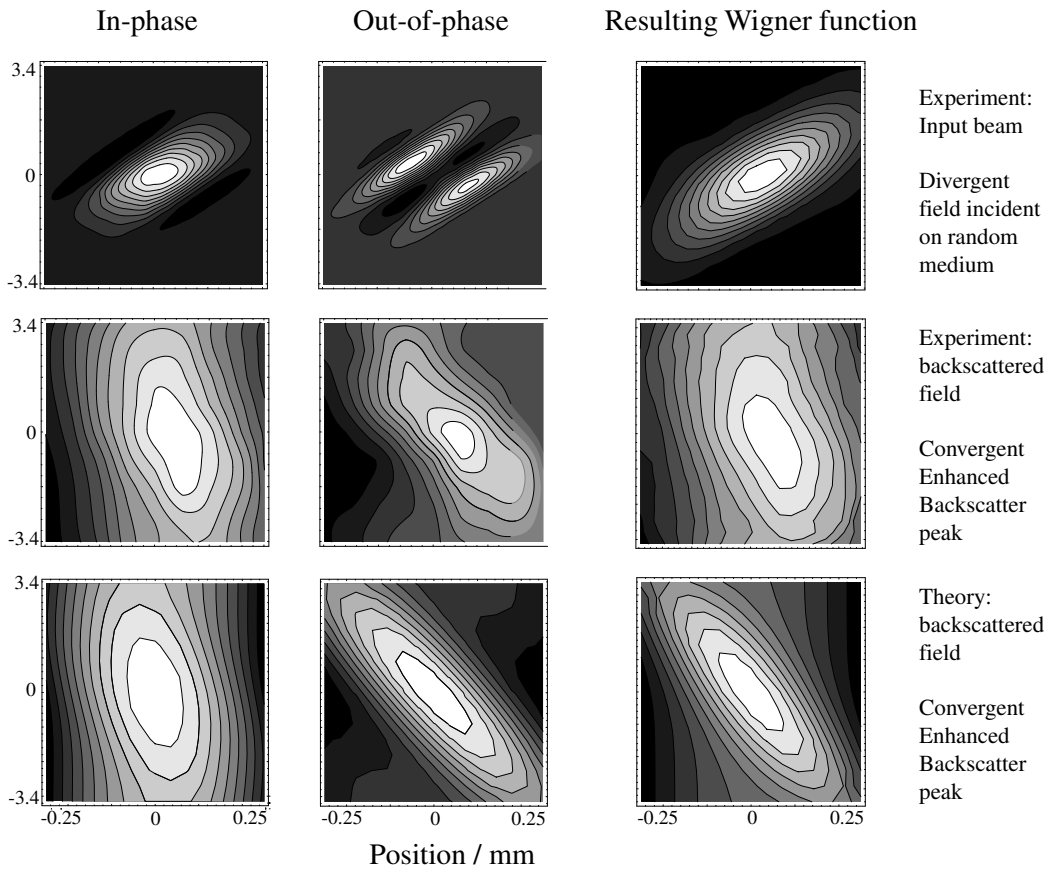

Figure 12.5: Top row: Measured complex beat signal and resulting Wigner function of the input field incident on the random medium. Middle row: Enhanced Backscatter cone of field shown in top row at a path delay of 300 μm (220 μm in the medium). Bottom row: Numerical simulation of backscattered field, using field parameters retrieved from incident field. The reversal of the tilt in the ellipses signifies the reversal of the curvature between the incident and backscattered field.

convergent.

The bottom row shows the theoretical prediction (see Appendix B) for the backscattered field, using the parameters of the incident field and the local oscillators beams used in the experiment. Theory correctly predicts the changing sign of the radius of curvature. Differences in the strength of the incoherent background between theory and experiment can be attributed mainly to uncertainties in the exact radius of curvature of the SLO at the detector input plane.

The out-of-phase part seems to be more sensitive to the coherent backscatter. This comes from the fact that the out-of-phase part is sensitive to phase changes with respect to the reference phase at $(x, p) = (0, 0)$ (compare Section 5.4.2). Since the incoherent background (ideally) does not change with momentum, and also not considerably over the measured position range, the out-of-phase part is less sensitive to that contribution. While the superposed incoherent background in the in-phase part seems to stretch the Enhanced Backscatter peak vertically, this influence is missing in the out-of-phase part. A difference in sensitivity towards the Enhanced Backscatter contribution between in-phase and out-of-phase part is less pronounced.

The radius of curvature R of just 8.8 cm is necessary in order to enhance the contrast between the enhanced backscattering and the incoherent background. For R smaller than a few centimeters on the other hand, the path delay for the center of the beam differs by more than the longitudinal spatial resolution (21 μm) from that of the outer regions of the beam, due to the curvature of the wavefront.

Furthermore, the small radius of curvature causes rapid phase variations over the area of incidence, according to the quadratic-phase approximations for lenses:

$$\phi(\vec{x}) = \exp\left(i\frac{k}{2R}\vec{x}^2\right). \tag{12.1}$$

For R=10 cm, the center region of the beam, defined by phase deviations of not more than $\pm\pi/2$ from the center itself, is just 200 μm wide, followed by rapidly shrinking concentric equal-phase regions. With increasing path delay, time-reversed paths with starting points from bordering regions can interfere *destructively*, resulting in what could be named *"Decreased Backscattering" or "DBS"*. The combination of DBS and EBS leads to a wash-out of the Enhanced Backscatter signal when these contributions cancel with constructively interfering time-reversed paths. We will refer to this effect from now on as *phase variation*.

In addition to the phase variation, which can be completely attributed to the properties of the Signal field, the imperfect Dual-LO introduces further problems: The rapid phase changes outside the beams center region for small R's in position and momentum quickly drop below the resolution limit of the SLO and the BLO. This leads to a smoothing and consequently a wash-out of these rapid oscillations, which destroys the phase-information containing the radius of curvature of the backscattered field.

Phase-variation and the finite resolution of the LOs are the reason why we get the best results when we limit our range of measurement to the center of the Enhanced Backscatter cone. If we include outer regions, the phase information washes out and gives the EBS cone a flat appearance.

12.2.3 Converging incident beam

The experimental setup for a convergent incident beam is identical to the one for a divergent incident beam, except that the distance between the sample and lens $S-L$ is now smaller than the focal length of $S-L$. Figure 12.7 shows the quadrature signals of the complex beat signal for an incident beam of σ_s=310 μm and R=9 cm

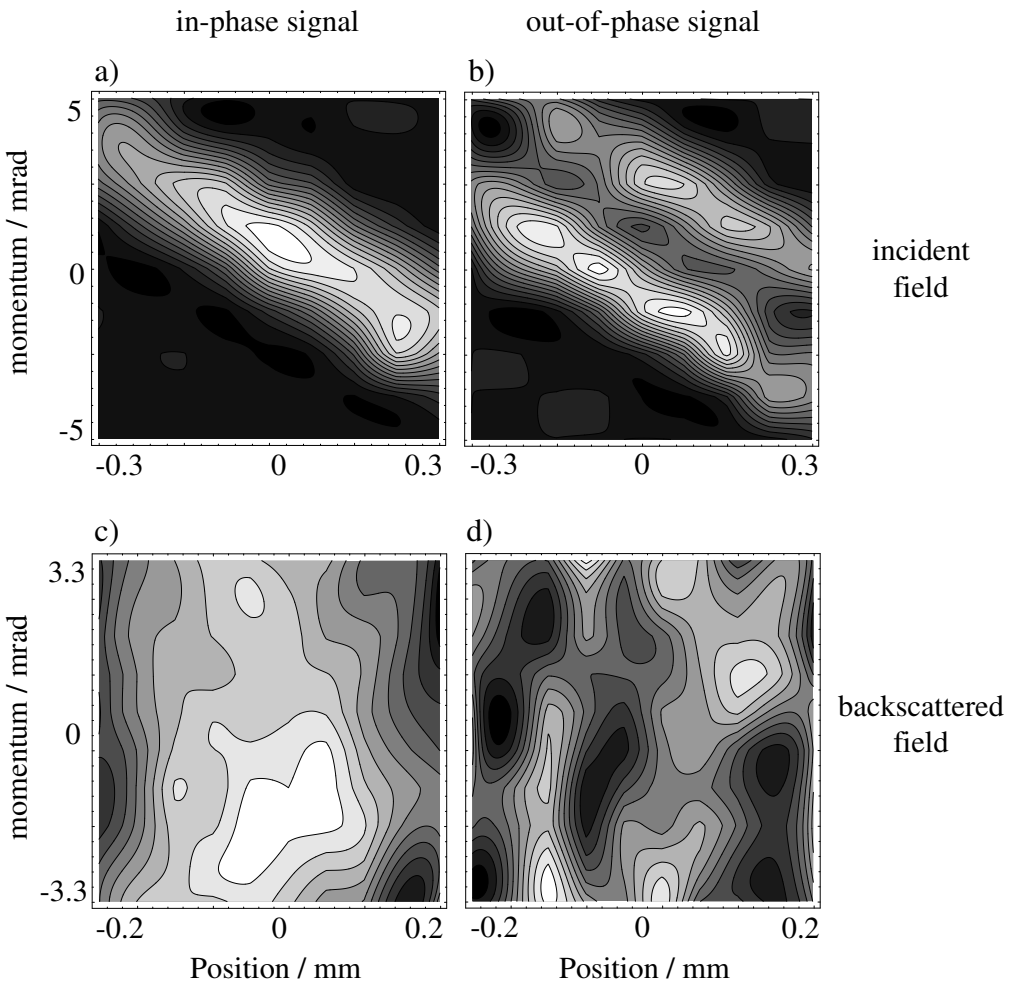

Figure 12.6: In-phase- (a) and out-of-phase (b) quadrature signals for convergent incident beam. In-phase- (c) and out-of-phase (d) quadrature signals for Enhanced Backscatter cone at a path delay of 300 μm (220 μm in medium). A calculation of the Wigner function for the backscattered field is not possible due to the low signal-to-noise ratio. The incident field is of the same quality as that used in Figure 12.5, but the scanning resolution is three times as small. The resolution for the backscattered field is the same in both cases.

(a), (b), and the EBS field (c), (d) at a path-delay of 300 μm (220 μm in sample).

Interestingly, the phase-conjugating properties of the Enhanced Backscatter cone seem to be much less pronounced than for the case of a diverging incident beam, which deteriorates the Signal-to-Noise ration to a degree which makes an inverse Margenau-Hill transformation impossible. For that reason, a plot of the resulting Wigner function has been omitted.

The reason for this obviously counter-intuitive discrepancy between the divergent- and convergent incident beam configuration is still unknown. Anisotropic scattering is a potential cause; a convergent incident beam would generate a stronger incoherent background compared to the coherent signal, due to a reluctance to change direction for the field scattered from a sphere. But, considering the large phase-function of the 0.5 μm-spheres in combination with the small difference in angle of incidence between convergent and divergent light, this contribution appears to be negligible. Another possibility could be a small drift in the phase of the complex beat signal, maybe caused by the phase-locked loop. According to a numerical simulation, a phase offset of just a few degrees can cause the center peak of the out-of-phase signal to split apart for a given radius of curvature of the EBS field, which increases the sensitivity to noise dramatically. But, the same offset has no considerable effect on an EBS field with a radius of curvature of the opposite sign.

12.2.4 Comparison of Single- and Two-Window technique

The divergent or convergent Enhanced Backscatter cone can also be detected by the Single-Window technique, with the typical smoothing associated with the Single-Window technique. Figure 12.7 shows a converging Enhanced Backscatter cone detected with the Two-Window technique (top) and the Single-Window technique

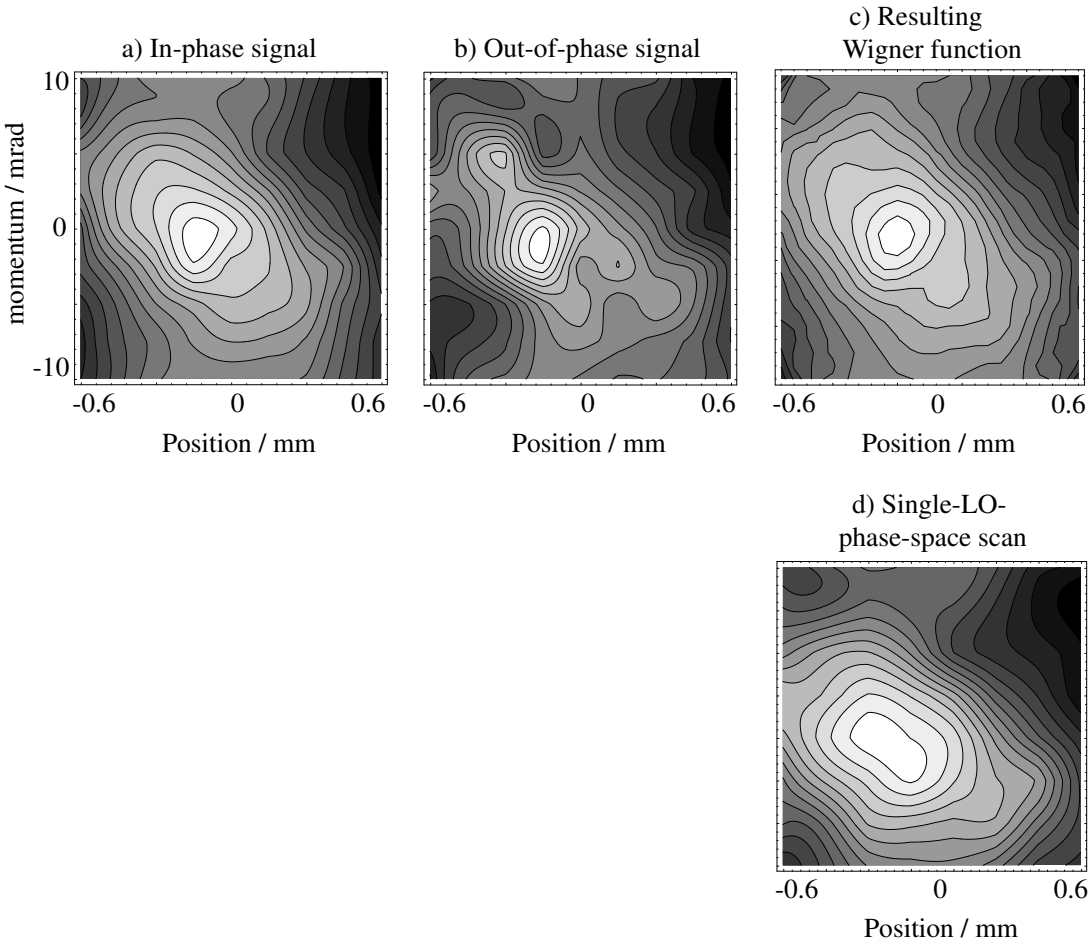

Figure 12.7: The same converging Enhanced Backscatter cone detected with the Two-Window technique (top) and Single-Window-technique (d). In-phase- (a), out-of-phase (b) quadrature signals, resulting Wigner function (c).

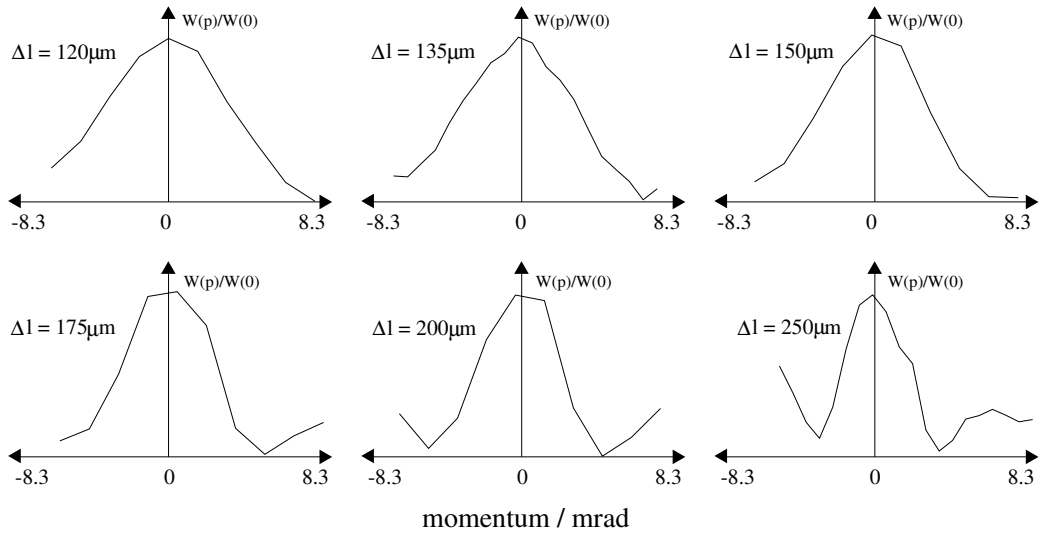

Figure 12.8: Position-integrated momentum distribution for various path delays.

(bottom), resulting from an incident beam of R=18 cm and σ_s=550 μm. The phase-space distribution measured in the Single-LO technique is broader in position than the Wigner function measured in the Two-Window technique, due to the convolution effect pointed out in Section 5.3.1. The momentum distribution on the other hand is approximately equally wide, since for both techniques the momentum resolution is determined by the angular spread of the BLO, which is negligible compared to that of the Enhanced Backscatter cone.

12.3 Momentum distribution of an EBS peak

In this section, we present the measured time-resolved momentum distributions for an Enhanced Backscatter peak at various path-delays. From Section 11.4 we know that the angular profile of the EBS peak for a flat incident beam is independent of position; the spatial characteristics of the backscattered Wigner function is identical to that of the incident Wigner function. When investigating the momentum

distribution, we can therefore integrate the measured Wigner function over position in order to improve ensemble averaging. Comparing the position-integrated momentum distribution with that at the center of the EBS peak, it has been shown that while the fluctuation are averaged out to a good degree, the shape of the EBS peak remains unchanged.

Figure 12.8 shows the position-integrated momentum distributions for six different path delays Δl between 120 and 250 μm. At 120 μm, the momentum distribution is Gaussian, because only the lowest scattering orders contribute. The distribution at 135 μm is approximately triangular, which - according to the theory to be discussed shortly - means that it contains contributions ranging from dual- to about 135 $\mu\text{m}/(n_0 l) \approx 13$ scatterers. According to theory, an EBS cone displays the well-known triangular shape with a cusp only for perfectly coherent light and absolutely loss-less scattering. The dual- and triple-scattering contributions which are broad in momentum fill the wings of the triangle. Higher scattering orders are narrow in momentum and shape the cusp. For Δl=135 μm the EBS cone is triangular because the longitudinal coherence length of our SLD of 25 μm is large enough to include both the scattering orders filling the wings and higher ones which fill the cusp.

For larger path-delays at 150 μm and up, the path-delay resolution suppresses the lowest scattering orders and the momentum distribution looses its wings. Also, the EBS-side peaks, already seen in Figure 12.3c), become more prominent.

The various shapes seen can not be explained by the our current model which employs the diffusion approximation and therefore a continuum of scatterers. In his paper [62], Akkermans derives an expression for the angle-dependent intensity for Enhanced Backscattering of a plane-wave incident on a semi-infinite medium, as a

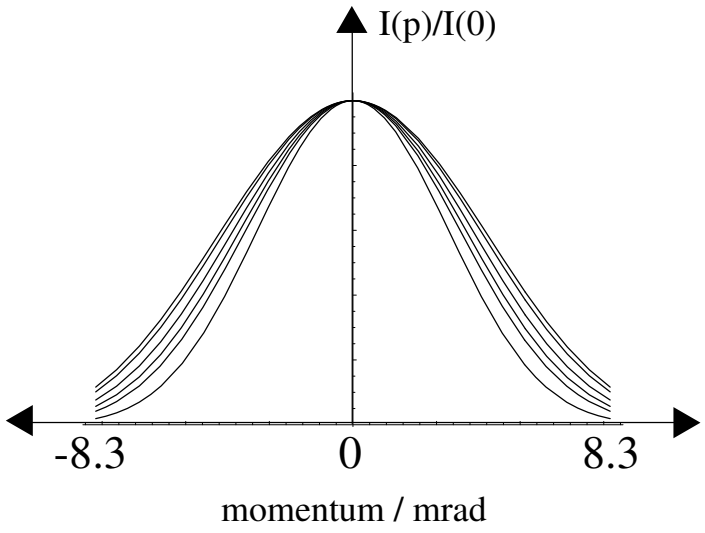

Figure 12.9: Angular intensity for path-delays in Figure 12.8. Outermost plot: Δl=120 μm, innermost plot: Δl=250 μm.

function of the number of scatterings encountered:

$$\begin{aligned} I_n(p) &= \frac{2^{n+1}n!}{(2n+1)!!}(1-(pl)^2)^{n+1/2} \\ &\times \left[1-(2n+1)!!\frac{j_n\left(\frac{a}{l}\sqrt{1-(pl)^2}\right)}{\left(\frac{a}{l}\sqrt{1-(pl)^2}\right)^n}\right] \end{aligned} \tag{12.2}$$

where n is the number of scatterings, p the transverse momentum of the outgoing field, l the mean free path and $a = 2(l + z_0)$ with $z_0 \approx 0.7l$. $j_n(x)$ is the spherical Bessel function of the first kind.

Using this formula, we can get an estimate of $I(p)$ for a fixed path delay Δl in the medium: We divide Δl in N discrete cells of length l. Within each cell, the probability of scattering is e^{-1}, by definition of l. The probability $P(N, n)$ to scatter exactly n times is given by the Binomial distribution:

$$P(N,n) = \left(\begin{array}{c} N \\ \\ n \end{array} \right) e^{-n}(1-e)^{-(N-n)}. \tag{12.3}$$

The intensity distribution for a fixed path delay in this model is then the sum over the intensities involving n=2...N scattering events, each weighted by its probability p(N,n):

$$I(N = \frac{\Delta l}{l}, p) = \sum_{n=2}^{N} I_n(p)\, P(N,n). \tag{12.4}$$

Figure 12.9 shows a plot of Eq. (12.3) for the values for the path-length in Figure 12.8. The outermost curve corresponds to Δl=120μm; it becomes more narrow with increasing Δl, leading to the innermost curve for Δl=250μm.

Theory predicts reasonably well the triangular shape observed for small path-delays. The cone-width is also in good agreement with the experiment. For larger path-delays, the experimentally observed width is much smaller than predicted, maybe do the superposed oscillations of unknown origin which were discussed in Section 12.2.3.

12.4 Discussion and Summary

The experimental results for a flat incident beam agree reasonably well with their theoretical prediction. With increasing path-delay, the momentum distribution of the EBS-peak narrows, while the position distribution remains unaffected. For a divergent incident beam, the EBS-peak shows inversion of the radius of curvature. Two incident wavelets can interfere even when they enter the medium at different locations, which is different from a true phase-conjugating mirror. Therefore, and

because of the finite size and angular spread of the Dual LO, inversion of curvature can be observed only close to the beam center, where the transverse phase of the incident beam changes slowly.

Interestingly, an incident *converging* beam generates a far less pronounced inversion than an incident *divergent* beam of the same absolute radius of curvature. So far, no satisfying explanation for this asymmetry has been found. The finite scattering angle of our polystyrene spheres could explain a higher concentration of incoherent light for an incident converging beam, which would outshine the coherent part. Although this assumption appears unlikely in light of the small differences in incident angle with respect to the angular smear of the spheres, this theory necessitates further study.

Position-integrated momentum distributions of the EBS peak display reasonably well the transition from Gaussian to triangular back to Gaussian shape, with increasing path-delay, as predicted by our time-dependent extension of Akkerman's theory [62]. With increasing path-delay, the measured momentum-distribution becomes much narrower than predicted, displaying additional side-peaks closing in on the main peak. The reason for those features, also seen in phase-space scans, is still unknown, but can probably also be attributed to anisotropic scattering. To our knowledge, there is no analytical method to calculate the shape of an EBS cone for anisotropic scattering; therefore, future numerical simulations might be required.

Chapter 13

Transmission through random media

Measurement of the transmission of light through a medium is the simplest way to determine parameters of the scatterers inside the medium. In the following, we will look at the transmission through a turbid medium consisting of 10 μm polystyrene spheres suspended in a neutral buoyancy solution. First, we will take measurements with the Single-Window technique which does not allow for the immediate distinction between coherent and incoherent contributions, but which can be modelled relatively easily, using a Monte-Carlo simulation I developed for two scatter events or more.

In the second part we employ the Two-Window technique which directly allows the detection of coherence but which poses a much greater challenge in modelling.

13.1 Experimental setup

The setup modifications for transmission measurements and its adjustment are relatively simple compared to that for backscattering measurements. Figure 13.1 shows those modifications close to the detection input plane. The Signal beam passes through the sample cell containing the turbid medium. The surface of the turbid

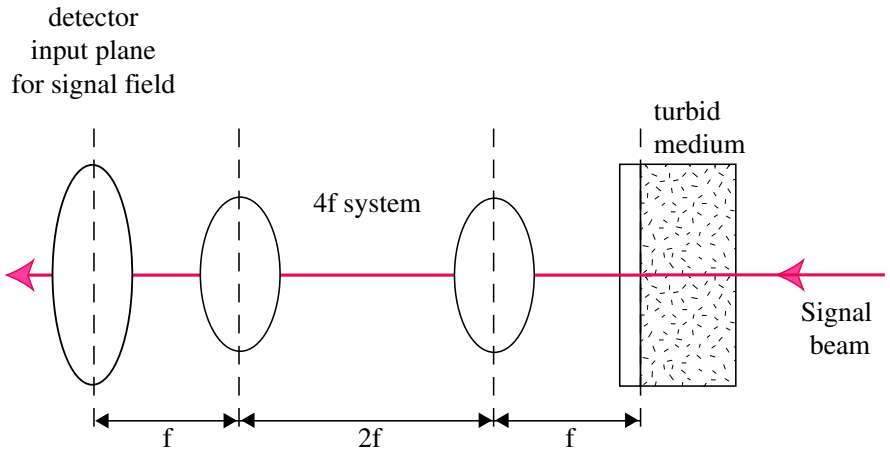

Figure 13.1: Modification for the measurement of transmission characteristics of a sample of turbid medium.

medium is in one focal plane of the 4f-system; the detection input plane is in the other focal plane. Thereby the Signal field emerging at the surface of the turbid medium is directly projected into the detection plane (compare Section 5.7).

13.2 Single-Window technique

In the following we investigate the scattering of a collimated beam through a tenuous medium using a single LO. In that case, the experimental results can be modelled using a relatively easy Monte-Carlo simulation for two-scattering events. Thereby, some previously reported, but hitherto unexplained phenomena [5], can be understood.

Figure 13.2 shows the measured phase-space distribution of a collimated Signal beam (σ_s=240 mm) through a turbid medium consisting of suspended polystyrene spheres with a diameter of 9.9 μm (cross-section: 156.5 μm^2) at a concentration of 4.2×10^6 spheres/cm^3. In this case, the light has a mean free path (mfp) of 1.96 mm,

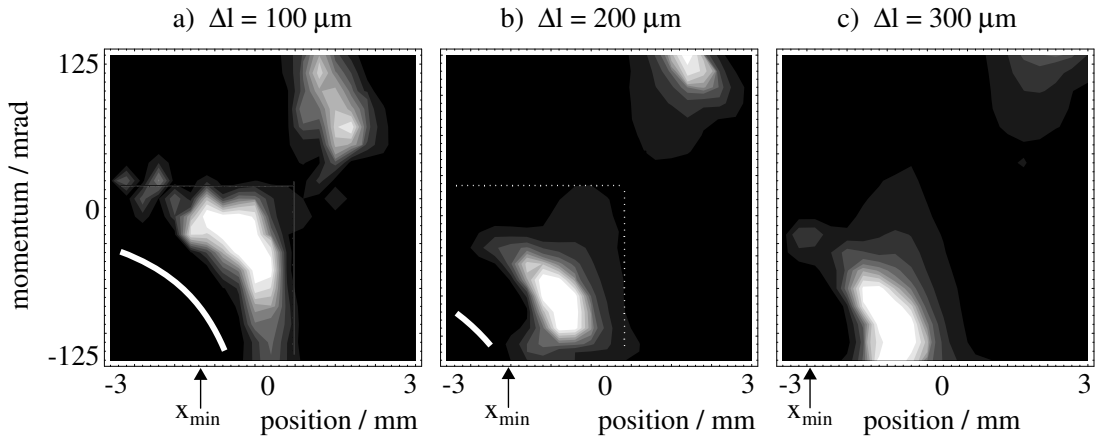

Figure 13.2: One-Window phase-space scan (high p-range) for Gaussian beam in transmission for path delays (from left to right) of 100, 200 and 300 μm (74, 147 and 221 μm in the medium). Sample: 4.2×10^6 spheres/cm^3, sphere diameter 9.9 μm; mfp=1.96 mm, cell length=10 mm. The white lines mark the phase-space line expected from single scattering; the x_{min} arrows mark the maximal distance allowed with respect to the center of an incident beam of zero diameter.

which is about 1/5 of the sample length (10 mm). The phase-space was scanned at three different path-delays; 100, 200 and 300 μm (74, 147 and 221 μm in the medium). The range of measurement is $\pm$3 mm in position and $\pm$125 mrad in momentum, which is close to the maximum momentum range of our system. The phase-space profiles exhibit a hyperbolic appearance with two maxima which move away from the phase-space center for increasing path delay. The white lines added to the plots and the arrows marked "x_{min}" will be explained further below.

Figure 13.3 shows a similar scan for two different scatterer concentrations of 4.2×10^6 spheres/cm^3 (a) and 7.5×10^6 spheres/cm^3 (b) at a path delay of 100 μm (74 μm in the medium). While the edge of the contour, describing a hyperbole, remains unaffected, the scattering contributions close to the zero position and momentum are stronger for higher concentration. This can intuitively be understood: Due to the fixed path-delay, light taking a straight line through a tenuous medium will

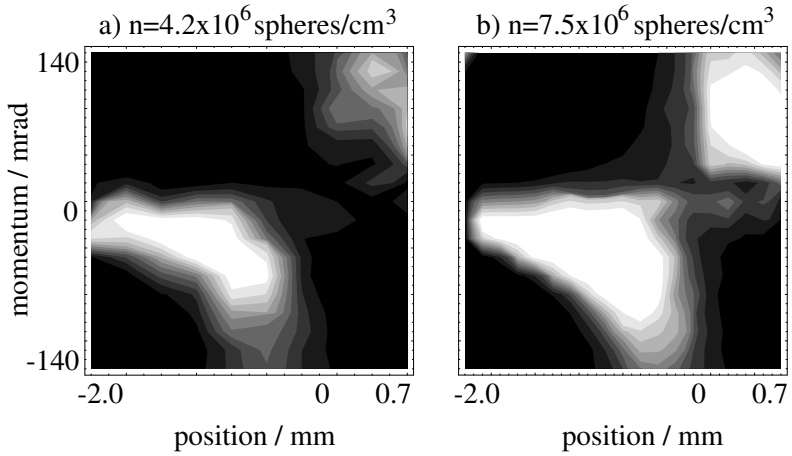

Figure 13.3: One-Window phase-space scan (high p-range) for Gaussian beam in transmission for various concentrations. Left: Sample 7.5×10^6 spheres/cm^3, mfp=1.01 mm. Right: Sample 4.2×10^6 spheres/cm^3, mfp=1.96 mm. Both samples: path delay 100 μm (74 μm in the medium), sphere diameter 9.9 μm, cell length=10 mm.

be discriminated against. If the light scatters only once, all detected contributions for non-zero path delay come from non-zero transverse position x and transverse momentum p. In fact, the relation between x and p for this case is

$$\begin{aligned} x &= \frac{\Delta l}{p/k}\left(1+\sqrt{1-(p/k)^2}\right) \\ &\approx 2\frac{\Delta l}{p/k}, \quad |p|/k \ll 1. \end{aligned} \tag{13.1}$$

which will be derived in Appendix C. Δl is again the selected path-delay in the medium. The approximation in Eq. (13.1) is more than 1% accurate for the momenta we measure in our experiment. If the concentration of scatterers is high enough, a photon can scatter more than once. For two scattering events, the photon might either regain its original momentum or position but not both, which can

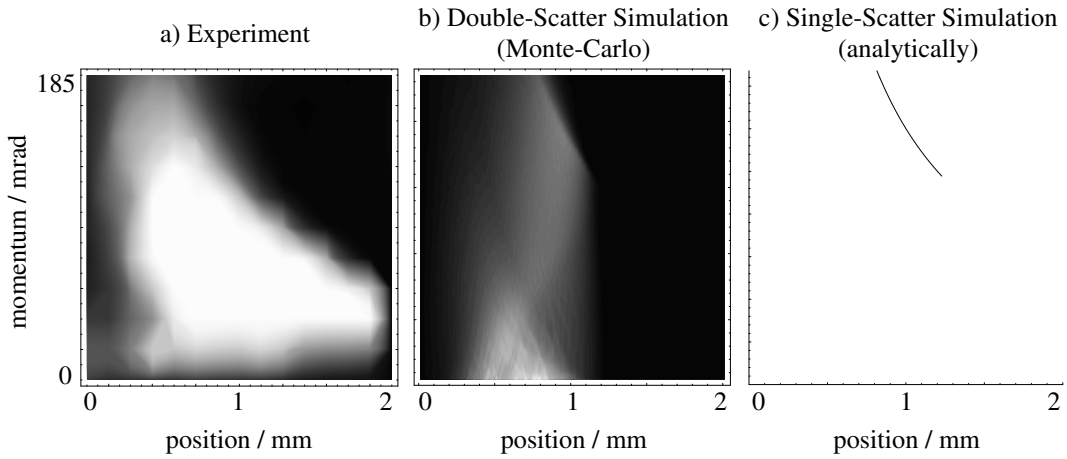

Figure 13.4: Comparison of the experimental results (a) for a sample of 7.5×10^6 spheres/cm^3 with double- (b) and single-scattering (c) theory, at a path-delay of 100 μm (74 μm in the medium). The double-scattering theory plot is evaluated numerically using a C++ Monte-Carlo algorithm, the single-scattering is calculated analytically.

easily be verified by drawing a ray diagram. For higher-order scattering events, the void at (x, p)=0 will be gradually filled.

Figure 13.4 shows the experimental data (a) for a concentration of 7.5×10^6 spheres/cm^3 and a path-delay of 100 μm (74 μm in the medium) from the left side of Figure 13.3 compared to a Monte-Carlo simulation of dual-scattering (b) and the analytical model for single scattering (c) in Eq. (13.1). Both the single- and dual-scattering model are described in Appendix C. The data shown has been taken from the third quadrant in Figure 13.3 and inverted in momentum and position for visual clarity. This can be done with impunity due to the mirror symmetry of the data.

The measured phase-space profile displays, as already described above, a filled area between a hyperbola and the point of incidence at (x,p)=0. The dual-scatter simulation in the middle shows the same hyperbolic edge as the single-scatter line,

both of which abruptly end at about 1.2 mm. This is the position at which a photon emerging at the sample output surface has moved as far away from the point of incidence as permitted by the fixed path-delay and the length of the sample, which is the case when the photon scatters right after entering the turbid medium (see Eq. (C.11))

$$x_{max} = \sqrt{2L\Delta l + (\Delta l)^2} \approx 1.22\,\mathrm{mm} \tag{13.2}$$

for Δl=74 μm in the medium and a sample length of L=10 mm.

The experimental data shows contributions outside the cut-off position which still seems to follow the hyperbolic shape dictated by a single-scatter event. This behavior suggests the contribution from much larger path-delays. So far, no satisfying explanation could be found.

In Figure 13.2 the phase-space line and x_{max} predicted from the single-scatter model were added to the measured phase-space plots. The phase-space line for Δl = 300 μm lies outside the depicted region. All contours lie inside the region confined by the single scatter line, and the transverse position of all contributions is smaller than x_{max}. There are no visible contributions from single scattering in the experimental data. Interestingly, the hyperbolic edge of the measured phase-space contour follows the phase-space line defined by single scattering, the reason of which is not yet understood.

For phase-space scans along a much smaller momentum range of $\pm$4 mrad, an interesting column structure can be found. Figure 13.5 shows the experimental data for 30, 100, 200, 300 and 400 μm path-delay. For Δl=30 μm, an incoherent single column is apparent. The ballistic contribution has been suppressed by slightly tilting the sample vertically, thereby shifting the beam slightly in y-direction. With

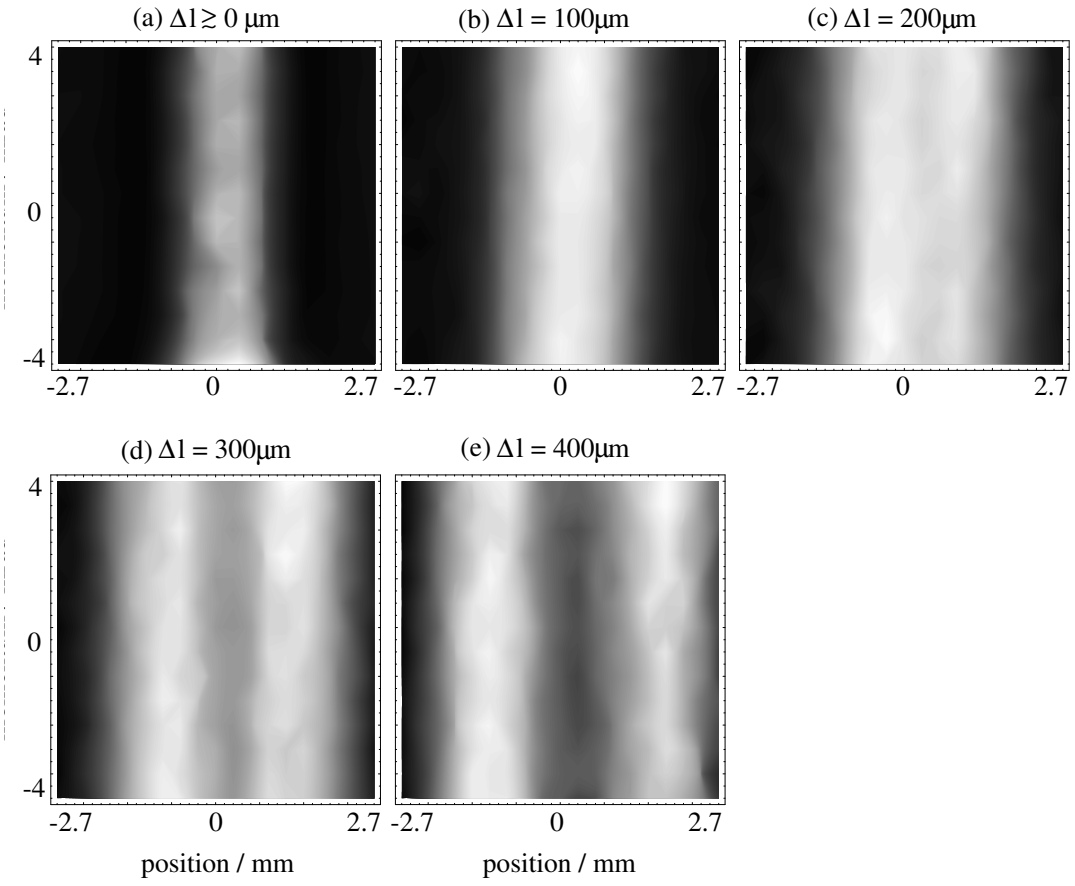

Figure 13.5: One-Window phase-space profile (low p-range) for Gaussian beam in transmission for various path delays. Sample: 4.2×10^6 spheres/cm^3, sphere diameter 9.9 μm; mfp=1.96 mm, cell length=10 mm.

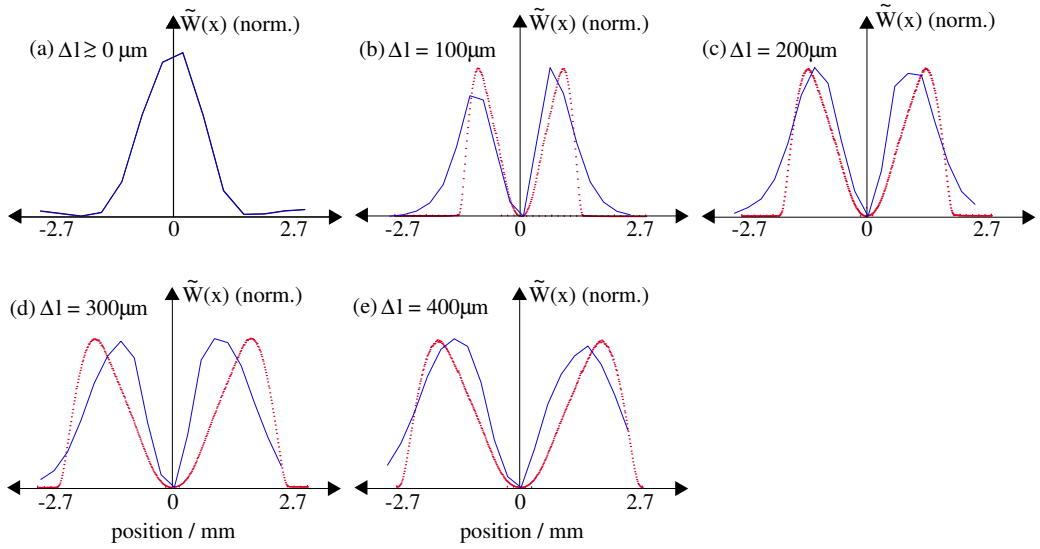

Figure 13.6: p-integrated phase-space profile from Figure 13.5. (a) Ballistic light, (b)-(e): ballistic contribution subtracted (solid line) and two-scatter numerical simulation (finely dotted line)

increasing path-delay, the column splits up into two columns which move away from the position of incidence.

Figure 13.6(b)-(e) show the momentum-integrated position distribution of the phase-space scan (solid line) from Figure 13.5, minus the momentum-integrated ballistic contribution seen in (a). There is still a ballistic contribution for larger path-delays, even though to a lesser degree. The dual-scattering Monte-Carlo model generates a similar double-column phase-space structure as seen in Figure 13.5. The finely dotted lines in Figure 13.6 show the momentum-integrated position distribution generated in this simulation. For small path-delays, the agreement between the measured position distribution and the dual-scattering model are very good; for larger path delay the model predicts a larger distance between the peaks than measured. This might be because of an increasing dominance of higher scattering

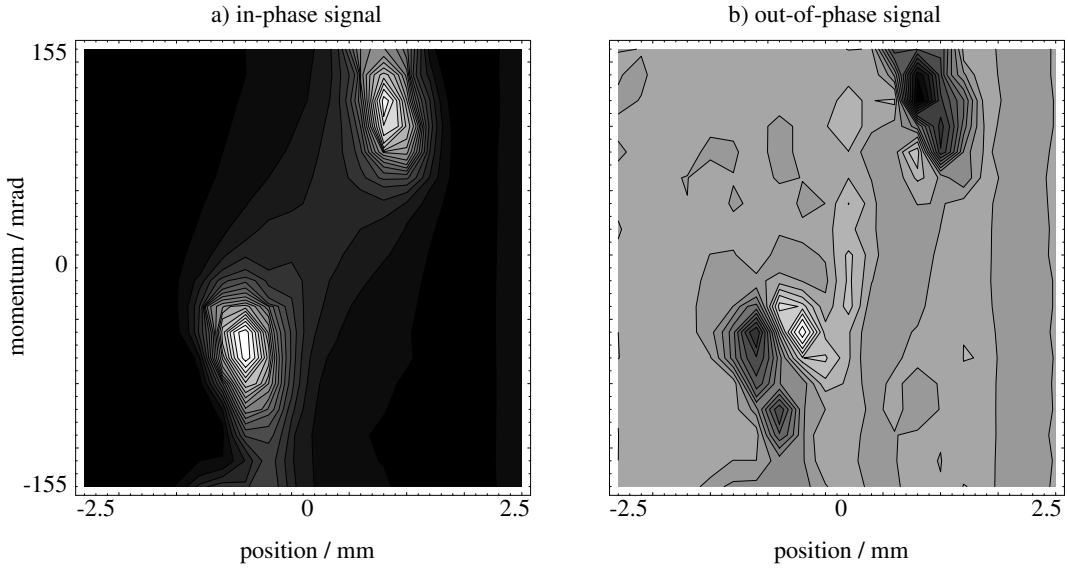

Figure 13.7: Dual-LO phase-space scan of collimated beam in transmission through turbid medium. Δl=100 μm (74 μm in the medium). Sample: 7.5×10^7 spheres/cm^3, sphere diameter 9.9 μm; mfp=1.1 mm, cell length=10 mm. a) in-phase, b) out-of-phase signal.

orders for larger path-delays, which contribute to the signal around x=0, thereby moving the peaks closer together.

13.3 Two-Window technique

In this section we investigate the coherence properties of low-coherence light scattered in turbid media by means of our Two-Window technique. A dual-scattering model that takes into account phase-information has not been developed yet. The experimental data shows some interesting preservation of coherence for low-order scattered light.

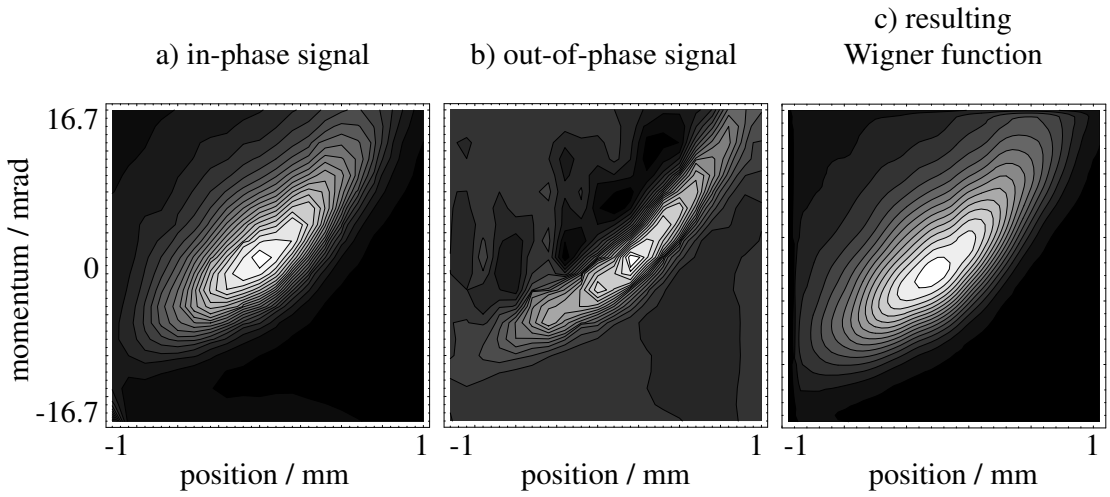

Figure 13.8: Close-up of the quadrature signals (a), (b) of the "upper right" peak in Figure 13.7 and the resulting Wigner function. The shape discrepancy between the phase-space profiles is due to the different ratio of scanned position and momentum range. Notice the negative-valued area bordering the positive-valued in the out-of-phase signal.

13.3.1 Gaussian input beam

Figure 13.7 shows a large-momentum range Dual-LO phase-space scan of a collimated beam of σ_s=240 μm passing through a tenuous medium at a path-delay of 100 μm, similar to the Single-LO scan in Figure 13.2. The out-of-phase signal displays areas with positive and negative values around the region where the peaks in the in-phase signal are. This means that there is a fixed phase-relation between the Signal field and the LO-beam in that phase-space region; in other words, the phase of the scattered field is at least partially preserved. The Wigner function can not be retrieved from the quadrature signals due to the small resolution of the scan.

A scan over a smaller phase-space region around the "upper right" peak in Figure 13.7 reveals the peak structure in more detail and enables the calculation of a Wigner function. Figure 13.8 shows the quadrature signals (a), (b) and the

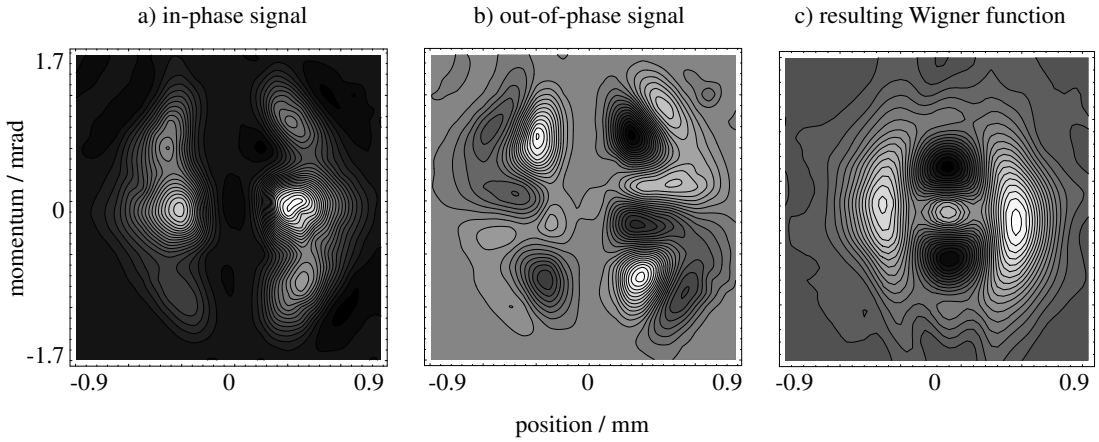

Figure 13.9: Quadrature signals (a), (b) and Wigner function (c) of the Signal beam blocked by wire in the center. The Signal beam, prepared like this, is incident on the turbid medium.

resulting Wigner function (c) over 10% of the momentum- and 40% of the position range of the scan in Figure 13.7. The out-of-phase signal displays 2 bordering areas with positive and negative values around the peak, implying the conservation of the phase of the incident field. The shape of the peak appears to be different than in the large-range scan in Figure 13.7, which is most likely due to the different ratio between measured position- and momentum range, as well as the different resolution grid of the scans.

13.3.2 Gaussian input beam blocked by a wire

In order to study the preservation of beam properties in more detail, the center of the Signal beam is blocked by a syringe tip with a diameter of 0.4mm before it is sent through the turbid medium. Figure 13.9 shows a high-resolution scan of the such prepared Signal beam taken prior to the transmission experiments. Depicted are the in-phase- (a) and out-of-phase (b) signal as well as the resulting Wigner function (c). The Wigner function shows the beam lobes passing left and right to

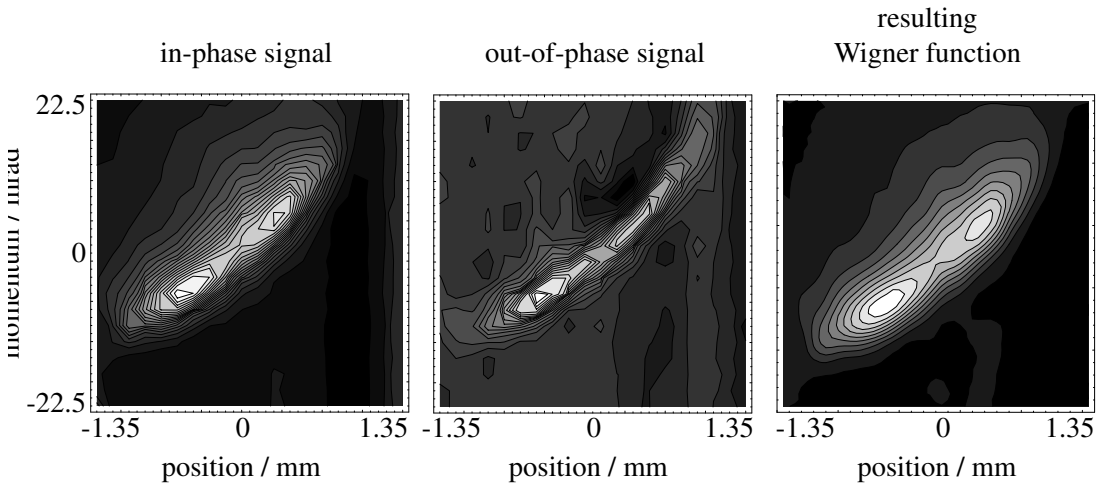

Figure 13.10: Close-up of "upper right" peak, this time with the center of the incident beam blocked by a wire. a) in-phase-, b) out-of-phase quadrature signal, c) resulting Wigner function.

the wire and the characteristic interference terms in momentum for zero position [1].

For this specially prepared incident Signal beam, the phase-space profile of the scattered field on the output surface of the turbid medium looks very similar to the one for an ordinary Gaussian incident beam, as shown in Figure 13.7. In particular, the "upper-right" peak in Figure 13.8 remains at the same location in phase-space, which is approximately (x,p)=(1 mm, 120 mrad).

But a close-up of this peak reveals that it has changed its shape: Figure 13.10 shows a scan of this peak in more detail. Remarkably, the two wings in position of the incident beam (Figure 13.9) can still be distinguished in the scattered field, even though their distance and angular distance have changed. Those wings seem to have preserved their coherence at least partially, since the out-of-phase signal displays the same distinctive regions with positive and negative values as in Figure 13.8. Interestingly, the interference pattern in momentum at zero position, visible in the Wigner function of the incident beam (Figure 13.9, on the right), can not be seen

for the scattered field, which could be due to a decrease in coherence.

13.4 Discussion and Summary

Both the Single- and Two-Window technique enable the characterization of the propagation of partially coherent light in turbid media. We have examined the path-length dependent locations in phase-space of two peaks resulting from low-order scattering (Section 13.2). We also demonstrated the greater contribution of higher-order scattering to the (smoothed) Wigner function in the phase-space region close to the incident beam. The borders of the (smoothed) Wigner function are defined by a hyperbola, independent on the number of scatterers involved, which agrees with predictions by an analytical calculation of time-resolved single-scattering as well as a Monte-Carlo simulation of time-resolved double-scattering.

For small transverse momenta the smoothed Wigner function consists of two incoherent, spatially confined structures, which move apart with increasing path delay. This phenomenon, which is due to the finite size of the incident beam, can not be explained by the single-scattering theory, which predicts two peaks with momenta 2 orders of magnitude larger than the ones contained in the phase-space measured in this scan. The double-scattering theory describes the location of the columns increasingly well for larger path-delays. The main contribution close to the location of the incident beam (x=0) for small path-delays can not be explained by either theory and is most likely due to multiple, almost forward scattered light.

The two phase-space peaks observed as a result of low-order scattering in Section 13.2 partially conserve the coherence of the incident field, as measurements with the Two-Window technique confirm (Section 13.3). Even the spatial profile of the incident field is to a good degree conserved, as measurements with a specially

prepared incident beam, a Gaussian beam whose center is blocked by a wire, show.

Chapter 14

Summary

In this dissertation, I presented a new Two-Window Heterodyne method which allows the direct measurement of the Wigner function of a light field. Wigner functions present a convenient way to fully characterize light fields up to their first-order-coherence properties; they simultaneously describe the transverse position and momentum of a light field while preserving all phase and amplitude information of the field. Wigner functions obey rigorous transport equations and are a convenient way to describe the propagation of fields. Our new technique also allows us for the first time to directly distinguish between coherent and incoherent parts of the field by means of the out-of-phase quadrature signal, which, together with the in-phase signal, comprises the measured complex beat signal. Due to the low-coherence light we employ, the measurements are time-resolved, which allows us to exclusively detect photons that have travelled a given path length in the medium under investigation. This time-resolution in combination with the combination of high position- and momentum resolution of this method will enable new ways of characterizing light fields scattered from, for example, biological samples and thereby refine the determination of their structural properties.

The Two-Window technique is based on the heterodyne detection of the two beat notes resulting from the superposition of the measured signal field and a so-

called Dual-LO, which consists of a superposed, phase-coupled set of a focused LO (SLO) and a collimated beam (BLO). The focused beam determines the spatial x resolution and the collimated beam the momental p resolution. This is different from the One-Window method we formerly employed where we used a single LO which determined the resolution of both x and p, leading to a trade-off between both resolutions. In that case, only smoothed Wigner functions can be measured, which are the convolution between the true Wigner function of the Signal field and the spatial and momental profile of the LO. The Two-Window technique on the other hand allows the measurement of true Wigner functions, given that the SLO is sufficiently focused and the BLO sufficiently collimated. The Wigner function can be retrieved from the measured complex beat signal by an inverse Margenau-Hill transformation.

By varying the relative path-delay between Signal beam and Dual-LO, photons that have travelled a given path in the medium can be detected exclusively. Since the measured beat signal is proportional to the square root of the power of the signal field rather than the power itself, as in direct intensity measurements, the dynamic range is very high: for a Dual-LO on the order of a milliwatt, signal fields of less than a femtowatt can be detected. The dynamic range is 130 dB.

The power of this method is first demonstrated in the determination of basic field parameters of a Gaussian Signal beam in Chapter 7 and Chapter 8, where we show how to retrieve its beam size, transverse coherence and radius of curvature. This method is also applicable to more complicated fields. In Chapter 9 we examine the longitudinal properties of the Signal field, which are related to its optical spectrum. The broad spectrum of the superluminescent diode we use as our light source is responsible for the short longitudinal coherence length of 25 μm that can

be experimentally verified straightforwardly. The origin of other features seen in the longitudinal scans, such as a phase-gradient, are still subject to debate. For a laser diode with several transverse modes, this technique offers the possibility of measuring the frequency-offset from the center-frequency as well as the spatial and momental profile of those modes.

The second part of this thesis examines the propagation of a partially coherent field in turbid media. Our turbid medium consists of polystyrene spheres suspended in a neutral-buoyancy glycerol-water solution. We use two different sphere diameters; 0.5 μm, which is close to the wavelength of our light (678.3 nm) and therefore provides a broad angular scattering distribution, and 10 μm, where the field scatters within a very narrow forward-cone.

In Chapter 11 and Chapter 12 we investigate the Enhanced Backscattering effect by measuring the Wigner function of a field scattered from a relatively dense turbid medium with highly scattering spheres (0.5 μm diameter). Enhanced Backscattering describes the phenomenon of constructive interference of two counter-propagating wavelets scattered in a turbid medium by the same sequence of scatterers. This leads to twice the intensity of the backscattered field opposite to the direction of incidence compared to other directions.

First, we shine a collimated beam onto the medium and observe how the Enhanced Backscattered peak becomes more narrow with increasing path-delay. We study the momentum distribution in more detail by position-integrating the backscattered field. The change in shape of the momentum distribution allows us to estimate the number of scatterers in a typical sequence.

For the first time we directly show the phase-conjugating properties of turbid media by having a divergent or convergent Signal beam incident onto the medium

and observe the change of sign of the radius of curvature of the Enhanced Backscattered field. This works best with a divergent incident beam, where the Enhanced Backscattered cone is convergent. The reason for the discrepancy between convergent and divergent incident beam configuration is still unknown, yet several possible explanations are discussed.

We can explain the general behavior of the Enhanced Backscattered field, such as the ratio of coherently and incoherently backscattered light, the narrowing of the momentum distribution for increasing path-delay, and the inversion of the radius of curvature for incident light with a curved wavefront, by a theory in which the propagation of the Wigner function in the medium obeys the diffusion equation.

We study the time-resolved propagation of partially coherent light through turbid media of various concentrations in the transmission regime in Chapter 13. For tenuous to intermediate scatterer concentrations we observe two peaks in phase-space probably as the result of low-order scattering and the path-length constraint imposed by the time-resolution of our technique. We demonstrate how their relative distance becomes bigger with increasing path-delay. The Wigner function of the transmitted field for a given path-delay is confined in phase-space by a hyperbolic edge which comes from single-scatter events. The contributions close to the region in phase-space where the incident beam is located are relatively small for tenuous media, but become stronger with increasing concentration of scatterers. This region displays two column-shaped incoherent structures which are due to the finite size in phase-space of the incident beam and which move apart with increasing path-delay. While the explanation for the short distance between the columns for small path-delays probably lies in higher-order scattering, for larger path-delay a two-scattering Monte-Carlo algorithm I developed models the distance of the

columns correctly. This suggests that for large path-delays, the path-length restriction, probably in combination with the narrow phase function of the 10 μm spheres, increases the contributions from scattering paths which follow those expected for double-scattering. Additional experiments with smaller scatterers could probably illuminate this question.

Measurements of the transmitted time-resolved Wigner function by means of the Two-Window technique reveal coherence of low-order scattered light, which manifests itself in a slowly changing phase distribution around the two peaks in phase-space which result from low-order scattering. Even spatial properties of the incident beams are conserved: When we block the center of the incident beam by a wire, the two lobes passing to the right and left of the wire show up in each of the two peaks. While the peaks still display coherence, they do so to a lesser degree than the incident field.

While many aspects of the propagation of partially coherent light in turbid media are understood, there are still many open questions. For example, the Enhanced Backscattered fields measured in our experiment averages over areas several times as large as the coherence area of the EBS cone, because of the finite size of our SLO. The coherence area of an EBS cone has a diameter the typical size of the diffusion path $\sqrt{Dt} = \frac{1}{3} l^* \Delta l / n_0$, where D is the diffusion constant of the intensity in the medium, t the time after entering the medium, l^* is the transport mean free path, Δl the length of the path in the medium and n_0 the refractive index of the solution between the scatterers. In future experiments, we plan to resolve the Wigner function *within* a single coherence area by using a magnifying 4f-system to gain a deeper understanding of the properties of the EBS field. This might also clarify the origin of the momentum-side peaks of the EBS cone as seen in

Figure 12.3, for example. Those peaks could hint towards aberrations from the diffusion equation usually used to model Enhanced Backscattering.

Appendix A

Circuit diagrams

A.1 Temperature control

Figure A.1 shows the temperature control for the SLD. It measures the temperature close to the SLD by means of a temperature-dependent resistor (NTC, *negative temperature coefficient*), which is mounted on top of the SLD in its casing. If the temperature deviates from a selected value, the temperature control sends a positive or negative current to a Peltier element which is mounted next to the SLD in its casing, until the temperature difference drops below a certain value.

The centerpiece of the temperature control consists of a Wien bridge, with the NTC being one of its four resistors. The reference resistance is selected by an array of resistors and a potentiometer as shown in Figure A.2. When the resistance of the NTC falls below or rises above that reference value, the Wien bridge delivers a positive or negative voltage, which is amplified in comparer IC1. A low-pass filter at its input slows down its operation to avoid oscillations. Operational amplifier IC2 buffers the voltage for an analog display. Switch S permits switching between two different resolutions of the voltage-proportional temperature inside the SLD casing. Operational amplifier IC3 amplifies the Wien bridge voltage and controls the power amplifier. It also acts as an integrator, with the RC-(glied) in its feedback

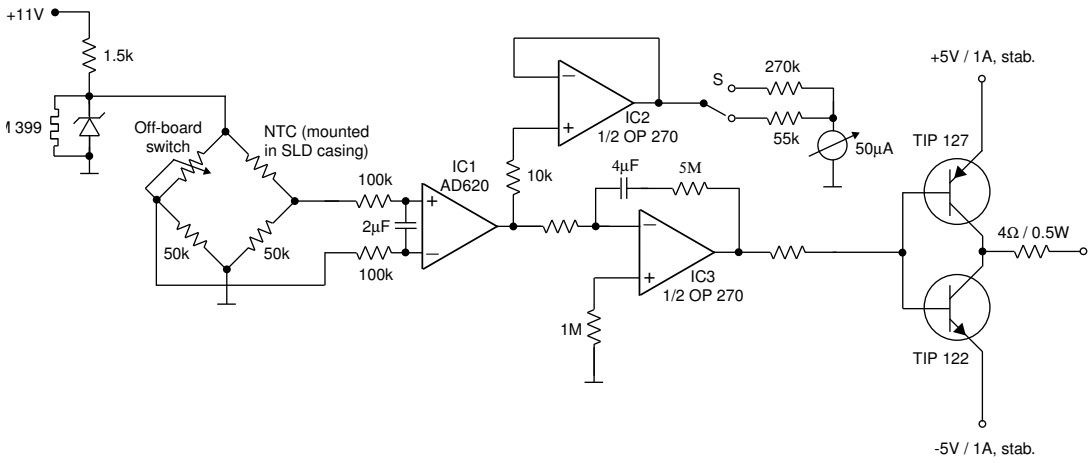

Figure A.1: Circuit diagram of the temperature control for the SLD. The variable resistor in the Wien bridge is the off-board switch shown in Figure A.2.

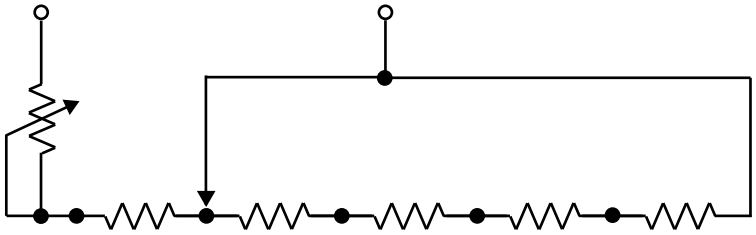

Figure A.2: Circuit diagram of the off-board switch used in the temperature control for the SLD.

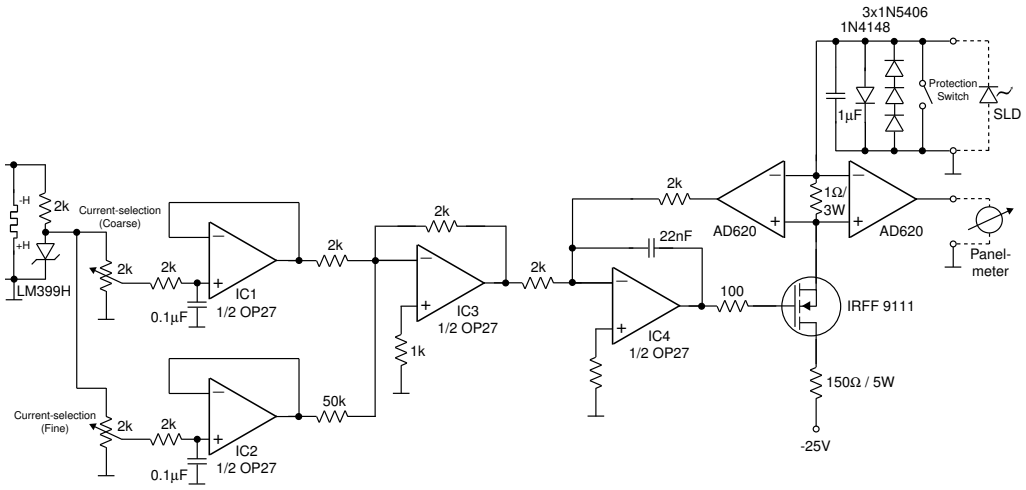

Figure A.3: Circuit diagram of the power supply for the SLD.

determining its time constant. This time constant has to be chosen so that the temperature control neither 'overreacts' nor 'underreacts'. In the former case, the response to a temperature difference from the selected value will be too strong, leading to overcooling and overheating in an oscillatory manner, with a slow overall convergence. In the latter case, the response will be too weak, also leading to a slow convergence.

The power amplifier feeding the Peltier element consists of two bipolar transistors in push-pull configuration, which can provide currents of both polarities for the Peltier element.

A.2 Power supply

The power supply (Figure A.3) works as a current source for the SLD. A current source is preferred over a voltage source because of the exponential I-V-characteristics of an SLD. The output current is selected by a reference voltage and stabilized by

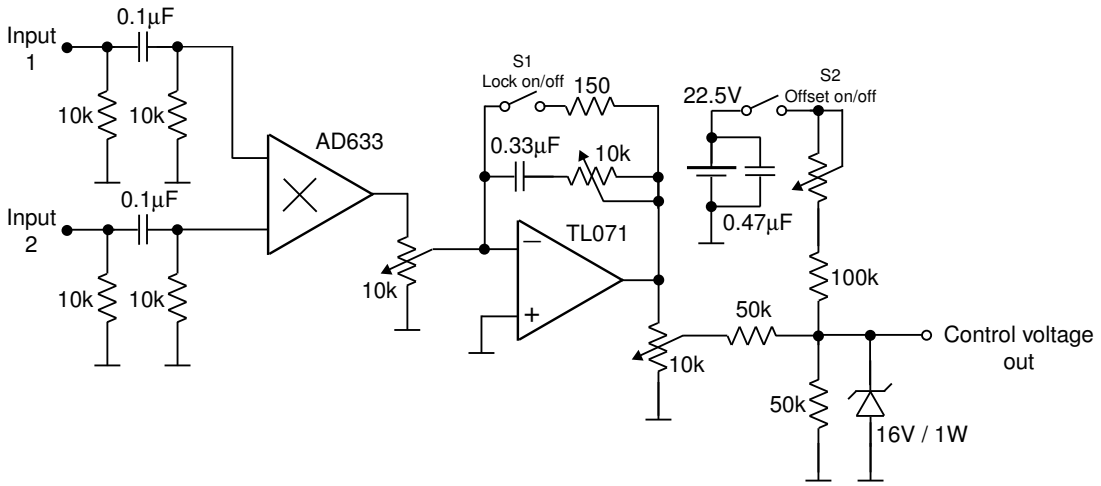

Figure A.4: Circuit diagram of the phase-locked loop.

comparing that voltage to the voltage drop across a resistor in the output circuit.

The reference voltage is generated by the operational amplifiers IC1-IC3. IC1 and IC2 both provide currents to IC3. IC3 adds both currents and generates am output voltage which is proportional to the sum. This voltage is added to the voltage drop across a low-ohmic resistor in the output circuit of the power MOSFET. The sum of the two voltages is fed into operational amplifier IC4, which acts a low-pass filter to filter out spikes (generated for example by dust in the potentiometer when selecting a current) and determines the time-constant of the feedback loop. Its output signal controls the gate of the power MOSFET IFF9111 which provides the current for the SLD.

A.3 Phase-locked loop

The phase-locked loop (Figure A.4) multiplies the two voltages at input 1 and 2 and generates an error voltage which is proportional to the the time-averaged product

of both voltages. This voltage is added to an offset-voltage provided by a battery; that sum is available at the 'Control voltage out' connector.

The high-passes at the inputs of multiplier AD633 block DC contributions and low-frequency noise. The fraction of the output voltage of the multiplier selected by the potentiometer is fed into a low-pass. The amplitude of the output voltage is selected by the *Amplitude* potentiometer. An offset voltage, which sets the center frequency of the AO-drivers, is added and the sum of both voltages is sent to the output connector of the PLL.

Appendix B

Various calculations

B.1 $\langle \mathcal{E}^*(x)\mathcal{E}(p)\rangle$ for finite R

In the following the explicit derivation of the additional phase contribution of $\langle \mathcal{E}^*(x)\mathcal{E}(p)\rangle$ for finite radii of curvature is presented. The Signal beam for a finite radius of curvature is

$$\begin{aligned} \mathcal{E}_S(x) &= \exp\left(-\frac{x^2}{a^2} + i\frac{k}{R}x^2\right) \\ &\equiv \exp(-\alpha x^2) \end{aligned} \tag{B.1}$$

where $\alpha = \frac{1}{a^2} - ib$ and $b = \frac{k}{R}$. a describes the diameter of the beam, R its radius of curvature and k is the wavenumber. $\mathcal{E}(p)$ follows by Fourier transformation of Eq. (B.1):

$$\begin{aligned} \mathcal{E}_S(p) &= \int dx\, e^{ipx} \exp(-\alpha x^2) \\ &= \frac{\pi}{\alpha} \exp(-\frac{p^2}{4\alpha}). \end{aligned} \tag{B.2}$$

$\langle \mathcal{E}^*(x)\mathcal{E}(p)\rangle$ then becomes

$$\begin{aligned}
\mathcal{E}_S^*(x)\mathcal{E}_S(p) &= \frac{\pi}{\alpha}\exp(-\alpha^* x^2)\exp(-\frac{p^2}{4\alpha}) \\
&= \frac{\pi\alpha^*}{\mid\alpha\mid^2}\exp[-\alpha^* x^2 - \frac{\alpha^*}{4\mid\alpha\mid^2}p^2] \\
&= \frac{\pi}{\mid\alpha\mid^2}(\frac{1}{a^2}+ib)\exp[-\frac{1}{a^2}(x^2+\frac{p^2}{4\mid\alpha\mid^2})]\exp[-ib(x^2+\frac{p^2}{4\mid\alpha\mid^2})] \\
&= \frac{\pi}{\mid\alpha\mid}\exp[-\frac{1}{a^2}(x^2+\frac{p^2}{4\mid\alpha\mid^2})] \\
&\times \exp\{i\,[\arctan(\frac{ka^2}{R}) - \frac{k}{R}(x^2+\frac{p^2}{4\mid\alpha\mid^2})]\}
\end{aligned} \tag{B.3}$$

with $\mid\alpha\mid = \sqrt{\frac{1}{a^4}+(\frac{k}{R})^2}$. In the last step we have made use of the general transformation

$$x + iy = \sqrt{x^2+y^2}\exp(i\,\arctan\frac{y}{x}). \tag{B.4}$$

which is unambiguous since $x = \frac{1}{a^2}$ is always positive.

B.2 Peak locations of out-of-phase signal

Solving Eq. (7.37) for $\tan\left(\frac{xp}{2}\right)$ leads to

$$\tan\left(\frac{x_m p_m}{2}\right) = \frac{p_m}{4ax_m} \tag{B.5}$$

and consequently

$$x_m p_m = 2\tan^{-1}\left(\frac{p_m}{4ax_m}\right). \tag{B.6}$$

Equating Equations (7.37) and (7.38) yields

$$\begin{aligned}
\frac{p_m}{4ax_m} &= \frac{x_m}{4bp_m} \\
\frac{b}{a} &= \frac{x_m^2}{p_m^2} && \text{(B.7)} \\
\frac{x_m}{p_m} &= \pm\sqrt{\frac{b}{a}} && \text{(B.8)} \\
x_m &= \pm p_m\sqrt{\frac{b}{a}}. && \text{(B.9)}
\end{aligned}$$

Inserting Equations (B.8) and (B.9) into Eq. (B.6) and replacing x_m gives us

$$\begin{aligned}
\pm p_m^2\sqrt{\frac{b}{a}} &= 2\tan^{-1}\left[\frac{1}{4a}\left(\pm\sqrt{\frac{a}{b}}\right)\right] = \pm 2\tan^{-1}\left(\frac{1}{4\sqrt{ab}}\right) \\
p_m^2 &= 2\sqrt{\frac{a}{b}}\tan^{-1}\left(\frac{1}{4\sqrt{ab}}\right) \\
p_m &= \pm\sqrt{2\sqrt{\frac{a}{b}}\tan^{-1}\left(\frac{1}{4\sqrt{ab}}\right)}. && \text{(B.10)}
\end{aligned}$$

We repeat this procedure, but this time we replace p_m:

$$\begin{aligned}
x_m^2\sqrt{\frac{a}{b}} &= 2\tan^{-1}\left(\frac{1}{4\sqrt{ab}}\right) \\
x_m &= \pm\sqrt{2\sqrt{\frac{b}{a}}\tan^{-1}\left(\frac{1}{4\sqrt{ab}}\right)}. && \text{(B.11)}
\end{aligned}$$

When we substitute a and b back into Equations (B.10) and (B.11) according to Equations (7.33) and (7.34) we receive Equations (7.41) and (7.42):

$$x_m = \sqrt{2\frac{d_x^e}{p_x^e}\tan^{-1}\left(\frac{d_x^e p_x^e}{4}\right)} \tag{B.12}$$

$$p_m = \sqrt{2\frac{p_x^e}{d_x^e}\tan^{-1}\left(\frac{d_x^e p_x^e}{4}\right)}. \tag{B.13}$$

B.3 Detection of misalignment by means of $S_B(z)$

For a perfect Gaussian-Schell source, we expect a potential phase-gradient detected in longitudinal scans in Chapter 9 be due to different-sized beam waists of the LO's comprising the Dual-LO, as discussed in that chapter. In the following we assume the phase-gradient is caused by the focused SLO.

If we set the phase of the lock-in amplifier to zero while there is a finite path-difference Δl_{off} between S and the dual-LO, we can express the $S_B(\Delta l)$ as

$$S_B(\Delta l) = \exp\left[-\frac{(\Delta l - \Delta l_{off})^2}{(\Delta l_B)^2} - i\frac{\Delta l}{z_0}\right], \tag{B.14}$$

The out-of-phase part is then

$$\begin{aligned} S_B^{OP}(\Delta l) &= \sin\left(-\frac{\Delta l}{z_0}\right)\exp\left[-\frac{(\Delta l - \Delta l_{off})^2}{(\Delta l_B)^2}\right] \\ &= \frac{\Delta l}{z_0}\exp\left[-\frac{(\Delta l - \Delta l_{off})^2}{(\Delta l_B)^2}\right]. \end{aligned} \tag{B.15}$$

To find the location of the peaks, we set the derivative of $S_B^{OP}(\Delta l)$ to zero:

$$\begin{aligned}\frac{d}{d\Delta l}S_B^{OP}(\Delta l) &= 0 \\ &= \frac{1}{z_0}\exp\left[-\frac{(\Delta l-\Delta l_{off})^2}{(\Delta l_B)^2}\right] \\ &+ \frac{\Delta l}{z_0}\left[-2\frac{\Delta l-z_0}{(\Delta l_B)^2}\right]\exp\left[-\frac{(\Delta l-\Delta l_{off})^2}{(\Delta l_B)^2}\right].\end{aligned} \tag{B.16}$$

For this expression to vanish, the pre-factors of the exponentials must cancel:

$$\begin{aligned}1-2\frac{\Delta l(\Delta l-\Delta l_{off})}{(\Delta l_B)^2} &= 0 \\ \Delta l(\Delta l-\Delta l_{off}) &= \frac{(\Delta l_B)^2}{2} \\ \Delta l^2-\Delta l\Delta l_{off}-\frac{(\Delta l_B)^2}{2} &= 0,\end{aligned} \tag{B.17}$$

which has the two solutions

$$\Delta l_{1,2} = \frac{\Delta l_{off}}{2} \pm \sqrt{\frac{\Delta l_{off}^2}{4}+\frac{(\Delta l_B)^2}{2}}. \tag{B.18}$$

If we add Δl_2 and Δl_1, the square root term cancels:

$$\Delta l_1 + \Delta l_2 = \Delta l_{off} \tag{B.19}$$

If we choose the phase to be zero at the exact path-length match of S and the Dual LO, i.e. $\Delta l_{off} = 0$, the peaks are symmetrically centered around this location; so that $\Delta l_1 + \Delta l_2 = 0$.

The difference between Δl_2 and Δl_1 on the other hand is

$$\begin{aligned}\Delta l_2 - \Delta l_1 &= 2\sqrt{\frac{\Delta l_{off}^2}{4} + \frac{(\Delta l_B)^2}{2}} \\ &= \sqrt{\Delta l_{off}^2 + 2(\Delta l_B)^2} \end{aligned} \tag{B.20}$$

which reproduces the result in Eq. (9.9) for $\Delta l_{off} = 0$.

B.4 Complex beat signal for EBS field

In the following we will derive the complex beat signal $S_B(d_x, p_x)$ for an enhanced backscattered field. It consists of two parts: S_B^{coh}, which describes the coherently backscattered field (Section B.4.1), and S_B^{incoh} which describes the incoherent part of the backscattered field (Section B.4.2). The global coherence of the light of our SLD is very high ($\sigma_{glob} > 7$), therefore we can view its light as transversely coherent. We derive the complex beat signals for both parts separately and add them later on.

B.4.1 Complex S_B^{coh}

In this section, we will derive the complex beat signal for the coherently backscattered light of an EBS field. In the following calculations, all integrals are two-dimensional. For simplicity, we write d^2x as dx etc.

The complex beat signal is

$$S_B^{coh}(d_x, d_p) = \int dx dp \; W_{LO}(x - d_x, p + k\frac{d_p}{f_0}) \; W_B^c(x, p) \tag{B.21}$$

where

$$W_{LO}(x-d_x, p+k\frac{d_p}{f_0}) = \int \frac{dq}{(2\pi)^2} e^{iq(p+k\frac{d_p}{f_0})} \langle \mathcal{E}^*_{LO}(x+\frac{q}{2}-d_x)\, \mathcal{E}_{LO}(x-\frac{q}{2}-d_x)\rangle \quad \text{(B.22)}$$

and

$$W^{coh}_B(x,p) = \int dp_0 W_0(x,p_0) \exp[-Dt(p+p_0)^2] \quad \text{(B.23)}$$

with

$$W_0(x,p_0) = \int \frac{dq'}{(2\pi)^2} e^{iq'p_0} \langle \mathcal{E}^*_0(x+\frac{q'}{2})\mathcal{E}_0(x-\frac{q'}{2})\rangle \quad \text{(B.24)}$$

the expression for the complex beat signal follows:

$$\begin{aligned} S^{coh}_B(d_x,d_p) &= \frac{1}{16\pi^4}\int dx dq dq' \\ &\quad \langle \mathcal{E}^*_{LO}(x+\frac{q}{2}-d_x)\mathcal{E}_{LO}(x-\frac{q}{2}-dx)\rangle \langle \mathcal{E}^*_0(x+\frac{q'}{2})\mathcal{E}_0(x-\frac{q'}{2})\rangle \\ &\times \int dp dp_0 e^{iq(p+k\frac{d_p}{f_0})} e^{iq'p_0} \exp[-Dt(p+p_0)^2]. \quad \text{(B.25)} \end{aligned}$$

We measure the statistical average of $\langle \mathcal{E}_{LO}\mathcal{E}_0\rangle$ rather than the averages of $\mathcal{E}_{LO}$ and $\mathcal{E}_0$ with itself. That means we need to switch the angular brackets in the expression above. The integral $\int dp dp_0$ can be simplified as follows:

$$\begin{aligned}\int dpdp_0... &= e^{ik\frac{d_p}{f_0}q}\int dpdp_0 e^{iqp}e^{iq'p_0}\exp[-Dt(p+p_0)^2] \\ &= e^{ip_xq}\int dpe^{iqp}e^{-iq'p}\int dp_0 e^{iq'p_0}\exp[-Dtp_0^2] \\ &= \frac{4\pi^3}{Dt}e^{ip_xq}\exp\left(-\frac{q'^2}{4Dt}\right)\delta(q-q') \end{aligned} \tag{B.26}$$

where we replaced $k\frac{d_p}{f_0}$ with p_x. Inserting the above expression and switching the angular brackets we get:

$$\begin{aligned}S_B^{coh}(d_x,d_p) &= \frac{z_0^2}{4\pi^2(Dt)^2}\int dxdq\exp(-ip_xq)\exp\left(-\frac{q^2}{4Dt}\right) \\ &\times \langle\mathcal{E}_{LO}^*(x+\frac{q}{2}-d_x)\mathcal{E}_0(x-\frac{q}{2})\rangle\langle\mathcal{E}_{LO}(x-\frac{q}{2}-d_x)\mathcal{E}_0^*(x+\frac{q}{2})\rangle.\end{aligned} \tag{B.27}$$

The electric field of the Dual-LO is

$$\mathcal{E}_{LO}(x)\propto\exp\left(-\frac{x^2}{4\sigma_s^2a^2}\right)+\beta e^{i\theta}\exp\left(-\frac{x^2}{4\sigma_s^2A^2}\right):=\mathcal{E}_{LO}^a(x)+\beta e^{i\theta}\mathcal{E}_{LO}^A(x) \tag{B.28}$$

and for the Signal beam

$$\mathcal{E}_0(x)\propto\exp\left(-\frac{x^2}{4\sigma_s^2B^2}+i\frac{k}{2RB^2}x^2\right). \tag{B.29}$$

Here we introduced scaling factors A and a for the BLO and the SLO, and B for the Signal beam, which describe the different relative sizes of the beams. β is the amplitude of the BLO relative to the SLO, $e^{i\theta}$ the phase, where $\theta=\omega t$ is the locking

frequency of the LOs.

Since the global coherence of our light source is much larger than 1 ($\sigma_{glob} > 7$), we can set the exponential containing σ_g in Eq. (3.2) to 1, so that the mutual coherence function is just the product of the electric fields itself. The product of electrical fields in Eq. (B.27) is

$$\begin{aligned}\langle \mathcal{E}^*_{LO}(x_1)\mathcal{E}_0(x_2)\rangle\langle \mathcal{E}_{LO}(x_3)\mathcal{E}^*_0(x_4)\rangle &= (\langle \mathcal{E}^{a*}_{LO}(x_1)\mathcal{E}_0(x_2)\rangle + \beta e^{i\theta}\langle \mathcal{E}^{A*}_{LO}(x_1)\mathcal{E}_0(x_2)\rangle) \\ &\times (\langle \mathcal{E}^{a}_{LO}(x_3)\mathcal{E}^*_0(x_4)\rangle + \beta e^{-i\theta}\langle \mathcal{E}^{A}_{LO}(x_3)\mathcal{E}^*_0(x_4)\rangle)\end{aligned} \tag{B.30}$$

where we replaced the variables as follows

$$\begin{aligned} x_1 &\rightarrow x + \frac{q}{2} - d_x \\ x_2 &\rightarrow x - \frac{q}{2} \\ x_3 &\rightarrow x - \frac{q}{2} - d_x \\ x_4 &\rightarrow x + \frac{q}{2}. \end{aligned}$$

We detect the cross-terms only:

$$\beta e^{i\theta}\langle \mathcal{E}^{A*}_{LO}(x_1)\mathcal{E}_0(x_2)\rangle\langle \mathcal{E}^{a}_{LO}(x_3)\mathcal{E}^*_0(x_4)\rangle + \beta e^{-i\theta}\langle \mathcal{E}^{A}_{LO}(x_3)\mathcal{E}^*_0(x_4)\rangle\langle \mathcal{E}^{a*}_{LO}(x_1)\mathcal{E}_0(x_2)\rangle. \tag{B.31}$$

One sees that x_1 and x_3 as well es x_2 and x_4 are identical except for the sign of q. When we put the cross-terms back into (B.27) we get

$$
\begin{aligned}
S_B^{coh}(d_x,d_p) &= \frac{z_0^2}{4\pi^2(Dt)^2}\int dxdq\exp(-ip_xq)\exp\left(-\frac{q^2}{4Dt}\right)\\
&\times \Big[\beta e^{i\theta}\mathcal{E}_{LO}^{A*}(x-d_x+\frac{q}{2})\mathcal{E}_0(x-\frac{q}{2})\mathcal{E}_{LO}^{a}(x-d_x-\frac{q}{2})\mathcal{E}_0^*(x+\frac{q}{2})\\
&+ \beta e^{-i\theta}\langle\mathcal{E}_{LO}^{A}(x-d_x-\frac{q}{2})\mathcal{E}_0^*(x+\frac{q}{2})\rangle\langle\mathcal{E}_{LO}^{a*}(x-d_x+\frac{q}{2})\mathcal{E}_0(x-\frac{q}{2})\Big]\\
&= \frac{z_0^2}{4\pi^2(Dt)^2}\int dxdq\exp(-ip_xq)\exp\left(-\frac{q^2}{4Dt}\right)\\
&\times \Big[\beta e^{i\theta}\mathcal{E}_{LO}^{A*}(x-d_x+\frac{q}{2})\mathcal{E}_0(x-\frac{q}{2})\mathcal{E}_{LO}^{a}(x-d_x-\frac{q}{2})\mathcal{E}_0^*(x+\frac{q}{2})\Big]\\
&+ \text{c.c.}\\
&= s_B^{coh}(d_x,d_p)\text{+c.c} \qquad \text{(B.32)}
\end{aligned}
$$

where $s_B^{coh}(d_x,d_p)$ is the *complex beat signal* and *c.c.* stands for 'complex conjugate'. If we make the following variable transformation:

$$
\begin{aligned}
\eta &= x+\frac{q}{2} \qquad \text{(B.33)}\\
\xi &= x-\frac{q}{2} \qquad \text{(B.34)}
\end{aligned}
$$

we get

$$
\begin{aligned}
S_B^{coh}(d_x,d_p) &= \frac{z_0^2}{4\pi^2(Dt)^2}\int d\eta\, d\xi\exp[-i(\eta-\xi)p_x]\exp\left[-\frac{(\eta-\xi)^2}{4Dt}\right]\\
&\times \mathcal{E}_{LO}^{A*}(\eta-d_x)\mathcal{E}_0(\xi)\mathcal{E}_{LO}^{a}(\xi-d_x)\mathcal{E}_0^*(\eta). \qquad \text{(B.35)}
\end{aligned}
$$

We now replace the electrical fields according to Equations (B.28) and (B.29):

$$\mathcal{E}_{LO}^{A*}(x_1)\mathcal{E}_0(x_2) \propto \exp\left(-\frac{x_1^2}{4\sigma_s^2 A^2} - \frac{x_2^2}{4\sigma_s^2 B^2} - \frac{ik}{2R}\frac{x_2^2}{B^2}\right) \tag{B.36}$$

$$\equiv \exp(-v_A x_1^2 - v_B x_2^2) \tag{B.37}$$

where we replaced the terms in the first line according with v_A and v_B in the second line. The second product of electrical fields in Eq. (B.35) is replaced accordingly, so that

$$\frac{1}{4\sigma_s^2 A^2} \rightarrow v_A \tag{B.38}$$

$$\frac{1}{4\sigma_s^2 a^2} \rightarrow v_a \tag{B.39}$$

$$\frac{1}{4\sigma_s^2 B^2} - \frac{ik}{2RB} \rightarrow v_B \tag{B.40}$$

$$\tag{B.41}$$

and

$$S_B^{coh}(d_x, d_p) = \frac{z_0^2}{4\pi^2(Dt)^2}\int d\eta\, d\xi \exp[-i(\eta-\xi)p_x]\exp\left[-\frac{(\eta-\xi)^2}{4Dt}\right]$$
$$\times \exp[-(\eta-d_x)^2 v_A - \xi^2 v_B]\exp[-(\xi-d_x)^2 v_a - \eta^2 v_B^*] \tag{B.42}$$

$$= s_B^{coh}(dx, dp) + \text{c.c.} \tag{B.43}$$

After straight-forwardly solving the two Gaussian integrals we get for the complex beat signal

$$
\begin{aligned}
s_B^{coh}(d_x, d_p) &= \frac{z_0^2}{4(Dt)^2} \frac{\alpha}{v_A + v_B + \beta} \\
&\times \exp\left\{ -d_x^2(v_A + v_a) + \alpha(v_A d_x - i\frac{p_x}{2})^2 \right. \\
&+ \left. \frac{\left[(v_a + \frac{v_A \alpha}{4Dt}) d_x + i 2Dt\beta p_x\right]^2}{v_a + v_B + \beta} \right\}
\end{aligned} \tag{B.44}
$$

where

$$
\alpha = \frac{1}{\frac{1}{4Dt} + v_A + v_B^*} \tag{B.45}
$$

$$
\beta = \frac{1}{4Dt + \frac{1}{v_A + v_B^*}}. \tag{B.46}
$$

Again, the in-phase quadrature signal is the real part of $s_B^{coh}(d_x, d_p)$ in Eq. (B.44), the out-of-phase signal is its imaginary part. Out of conformity, we will use $S_B^{coh}(d_x, d_p)$ instead of $s_B^{coh}(d_x, d_p)$ to denote the complex beat signal.

B.4.2 Complex S_B^{incoh}

In this section we are going to derive the incoherently backscattered light of an EBS field, commonly referred to as the 'incoherent background'. Again, all integrals in the following are two-dimensional; we write dx instead of d^2x for simplicity.

The complex beat signal can be written as

$$
S_B^{incoh}(d_x, d_p) \propto \int dx dp \; W_{LO}(x - d_x, p + k\frac{d_p}{f_0}) \; W_B^{incoh}(x, p) \tag{B.47}
$$

where

$$W_{LO}(x-d_x, p+k\frac{d_p}{f_0}) = \int \frac{dq}{(2\pi)^2} e^{iq(p+k\frac{d_p}{f_0})} \langle \mathcal{E}^*_{LO}(x+\frac{q}{2}-d_x)\, \mathcal{E}_{LO}(x-\frac{q}{2}-d_x)\rangle \quad \text{(B.48)}$$

and

$$W_B^{incoh}(x) = \frac{z_0^2}{(4\pi)^{3/2}(Dt)^{3/2}} \int dx' \int dp' W_0(x', p') exp\left[-\frac{(x-x')^2}{4Dt}\right] \quad \text{(B.49)}$$

with

$$W_0(x', p') = \int \frac{dq'}{(2\pi)^2} e^{iq'p'} \langle \mathcal{E}^*_0(x'+\frac{q'}{2})\mathcal{E}_0(x'-\frac{q'}{2})\rangle. \quad \text{(B.50)}$$

Inserting Equations (B.47)-(B.49) into Eq. (B.50) yields

$$\begin{aligned} S_B^{incoh}(d_x, d_p) &= \frac{1}{(2\pi)^4} \frac{z_0^2}{(4\pi)^{3/2}(Dt)^{5/2}} \int dx dp dx' dp' dq dq' \\ &\times \; e^{iq(p+p_x)} \exp\left[-\frac{(x-x')^2}{4Dt}\right] e^{iq'p'} \\ &\times \; \langle \mathcal{E}^*_{LO}(x+\frac{q}{2}-d_x)\mathcal{E}_{LO}(x-\frac{q}{2}-d_x)\mathcal{E}^*_0(x'+\frac{q'}{2})\mathcal{E}_0(x'-\frac{q'}{2})\rangle. \end{aligned} \quad \text{(B.51)}$$

$\int dp e^{iqp} \int dp' e^{iq'p'}$ are replaced by delta functions, yielding

$$S_B^{incoh}(d_x) = \frac{z_0^2}{(4\pi)^{3/2}(Dt)^{5/2}} \int dx dx' \exp\left[-\frac{(x-x')^2}{4Dt}\right] \langle \mathcal{E}_{LO}^*(x-d_x)\mathcal{E}_0(x')\rangle \langle \mathcal{E}_{LO}(x-d_x)\mathcal{E}_0^*(x')\rangle \tag{B.52}$$

where $\langle ... \rangle\langle ... \rangle = \mid \langle ... \rangle \mid^2$. We again express the mutual coherence functions as the product of the Signal- and LO-fields in Equations (B.28) and (B.29). The product of the electrical fields is of the form as in Eq. (B.30), and again we detect only the cross-terms shown in Eq. (B.31). Replacing the electrical fields in this equations according to Eq. (B.37), we get

$$\begin{aligned} S_B^{incoh}(d_x) &= \frac{z_0^2}{(4\pi)^{3/2}(Dt)^{5/2}} \int dx dx' \exp\left[-\frac{(x-x')^2}{4Dt}\right] \\ &\times \exp[-v_A(x-d_x)^2 - v_B(x')^2 - v_a(x-d_x)^2 - v_B^*(x')^2] \end{aligned} \tag{B.53}$$

Solving the two Gaussian integrals is again very straight-forward; after a few lines of transformation one gets:

$$\begin{aligned} S_B^{incoh}(d_x) &= \sqrt{\frac{\pi}{4}} \frac{z_0^2}{(Dt)^{3/2}} \frac{1}{(v_B + v_B^*)(v_A + v_a)} \\ &\times \exp\left(-\frac{d_x^2}{\frac{1}{v_A+v_a} + \frac{1}{v_B+v_B^*} + 4Dt}\right). \end{aligned} \tag{B.54}$$

Appendix C

C++ codes

C.1 Inverse Margenau-Hill transformation

I wrote the following program code to retrieve the Wigner function from the measured complex beat signal.

```
const ppoints=901;
// insert number of points in p

const xpoints=901;
// insert number of points in x

double x,p, x0,p0, dxmax,dpmax, dxcrop, dpcrop, kcorr, dummy;
double i,j, n,m, nmin,nmax, mmin,mmax, nspan,mspan;
double IPnum[ppoints+1][xpoints+1], OOPnum[ppoints+1][xpoints+1];

FILE *ifp, *jfp, *outfp;

int main(void) {
```

```
// insert dxmax, pxmax
dxmax = 500*9*0.00005;
dpmax = 75*9*0.00005/60*1000; kcorr=9263.1*0.001;

cout << "Fourier transformation of IP and OOP
    into Wigner function\nFrank Reil\n\n";

if (( ifp=fopen("iplist1.dat","r")) == NULL) {
    printf("Can't open iplist.dat\\n");
    exit(1);
    }

if (( jfp=fopen("ooplist1.dat","r")) == NULL) {
    printf("Can't open ooplist.dat\n");
    exit(1);
    }


for(n=1; n<=xpoints; n++){
    for(m=1; m<=ppoints; m++){
    fscanf(ifp, "%lf", &IPnum[int(m)][int(n)]);
    fscanf(jfp, "%lf", &OOPnum[int(m)][int(n)]);
}

}
```

```
nmin = 1;
nmax = xpoints; mmin = 1;
mmax = ppoints; nspan = nmax - nmin;
mspan = mmax - mmin;

if (( outfp=fopen("outlist.dat","w")) == NULL) {
    printf("Can't open iplist.dat\n");
    exit(1);
    }
for(x=-dxmax; x<=dxmax*1.001; x+=0.04*dxmax){
    for(p=-dpmax; p<=dpmax*1.001; p+=0.04*dpmax){
    dummy=0;
    for(n=1; n<=xpoints; n++){
    for(m=1; m<=ppoints; m++){

    dummy += IPnum[int(m)][int(n)]
    *cos(2*kcorr*(x-(2*(n-nmin)/nspan-1)*dxmax)
                *(p-(2*(m-mmin)/mspan-1)*dpmax))
            +OOPnum[int(m)][int(n)]
    *sin(2*kcorr*(x-(2*(n-nmin)/nspan-1)*dxmax)
                *(p-(2*(m-mmin)/mspan-1)*dpmax));
    }
    }
```

```
    fprintf(outfp, "%lf\n",dummy);
    printf("%lf\n",dummy);
    }
    }
    fclose(outfp);

}
```

C.2 Time-resolved single-scattering in transmission

For very dilute solutions, where the mean free path is comparable to or larger than the sample length, the single-scatter model can be applied. Figure C.1 shows a ray entering a sample container of length d from the left, getting scattered once and leaving the container. The path-length in the medium is determined by the chosen path-delay ΔL of corner-cube C_1 in the experiment (see Figure 5.6).

The phase-space coordinates are

$$x = r_1 \sin\theta \tag{C.1}$$

$$p = \sin\theta \tag{C.2}$$

The difference between r_1 and z_1 is just the selected path-delay Δl:

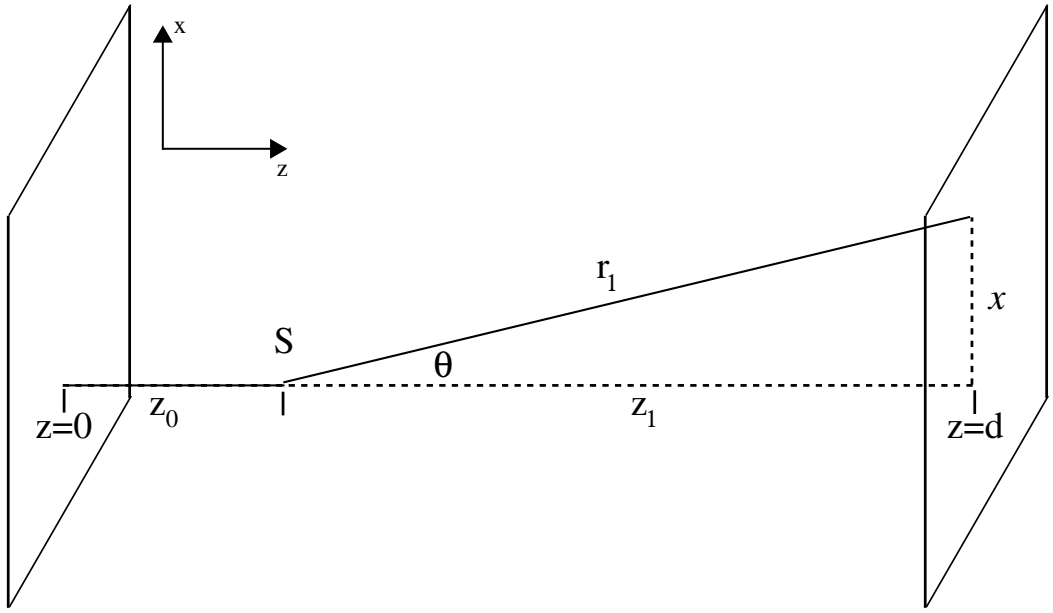

Figure C.1: Single-scattering model. A photon enters the medium on the left, gets scattered once and leaves the medium on the right.

$$r_1 = z_1 + \Delta l = r_1 \cos\theta + \Delta l \tag{C.3}$$

so that

$$r_1 = \frac{\Delta l}{1 - \cos\theta} \tag{C.4}$$

x can then be expressed as a function of p and Δl only by inserting Eq. (C.4) into Eq. (C.1):

$$
\begin{aligned}
x &= r_1 \sin\theta \\
&= \Delta l \frac{\sin\theta}{1-\cos\theta} \\
&= \Delta l \frac{1+\cos\theta}{\sin\theta} \\
&= \Delta l \frac{1+\sqrt{1-(p/k)^2}}{p/k} \\
&= \Delta l \left(\frac{1}{p/k} + \sqrt{\frac{1}{(p/k)^2} - 1} \right) \qquad \text{(C.5)} \\
&\approx \Delta l \frac{2}{p/k}, \quad (p/k)^2 \ll 1 \qquad \text{(C.6)}
\end{aligned}
$$

which is a hyperbola. The approximation in Eq. (C.6) has an accuracy of better than 1% for the momentum range we measure. Figure 13.4(c) shows a plot of Eq. (C.5) for a path-delay of $\Delta l = 100$ μm in air. The valid range for Eq. (C.5) is restricted by the cell size d:

$$
r_1 \cos\theta < d \qquad \text{(C.7)}
$$

which is equivalent to

$$
\frac{1}{\sqrt{1-(p/k)^2}} - 1 > \frac{\Delta l}{d}. \qquad \text{(C.8)}
$$

C.2.1 Calculation of x_{max}

The transverse position x can be expressed as a function of z_1:

$$
x^2 = r_1^2 - z_1^2 = (z_1 + \Delta l)^2 - z_1^2. \qquad \text{(C.9)}
$$

Simplifying yields

$$x = \sqrt{2z_1\Delta l + (\Delta l)^2} \tag{C.10}$$

Eq. (C.10) shows that the earlier the photon scatters, the larger the transverse position of the scattered photon at the sample output plane. The maximal transverse position x_{max} results when the photon scatters right after entering the turbid medium, i.e. for $z_1 = L = 10$mm:

$$x_{max} = \sqrt{2L\Delta l + (\Delta l)^2}. \tag{C.11}$$

C.3 Time-resolved double-scattering in transmission

The time-dependent Double-Scattering algorithm I developed is a Monte-Carlo computer algorithm that calculates the intensity at the sample output as a function of position and momentum for an incident light ray, as a function of path delay. The output intensity of a finite-sized collimated beam can then be calculated by convolving the input beam numerically with the calculated 'Green-function'.

Figure C.2 shows two scatterers in a sample container of length d. The ray comes in from the left, scatters at the first scatterer S_1 at z_0 and then at the second scatterer S_2 at $z_0 + z_1$. From there it travels to the output surface and leaves the medium.

The intensity distribution at $z = d$ is rotationally invariant with respect to ϕ_1, we therefore choose $\phi_1 = \pi/2$, which fixed the scattering at S_1 in the $y - z$-plane, and rotate the intensity distribution after the rest of the calculation is done.

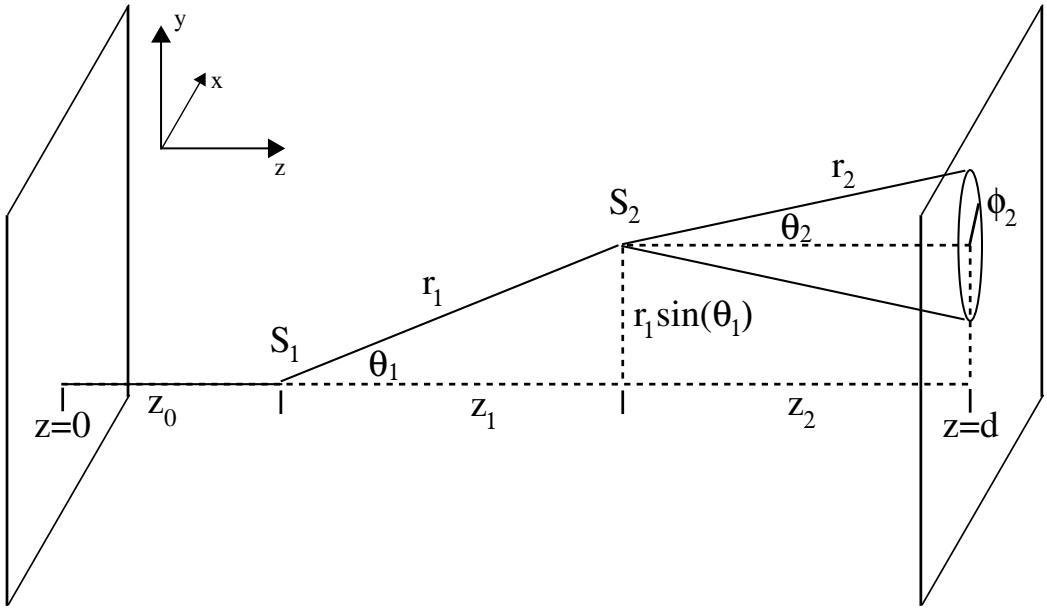

Figure C.2: Double-scattering model. A photon enters the medium on the left, gets scattered twice and leaves the medium on the right.

After scattering at S_2, the range of allowed paths r_2 to the sample output plane is narrowed down to those forming a cone between S_2 and a circular cone at $z = d$ by two constraints:

1. The chosen path delay Δl requires that $r_2 = \Delta l - r_1 + z_1 + z_2$ for the photon to be detected

2. The chosen observation place at $z = d$ requires $r_2 \cos\theta_2 = z_2$, this is the circular intersection between the sphere defined by 1. with S_2 in the center and the plane defined by $z = d$.

For a given z_0, θ_1 and r_1, all other parameters are determined (z_1, z_2, r_2 and θ_2), assuming of course that Δl and d are fixed and known.

We thus have two conditions:

$$
\begin{aligned}
r_2 &= \Delta l - r_1 + z_1 + z_2 && \text{(C.12)} \\
z_2 &= d - z_0 - z_1 \\
&= d - z_0 - r_1 \cos\theta_1 && \text{(C.13)}
\end{aligned}
$$

which determines sine and cosine of θ_2:

$$
\begin{aligned}
\sin\theta_2 &= \frac{\sqrt{r_2^2 - z_2^2}}{r_2} && \text{(C.14)} \\
\cos\theta_2 &= \frac{z_2}{r_2} && \text{(C.15)}
\end{aligned}
$$

The relative angle between unit vectors $\hat{r}_1$ and $\hat{r}_2$ which is necessary to calculate the phase function, i.e. the relative intensity of the ray scattering at S_2, can be calculated through its directional cosine:

$$
\begin{aligned}
\angle(\hat{r}_1, \hat{2}) &= \hat{r}_1 \cdot \hat{r}_2 = (0, \sin\theta_1, \cos\theta_1) \begin{pmatrix} \sin\theta_2\cos\phi_2 \\ \sin\theta_2\sin\phi_2 \\ \cos\theta_2 \end{pmatrix} \\
&= \sin\theta_1\sin\theta_2\sin\phi_2 + \cos\theta_1\cos\theta_2 \\
\angle(\hat{r}_1, \hat{r}_2) &= \arccos(\sin\theta_1\sin\theta_2\sin\phi_2 + \cos\theta_1\cos\theta_2) && \text{(C.16)}
\end{aligned}
$$

Finally, x and y on the sample output plane are

$$x = \sqrt{\vec{r}_2^2 - z_2^2}\cos\phi_2 \tag{C.17}$$

$$y = \sqrt{\vec{r}_2^2 - z_2^2}\sin\phi_2 + r_1\sin\theta_1 \tag{C.18}$$

The intensity contribution by a ray with the initial parameters z_0,r_1 and $theta_1$ is then

$$U(z_0, r_1, \theta_1; \phi_2) = p(z_0)f(\theta_1)p(r_1)f[\angle(\hat{r}_1, \hat{r}_2)]p(r_2) \tag{C.19}$$

where $p(z_0)$, $p(r_1)$ and $p(r_2)$ are the probabilities not to scatter over their respective distances. $p(z)$ is proportional to $e^{-\frac{z}{l}}$, where l is the mean free path. Since z_0+r_1+r_2 is constant for fixed Δl and d, the product of the probabilities is constant as well and can be neglected.

$f(\theta_1)$ and $f[\angle(\hat{r}_1, \hat{r}_2)]$ are the relative intensities after scattering over the respective angle. They can be approximated to a good degree as Gaussian. The only remaining free parameter is ϕ_2 which is included in $\angle(\hat{r}_1, \hat{r}_2)$. Neglecting the probabilities p as announced we rewrite Eq. (C.19):

$$U(z_0, r_1, \theta_1; \phi_2) = f(\theta_1)f[\arccos(\sin\theta_1\sin\theta_2\sin\phi_2 + \cos\theta_1\cos\theta_2)] \tag{C.20}$$

We now numerically assume all possible and reasonable values for z_0, r_1, θ_1 and ϕ_2 and calculate the resulting two-dimensional positions and momenta in the sample output plane:

$$x(z_0, r_1, \theta_1; \phi_2) = \sqrt{r_2^2 - (d - z_0 - r_1 \cos\theta_1)^2}\cos(\phi_2) \quad \text{(C.21)}$$

$$y(z_0, r_1, \theta_1; \phi_2) = \sqrt{r_2^2 - (d - z_0 - r_1 \cos\theta_1)^2}\sin(\phi_2) + r_1 \sin\theta_1 \quad \text{(C.22)}$$

$$p_x(z_0, r_1, \theta_1; \phi_2) = \sin\theta_2 \cos\phi_2 = \sqrt{1 - \frac{z_2^2}{r_2^2}}\cos\phi_2 \quad \text{(C.23)}$$

$$p_y(z_0, r_1, \theta_1; \phi_2) = \sin\theta_2 \sin\phi_2 = \sqrt{1 - \frac{z_2^2}{r_2^2}}\sin\phi_2 \quad \text{(C.24)}$$

z_2 and r_2 can be expressed in terms of z_0, r_1 and θ_1. The resulting values (x, y, p_x, p_y) are, as mentioned, for a fixed angle ϕ_1. In our experiment, we measure the (x, p)-distribution along a line through the center of the expected rotationally symmetrical intensity distribution. We integrate over all ϕ_1 by lumping all (x, y) into the same variable r:

$$r(z_0, r_1, \theta_1; \phi_2) = \sqrt{x^2(z_0, r_1, \theta_1; \phi_2) + y^2(z_0, r_1, \theta_1; \phi_2)} \quad \text{(C.25)}$$

and define the momenta with respect to this 'radius'-variable as well:

$$p_r = p_x * |\frac{x}{r}| + p_y * |\frac{y}{r}| \quad \text{(C.26)}$$

Writing (r, p_r) into a two-dimensional array we get the phase-space intensity distribution for all z_0, r_1, θ_1 and ϕ_2. The resulting array can be read in and displayed by a Mathematica program, for example. The next section contains the C++ code of the Monte-Carlo algorithm just described.

C.3.1 C++ Code

```
#include <iostream> #include <math.h> #include <stdio.h>


using namespace std;


// good values are:
//  thetamax:   7*theta0
//  zstep:      zmax/40
//  r1step:     r1max/40
//  phi2step:   0.005;
//  theta1step: theta0/80


const double Pi=3.1415926;
const double mu =   3.33; // transport mean free path [mm]
const double lstar = 1.96;  // mean free path [mm]
const double theta0 = 0.412;
// angular width [rad] of scatter, was 0.0396 until Oct 5,02
const double thetamax = 10*theta0;
// [rad] upper bound for theta we use const
double thetamaxsq = pow(thetamax,2);
const double d=10;
// length of sample [mm]
const double dell=0.1/1.33; // path delay [mm]
const double zmin = 0.01*lstar; // [mm]
const double zmax = d; // [mm]
```

```
const double zstep=zmax/57;
// constant makes for loop faster
const double r1min = 0.1*lstar;
const double r1max = 2.43*d; // was d
const double r1step=r1max/49
const double phi2step=0.007; // was 0.005
const double theta1step=theta0/110;
double z0,z1,z2, r1,r2, theta1, theta2, phi2, rho1, rho2;
double x, y, r, px, py, pr;
double sintheta1,costheta1, sintheta2, costheta2, sinphi2, cosphi2;
double integphi1, integphi, spatpartial, rperp;
double shift, beamradi, bsteps, expfac;
double U[600][600]; // [r,px]

int rintel, pintel; int cr;

FILE *Ufp, *Vfp;



int main(void) { cout << "Monte-Carlo Simulation of two-scatter events
in turbid medium, time resolved\nFrank Reil\n\n";

if (( Ufp=fopen("outarray.dat","w")) == NULL) {
    printf("Can't open outarray.dat\n");
    exit(1);
```

```
    }

if (( Vfp=fopen("genauarray.dat","w")) == NULL)
    { printf("Can't open genauarray.dat\n"); exit(1); }

for(z0=zmin; z0<zmax; z0+=zstep) {
    printf("z0 = %lf*d\n ...",z0/d);
    for(theta1=-thetamax; theta1<thetamax; theta1+=theta1step)
    sintheta1 = sin(theta1);
    costheta1 = cos(theta1);
        for(r1=0; r1<r1max; r1+=r1step) {
            z1=r1*costheta1;
            z2 = d - z0 - z1;
            if (z2>0) {
            r2 = z1 + z2 + dell - r1;

            if (z2<=r2) { // r2<0 statement superfluous

            spatpartial = exp(-z0/mu)*(1-exp(-z0/mu)) * exp(-r1/mu)
                    *(1-exp(-r1/mu)) * exp(-r1/mu)*(1-exp(-r1/mu));
                         // replaced r2 by r1
            sintheta2 = sqrt(1 - pow(z2,2)/pow(r2,2));
            costheta2 = z2/r2;

            rperp = sqrt(pow(r2,2) - pow(z2,2));
```

```
for(phi2=-Pi; phi2<=Pi; phi2+=phi2step)
{ // that will give all radii with x positive !
 cosphi2 = cos(phi2);
 sinphi2 = sin(phi2);
 if (rperp*sinphi2 + r1*sin(theta1) > 0) {
 integphi=exp(-pow(acos(sintheta1*sinphi2*sintheta2
            + costheta1*costheta2),2)/thetamaxsq);
 integphi1=exp(-pow(theta1,2)/thetamaxsq);
x = rperp*sinphi2 + r1*sin(theta1);
y = rperp*cosphi2;
r = sqrt(pow(y,2) + pow(x,2));
px = sintheta2*cosphi2;
py = sintheta2*sinphi2;
pr = px*abs(x/r) + py*abs(y/r);
// projection of (px,py) on r, where we measure everything.
// should be independent of sign of x and y
if (pr<15000000 && pr>0) {
U[int(r*74)][300+int(pr*50000)]
    +=1000000*integphi*integphi1*spatpartial;}
} // if (rperp*sinphi2 + r1*sin(theta1) > 0)
} // phi2-loop
} // if (z2<=r2)

} // if (z2>0)
```

```
            } // r1-forloop
    }
}


beamradi=0.1/1 * 74; // intensity: radius in mm times 100 pts/mm
 bsteps = beamradi/20;

for (shift=-2*beamradi; shift<=2*beamradi; shift+=bsteps) {
    expfac = exp(-pow(shift/beamradi,2)); // Gaussian factor
    for (rintel=0; rintel<=200; rintel++) {
        if (rintel+shift > 0) {
            for (pintel=200; pintel<=400; pintel++) {
            U[rintel][pintel]+=U[rintel+int(shift)][pintel]*expfac;
        }
    }
} }

for(rintel=0; rintel<=200; rintel++)
    { for(pintel=200; pintel<=400; pintel++) {    //  300 is px=0
fprintf(Ufp, "%lf\n", U[rintel][pintel]);
} } fclose(Ufp);
```

Appendix D

Speckle

Figure D.1 shows the quadrature signals for a scan of a speckle field which was generated by shining a Gaussian SLD beam on to a glass containing tiny air bubbles. The smallest range (bottom row) presents a view inside a speckle; the product of position- and momentum range is

$$0.5\,\mathrm{mm} \times 1.3\,\mathrm{mrad} = 650\,\mathrm{nm} \tag{D.1}$$

which is smaller than the wavelength of 678.3 nm we use. The same phase-space are scanned by only the BLO and only the SLO is shown in Figure D.2. Clearly, the resolution provided by a single LO is not sufficient to resolve the speckle. The Wigner function retrieved from the quadrature signals in Figure D.1 is shown in Figure D.3.

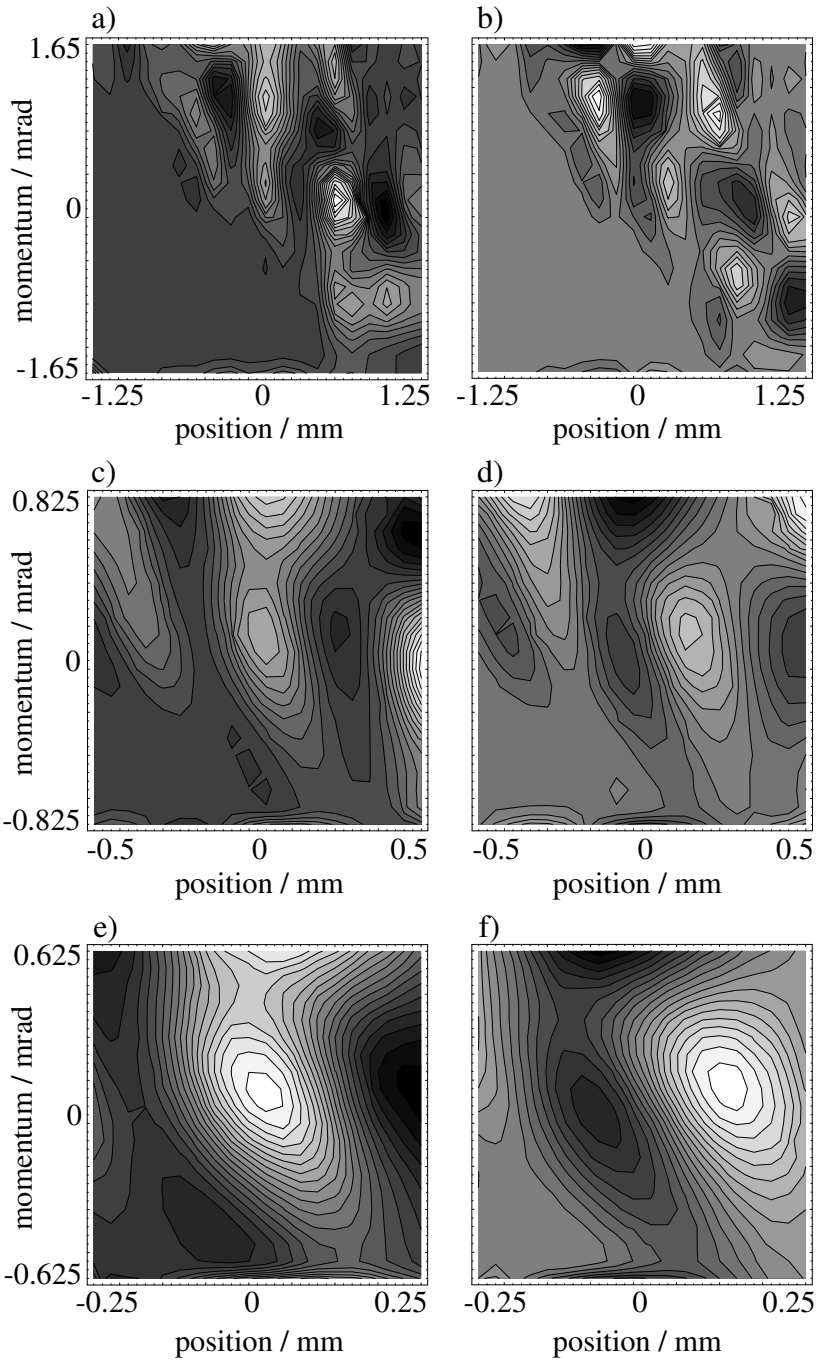

Figure D.1: Quadrature signal phase-space profiles of a speckle field generated by a SLD beam incident on a piece of glass containing air bubbles. Left columns: in-phase signal, right columns: out-of-phase signal; increasing magnification from top to bottom.

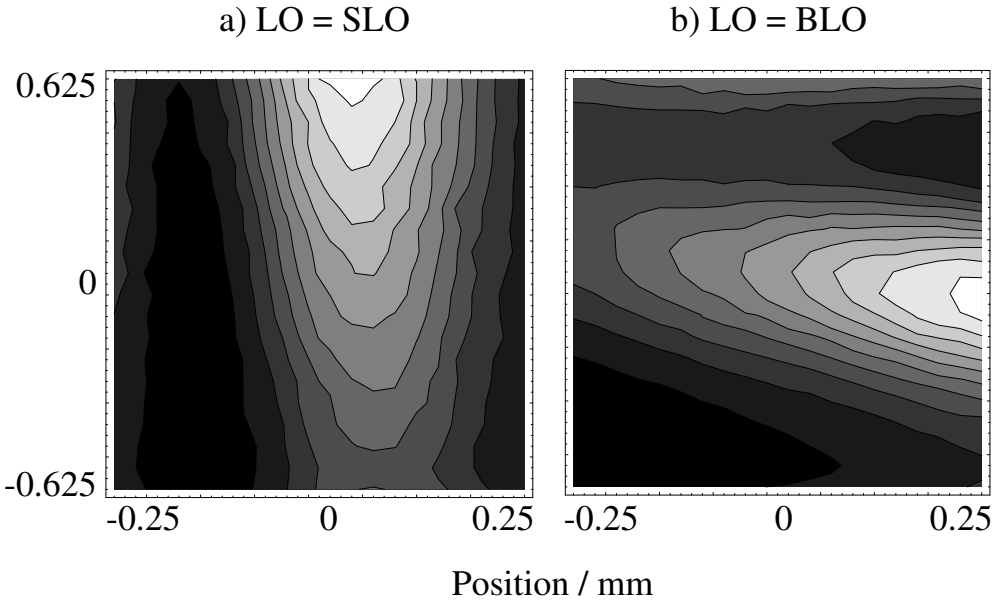

Figure D.2: Single LO-scans of the speckle field shown in Figure D.1e) and f). a) SLO only and b) BLO only.

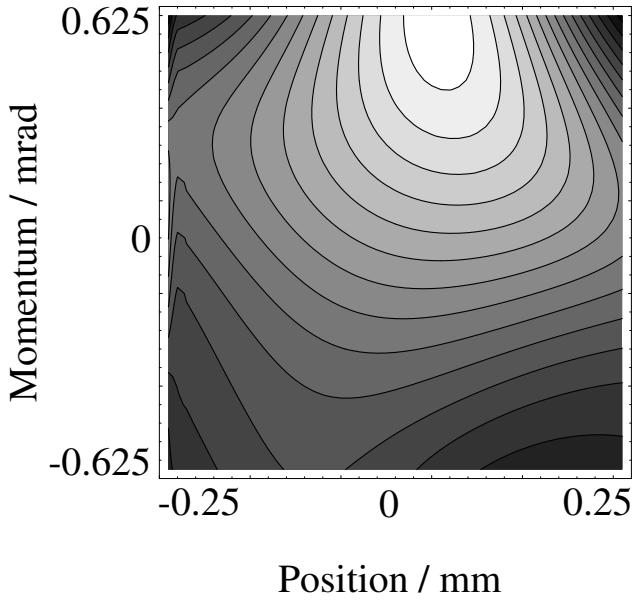

Figure D.3: Wigner function of speckle field shown in Figure D.1e) and f).

Bibliography

[1] K. F. Lee, F. Reil, S. Bali, A. Wax, and J. E. Thomas. Heterodyne measurement of wigner distributions for classical optical fields. *Opt. Lett.*, 24:1370, 1999.

[2] A. Wax, S. Bali, G. A. Alphonse, and J. E. Thomas. Characterizing the coherence of broadband sources using optical phase space contours. *J. Biomed. Opt.*, 4:482, 1999.

[3] A. Wax, S. Bali, and J. E. Thomas. Optical phase-space distributions for low-coherence light. *Opt. Lett.*, 24:1188, 1999.

[4] A. Wax, S. Bali, and J. E. Thomas. Time-resolved phase-space distributions for light backscattered from a disordered medium. *Phys. Rev. Lett.*, 85:66, 2000.

[5] A. Wax. Optical phase space distributions for coherence tomography. *Ph.D. Dissertation, Duke University, 1999, unpublished.*

[6] S. K. Gayen, M. E. Zevallos, B. B. Das, and R. R. Alfano. Time-sliced transillumination imaging of normal and cancerous breast tissues. *OSA Trends in Optics and Photonics on Advanaces in Optical Imaging and Photon Migration*, 21:63–66, 1998.

[7] H. Rinneberg, D. Grosenick, H. Wabnitz, H. Danlewski, K. Moesta, and P. Schlag. Time-domain optical mammography: results on phantoms, healthy volunteers and patients. *OSA Trends in Optics and Photonics on Advanaces in Optical Imaging and Photon Migration*, 21:278–280, 1998.

[8] J. C. Hebden and S. R. Arridge. Imaging through scattering media by the use of an analytical model of perturbation amplitudes in the time domain. *Appl. Opt.*, 35:6788–6796, 1996.

[9] Jeremy C. Hebden. http://www.medphys.ucl.ac.uk/research/borg/research /fundedprojects/jemfell.htm. Website.

[10] K. M. Yoo and R. R. Alfano. Time-resolved coherent and incoherent components of forward light scattering in random media. *Opt. Lett.*, 15:320–322, 1990.

[11] M. S. Patterson, B. Chance, and B. C. Wilson. Time resolved reflectance and transmittance for the non-invasive measurement of tissue optical properties. *Appl. Opt.*, 28:2331–2336, 1989.

[12] K. M. Yoo, B. B. Das, and R. R. Alfano. Imaging of a translucent object hidden in a highly scattering medium from the early portion of the diffusive component of a transmitted ultrafast laser pulse. *Opt. Lett.*, 17:958–960, 1992.

[13] Hamamatsu Co. Streak cameras and their features, http://usa.hamamatsu.com/sys-streak/operating/default.htm. Website.

[14] L. Wang, P. P. Ho, X. Liang, H. Dai, and R. R. Alfano. Kerr-fourier imaging of hidden objects in thick turbid media. *Opt. Lett*, 18:241–243, 1993.

[15] L. Wang, P. P. Ho, C. Liu, G. Zhang, and R. R. Alfano. Ballistic 2-d imaging through scattering walls using and ultrafast opical kerr gate. *Science*, 253:769–771, 1991.

[16] Y. Wang J. Wu, L. Perelman, I. Itzkan, R. R. Dasari, and Michael Feld. Time-resolved multichannel imaging of fluorescent objects embedded in turbid media. *Opt. Lett.*, 20:489–491, 1995.

[17] A. Yodh and B. Chance. Spectroscopy and imaging with diffusing light. *Physics Today*, 48(3):34–40, 1995.

[18] M. A. O'Leary, D. A. Boas, B. Chance, and A. G. Yodh. Refraction of diffuse photon density waves. *Phys.Rev.Lett.*, 69:2658–2661.

[19] D. A. Boas, M. A. O'Leary, B. Chance, and A. G. Yodh. Scattering and wavelength transduction of diffuse photon density waves. *Phys. Rev. E*, 47:2999–3002, 1993.

[20] J. M. Schmitt, A. Knuttel, and J. R. Knutson. Interference of diffusive light waves. *J. Opt.Soc.Am.A*, 9:1832–1843, 1992.

[21] B. W. Pogue, M. Testorf, U. L. Osterberg, and K. Paulsen. Development of quantitative imaging in frequency-domain diffuse optical tomography for breast cancer detection. *OSA Trends in Optics and Photonics on Advances in Optical Imaging and Photon Migration*, 21:245–250, 1998.

[22] X. D. Li, J. P. Culver, T. Durduran, B. Chance, A. G. Yodh, and D. N. Pattanayak. Diffraction tomography with diffuse photon density waves: Clinical studies and background subtraction. *OSA Trends in Optics and*

Photonics on Advances in Optical Imaging and Photon Migration, 21:281–283, 1998.

[23] S. Fantini, S. A. Walker, M. A. Franceschini, A. E. Cerussi, J. Edler, K. T. Moesta, P. M. Schlag, M. Kaschke, and E. Gratton. Optical characterization of breast tumors by frequency-domain optical mammography. *OSA Trends in Optics and Photonics on Advances in Optical Imaging and Photon Migration*, 21:289–293, 1998.

[24] Kottan Labs. http://kottan-labs.bgsu.edu/presentations/modspec1-wg.htm. Website.

[25] Florida State University. http://www.microscopy.fsu.edu/primer/techniques /fluorescence/multiphoton/multiphotonhome.html. Website.

[26] Kentech Company. http://www.kentech.co.uk/fluorlifeimage.html. Website.

[27] W. M. Keck Center for Cellular Imaging/University of Virginia. http://www.cci.virginia.edu/flimtheory.html. Website.

[28] The Photonics Center. http://www.thephotonicscenter.com/new/laboratories. Website.

[29] W. M. Keck Center for Cellular Imaging/University of Virginia. http://www.cci.virginia.edu/decon.html. Website.

[30] Worcester Polytechnic Institute N. Kildahl. http://www.wpi.edu/academics/depts/chemistry/courses /ch2670/infrared.html. Website.

[31] Michigan State University William Reusch. http://www.cem.msu.edu/ reusch/OrgPage/VirtualText/Spectrpy/ InfraRed/infrared.htm. Website.

[32] Inphotonics.com. http://www.inphotonics.com/raman.htm. Website.

[33] Austria FELMI-ZFE, Technische Universitaet Graz. http://www.cis.tugraz.at/felmi/researchraman.html. Website.

[34] Physics Department at University of Parma Danilo Bersani. http://www.fis.unipr.it/ bersani/raman/raman/ramtutor.htm. Website.

[35] Robert H. Webb. Confocal optical microscopy. *Rep. Prog. Phys.*, pages 427–471, 1996.

[36] W. M. Keck Center for Cellular Imaging/University of Virginia. http://www.cci.virginia.edu/confocaltheory.html. Website.

[37] Digital Instruments. Applications to atomic force microscopy, http://www.veeco.com/pdf/clmain.pdf. Website, 1998/99.

[38] Joseph A. Izatt, Manish D. Kulkarni, Kenji Kobayashi, Michael V. Sivak, Jennifer K. Barton, and Ashley J. Welch. Optical coherence tomography for biodiagnostics. *Optics & Photonics News*, pages 41–47, May 1997.

[39] J. A. Izatt and M. D. Kulkarni. Doppler flow imaging using optical coherence tomography. *presented at OSA Conference on Lasers and Electro-Optics, Anaheim, CA, 1006, post-deadline paper CPD3-1.*

[40] Z. Chen et. al. Optical doppler tomographic imaging of fluid flow velocity in highly scattering media. *Opt. Lett.*, 22:64–66, 1997.

[41] Martin J. Bastiaans. Application of the wigner distribution function to partially coherent light. *J. Opt. Soc. A*, 3:1227, 1986.

[42] Chung-Chieh Cheng and M. G. Raymer. Long-range saturation of spatial decoherence in wave-field transport in random multiple-scattering media. *Phys. Rev. Lett.*, 82:4807, 1999.

[43] Leonard Mandel and Emil Wolf. *Optical Coherence and Quantum Optics*. Cambridge University Press, 1995.

[44] Charles Kittel and Herbert Kroemer. *Thermal physics*. W.F. Freeman and Company, 1980.

[45] Martin J. Bastiaans. Second-order moments of the wigner distribution function in first-order optical systems. *Optik*, 88:163–168, 1991.

[46] A. Wax and J. E. Thomas. Optical heterodyne imaging and wigner phase space distributions. *Opt. Lett*, 21:1427–1429, 1996.

[47] Melles Griot. Tutorial. Catalog.

[48] photonics.com. Tutorial, http://www.photonics.com. Website.

[49] email exchange with Vladimir Shidlovski from Superlum Co.

[50] Peter W. Milonni and Joseph H. Eberly. *Lasers*. John Wiley and Sons, 1988.

[51] V. K. Batovrin, I. A. Garmash, V. M. Gelikonov, G. V. Gelikonov, A. V. Lyubarskii, A. G. Plyavenek, S. A. Safin, A. T. Semonov, V. R. Shidlovskii, M. V. Shramenko, and S. D. Yakubovich. Superluminescent diodes based on single-quantum-well (gaal)as heterostructures. *Quantum electronics*, 26(2):109–114, 1996.

[52] Akira Ishimaru. *Wave propagation and scattering in random media.* Academic press, 1978.

[53] M. Kerker. *The Scattering of Light and Other Electromagnetic Radiation.* Academic Press, 1969.

[54] Craig F. Bohren and Donald R. Huffman. *Absorption and scattering of light by small particles.* Wiley-Interscience, 1983.

[55] Diederik S. Wiersma, Paolo Bartolini, Ad Lagendijk, and Roberto Righini. Localization of light in a disordered medium. *Nature*, 390:671–673, 1997.

[56] P. W. Anderson. The question of classical localization: a theory of white paint? *Phil. Mag. B*, 52:505–509, 1095.

[57] E. Abrahams, P. W. Anderson, D. C. Licciardello, and T. V. Ramakrishnan. Scaling theory of localization: absence of quantum diffusion in two dimensions. *Phys. Rev. Lett*, 42:673–676, 1979.

[58] N. F. Mott. *Metal-Insulator Transitions.* Taylor and Francis, 1974.

[59] M. van Albada and A. Lagendijk. Observation of weak localization of light in a random medium. *Phys. Rev. Lett.*, 55:2692, 1985.

[60] P. E. Wolf and G. Maret. Weak localization and coherent backscattering of photons in disordered media. *Phys. Rev. Lett.*, 55:2696, 1985.

[61] M. Kaveh, M. Rosenbluh, I. Edrei, and I. Freund. Weak localization and light scattering from disordered solids. *Phys. Rev. Lett*, 57:2049–2052, 1986.

[62] E. Akkermans, P. E. Wolf, R. Maynard, and G. Maret. Theoretical study of the coherent backscattering of light by disordered media. *J. Phys. (Paris)*, 49:77, 1988.

[63] Ping Sheng. *Introduction to Wave Scattering, Localization, and Mesoscopic Phenomena.* Academic Press, Inc., 1995.

[64] L. Tsang and A. Ishimaru. *J. Opt. Soc. Am.*, A 2:1331, 1985.

[65] D. Lacoste and B. A. van Tiggelen. Coherent backscattering of light in a magnetic field. *Phys. Rev. E*, 61:4556–4565, 2000.

Biography

Frank Reil was born and grew up in Münster, Germany on June 23, 1970. He graduated from Gymnasium Kinderhaus in 1989 and served in the military from June 1989 until late summer 1990. Frank enrolled in the physics program at the Westfälische Wilhelms-Universität Münster in the fall of 1990 and received his Vordiplom in 1993. He started working on his Diplom thesis in the research group of Professor Hans-Georg Purwins at the Institute of Applied Physics in the spring of 1994, investigating the interaction of laser radiation with *pnpn*-semiconductor structures. After receiving his Diplom in 1995, Frank worked as a research assistant in the same group until summer 1996. In September 1996 he enrolled in the graduate physics program at Duke University. After finishing the required course work and gaining teaching experience as a Teaching Assistant, he began his Ph.D. work in the research group of Professor John Thomas in September 1998, where he characterized light fields propagating through turbid media by means of a newly developed Two-Window heterodyne technique. He received his M.A. in May 1999 and his Ph.D. in April 2003, both in Physics.

Publications

F. Reil and J. E. Thomas. Heterodyne techniques for characterizing light fields. Book chapter 9 in *Coherent-Domain Optical Methods for Biomedical Diagnostics, Environmental and Material Science - Volume 1.* Ed.: Valery V. Tuchin (to be published).

F. Reil and J. E. Thomas. Measurement of time-resolved Wigner functions for coherent backscatter from a turbid medium:, *SPIE-Int. Soc. Opt. Eng. in Trends in Optics and Photonics Series, Biomedical Topical Meetings*. 71:(page numbers not known yet), 2002.

F. Reil and J. E. Thomas. Time-resolved, Two-Window measurement of Wigner functions for Coherent Backscatter from a Turbid Medium. *SPIE-Int. Soc. Opt. Eng. in Coherent Optics of Ordered and Random Media II*. 4705:22-29, 2001.

K. F. Lee, F. Reil and J. E. Thomas. Classical wave analog of quantum state measurement. *Quantum Electronics and Laser Science Conference (QELS' 2001) Technical Digest*.

F. Reil, K. F. Lee and J. E. Thomas. Two-window heterodyne methods for measurement of optical coherence in multiple scattering media. *Quantum Electronics and Laser Science Conference (QELS' 2001) Technical Digest*.

A. Wax, F. Reil, K. F. Lee, S. Bali and J. E. Thomas. Time-resolved Optical Phase Space Distributions for Coherent Backscatter. *Proc. SPIE-Int. Soc. Opt. Eng. in Optical Technologies in Biophysics and Medicine*. 4001:130-134, 2000.

J. E. Thomas, F. Reil, K. F. Lee, A. Wax and S. Bali. Wigner phase space distribution and coherence tomography. *Proc. SPIE-Int. Soc. Opt. Eng. in Optical Pulse and Beam Propagation II*. 3927:147-155, 2000.

K. F. Lee, F. Reil, S. Bali, A. Wax and J. E. Thomas. Heterodyne measurement of Wigner distributions for classical optical fields. *Optics Letters*, 24:1370-1372, 1999.

B. Kukuk, F. Reil, F.-J. Niedernostheide and H.-G. Purwins. Interaction of Laser Radiation and PNPN Semiconductor Devices. *Self-Organization in Activator-Inhibitor-Systems: Semiconductors, Gas-Discharge, and Chemical Active Media*, Eds.: H. Engel, F.-J. Niedernostheide, H.-G. Purwins and E. Schll. Wissenschaft- und Technik-Verlag Berlin, 62-66, 1996.

Presentations

"Measurement of time-resolved Wigner functions for coherent backscatter from a turbid medium", F. Reil and J. E. Thomas, The 2nd Annual Meeting of the Fitzpatrick Center, Duke University, Durham, NC, 2002.

"Measurement of time-resolved Wigner functions for coherent backscatter from a turbid medium", F. Reil and J. E. Thomas, Biomedical Topical Meetings, Miami Beach, FL, 2002.

"Time-resolved, Two-Window measurement of Wigner functions for Coherent Backscatter from a Turbid Medium", F. Reil and J. E. Thomas, Webtalk, Saratov Fall Meeting 2001, Russia.

"Two-window heterodyne methods for measurement of optical coherence in multiple scattering media", F. Reil and J. E. Thomas, Quantum Electronics and Laser Science Conference (QELS' 2001), Baltimore, MD, 2001.